Gas Adsorption Studies on Vertically Aligned Carbon Nanotubes

Dissertation von Deepu J. Babu aus Kerala, Indien
September 2016, Darmstadt

TECHNISCHE
UNIVERSITÄT
DARMSTADT

Fachbereich Chemie
Eduard-Zintl-Institut für Anorganische und Physikalische Chemie

Gas Adsorption Studies on Vertically Aligned Carbon Nanotubes

Vom Fachbereich Chemie

der Technischen Universität Darmstadt

zur Erlangung des akademischen Grades eines

Doctor rerum naturalium (Dr. rer. nat.)

genehmigte

Dissertation

vorgelegt von

M.S. Deepu J. Babu
aus Kerala, Indien

Referent:	**Prof. Dr. Jörg J. Schneider**
Korreferenten:	**Prof. Dr. Florian Müller-Plathe**
	Prof. Dr. Michael Fröba (Universität Hamburg)
Tag der Einreichung:	14. September 2016
Tag der mündlichen Prüfung:	07. November 2016

Darmstadt 2016

D 17

Deepu J. Babu
Roßdörferstr. 48
64287 Darmstadt

Datum: 14.09.16

Erklärung

Ich erkläre hiermit, dass ich meine Dissertation selbstständig und nur mit den angegebenen Hilfsmitteln angefertigt habe.

Deepu

Deepu J. Babu

Deepu J. Babu

Roßdörferstr. 48

64287 Darmstadt

Datum: 14.09.16

Erklärung

Ich erkläre hiermit, noch keinen Promotionsversuch unternommen zu haben.

Deepu

Deepu J. Babu

Acknowledgment

I express my sincere gratitude towards **Prof. Dr. Jörg J. Schneider** for his constant support and guidance during the course of my phd work. It was a great learning experience with him and undoubtedly I benefited from his experience as a teacher, a guide and an editor. He was always approachable and open to new ideas. I am thankful for the flexibility he offered in research and the trust he placed in me.

I express my gratitude to **Prof. Reiner Staudt** for his valuable suggestions and discussions regarding the adsorption measurements. I thankfully recall the help he extended in getting the initial high pressure measurements done on CNT which later paved the way for the high pressure adsorption studies. His support and guidance were crucial in the design and development of the volumetric setup.

I am grateful to **Prof. Florian Müller-Plathe**, **Prof. Jayant K. Singh** and **Dr. Mahshid Rahimi** for the collaborative work and fruitful discussions. These exchanges helped me gain a deeper insight and provided an additional dimension to the work. The collaborations were always hassle free and it was a pleasure working with them.

I am indebted to **Dr. Gennady Cherkashinin** and **Dr. Michael Bruns** for the XPS measurements, **Dr. Jörg Engstler** and **Dr. Reinhard Schneider** for the TEM measurements and **Dr. Rudolf Hoffmann** for help with the TG setup.

I am grateful to my group mates **Tobias Wombacher**, **Peter Krauß**, **Tim Herdt**, **Sandeep Yadav**, **Shawn Sanctis**, **Sherif Okeil**, **Jonathan Stott**, **Silvio Heinschke**, **Jan Krausmann**, **Dr. Mikhail Pashchannka**, **Dr. Mathias Nowotny**, **Ildiko Balog**, **Ute Schmidt** and ex-colleagues **Dr. Ravi Joshi**, **Dr. Hermann Tempel** and **Dr. Julia Patzsch** for their support and making these past years memorable.

I extend my special gratitude to my friends **Felix Roth**, **Katharina Schön**, **Dr. Ditty Dixon**, **Dr. V. S. Namboodiri**, **Sharath S.U.**, **Tamal Roy**, **Stephen George** and **Deepak P. V.** for the help they have rendered at crucial times.

I express my deepest gratitude towards my parents for their unwavering support and constant source of inspiration. Their prayers and blessings are the source of my strength. I am indebted to my brother, sisters and in-laws for their love, support and encouragement. Last but not the least, I extend my sincere gratitude to my better half: Mrs. Merin Jissy Joseph. Her motivation and support played a major role in the progress of my work. Even during her own busy Master's curriculum, she was never reluctant to offer her help and made sure my work never suffered.

I hope I have not overlooked anyone but if I have, its not for the lack of appreciation.

"For I am not a special sapling
but nurtured in the warmth and love of my beloved ones
& like a leaf, I stay humble"

Zusammenfassung

Kohlenstoffbasierte Adsorptionsmittel zählen zu den gängigsten Adsorbenzien. Dies beruht auf ihrem exzellenten Adsorptionsvermögen, sowie der hohen Stabilität in Gegenwart von Feuchtigkeit und korrosiven Gasen. Jedoch sind die Poren dieser Kohlenstoffspezies unregelmäßig und nicht reproduzierbar. Das reale Porensystem z.B. von Aktivkohle ist jedoch zu komplex für eine Modellierung, wodurch das Verständnis der Adsorptionsprozesse an diesem Material sehr begrenzt ist. Kohlenstoffnanoröhren (CNTs) weisen dagegen eine definierte, einheitliche und reproduzierbare Porenstruktur auf. Im Vergleich mit ungeordneten CNTs ermöglicht eine vertikale Anordnung die Erzeugung einer definierten Struktur, welche in unterschiedlichen, eindeutig definierten Adsorptionsstellen resultiert. Vertikal angeordnete Kohlenstoffnanoröhren (VACNTs) bilden ein ideales Modellsystem für das Verständnis der Gasadsorption an kohlenstoffbasierten Materialien.

In dieser Arbeit werden VACNTs mittels chemischer Gasphasenabscheidung synthetisiert. Die hergestellten CNTs besitzen standardmäßig zwei oder mehr Wände mit einem Innendurchmesser von ca. 8 nm und einer spezifischen Oberfläche von $500\,\mathrm{m^2\,g^{-1}}$. Zur Bewertung der Adsorptionscharakteristika dieser VACNTs wurden zwei unterschiedliche Anlagen aufgebaut. Eine kommerziell erhältliche TG-Anlage wurde für die Messung der Adsorptionskapazität bei Umgebungsdruck modifiziert. Zur Bestimmung des Adsorptionsvermögens in einem größeren Temperatur- und Druckbereich wurde eine maßanalytische Hochdruckanlage entworfen, aufgebaut und kalibriert. Mit dieser können geringe Probenmengen (< 100 mg) im Temperaturbereich von 10–50 °C für Drücke bis zu 100 bar vermessen werden. Der Aufbau ermöglicht zusätzlich die Vermessung von Adsorptionsisothermen für Gasgemische. Unter Verwendung dieser beiden Techniken werden die Adsorptionscharakteristika für CO_2 an den synthetisierten VACNTs bestimmt und der Einfluss verschiedener Parameter, wie der Durchmesser und der Abstand der Nanoröhren, systematisch analysiert. Zusätzlich werden unterschiedliche Funktionalisierungen an den VACNTs unter Erhalt der vertikalen Anordnung durchgeführt und die Effekte auf die Adsorptionscharakteristika untersucht. Abschließend wird das Adsorptionsvermögen der VACNTs mit anderen kohlenstoffbasierten Adsorptionsmitteln verglichen. Die Adsorptionskapazität der VACNTs steigt linear mit dem Druck und unter hohen Drücken besitzen die modifizierten VACNTs bessere Adsorptionscharakteristika als standardmäßig verwendete Adsorptionsmittel.

Abstract

Carbon based adsorbents, especially activated carbons are one of the most widely used adsorbents. This is attributed to its excellent adsorption capacity as well as its better stability in the presence of moisture and corrosive gases. However the pores in these activated carbons in general, are often ill-defined, irregular and irreproducible. Modeling the actual pore system in activated carbon is far too complex and this seriously hinders a deeper understanding of the adsorption phenomenon in these materials. Carbon nanotubes (CNTs), on the other hand, have a defined, uniform and a reproducible pore structure. Compared with randomly oriented CNTs, a better well-defined structure is obtained by aligning the carbon nanotubes in a vertical manner. The vertically alignment of carbon nanotubes leads to the creation of multiple well-defined adsorption sites and results in an enhanced adsorption capacity. Vertically aligned carbon nanotubes (VACNTs) can thus serve as an ideal model structure for understanding gas adsorption in carbon materials.

In this work VACNTs are synthesized by water assisted chemical vapor deposition technique. The as-prepared CNTs are usually double to multi-walled with an average internal diameter of 8 nm and have a specific surface area of $500\,\mathrm{m^2\,g^{-1}}$. To assess the adsorption characteristics of these VACNTs, two different experimental adsorption setups are constructed. A commercially available TG setup is modified to measure the adsorption capacity at ambient pressures. To determine the adsorption characteristics over a wider temperature and pressure range, a high pressure volumetric setup is designed, built, calibrated and installed as a fully operable high pressure device which can handle smaller sample quantities ($< 100\,\mathrm{mg}$) and can determine adsorption up to a pressure of 100 bar in the temperature range 10–50 °C. In addition, the volumetric setup is designed to measure adsorption isotherms of gas mixtures as well. Using these two techniques, the CO_2 adsorption characteristics of the as-prepared VACNTs are determined and the influence of various other parameters like diameter, intertube distance etc. are explored systematically. Functionalization of VACNTs is carried out by preserving the alignment and the effect of addition of various functional groups on gas adsorption characteristics are investigated. Finally the adsorption characteristics of VACNTs are compared with other carbon based adsorbents. The adsorption capacity of VACNTs is found to increase linearly with pressure and at high pressure, the adsorption characteristics of modified VACNTs is found to be superior to that of other standard adsorbents.

Contents

Abbreviations

ACF	Activated carbon fiber
AFM	Atomic force microscopy
BSU	Basic structural unit
CNH	Carbon nanohorn
CNT	Carbon nanotube
CVD	Chemical vapor deposition
DWNT	Double walled nanotube
FWHM	Full width at half maximum
GO	Graphene oxide
IAST	Ideal adsorbed solution theory
MOF	Metal organic framework
MWNT	Multi walled nanotube
NLDFT	Non-local density functional theory
PECVD	Plasma enhanced chemical vapor deposition
PSD	Pore size distribution
RBM	Radial breathing mode
rf	Radio frequency
RPS	Remote plasma source
sccm	Standard cubic centimeter per second
SEM	Scanning electron microscopy
SWNT	Single walled nanotube
TEM	Transmission electron microscopy
TG	Thermogravimetry
VACNT	Vertically aligned carbon nanotube
VLS	Vapor liquid solid
VSS	Vapor solid solid
WACVD	Water assisted chemical vapor deposition
XPS	X-ray photoelectron spectroscopy

1 Introduction

In this introductory chapter, some basic concepts of adsorption are presented. Different classes of adsorbents with special focus on carbon based adsorbents are described. A brief review of gas adsorption studies on carbon nanotubes are presented and finally the motivation and objectives of the present work are presented.

1.1 Adsorption: basic concepts

Adsorption is a ubiquitous phenomenon that occurs on all surfaces regardless of the material. According to the IUPAC recommendation of 1985 [1] and the revised technical report of 2015 [2], *adsorption* is defined as the enrichment of molecules, atoms or ions in the vicinity of an interface. As the atoms at the interface are at a higher energy than the atoms in bulk, the driving force for adsorption is the minimization of this excess surface energy by accumulating atoms, molecules or ions at the interface. The material in the adsorbed state is known as the *adsorbate* while *adsorptive* is the same component in the fluid phase which is capable of being adsorbed. The solid surface on which adsorption occurs is termed as the *adsorbent*. A schematic representation of an adsorption system is shown in figure 1.1

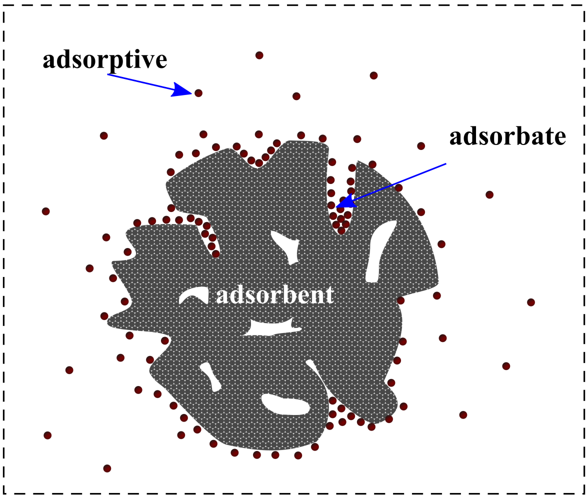

Figure 1.1: Schematic representation of an adsorption system.

Since adsorption is a spontaneous process, the change in Gibbs free energy (ΔG) should be negative. Upon adsorption, the adsorbate loses at least one degree of translational freedom and therefore, is in a more ordered state than the prior fluid phase. The change in entropy (ΔS) is thus negative. From the thermodynamic equation:

$$\Delta H = \Delta G + T \Delta S \tag{1.1}$$

it follows that the change in enthalpy (ΔH) is negative, indicating adsorption is an exothermic process. *Desorption* on the other hand, is an endothermic process and the amount adsorbed progressively decreases in desorption. *Adsorption hysteresis* arises when the adsorption and desorption curves do not coincide.

Based on the strength of interaction, adsorption process can be classified into physisorption or chemisorption. Physisorption is a reversible phenomena and the adsorbed molecules are weakly bound by van der Waals forces. Physical adsorption is usually characterized by low heat of adsorption ($\leq$ 40 kJ mol^{-1}) and the amount adsorbed decreases with an increase in temperature. The adsorption process is multilayer leading to a complete surface coverage and kinetics are often rapid [3]. On the other hand, in chemisorption the adsorbed molecules undergo irreversible chemical reactions and are strongly bound to the surface. Chemisorption is characterized by high heat of adsorption (~80 kJ mol^{-1}) and is often associated with an activation energy. Chemisorption leads to monolayer coverage and are localized/site specific [4]. Since chemisorption processes are irreversible and regeneration of adsorbent is energy intensive, adsorption based on physisorption is preferred for gas storage/capture applications.

Since adsorption is a surface phenomenon, a primary requisite for a good adsorbent is the availability of a large surface for gas molecules to adhere to. Porous materials having large specific surface areas are typically used as standard adsorbents. The size of the pore determines the surface area as well as the mechanism of adsorption. The classification of pores are therefore based on pore size or pore width (w). For a cylindrical shaped pore, pore width is the diameter and for a slit shaped pore, pore width is the distance between the two walls (figure 1.2). Based on the pore width, International Union of Pure and Applied Chemistry (IUPAC) [1] have classified pores into three categories:

- micropores: w $\leq$ 2 nm
- mesopores: 2 $\leq$ w $\leq$ 50 nm
- macropores: w $\geq$ 50 nm

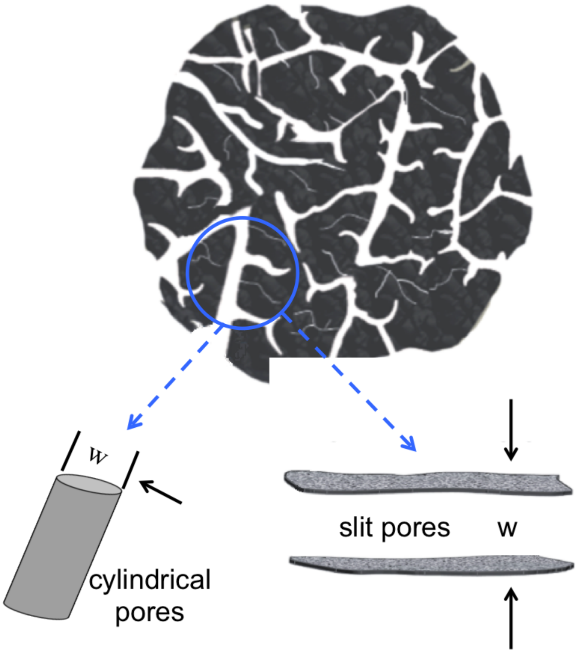

Figure 1.2: Schematic of cylindrical and slit type pores. For a cylindrical pore, pore width is its diameter and for a slit shaped pore, pore width refers to the separation between the two walls.

The adsorption mechanism is different for the three different pore regimes. Adsorption proceeds via a volume filling mechanism in micropores while in mesopores, adsorption is a layer by layer process (see figure 1.3) leading to capillary condensation at high saturation pressures. Macropores act as gateways for the gas molecules and does not contribute to adsorption in general. An ideal adsorbent should have a combination of all the three pore regimes to facilitate a high adsorption capacity over a wider pressure regime as well as for a faster loading and unloading of the adsorbate.

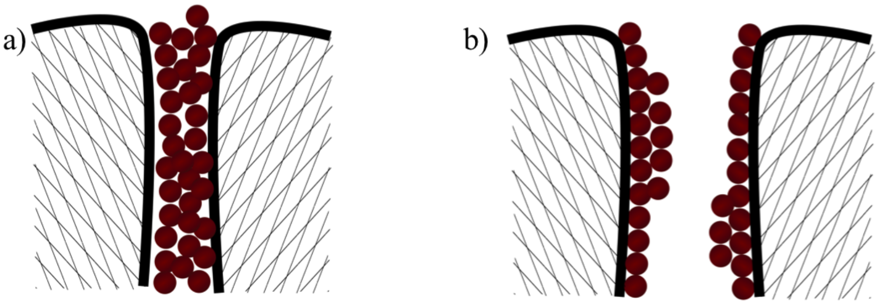

Figure 1.3: Schematic representation of adsorption process in a) micropores and b) mesopores. Adsorption proceeds by a volume filling mechanism in micropores while in mesopores adsorption is a layer by layer process.

1.2 Types of adsorbents

The general requirements for a standard adsorbent are good adsorption capacity, physical as well as chemical stability under operating conditions, ease of availability and regenerability. Most of the modern day adsorbents are porous materials with specific surface area in excess of $500\,\mathrm{m^2\,g^{-1}}$ [3]. The different types of adsorbents include, but are not limited to, carbon based adsorbents, silica based adsorbents, zeolites and metal organic frameworks (MOF). These adsorbents vary in their pore structure, pore size distribution, surface area and surface chemistry. The major characteristics of these standard adsorbents are discussed briefly.

1.2.1 Carbon based adsorbents

Porous carbon materials especially activated carbons are one of the most widely used adsorbents. The global consumption of activated carbon is projected to reach 2.4 million metric tons by the year 2020 [5]. Activated carbons have excellent adsorption characteristics and are produced in multi-ton quantities. There are several hundred activated carbon types available commercially with different pore size distributions for specific applications [6]. Although, in principle, any natural organic material can be used as a parent material for activated carbon production, only a few of these are economically viable.

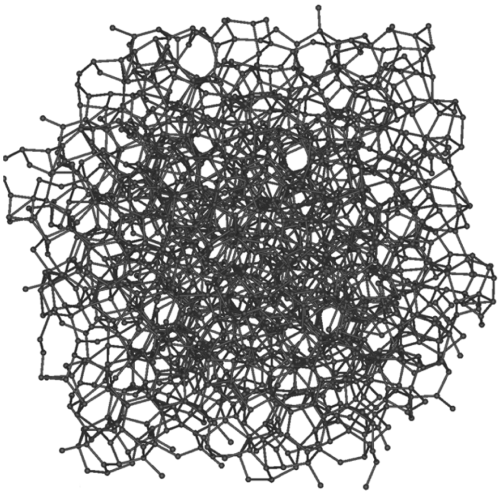

Figure 1.4: Schematic representation of an activated carbon structure. Activated carbons do not have a well-defined structure and modeling of such a structure is extremely complex.

Activated carbons are generally produced by first carbonizing peat, coal, lignite, wood or coconut shell in an inert atmosphere at temperatures around 500–600 °C [7, 8]. The carbonized material have low specific surface area and are therefore subjected to an activation process for the development of microporosity. The activation process can either be chemical involving the addition of compounds like $ZnCl_2$, H_3PO_4, KOH etc. or physical involving heating in CO_2 or steam at elevated temperatures (700–1100 °C) [7]. The as-obtained activated carbons have specific surface area typically in the range 1000–1500 $m^2\,g^{-1}$. Activated carbons do not have a well-defined structure (figure 1.4) and are mostly microporous. More details about the structural characteristics and origin of porosity in activated carbons are discussed in section 1.3.

The surface of activated carbons are generally non-polar; hence they tend to exhibit a hydrophobic but organophilic character [9]. Activated carbons are widely used for air separation, water purification, natural gas purification and for general purpose adsorption processes [3, 9]. Compared to other adsorbents like zeolites and MOFs, carbon based adsorbents have better stability against moisture and corrosive gases. As a result carbon based materials are widely used for flue-gas purification [10].

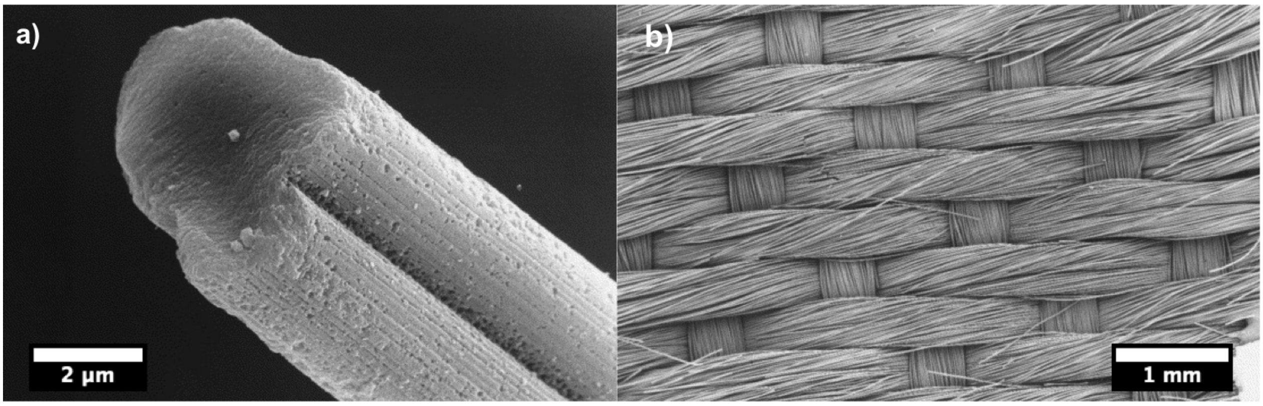

Figure 1.5: a) SEM image of an activated carbon fiber b) SEM image of a woven activated carbon fiber. Image source ref. [11].

Activated carbon fibers (ACFs) are another important class of carbon based adsorbents. They are typically produced from synthetic fibers like phenolic resin, polyacrylic resin (PAN) or viscous rayons by first carbonizing them at high temperatures and then subsequently activating them by physical or chemical means [12]. The diameter of these fibers are in the micrometer range and these fibers can be woven into various forms (figure 1.5). Similar to activated carbons, the pores produced by the activation process in ACF are in the microporous regime. The fiber morphology offers very little resistance to fluid flow and together with the short molecular diffusion path within the fiber, the adsorption kinetics are quite rapid in these activated carbon fibers, finding interesting applications in separational and catalytic technology [4].

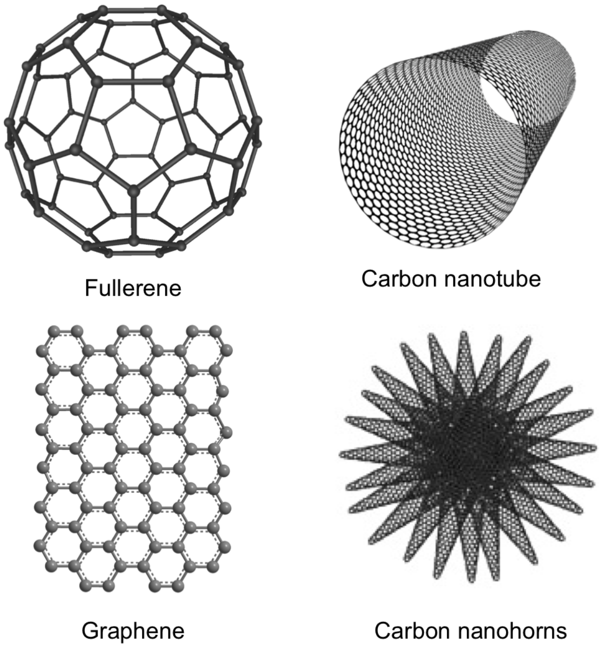

Figure 1.6: Unlike activated carbons or activated carbon fibers, carbon nanomaterials like fullerenes, carbon nanotubes, graphene and carbon nanohorns have a well defined pore structure. [*]

Nano carbon materials like fullerenes, carbon nanotubes, carbon nanohorns, graphene, graphene oxide etc. are the latest additions to the carbon adsorbent family (figure 1.6). Unlike activated carbon and activated carbon fibers, these nano materials have a well-defined pore structure, details of some of these structures are described in the later sections. In the subsequent sections, silica based adsorbents, zeolites and metal organic frameworks will be briefly introduced as these are the standard non-carbon based adsorbents and materials of choice for comparing the adsorption behavior of carbon materials.

1.2.2 Silica based adsorbents

Among the different silica based adsorbents, by far silica gel is the most widely known. Silica gels are partially dehydrated form of polymeric colloidal silicic acid. Silica gels generally have a unimodal pore size distribution and the size of the pore can be tuned by varying the pH of the solution during its synthesis. The typical specific surface area of silica gels are in the range

---

[*] Image source of fullerene and carbon nanohorns: Wikipedia

$340–840\,m^2\,g^{-1}$ [9]. The presence of hydroxyl groups renders the surface hydrophilic and silica gels typically exhibits high capacity for water adsorption. Hence they are widely used as desiccants.

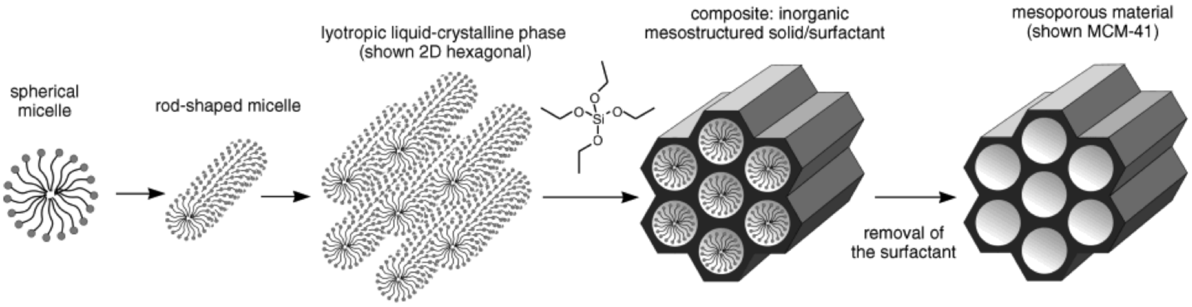

Figure 1.7: Formation of MCM-41 by using long chain surfactant molecules as templates. Image source ref. [13].

In the early 1990's a new class of highly ordered mesoporous silicas were developed by using long chain surfactant molecules as templates (see figure 1.7) [14, 15]. Well-defined pore size in the mesoporous range and uniform pore shape distributed over micrometer scale were characteristic features of these materials. Among the different mesophases initially synthesized, hexagonally ordered MCM-41 received much attention because of its better thermal stability and ease of formation [16]. MCM-41 typically has pores in the range 1.6–10 nm with a specific surface area of $> 700\,m^2\,g^{-1}$. The pore size and morphology of such structures could be tuned by varying the reaction stoichiometry, nature of the surfactant and reaction conditions [17]. Materials with still larger pore sizes of 5–30 nm, known as SBA-16, were developed subsequently [18, 19]. Though these materials, in general, have an ordered pore structure, the walls of almost all mesoporous silicate structures are amorphous by nature, limiting its applications [20]. Nevertheless, ordered mesoporous silicas are used in gas purification, gas separation, drug delivery and as catalyst supports [13, 16, 17].

1.2.3 Zeolites

Though zeolites are also silica based adsorbents, the distinct pore structure and the resulting different adsorption properties as well as its widespread usage, justifies its independent classification. In its most general form, zeolites are crystalline aluminosilicates composed of an assemblage of SiO_4 and AlO_4 tetrahedra which are joined together in various regular arrangement through a shared oxygen atom [9]. The resulting porous structure has a very precise pore size and is always in the lower micropore regime. They have a specific surface area typically in the range 500–700 $\mathrm{m^2\,g^{-1}}$. Zeolites are naturally occurring and can be produced synthetically as well.

The ratio of Si/Al is one of the defining parameters determining the zeolite characteristics. Though there is no upper limit for the Si/Al ratio, the lowest value is never less than one. Si rich zeolites have a hydrophobic character and the hydrophobicity decreases with a decrease in the Si/Al ratio. The cross over from hydrophobic to hydrophilic zeolite occurs at a ratio between 8–10 [9]. When a silicon atom in the tetrahedral unit is replaced by aluminum, the resulting positive valency requires the addition of a cation. Alkaline or alkaline earth cations are the most common substituents and are readily exchangeable. The nature and size of these cation significantly influences the adsorption characteristics [12].

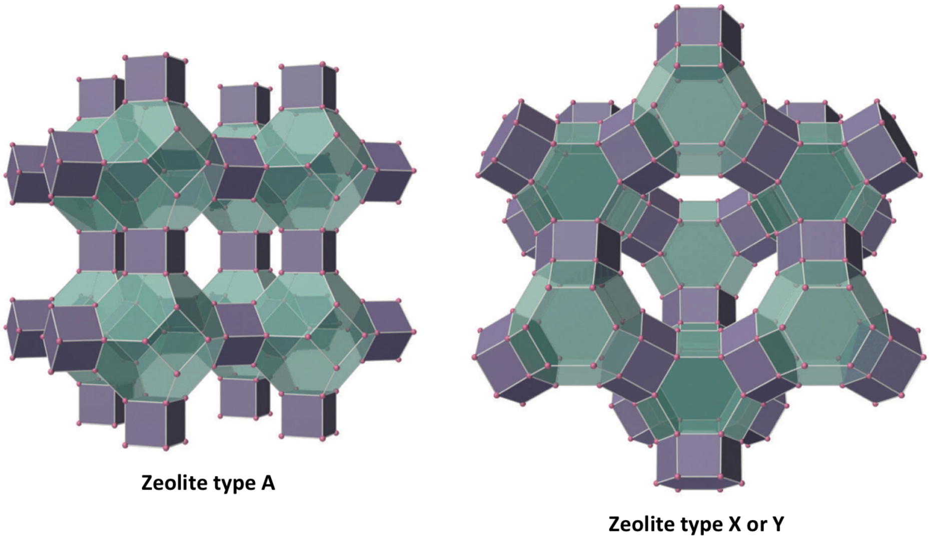

Figure 1.8: Schematic illustration of the structure of zeolite type A and zeolite type X or Y. [†]

Zeolite A and zeolite X/Y, shown in figure 1.8, are two of the most important types of zeolite for gas adsorption [21]. The unit cell of zeolite type A consist of 24 tetrahedra with a Si/Al ratio close to 1 and has an unobstructed diameter of 4.4 Å. The pore size varies depending on the cation. For example, type 4A zeolites have sodium cations and have an effective pore size of 3.8 Å while type 3A zeolites have larger potassium cations resulting in a smaller effective pore size of 3 Å [21]. The unit cell of type X or Y zeolite consist of 192 tetrahedra with an unobstructed diameter of 8.1 Å. The difference between type X and type Y zeolites is in the ratio of Si/Al. Type X zeolites have a Si/Al ratio of 1–1.5 while type zeolites have a Si/Al ratio > 1.5 [22]. Zeolite 10X has calcium as the major cation while zeolite 13X mainly consist of sodium cations.

[†] Image source: Principles of General Chemistry (v. 1.0); Creative Commons license.

1.2.4 Metal organic frameworks

Metal Organic Frameworks (MOFs) are a recent class of porous materials with an organic-inorganic hybrid framework. These are crystalline solids with a well-defined pore structure made by joining metal containing units with organic linkers [23]. They have enormous surface area in the range of 1000–10 000 $\mathrm{m^2\,g^{-1}}$ [24]. They have a highly customizable framework with flexibility in pore size, shape and structure [25]. The pore size can be adjusted by varying the length of the organic linker and can vary from micro-mesopores (see figure 1.9).

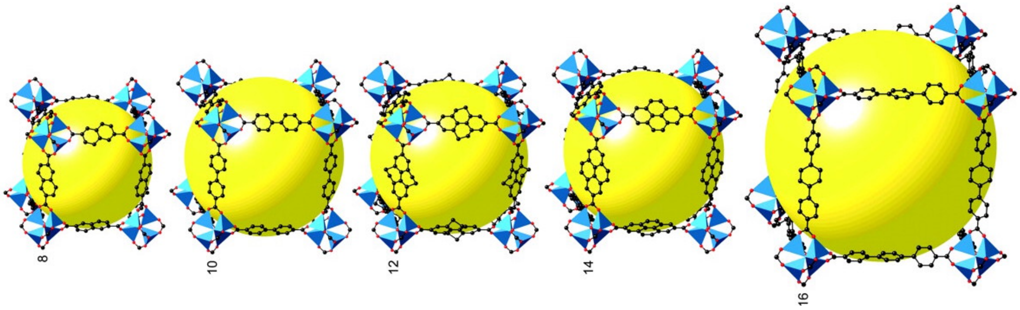

Figure 1.9: Series of isoreticular metal organic frameworks IRMOF-n (n = 1-8, 10, 12, 14 and 16) in which the internal void space increases as a function of linker length. [Zn: blue polyhedra, O: red spheres, C: black spheres. The yellow spheres represent the largest van der Waals spheres that would fit in the cavities without touching the framework; Image source ref. [26].

Due to their very high specific surface area, MOFs are widely investigated for gas adsorption properties especially for H_2, CH_4 and CO_2 storage [27–30]. In addition, MOFs are also extensively investigated for catalysis, energy technology, biomedical imaging, photonics etc. [24, 25, 31, 32].

1.3 Understanding adsorption in carbon materials

To understand the adsorption process in carbon materials, it is imperative to have an understanding of the origin of the porosity in these materials. The versatility of element carbon stems not only from its ability to bond with other elements like oxygen, hydrogen, nitrogen etc. but also to bond with itself (concatenation) creating a wide variety of structures. The concept of hybridization is very useful in explaining the large number of carbonaceous structures. Based on hybridization, the carbon structures can be classified [33] as shown in figure 1.10.

Diamond, with sp^3 hybridization, forms a tight pack structure with no voids and hence is not interesting for adsorption studies. Carbynes, the sp hybridized form, forms an infinite carbon chain

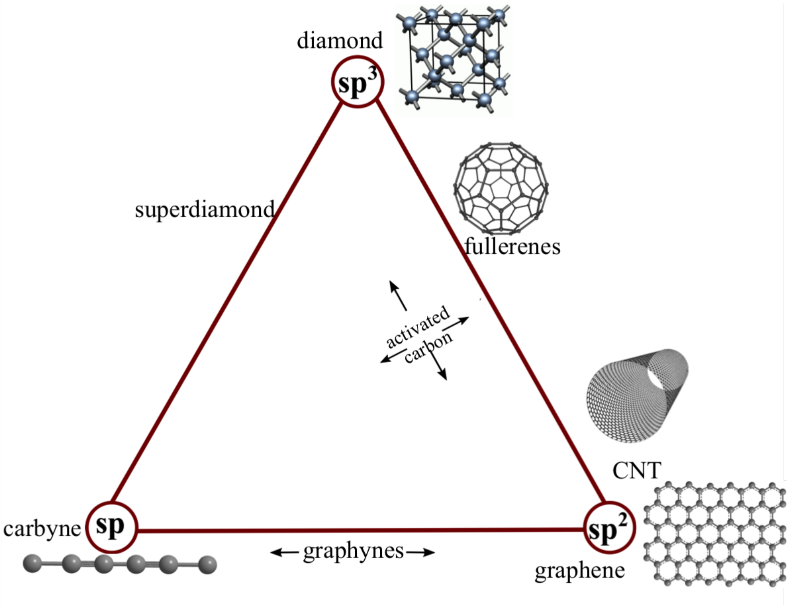

Figure 1.10: Ternary diagram of carbonaceous solids. Almost all of the carbon based adsorbents have carbon in its sp^2 hybridized form. Figure adopted from ref. [33].

and are characterized by strong chemical activity and extreme instability at ambient conditions [34]. Almost all of the carbon based adsorbents have carbon in its sp^2 hybridized form, the extent of which determines the porosity. In a perfect graphite, the sp^2 hybridized carbon atoms form a layered structure (graphene) and the different layers are held together by strong van der Waals interaction with an interlayer separation of 0.335 nm. This spacing is too low for gases to penetrate and as a result, perfect graphite is often regarded as a non-porous material with a very low surface area. However due to the well-defined and homogeneous nature of the surface, graphite is often used as a model structure to simulate adsorption of different molecules on its surface.

Though activated carbons are highly disordered carbon materials, yet they cannot be described as amorphous materials. Activated carbons do not exhibit a 3D ordering like in graphite but they often possess a certain extent of 2D order. The disorder in the c-direction is termed as turbostratic [35]. Several models exist to explain the porosity in carbon materials and they differ mostly in the type of the basic building block. In one such model, the basic structural unit (BSU) of activated carbon is considered as a planar aromatic structure of less than 10–20 rings extending two to four layers [36]. Other models assume fullerene-like [37] or defective micro graphene layer [6] as the basic structural feature. Nevertheless all these models suggest the random intermingling of BSU as the reason for pores or voids (figure 1.11) in these structures. Carbon atoms with sp^3 bonding may act as bridges between these units providing a certain continuity and rigidity to the structure [6].

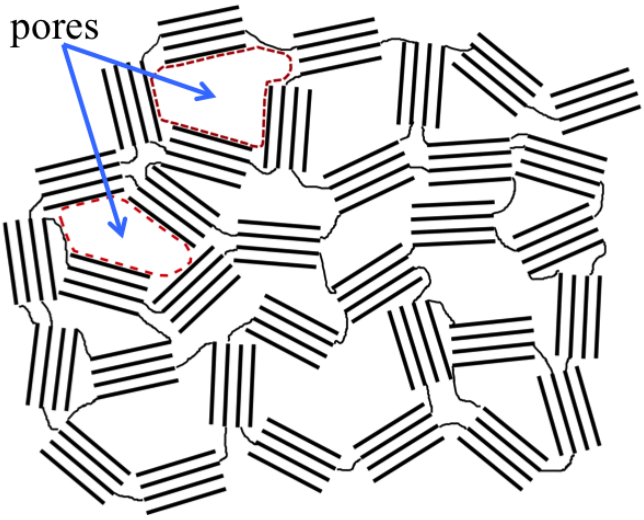

Figure 1.11: Random ordering of the basic structural unit (BSU) is the basis of origin of pores in activated carbon.

However all these models are idealized cases and are far from reality. The actual structure of activated carbon is far too complex and the situation is further complicated by the presence of heteroatoms in the structure. In addition there are several hundred activated carbons available, each with different pore size and shapes [6]. Even for activated carbons derived from the same parent feedstock prepared under similar pyrolysis and activation conditions, the pore development and its distribution is never identical.

Understanding the structure and surface chemistry of an adsorbent is crucial for understanding the adsorption process. This is because the cornerstone of an adsorption process is the confinement of a molecule on a surface dictated by the adsorption potential of the host material structure. For a given system the adsorption potential is intimately related to the pore width, shape and specific bonding arrangement. Therefore to accurately model, predict and finally understand an adsorption process, a well-defined structure with a defined surface chemistry is absolutely essential.

Among the different carbon based structures, carbon nanotubes (CNTs) have a defined pore geometry and surface structure. The all carbon framework of CNTs, make the adsorption studies on these structures relevant for interpreting adsorption process in carbon materials in general. In addition, the possibility of a combined theoretical as well as experimental investigation on to problems of more fundamental nature like the effect of curvature, influence of the addition of various heteroatoms, effect of dangling bonds etc. make CNTs an interesting material for a deeper understanding of the fundamental adsorption phenomena.

1.4 Carbon nanotubes

Carbon nanotubes (CNTs) can be envisioned as a seamlessly rolled up graphene sheet. Though there were few earlier reports of hollow tube shaped nano carbon materials, the field received much impetus after the discovery of multiwalled CNTs by Iijima [38]. The first reports were of multiwalled-carbon nanotubes (MWNTs), which are multiple graphene sheets rolled up in a concentric manner. Two years later, the first single walled carbon nanotubes (SWNTs) were synthesized and characterized by the covaporization of carbon and cobalt in an arc generator [39]. CNTs characteristics are mainly determined by the diameter, number of walls and chirality.

The diameter of all the carbon nanotubes: single, double or multiwalled, fall in the nanometer regime. SWNTs have the smallest diameter and are usually $\leq 2\,\mathrm{nm}$, while for multiwalled nanotubes the diameters can be even as large as few tens of nanometers. The different concentric tubes in a MWNT are held together by van der Waals attraction and the distance between the concentric tubes is 0.34 nm, slightly greater than the intergraphitic spacing. Larger diameter CNTs, are often metallic in nature while smaller diameter CNTs, especially SWNTs, exhibit semi-conducting nature depending on the chirality. In addition to the interesting structure dependent electronic properties, CNTs have attractive mechanical and electrical characteristics as well. The σ bond in sp^2 configuration is about $250\,\mathrm{kJ\,mol^{-1}}$ more stronger than the σ bond in sp^3 configuration [40], making the bonding in graphene one of the strongest. In CNT, the curvature induced by the rolling up of graphene sheet leads to quantum confinement and σ-π rehybridization, resulting in a slightly out of plane σ bonds and further delocalization of π orbital. In addition to the enhanced electrical and thermal conductivity, this unique structural configuration makes CNTs mechanically stronger with exceptional tensile strength and high ductility.

Carbon nanotubes can be envisaged as ideal gas storage/capture materials with their walls made up of carbon atoms. For a SWNT, each carbon atom can provide two surfaces (inside and outside) for gases to adhere to, resulting in a theoretical surface area exceeding $2500\,\mathrm{m^2\,g^{-1}}$ [41]. Soon after their discovery, the feasibility of CNTs as a potential gas storage, especially hydrogen storage, material was intensely researched.

1.5 Gas adsorption on Carbon nanotubes

Gas adsorption studies on carbon nanotubes are perhaps one of the most controversial research areas in the study of CNTs. Hydrogen adsorption on CNTs is at the center of the controversy. Irrespective of the gases studied, understanding the origin of this dispute is crucial for avoiding the recurrence of such mistakes.

1.5.1 H_2 adsorption on CNTs

Early gas adsorption studies on CNTs were stimulated by a claim of unexpectedly high H_2 adsorption capacity of 5–10 wt% on SWNTs [42]. These studies were reported on the backdrop of intense research efforts to find a suitable material for H_2 storage which has long been the bottleneck for a viable hydrogen economy. This report of high adsorption capacity in 1997, created a flurry of research activity on gas adsorption on CNTs. Two years later, Chen et al. [43] reported an even higher H_2 adsorption capacity of 20 wt % for alkali doped SWNTs. Under cryogenic conditions and at high pressures ($>$ 40 bar), Ye et al. [44] reported the debundling of SWNT bundles and subsequent high H_2 intake of 8 wt %. In the same year, Liu et al. [45] reported a hydrogen storage capacity of 4.2 wt % on SWNTs soaked in HCl and then heat treated in vacuum. Four years after their first report, Dillon et al. further reported a high intake of H_2 on SWNTs subjected to sonication in nitric acid [46]. However none of these exceptional adsorption capacities were found to reproducible. Further studies attributed these exceptional adsorption capacity results to various factors like faulty interpretation of data, leakage, contamination of CNT samples, presence of water etc. [47–51].

The studies that followed, reported very low hydrogen uptake [52, 53]. At ambient temperature even under very high pressures exceeding 100 bar, CNTs were found to found to adsorb only less than 1 wt % of H_2 [54–57]. Some studies also reported very low H_2 intake even at cryogenic temperatures [58, 59]. The controversy ensued with further reports of high H_2 storage (2–4 wt %) [60–62] as well as low storage ($<$ 1 wt %) [63] at ambient conditions. Especially interesting was the higher adsorption capacity observed with aligned carbon nanotubes at ambient conditions [64–66]. Aligned carbon nanotubes are materials of special interest for gas adsorption studies and are therefore discussed separately in the next section.

After more than a decade long research, the general consensus is that carbon nanotubes can store reasonable amount of H_2 only under cryogenic temperatures and high pressure but not at ambient conditions [67–72]. Over the years, the spread in the experimentally reported values of hydrogen storage by CNTs is more than two orders of magnitude. As noted by Xia et al. [72], theoretical studies of H_2 adsorption on CNTs have produced a more coherent result than experimentally reported values. This is due to the fact that most of the molecular simulations consider near perfect scenarios with completely pure crystalline CNTs having open ends and freely accessible pore systems. The discrepancies in the experiments, to a certain extent, can be attributed to wide variations in CNTs in terms of open/closed ends, presence of catalyst particles and other impurities, distribution of functional groups, defects etc. The CNTs used in these studies were obtained by different synthesis techniques and varying purification methods were employed which made the early results difficult to compare. Nevertheless the intense research efforts have lead to an overall development of the field of adsorption with recognizing common pitfalls and realizing the need for a combined experimental and theoretical approach towards understanding gas adsorption in such novel nanostructured materials.

1.5.2 CO_2 adsorption on CNTs

Adsorption behavior of various other gases like CH_4 [73–75], N_2 [76–78], Ar [79, 80], NO [81, 82] and SO_2 [81, 83] on CNTs have been investigated over the last years. Of special importance are the CO_2 gas adsorption studies on CNTs. Adsorptive removal of CO_2 gas is reported to be an attractive option for carbon capture and storage approach [84–86]. Naturally carbon based materials are an important class of adsorbents considered for this purpose [87–93].

Consequently, from a fundamental and a technological perspective, CNTs as an adsorbent for CO_2 storage were investigated by many research groups. Early experimental works studied CO_2 adsorption on purified SWNTs in a temperature range of 0–200 °C and observed a clear decrease in the adsorption capacity with an increase in temperature indicating a physisorption mechanism [94]. Under similar conditions of temperature and pressure, SWNTs with a surface area of $1617\,\mathrm{m^2\,g^{-1}}$ were found to have an adsorption capacity twice that of activated carbon ($1284\,\mathrm{m^2\,g^{-1}}$) [94]. Zhao et al. [95] investigated the interaction of various gas molecules including CO_2 on SWNT bundles by DFT method. CO_2 was found to weakly interact with SWNTs and adsorption sites between the intersection of tubes known as groove and interstitial sites were found to be more favorable for adsorption than the interior of the tubes (see figure 1.12).

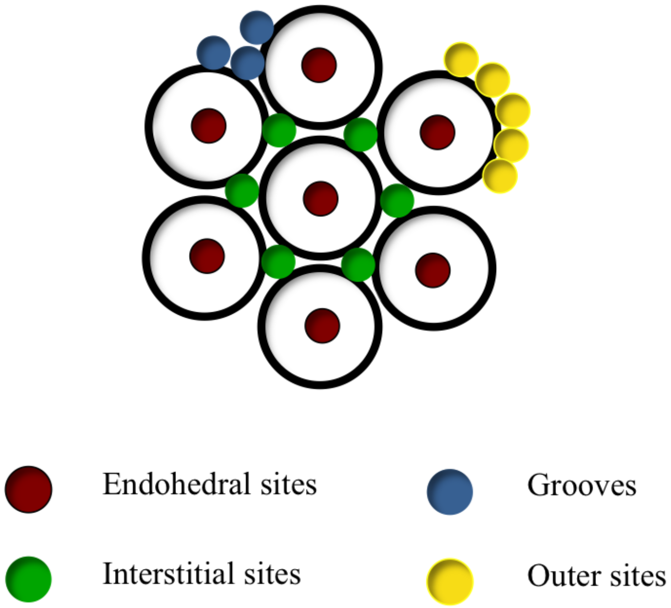

Figure 1.12: Schematic of different adsorption sites on a CNT bundle

Kleinhammes et al. [96] studied gas adsorption in SWNT bundles by NMR spectroscopy. By recording the ^{13}C saturation recovery curve of SWNTs exposed to various gas like O_2, CO_2, H_2 and He, it was found that at ambient conditions, only He atoms could access the interstitial sites. In a series of studies, Johnson et al. investigated the adsorption of CO_2 on SWNT bundles using in-situ IR technique and by Grand Canonical Monte Carlo (GCMC) simulations [97–99]. An IR peak at $2330\,\mathrm{cm}^{-1}$ corresponding to endohedral adsorption and another peak at $2340\,\mathrm{cm}^{-1}$ corresponding to groove/external adsorption were observed upon CO_2 adsorption especially at low temperatures. In addition, they also observed a sequential filling of adsorption sites with interstitial/groove sites preceding endohedral sites, consistent with the earlier DFT calculations by Zhao et al. [95]. Similar observation of adsorption on grooves were also made by Bienfait et al. [100] by studying adsorption of different gases on closed capped SWNT bundles. The discrepancy between the NMR and IR studies could be attributed to the different diameters of CNTs used for both studies. SWNTs used in the NMR study had a mean diameter of about 0.85 nm while the SWNTs used in the IR studies had a slightly larger diameter of ~1.3 nm, implying larger interstitial sites that could be accessed by CO_2 molecules.

Hu et al. [101] studied CO_2 adsorption on SWNTs at 273 K and 298 K and explored the applicability of BET, Langmuir and Dubinin-Astakhov equations to describe the experimental isotherms. DA equation with Astakhov exponent value of < 2 was found to best describe the observed isotherm indicating presence of heterogeneous pore system in-line with the earlier DFT and IR studies.

With the research on CO_2 capture gaining more momentum over the last years, studies focusing on further enhancement of CO_2 adsorption capacity of CNTs were reported. These include grafting amine groups on CNTs by treating with 3-aminopropyltriethoxysilane (APTS) [102–106], polyethyleneimine (PEI) [107, 108], tetraethylenepentamine (TEPA) [109, 110] etc. In addition, composites of CNTs with metal-organics frameworks [111–113] or carbon fibers [114, 115] were also investigated for its enhanced CO_2 adsorption characteristics. Some of the main experimental CO_2 adsorption studies on CNTs are summarized in table 1.1.

Table 1.1: List of major experimental CO_2 adsorption studies on CNTs till 2015.

Type of CNT	**Modification/method**	**T (K)**	**P (bar)**	**Year**	**Ref.**
SWNT	two-step purification	273–473	1	2003	[94]
SWNT	NMR	R.T.	≤ 10	2003	[96]
SWNT	in-situ IR	50–700	10^{-10}	2003	[97]
SWNT	in-situ IR	105	10^{-8}	2004	[98]
SWNT	in-situ IR	77	10^{-9}	2004	[99]
SWNT	isotherms & neutron diffraction	124	-	2004	[100]
SWNT	-	273, 298	≤ 1	2006	[101]
MWNT	3-aminopropyl-triethoxysilane	298	-	2008	[102]
SWNT	polyethyleneimine	298–348	1	2008	[107]
MWNT	3-aminopropyl-triethoxysilane	293–373	-	2009	[103]
MWNT	3-aminopropyl-triethoxysilane	298–423	-	2010	[104]
SWNT	opening & annealing	298	20	2010	[116]
MWNT	magnetite	298–473	≤ 13	2011	[117]

MWNT	3-aminopropyl-triethoxysilane	298–373	-	2011	[105]
MWNT	NH_3	298	≤ 30	2011	[118]
MWNT	MWNT+MOF composite	298	≤ 20	2011	[111]
MWNT	polyaniline	298–370	≤ 13	2012	[119]
MWNT	tetraethylenepentamine	283–313	-	2012	[109]
MWNT	-	298–318	≤ 40	2012	[120]
MWNT	layered double hydroxide	573	1	2012	[121]
MWNT	MWNT+MOF composite	298	≤ 10	2012	[112]
MWNT	MWNT+ACF+PEI	303–348	1	2013	[114]
MWNT	phenolic resin+activation	298	0.153	2013	[122]
SWNT	Zwitterion	308	≤ 10	2013	[123]
MWNT	1,3-phenylenediamine	298–318	≤ 40	2013	[124]
MWNT	(3-aminopropyl) triethoxysilane	333	-	2013	[106]
MWNT	tetraethylenepentamine	293–353	-	2014	[110]
MWNT	MWNT+MOF composite	308	≤ 40	2014	[113]
MWNT	N-(2-aminoethyl)-3-aminopropyltrimethoxysilane	288–313	-	2014	[125]
MWNT	MWNT+MOF composite	298–343	1	2014	[126]
MWNT	polyether amine	298	≤ 60	2015	[127]
MWNT	polyethyleneimine	298	1	2015	[108]
MWNT	MWNT+Carbon fiber/resin composite	298	≤ 1	2015	[115]

1.6 Vertically aligned CNTs for gas adsorption

Due to the strong van der Waals interaction, CNTs naturally tend to aggregate and typically exist in the form of bundles. These bundles are a few nanometers wide and give rise to multiple adsorption sites as shown in figure 1.12. These adsorption sites are not homogeneous but differ in their individual adsorption energies [128]. In randomly oriented CNTs, there is no long range ordering of these bundled structures (see figure 1.13a). However a 3D alignment of CNTs essentially preserve the characteristic bundle morphology (figure 1.13b) and is even able to extend it over macro size dimensions. Such well-ordered vertically aligned carbon nanotube (VACNT) structures can be realized experimentally and modeling of such a well-defined system is possible as well. Combining both experimental as well as theoretical approach, VACNTs can be regarded as an ideal model structure allowing a symbiosis between experiment and theory.

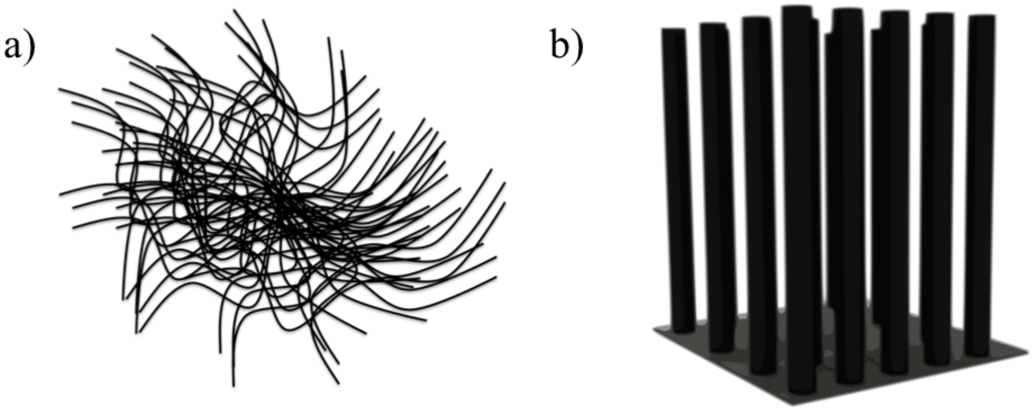

Figure 1.13: Schematic of a) randomly oriented CNTs and b) vertically aligned CNTs.

The curvature effects and the different coordination number of carbon atoms at different sites (see figure 1.12) are the main reasons for the observed heterogeneity of the pore system in VACNTs [41, 129]. The interior of the CNT, which represent the *endohedral sites*, has a pore width in the upper micrometer regime (for SWNT) or more often in the mesopore regime (for DWNT and MWNT). The endohedral sites are accessible only if the ends of the tubes are open. The *interstitial sites* are the channels between CNTs and are the direct result of alignment of CNTs. The diameter of CNT and the intertube distance determines the adsorption characteristics of interstitial sites. *Groove sites* are formed at the intersection of two tubes and are characterized by a high coordination number of carbon atoms. Grooves are energetically favorable adsorption sites with a typical binding energy 1.7 times greater than that of a planar graphite surface [41, 130]. Gases can also adsorb on the outer curved surface or *external surfaces* on the periphery of the CNT arrays as well.

Several experimental studies have confirmed the enhanced gas adsorption on aligned CNTs. Cao et al. [65] and Zhu et al. [64] studied H_2 adsorption on vertically aligned CNTs and randomly oriented CNTs for a range of pressures. In both these studies, VACNTs were found to exhibit higher H_2 storage in the entire pressure regime. Gundiah et al. [66] compared the H_2 adsorption properties of different SWNTs, MWNTs and aligned MWNTs and observed the maximum H_2 storage capacity for aligned MWNTs. To confirm the role of alignment, Zilli et al. [131] compared the N_2 adsorption isotherm of aligned CNTs with the isotherm of disheveled CNTs produced by the ultrasonication of originally aligned CNTs. The volume of N_2 adsorbed on ultrasonicated CNTs was found to be lower than that of the parent sample over the complete range of relative pressures. Consequently significant reduction in BET surface area and pore volume was observed for the ultrasonicated CNTs, confirming the important role of alignment.

1.7 Motivation and objectives

From the numerous studies of H_2 adsorption on CNTs spanning more than a decade, the need for a combined experimental and theoretical approach on a well-defined adsorbent system is apparent for interpreting gas adsorption on CNTs in particular and carbon systems in general. Vertically aligned CNTs with their multiple and defined gas adsorption sites can serve as a model structure for such a study. However only few studies have investigated the adsorption characteristics of VACNTs and the focus of these studies were to point out the enhanced adsorption characteristics of VACNTs. The potential of VACNTs as a test bed for a combined experimental and theoretical investigation for gas adsorption in carbon materials is thus largely unexplored.

The present work aims to provide the experimental studies of gas adsorption on VACNTs and is complimented by the theoretical calculations carried out by Dr. Mahshid Rahimi in the research group of Prof. Florian Müller-Plathe. CO_2 is chosen as the adsorbate gas due to the experimental simplicity in its handling and measurement as well as due to the availability of well-established force fields for simulation studies. It is also well known that a material capable of adsorbing CO_2, can easily adsorb polar gases like SO_2 but not vice-versa. In addition, due to the global climate change concerns, there is an increasing interest in carbon capture and storage related research.

To this end the primary objectives of the work are as follows:

- To prepare catalyst free vertically aligned CNTs in reasonable quantities for gas adsorption studies, characterize its pore system as well as its surface chemistry.
- To establish an experimental setup for measuring gas adsorption on VACNTs, preferably over a wide temperature and pressure range

- To optimize the VACNT structure by investigating the influence of CNT diameter, intertube distance, opening tips etc. on gas adsorption.
- To graft various functional groups and hetero-atoms on VACNTs and study their influence on gas adsorption.
- To carry out a comparative study with other carbon adsorbents like activated carbon, carbon nanohorns and graphene oxide.

2 Vertically Aligned Carbon Nanotubes

In this chapter various techniques for aligning CNTs, vertically and horizontally, are presented followed by a brief description about the CNT growth mechanism. Synthesis of vertically aligned CNTs by a water assisted CVD process is presented in detail as it is the general technique used in this work for obtaining VACNTs. Representative techniques for characterization of VACNTs are presented as well.

2.1 Alignment of carbon nanotubes

CNTs can be aligned horizontally as well as vertically with respect to the substrate. Horizontal alignment of CNTs is generally achieved by a post-synthesis process and is therefore not limited by substrate or high temperature. Vertical alignment, on the other hand, is typically achieved in the CNT growth phase and as such the process is simple and straightforward [132–136].

2.1.1 Techniques for horizontal alignment of CNTs

In general, to horizontally align CNTs, the as-synthesized randomly oriented CNTs are subjected to a force field in the horizontal direction. The nature of the applied force for aligning CNTs include mechanical, electrical or magnetic. Mechanical method is the simplest technique for aligning CNTs horizontally wherein randomly oriented CNTs on a substrate or embedded in a polymer matrix, are stretched after breaking the support [137, 138]. The obtained alignment of CNTs is parallel to the tensile force applied and is perpendicular to the crack. Ajayan et al. [139] have shown that the shear stress induced by the cutting of thin slices (~50 - 200 nm) of a nanotube-polymer composite, align the CNTs along the cutting direction.

Dielectrophoresis is another method for horizontally aligning CNTs. In this method, CNTs dispersed in solution align along the electric field applied across the electrodes. Both DC [140] and AC [141, 142] fields can be used and for an AC field, the degree of alignment is found to be proportional to the applied frequency.

CNTs can also be aligned horizontally under a strong magnetic field. Theoretical calculations by Lu et al. [143] have shown that SWNTs have an anisotropic magnetic susceptibility. Depending on the field direction, nanotubes exhibit paramagnetic and diamagnetic responses. In practice, the field strength required for alignment, however, is usually large ($>$ 10 T) [144, 145]. To obtain a better alignment in a lower field, CNTs need to be filled with magnetic nanoparticles. Other methods for horizontally aligning CNTs uses acoustic waves [146], spinning method [147], Langmuir-Blodgett techniques [148] etc.

All the techniques for horizontally aligning CNTs offers very limited control over the intertube separation between the aligned CNTs and as such dense horizontal alignment of CNTs is rather difficult to realize.

2.1.2 Techniques for vertical alignment of CNTs

Vertical alignment is realized by various modifications of chemical vapor deposition (CVD) process. CVD is a very versatile technique as it offers flexibility in the use of various substrates and choice of wide range of precursors of any desired state (solid, liquid or gas) [149]. Even prior to the discovery of carbon nanotubes, CVD methods were already used for producing carbon filaments and fibers [150]. In a typical CVD process, a carbon containing precursor is decomposed at high temperature (with or without catalyst) to form carbon species which are then deposited on the substrate. Depending on the decomposition method of the carbon precursor, CVD is categorized into thermal CVD and plasma enhanced CVD (PECVD). In a thermal CVD, temperature of synthesis depends on the substrate-catalyst-precursor system but is typically in the range 600–1200 °C. When a plasma is coupled to CVD, energy from a plasma can bring about decomposition of hydrocarbon vapor at much lower temperatures (even close to room temperature) [151, 152]. Such a process is known as plasma enhanced CVD and has facilitated the growth of CNTs on temperature sensitive substrates. Compared to thermal CVD better alignment is obtained by PECVD.

Alignment of CNTs in CVD method can be achieved either by template assisted approach or by using a suitable catalyst system. In template assisted synthesis technique, carbon species formed by the decomposition of hydrocarbon vapor, precipitates inside the nanochannels of the inorganic porous template material. After the synthesis, the template is etched away using concentrated acids. The presence of catalyst is not mandatory [153, 154]. Highly ordered porous anodic aluminum oxide (PAOX) membranes [155, 156] or MCM-41 [132, 157] are the most commonly used templates for obtaining vertically aligned CNTs. Though well-aligned CNTs can be prepared by this method, the CNTs produced are usually multi-walled and display low degree of crystallinity [136].

CNTs with high degree of vertical alignment and crystallinity can be obtained by a catalyst driven CVD process. A thin film of catalyst, usually few nanometers in thickness, is typically used for the CVD synthesis of aligned CNTs. Due to the non-equilibrium structure and restricted diffusion of atoms, as-deposited thin films are usually metastable. The instability increases with a decrease in film thickness and a rise in temperature. With an increase in temperature, on account of higher diffusivity, these films tend to form arrays of islands or agglomerates so as to minimize the surface energy [158]. This can occur at a temperature much lower than the melting point of the film. Though this solid state dewetting is a cause of major concern in microelectronics, it is made to good use in the synthesis of well-aligned CNT synthesis. As the substrate with the catalyst is heated in a CVD setup under a reducing atmosphere, dense islands of catalyst particles are formed. When a suitable carbon precursor is passed, the decomposed carbon species can dissolve in these catalyst particles and precipitate out as a graphitic framework which later develops into CNT. Since the catalyst particles are densely packed, the van der Waals interaction between the neighboring CNTs force the CNTs to grow in a vertical direction [159]. This phenomenon is known as crowding effect [136, 160–163]. The choice of substrate-catalyst combination is crucial to both CNT quality and quantity. Well-aligned millimeter long CNTs can be produced by this method. Structuring of the catalyst during the deposition stage, enables spatial selective growth of CNTs. Moreover by modifying the catalyst employed, the diameter, density, number of walls and intertube distance between the aligned CNTs can be controlled.

2.2 Catalyst driven CNT growth mechanism

Transition metals like Fe, Co or Ni are typically used as the catalyst for the synthesis of CNTs. The catalytic activity of these metals is due to their ability to dissolve carbon to a certain extent at elevated temperatures [150]. At high temperatures, thin films of catalyst breaks into closed packed tiny islands of catalyst particles. The carbon species formed by the decomposition of the precursor molecule, dissolves in these catalyst particles and move on to the particle surface by diffusion. Upon supersaturation, they precipitate out to form carbon nanotubes. This process is known as *vapor liquid solid process* (VLS). VLS model was originally proposed in the 1960's by Wagner to explain the growth of silicon whiskers [164]. In the early 1970's Baker and co-workers, extended the VLS model to explain the formation of carbon fibers [165, 166]. The growth of CNTs also proceeds by a similar mechanism as shown schematically in figure 2.1. The carbon species from the precursor constitutes the ‘vapor’ in the process. Carbon dissolving in elements of iron group is a strong exothermic process and the heat generated can locally melt the catalyst particles [150]. Carbon diffuses into the catalyst melt and upon supersaturation of this ‘liquid’ melt, carbon precipitates out (‘solid’) and organize into a graphitic framework structure. This is an endothermic process (~$40\,\mathrm{kJ\,mol^{-1}}$). The thermal gradient is supposed to be the driving force behind the migration of carbon atoms from the bulk to the surface.

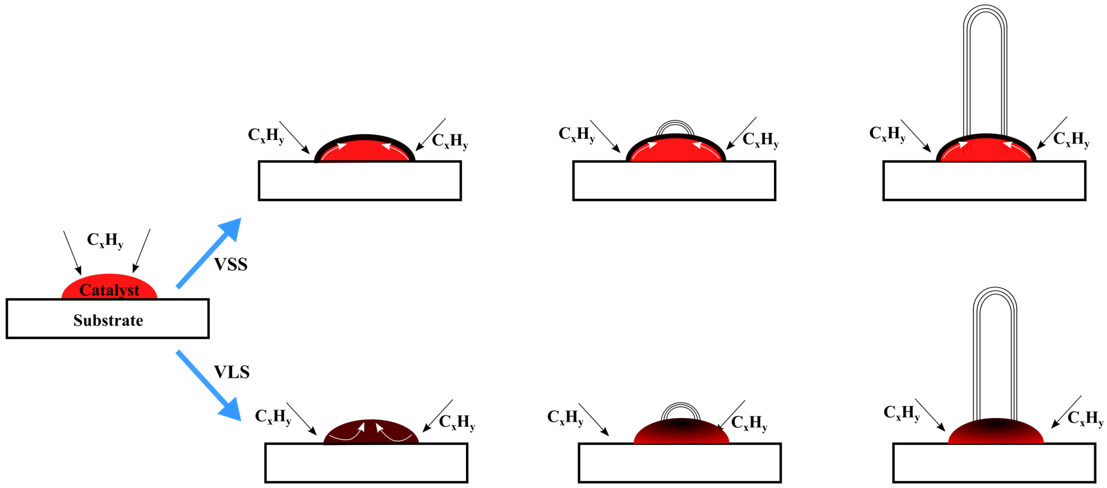

Figure 2.1: Vapor liquid solid (VLS)process involves diffusion of carbon atoms from the bulk to the catalyst surface while vapor solid solid (VSS) process proceeds by the diffusion of carbon atoms along the surface.

More recent studies have questioned the validity of the second stage of the process: the liquid phase [167]. A metal carbide phase is expected to be formed as a result of bulk diffusion. Recent in-situ experimental observations however, rules out the formation of bulk iron carbide phases and favor surface diffusion of carbon atoms [168–170]. Catalyst particles remain in the solid state and carbon atoms diffuse on its surface and precipitate out as CNT favoring a VSS (vapor-solid-solid) mechanism over VLS. Surface diffusion alone cannot explain convincingly the formation of multi-walled CNT. Inner nanotubes will be devoid of fresh carbon source and the growth will not proceed if only surface diffusion is taken into account. Recent DFT calculations [171, 172] indicated a sub-surface diffusion (extending up to 2 or 3 atomic layers from the surface), to be the possible mechanism behind the growth of multiwalled CNT.

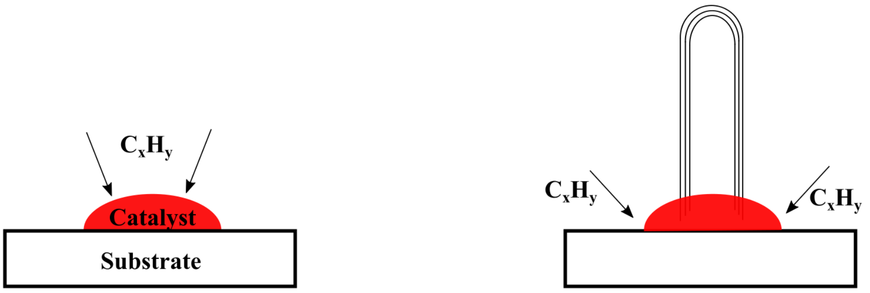

Figure 2.2: Root growth: The strong adhesion between catalyst particles and substrate causes the catalyst particles to remain anchored to the substrate as CNT growth proceeds.

However, there is clear consensus over the final phase of the growth process. Depending on the nature of the catalyst-substrate system, two modes of growth are possible namely root growth and tip growth. Root growth occurs when the adhesion between catalyst particles and substrate is strong. In such cases, as the growth proceeds, the catalyst particles remain anchored to the substrate as shown in figure 2.2. The newly formed carbon species formed by the decomposition of the carbon compound has to find its way to the catalyst particles as the growth proceeds. The main advantage of root growth process is that the catalyst particles remain on the substrate when the arrays of CNTs formed are peeled off. The as-obtained CNTs are thus free of catalyst particles. Since the catalyst particles are left behind on the substrate, they can even be reused for another growth cycle, albeit with slightly inferior CNT quality. Iron on Si/SiO_2 generally favors root growth mechanism [173].

When the adhesion between the catalyst particles and the substrate is weak, the catalyst particles are lifted off from the substrate surface as the growth proceeds [165]. They remain on top of the growing CNTs and hydrocarbon species continually diffuse into the catalyst particles (see figure 2.3). The growth continues till a carbon layer covers the catalyst particles. The catalyst particles are therefore embedded in the as-prepared CNT. Ni based catalyst on Si substrates normally give rise to tip growth mechanism [174]. In general, however, the mode of growth depends upon catalyst-substrate system, hydrocarbon source and growth parameters [175]. For example, for the same catalyst-substrate system, switching from one mode to the other was shown by means of a fast ramping rate [176] or by adjusting the catalyst size [177] or by a plasma pretreatment of catalyst particles [178]. Bimetallic combinations of elements especially of 3d transition metals have shown to exhibit higher catalytic activity for the formation of CNTs [179]. Common bimetallic

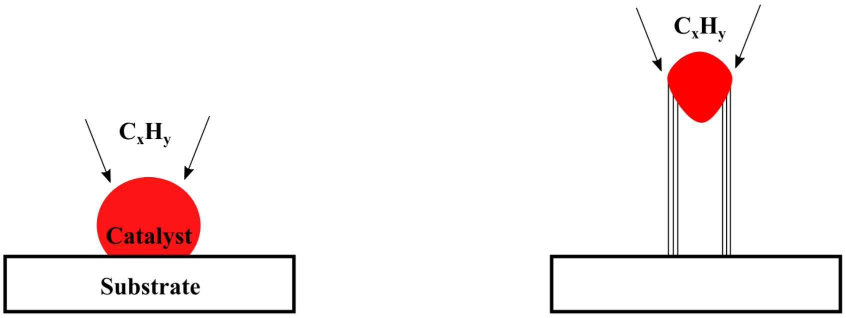

Figure 2.3: Tip growth: The weak adhesion between the substrate and catalyst particle leads to lifting of the catalyst particles during CNT growth.

systems employed are Fe-Co, Fe-Ni, Ni-Co or Fe-Al, Fe-Mo etc. The coefficient of carbon diffusion in iron is more than 2 orders of magnitude higher than in other elements like cobalt or nickel [180]. This results in a higher growth rate for iron based catalyst systems. Among the different iron based bimetallic systems, iron-alumina/aluminum have garnered special attention due to the synergistic effect between the two. Alumina is known to prevent the sintering of iron particles resulting in a narrow diameter distribution and high CNT density [181].

2.3 Water assisted chemical vapor deposition technique

For conventional hydrocarbon CVD, though the growth rate is very high, the catalyst life time is less than a minute [168]. The catalyst undergoes deactivation due to the formation of an amorphous carbon layer on its surface. In 2004, Hata et al. synthesized millimeter long vertically aligned single walled CNTs by a modified chemical vapor deposition process in which ppm quantities of water was added during the synthesis stage [173]. The presence of water dramatically enhanced the catalytic activity and lifetime, resulting in the massive growth of superdense carbon nanotubes. In the original work a thin layer of iron (1 nm) supported on a 10 nm layer of aluminum served as the catalyst. SWNTs with a height of up to 2.5 mm were produced in a growth time of 10 minutes. The SWNTs grew by a root growth mechanism and the as-prepared CNTs were free from catalyst with a purity of ~99.98%. The growth rate (~$20\,\mu\mathrm{m\,s^{-1}}$) was found to be highest at the onset of growth and gradually decreased after about 8 minutes of synthesis [182]. Further work by the same group found that by varying the thickness of the catalyst layer especially iron, it is possible to selectively synthesize single, double or multi-walled CNTs [183].

2.3.1 Role of water and hydrogen in the growth of VACNTs

From the first report of Hata et al. [173], it was clear that balancing the ratio of carbon to water was crucial in maximizing the catalyst lifetime. Further research underscored the fact that there is an optimum level of water that is required for obtaining super growth; too low an amount will lead to catalyst deactivation and too high water content will attack the carbon species responsible for CNT growth thereby retarding the process. In the years followed, the role of water was explored in more detail by the research community. By direct microscopic and spectroscopic analysis, Yamada et al. showed conclusively that the catalyst deactivation readily occurs due to carbon coating and water acted to remove the carbon layer and revive the catalyst [184]. Water removes the amorphous carbon and cleans the catalyst surface according to the reaction:

$$C + 2H_2O \xrightarrow{\Delta} CO_2 \uparrow + 2H_2 \uparrow \tag{2.1}$$

The separation of carbon and oxygen sources to enable tuning and optimizing the levels of carbon and oxygen independently was elucidated as the central concept of water assisted CVD. It was further demonstrated that alcohols, ethers, esters, ketones, aldehydes and even carbon dioxide can act as growth enhancers [185, 186]. In light of these revelations, it was further generalized that an oxygen containing growth enhancer and a carbon source not containing oxygen are the primary requisites for highly efficient CNT growth. The role of oxygen is two fold: it not only cleanses the catalyst particles but also act as a scavenger of hydrogen radicals.

Joshi et al. [187] studied in depth the interaction between water molecules and the catalyst subjected to typical WACVD conditions and investigated the evolution of catalyst morphology and composition for Fe/Al catalyst. High angular dark field STEM images and bright field tomography measurements revealed core shell structure with a void within the core. EELS, XPS and gracing incidence X-ray diffraction confirmed the bimetallic nature of the catalyst containing metallic iron and aluminum as well as their mixed oxidic species. No intermetallic phases were observed at all. From these observations a plausible reaction pathway was outlined. It was proposed that aluminum metal clusters adsorb water as hydroxy groups and these surface bound hydroxy groups bonded to aluminum are crucial in the growth of ‘super-long CNT’. The hydroxy groups react with the carbonaceous deposits to form CO and CO_2 thereby keeping the catalyst active and maintaining the ‘supergrowth’ conditions. In addition, Amama et al. revealed another major role of water in the CNT growth phase [188]. It was found that water also inhibits Ostwald ripening effect occurring during CNT growth phase and aids in extending the catalyst lifetime.

Hydrogen also plays a crucial role in the synthesis of CNTs by WACVD method. Hydrogen assumes different roles in the 3 different stages: pre-growth, growth and post-growth stages of WACVD synthesis. During the pre-growth ramping stage, the catalyst particles are normally heated to the synthesis temperature in a reducing atmosphere to prevent the oxidation of catalyst particles. This is normally achieved by passing a mixture of Ar/H_2. Some reports have also speculated that hydrogen impedes Ostwald ripening of the catalyst particles during the ramping stage and helps in attaining a narrow CNT diameter distribution.

During the growth stage, hydrogen helps in controlling the rate of hydrocarbon decomposition. At high temperature, ethylene decompose to form different carbon and hydrogen species. If the partial pressure of the hydrogen in the system is already high, the decomposition will be suppressed. Thus at the synthesis temperature, a control over ethylene decomposition can be achieved by varying the H_2 flow rate [189]. In addition, by adjusting the H_2 concentration, etching of amorphous carbon and control over number of walls can be achieved as well [189–191].

During the post-growth stage, passing H_2 over the synthesized CNTs helps to detach the CNT arrays from the catalyst particles. This give rise to free standing CNTs free from catalyst particles, which are ready to use without the need for any further purification step.

2.4 Details of VACNTs synthesis by WACVD

Water assisted CVD technique is capable of producing not only well-aligned CNTs free from catalyst particles but also the process is flexible enough to bring about changes in the type of CNT (diameter, no. of walls etc.) produced. This flexibility in the synthesis is very important when carrying out a combined theoretical-experimental work. Moreover from a practical perspective, for adsorption experiments, access to reasonably large quantities of sample, at least of the order of few tens of milligrams, is important and WACVD technique is particularly interesting due to its high yield. While most of the lab scale WACVD systems uses a smaller quartz tube of diameter 2.54 cm, to meet the sample quantity requirements, an up-scaled CVD system with a larger diameter (7.62 cm) quartz tube which can hold a 5 x 5 cm^2 substrate was used in the present study. This section discusses in detail, various steps involved in the synthesis of VACNTs.

2.4.1 Catalyst preparation

In CVD synthesis, CNT yield and quality is greatly influenced by the substrate type, its surface homogeneity and textural properties. The basic requirement for a substrate is that the material selected should be chemically and physically stable at the synthesis temperature. Hence many materials have been investigated as substrate materials e.g. glass, quartz, alumina, steel, Si etc. [136, 149, 192]. Among the different substrate materials, Si with a few hundred nm coating of SiO_2 is known to produce good quality CNTs in high yield [173]. It has been found that the presence of a thin layer of SiO_2 leads to the formation of smaller catalyst particles that are densely packed. More importantly, SiO_2 layer prevents the diffusion of catalyst particles into the Si layer and inhibits the formation of iron silicide or iron silicate [193]. In the present study, p-doped (Boron) 525 µm silicon with a 600 nm coating of SiO_2 was used as the substrate.

It is known that compared to a single catalyst, a bimetallic catalyst system exhibit higher catalytic activity [179]. For the Al/Fe bimetallic catalyst system, a thicker layer of aluminum followed by a thinner layer of iron is commonly employed. Aluminum layer helps in better wetting the substrate surface, thereby promoting good adhesion between the substrate and catalyst layer. The role of aluminum is not limited to a buffer layer which helps to achieve a better adhesion as speculated in the early years, but is found to play an active role in the CNT growth. In the absence of an aluminum layer, CNT growth is not observed. When heated to the synthesis temperature of $\geq 750\,^\circ\mathrm{C}$, aluminum (melting point $= 660\,^\circ\mathrm{C}$) melts, breaking the thin iron layer on top, leading to the formation of small islands of mixed catalyst particles. Joshi et al. studied in detail the role of aluminum and found that thickness of aluminum layer plays a vital role in determining the size of the catalyst particles [189]. In addition, during the water-assisted CVD growth of CNT, water adsorbs on to the aluminum metal clusters as hydroxy groups (see section 2.3.1) which is crucial for extending the catalyst lifetime. In the present study, 10–13 nm thick Al layer was deposited on to the substrate by thermal evaporation technique. In our experiments, it was observed that the rate of Al deposition has an effect on the synthesized CNTs. Too high or too low deposition rate leads to CNT arrays with lower height. Aluminum deposition was typically carried out at a rate of $1.5\,\mathrm{nm\,min^{-1}}$ using a tungsten coil at a pressure of 10^{-6} mbar.

Thickness of the iron layer is one of the most important parameters in WACVD synthesis. Yamada et al. [183] have shown that by varying the catalyst thickness from 1–2.5 nm, diameters and number of walls of the CNT can be varied. Increasing iron thickness by few angstroms can lead to larger diameter and multiwalled CNT. There is also a minimum threshold of iron thickness ~0.6 nm below which CNT growth does not take place [189]. So precise control over iron deposition is required. In the present study, iron deposition (typically 1.2–1.4 nm) was carried out by magnetron sputtering.

2.4.2 WACVD setup

The main parts of the WACVD setup are the mass flow controllers along with its controller unit, bubbler unit filled with deionized water, water sensor (hygrometer) for determining the amount of water and a three zone CVD furnace as shown in the schematic 2.4. Four mass flow controllers (MKS instruments Deutschland GmbH) were used for introducing pre-determined quantities of ethene, hydrogen and argon (for the bubbler as well) required for the experiment. The flow rates for the different stages of the synthesis were programmed into the MKS controller unit and typical values are given in Table 2.1. During the synthesis stage, ppm quantities of water was introduced into the gas stream by bubbling argon gas through the bubbler filled with millipore water. Hygrometer (Michell Instruments, UK), placed before the entry to the CVD furnace, measures the amount of water present in the gas stream by a dew point method. In order to meet the requirement of larger amount of CNTs for adsorption studies, synthesis was carried out in an upscaled CVD reactor. A three zone CVD furnace (Horst, Germany) was used for heating the large quartz tube. The exhaust from the CVD setup opens to a fume hood. A photograph of the complete setup is shown in figure 2.5

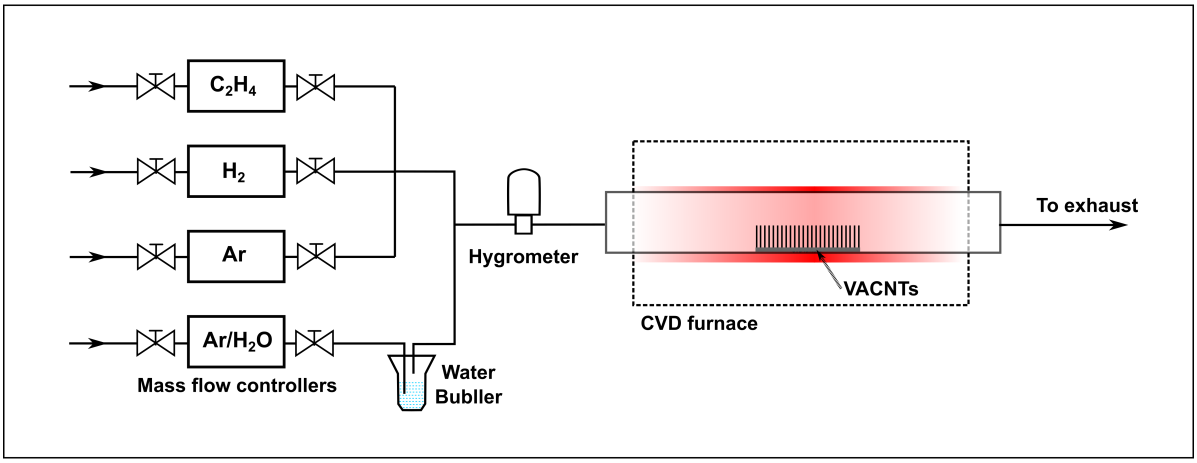

Figure 2.4: Schematic of the water assisted CVD setup.

Figure 2.5: Photograph of the upscaled WACVD setup.

Stage	**Ethene**	**Hydrogen**	**Argon**	**Argon for bubbler**	**Temperature**
1	0	800	1200	0	450 - 850 °C
2	200	800	1200	160 *	850 °C
3	0	800	1200	0	850 °C
4	0	0	1200	0	till 600 °C
5	0	0	200	0	$\leq$ 475 °C

Table 2.1: Typical gas flow rates (in sccm) used for VACNTs synthesis.

The substrate with the catalyst deposited was introduced into the CVD oven at 450 °C. For the ease of introducing and withdrawing substrate from the center of the CVD oven, an inner quartz tube with a quartz plate was used. The substrate was then heated to the synthesis temperature of 850 °C under a reducing atmosphere of hydrogen and argon (stage 1). During the synthesis stage (stage 2), ethene as well as water was introduced along with hydrogen and argon. Argon gas bubbled through water was adjusted so as to obtain around 420 ppm of water in the gas stream. From numerous experiments, this value was found to be the optimum [194]. The rate of argon gas through the bubbler to obtain the desired ppm, varies with humidity and room temperature.

---

* Value speicified may vary depending on the ambient conditions

Synthesis was typically carried out for 15 min. After the synthesis stage, the substrate along with the obtained CNTs was annealed for 5 min in the presence of hydrogen at the synthesis temperature (stage 3). This helps in the easier peeling off the CNT arrays from the substrate. The oven was then cooled down in an argon atmosphere (stage 4 & 5). Once the oven cools below 475 °C substrate along with the CNTs was pulled out. A photograph of the as-obtained CNTs on a 4 cm × 4 cm substrate is shown in figure 2.6.

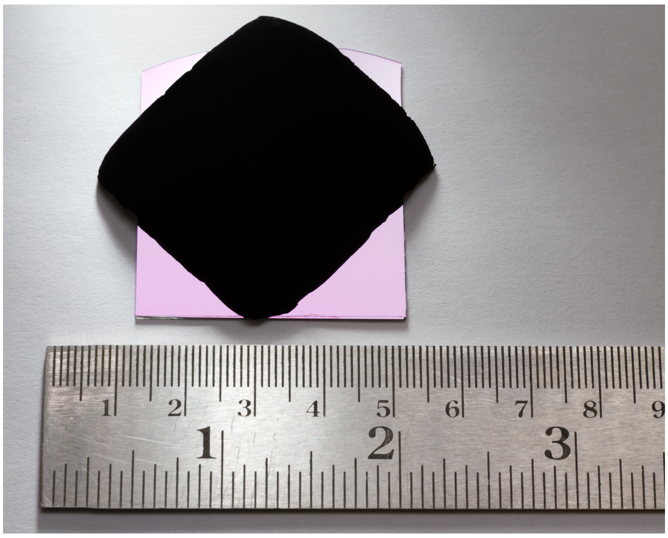

Figure 2.6: Photograph of the as-prepared vertically aligned CNTs on a 4 cm x 4 cm Si wafer.

2.5 Characterization of VACNTs

The as-synthesized VACNTs were characterized by various microscopic, spectroscopic and gas adsorption methods. In this section, the different characterization techniques used in the study are described in detail. The basics of each characterization technique is briefly explained followed by a discussion about the actual measurement on as-prepared VACNTs.

2.5.1 Scanning electron microscopy

Since the wavelength of the electrons are much lower than the wavelength of visible light, much higher resolution can be obtained when imaging with electrons. When a beam of high energy electrons (few 1000 eV) strike a sample surface, three interactions can occur: a) the beam passes through the sample b) beam hits the nucleus of the sample atom and is backscattered c) the high energy electrons of the beam knock out the outer shell electrons from the sample atom. These knocked out electrons are called secondary electrons and are usually very weak in energy (few hundred eV). By placing a detector close to the sample surface, these secondary electrons can be collected. A single electron from a high energy electron beam can typically give rise to a shower of secondary electrons. The amount of secondary electrons (and thus the contrast) escaping from the surface depends upon the surface morphology. By raster scanning the electron beam over the sample surface, topographical information of the sample can be obtained.

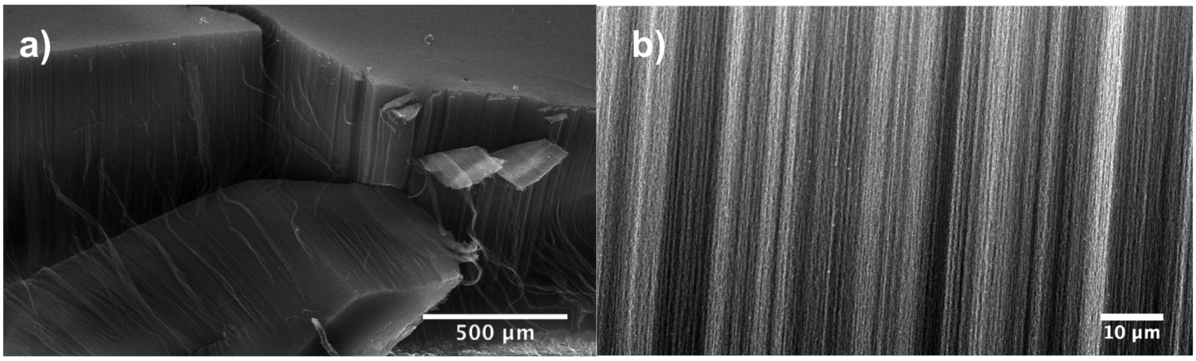

Figure 2.7: a) SEM image of as-prepared CNTs b) High magnification image showing the vertical alignment.

In the present work, SEM was mostly used to measure the height of the VACNT array and to ensure uniformity of alignment. Figure 2.7a shows a typical SEM image of the as-synthesized CNTs. The dense CNT structures obtained after 15 min of synthesis is found to have a height of ~600 - 800 µm. The high magnification image in figure 2.7b, shows the vertical alignment of the as-prepared CNTs. Functionalization of these pristine CNTs, leads to changes in the surface morphology and SEM proved to be a vital tool in characterizing such morphological changes.

2.5.2 Transmission electron microscopy

When the energy of the electron beam is high (few 100 keV) and the sample is thin enough (few nm), electrons can pass through the sample. Extremely high resolution can thus be obtained with transmission electron microscopy. In the present study, TEM is primarily used to determine the diameter and the number of walls of the CNT. Though there is no contrast difference between the amorphous carbon and CNT, the presence of long range ordering in CNT can differentiate it from the amorphous phase. 2D projection of multiwalled CNT appear as equidistant lines symmetrically arranged around a central void.

Samples for TEM investigation were prepared by first dispersing the vertically aligned CNTs in ethanol by ultrasonication followed by placing a few drops of the suspension on a lacey carbon

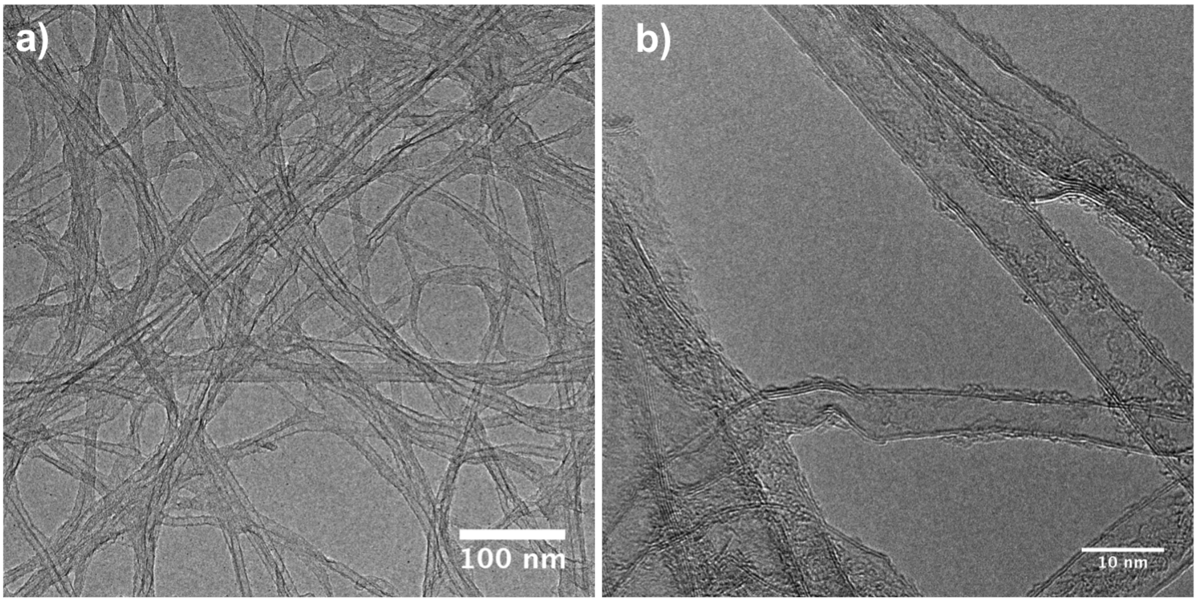

Figure 2.8: a) TEM image of as-prepared CNTs b) high resolution image showing the number of walls and diameter of CNTs.

grid. Imaging was typically carried out at 200 keV. TEM image of an as-prepared CNTs is shown in figure 2.8a. From the low magnification image it can be seen that the as-prepared CNTs are free from catalyst particles and contains only very small amount of amorphous carbon. A representative high magnification TEM image of VACNTs is shown in figure 2.8b. From numerous TEM measurements it is found that the as-prepared CNTs are usually double or multiwalled (no. of walls ≤ 6). The average internal diameter of these CNTs are determined to be around 8 nm.

2.5.3 Thermogravimetry measurements

In thermogravimetric (TG) analysis of CNTs, few milligrams of the sample is placed on a microbalance and is heated to high temperature in a controlled atmosphere. The resulting changes in mass recorded, provides information about the stability and purity of CNTs. Heating in air or in oxygen is the most common method adopted. When heated slowly to a temperature of 900 °C in an oxidizing atmosphere, all forms of carbon completely burn off at temperatures $\leq$ 750 °C. The catalyst metal particles, if present, are left behind and the resulting mass can be used for quantifying the metal content. TG can also yield useful information regarding the nature of carbon present in the sample. The reactivity of different carbon species like amorphous carbon, SWNT, DWNT and MWNT towards oxygen, decreases in the given order. The onset and slope of the weight loss curve can therefore provide valuable information regarding the quality of the CNTs.

Heating in an inert atmosphere like argon or helium, can provide an indirect information regarding the extent of functionalization. When heated in an inert atmosphere, highly functionalized CNTs suffers a greater weight loss compared to unfunctionalized CNTs.

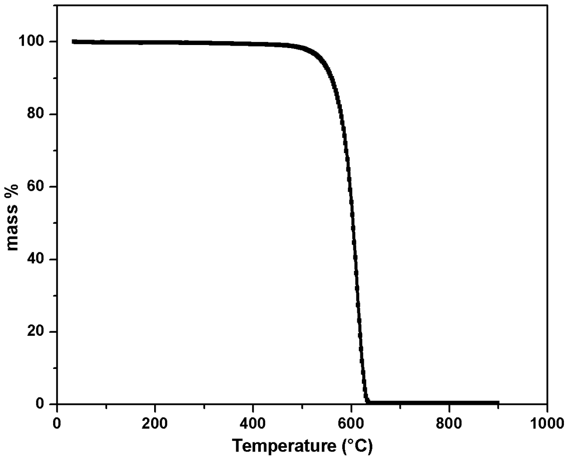

Figure 2.9: TG of as-prepared CNTs.

Figure 2.9 shows the TG curve of as-prepared VACNTs heated to 900 °C in air. No noticeable weight loss is observed below 400 °C indicating a near absence of functional groups (e.g. -OH). Negligible weight loss is observed below 550 °C indicating high quality CNTs with little amorphous carbon. A complete burn off is observed at temperature around 650 °C confirming the absence of catalyst particles consistent with the TEM observations. More detailed information can be obtained by deconvoluting the derivative of the TG curve and is discussed in more detail in section 4.4.

2.5.4 X-ray photoelectron spectroscopy

When the energy of an incident photon is high enough, it can knock out an electron from the inner core shell of the material irradiated. The ejected electron carries information about the chemical state of the material. The mean free path of ejected electrons in a solid is very small and therefore X-ray photoelectron spectroscopy (XPS) is an extremely surface sensitive technique. It typically probes the top few atomic layers of the sample (few nanometers).

A schematic of the XPS process is shown in figure 2.10. When the incident photon energy ($h\nu$) is higher than the inner shell electron binding energy (E_B), electrons are ejected with a kinetic energy (E_k) according to the relation:

$$E_k = h\nu - E_B - W \tag{2.2}$$

where W is the spectrometer work function. Since the energy of the incident beam varies with the wavelength, a monochromatic radiation is typically preferred. XPS mostly make use of monochromatic soft X-rays like Al K$_\alpha$ (1486.3 eV) or Mg K$_\alpha$ (1253.6 eV).

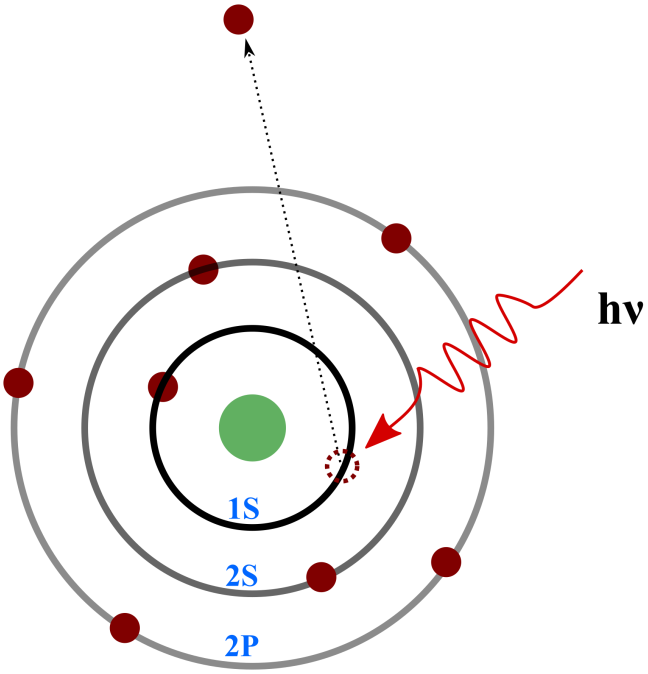

Figure 2.10: Schematic of XPS process. When an incoming photon has sufficient energy, it can knockout an electron from the inner core shell of the material irradiated and the ejected electron carries chemical information about the material.

XPS spectrum is plotted on a binding energy scale and different elements are characterized by their unique peak positions. The electrons which are emitted without any energy loss contribute to the characteristic peaks and those electrons which suffers an inelastic collision, contribute to the background spectrum [195]. The intensity of the peaks can be used to quantify the elements present. Peak shifts or chemical shifts are useful in analyzing the chemical state of the materials. Differences in chemical potential and polarizability leads to variation in the binding energies, shifting the characteristic peaks.

Since XPS probes only the top few nanometers, information from the bulk of the sample is not obtained. This is disadvantageous when analyzing the uniformity of a certain functionalization process. A rudimentary approach to overcome this problem is to break the sample into 2 halves and perform a line scan of the cross-section. However, this is not always feasible as the freshly cleaved pieces of wafer or CNTs can lead to sample as well as XPS chamber contamination. A more elegant approach is to use an argon ion or a gas cluster source to etch the top surface followed by recording the spectra. By carrying out these two steps in succession for a certain number of cycles or time frame, depth profile information can be obtained. These depth profile measurements can provide valuable information regarding extend and uniformity of functionalization.

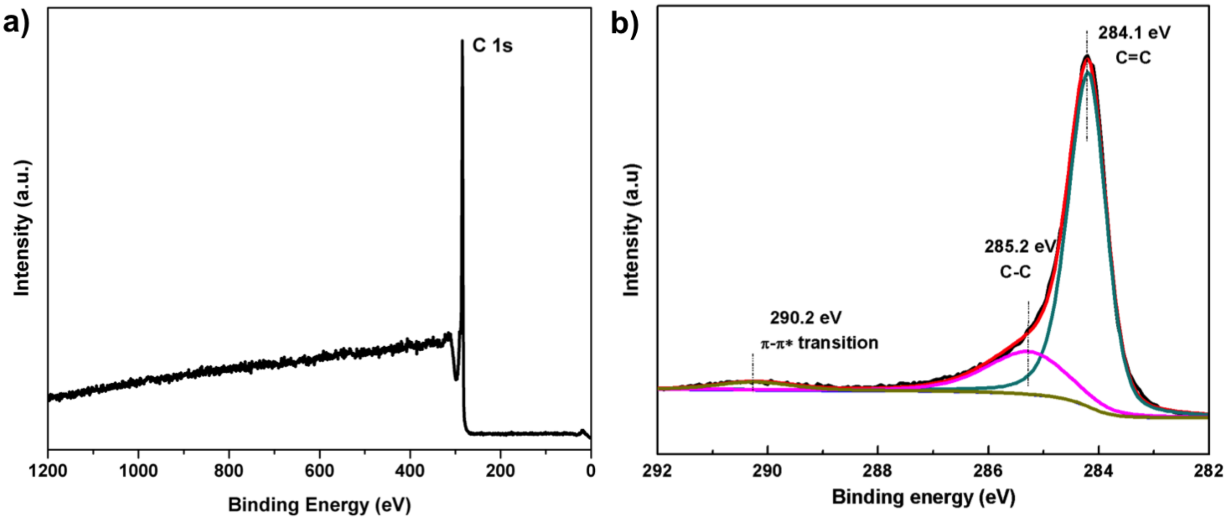

Figure 2.11: a) XPS survey spectrum of as-synthesized VACNTs b) high resolution C 1s spectrum with deconvoluted peaks.

Figure 2.11a shows the XPS survey spectra of the as-prepared vertically aligned CNTs. No peak other than the C 1s peak of carbon, is present in the spectra. This reiterates the absence of catalyst particles in the as-synthesized CNTs. To obtain a more accurate and detailed information on the nature of carbon bonding, high resolution C 1s spectrum was measured. The obtained spectrum is deconvoluted into three peaks as shown in figure 2.11b. The strong photo emission at 284.1 eV is attributed to the graphitic structure (sp^2) of CNTs [196]. The pronounced asymmetry of the peak to higher binding energies is inherent for graphite [197] and is known to result from neutralization of the holes by conduction electrons created during photoionization [198]. The structural defects of CNTs or the presence of amorphous carbon is responsible for the peak at 285.2 eV and leads to a broadening of the corresponding C 1s signal. The high energy peak at 290.2 eV is assigned to $\pi - \pi^*$ transition.

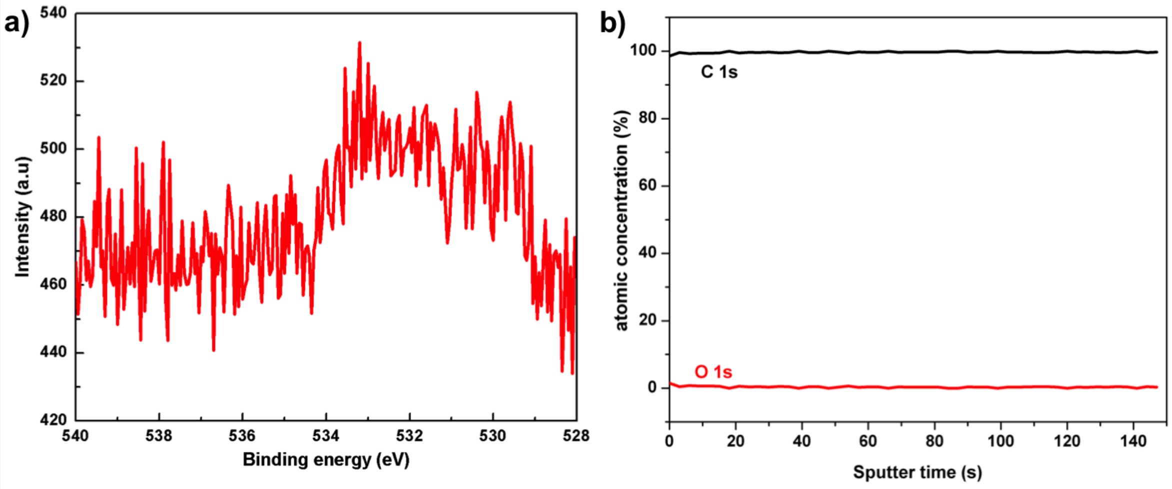

Figure 2.12: a) High resolution O 1s spectra of as-synthesized VACNTs b) depth profile measurement of VACNTs.

The high resolution O 1s photoelectron spectra is shown in figure 2.12a. Even for longer measuring times in the O 1s region, only traces of oxygen were detected for the as-synthesized CNTs. These are certainly due to the adsorption of ubiquitous oxygen from the atmospheric handling of the samples. To further verify this, depth profiling measurements were performed on these samples. The concentration of oxygen falls rapidly after a few seconds of argon sputtering as shown in figure 2.12. It can thus be concluded that virtually no oxygen moieties are inherently present in the pristine VACNT sample.

The well-defined structure and the absence of heteroatoms or functional groups make VACNTs an ideal model structure for a combined theoretical and experimental approach for understanding gas adsorption on carbon materials.

2.5.5 Raman spectroscopy

With the advent of nanotechnology, Raman spectroscopy has received a renewed interest both from a fundamental and practical perspective. Today Raman spectroscopy is a widely used characterization tool due to its simplicity and non-destructive nature of measurement. The analysis can be carried out at ambient conditions without the need for elaborate sample preparation steps. Raman spectroscopy is one of the very few characterization techniques, that can clearly distinguish between different forms of sp^2 carbon like highly ordered graphite, graphene, single walled nanohorns, SWNT and MWNT. The main features of a typical Raman spectrum for CNTs are explained one by one.

RBM: Radial breathing modes are unique for CNTs and its intensities are especially strong for SWNTs. RBM appears in the lower energy region between 100–300 cm^{-1}. It originates from the symmetric in-plane displacement of all carbon atoms in the radial direction as shown in figure 2.13. An important characteristic of RBM modes is its frequency dependence on CNT diameter. RBM modes can be used for determining the diameter of the SWNTs according to the relation:

$$\omega_{RBM} = A/d_t + B, \tag{2.3}$$

where ω is the wavenumber in cm^{-1}, A and B are constants. Different values of A and B are reported in literature. A is associated with an intrinsic property and the most common value of 227 cm^{-1} is in agreement with the elastic properties of graphene. B is a non-zero value and its values is based in extrinsic characteristics like bundling, substrates, measuring atmosphere etc. [199].

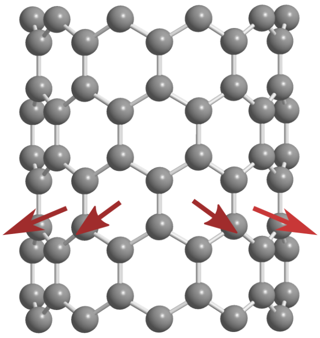

Figure 2.13: Schematic of atomic displacement in RBM mode in CNTs.

G-band: G-band or graphite band is the Raman signature for all sp^2 carbon materials and is centered at ~1585 cm^{-1}. It arises from the in-plane C-C bond stretching as shown in figure 2.14a. There are two optical in-plane stretchings: a) along the CNT axis, known as longitudinal optical (LO) phonon and b) along the nanotube circumference, known as transverse optical (TO) phonon. G-band is highly sensitive to strain effects. For a perfect graphene, the two stretchings have the same frequency. However, under strain, like the curvature induced strain in CNTs, the G band splits into these two peaks: G$^+$ and G$^-$ and its assignment to a particular stretching mode varies with the type of nanotube. G-band in graphene is a one phonon resonant Raman process

[200, 201] as shown in figure 2.14b. (In a resonant Raman process, the energy of the incident photon matches the energy of the optical absorption electron transition). G-band usually has a very narrow linewidth of ~10 cm^{-1} and is found to change with strain, temperature and doping [199].

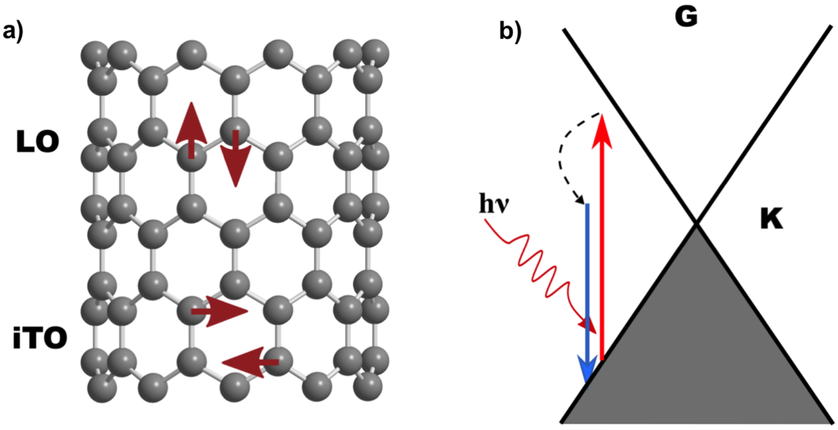

Figure 2.14: a) Schematic of atomic displacement in G-band mode in CNTs b) One-phonon process responsible for G-band in graphene (red arrow: photon absorption, blue arrow: emission, shaded areas: occupied states. adopted from ref. [201]).

G' or 2D band: G' band is also a Raman allowed band for sp^2 carbon materials and falls in the range 2500–2800 cm^{-1}. The G' frequency varies with the incident laser energy and for 514 nm laser (E_{laser} = 2.41 eV), G' appears at ~2700 cm^{-1}. It is sometimes referred to also as 2D band [201]. In graphene, it is a double resonance (DR) 2 phonon process as shown in figure 2.15a. It is the most intense double resonance process and is sensitive to the number of layers of sp^2 carbon. Therefore G' band is used widely for quantifying the number of layers and stacking order in few layer graphene.

D-band: D-band or defect band is not a Raman allowed mode for perfect sp^2 carbon materials. Due to its hexagonal structure, sp^2 carbons have a high symmetry and are therefore sensitive to symmetry breaking defects. In the presence of defects, D-band is activated and is formed due to the breathing mode of six-atom rings [201] as shown in figure 2.15b. Like G'-band, D-band is also sensitive to the incident laser energy and appears at ~1350 cm^{-1} for E_{laser} = 2.41 eV. D-band is a double resonance process activated by a phonon and a defect as shown in figure 2.15c. The ratio of intensity of D-band to G-band can be used to quantify disorder/defect in sp^2 carbon systems. The ratio, however, strongly depends upon the energy of the laser excitation and is inversely

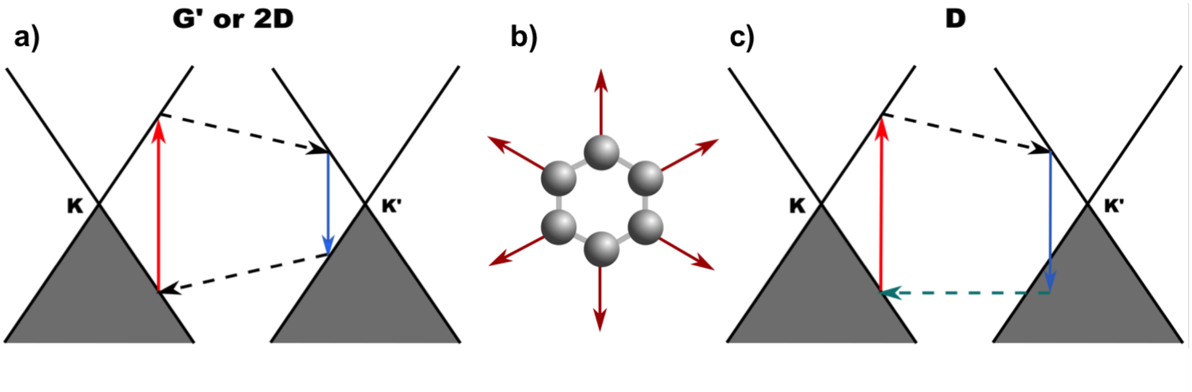

Figure 2.15: a) 2-phonon process responsible for G' or 2D band in graphene b) Schematic of atomic displacement in D band c) 2-phonon process responsible for D band. In the presence of defects, phonon wavevector (dashed line), need not be zero. (red arrow: photon absorption, blue arrow: emission, shaded areas: occupied states. adopted from ref. [201]).

proportional to the fourth power of E_{laser} [199]. So care must be taken to use the same excitation wavelength, when investigating the effect of a process on a given sample.

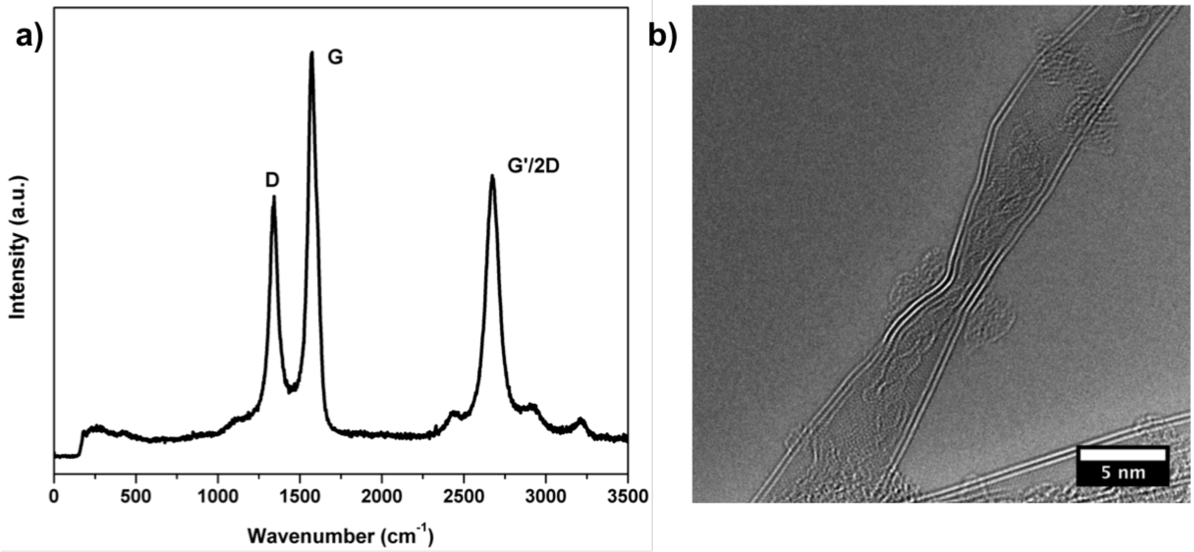

Figure 2.16: a) Raman spectrum of as-prepared VACNTs b) Variation of diameter along the length of the CNT observed under TEM.

Figure 2.16a shows a typical Raman spectrum obtained from as-prepared VACNT arrays. In the low energy regime, there are no distinct RBM peaks. This is expected as the as-prepared CNTs are usually double or multi-walled as seen from the TEM images. A very narrow but prominent D-band is present. It is known that CNTs prepared by CVD technique have a slightly lower crystallinity than the arc or laser grown CNTs [149]. From several TEM measurements, variations in diameter along the tube are seen (2.16b) which are also known to contribute to the D-band intensity [202]. Id/Ig ratio of ~0.7 is typically observed for the as-prepared CNTs.

2.5.6 Nitrogen adsorption isotherm

Characterization of the pores and its size distribution is a very important parameter for understanding gas adsorption on a material. Pore width can be estimated by different techniques like microscopy, radiation scattering, gas adsorption etc. [203]. Among the different methods mentioned above, gas adsorption is the most widely used method to estimate pores ranging from 0.35–100 nm [204]. It is a bulk technique and therefore, it gives an average picture of the material.

Adsorption isotherm is obtained by measuring the amount adsorbed at a given pressure under constant temperature conditions. N_2 at 77 K is the most widely used adsorbate for determining the surface area and pore size distribution. The saturation pressure (P_0) of N_2 at 77 K is ~1 bar. The micropores are filled at very low partial pressures ($P/P_0 \leq 0.2$) and multi layer adsorption on mesopores occur in the intermediate pressure range ($P/P_0 \geq 0.2$). At still higher relative pressures capillary condensation occurs in mesopores. The adsorption isotherm thus obtained for various materials, fall into one of the eight categories of isotherm (figure 2.17) proposed by IUPAC [2].

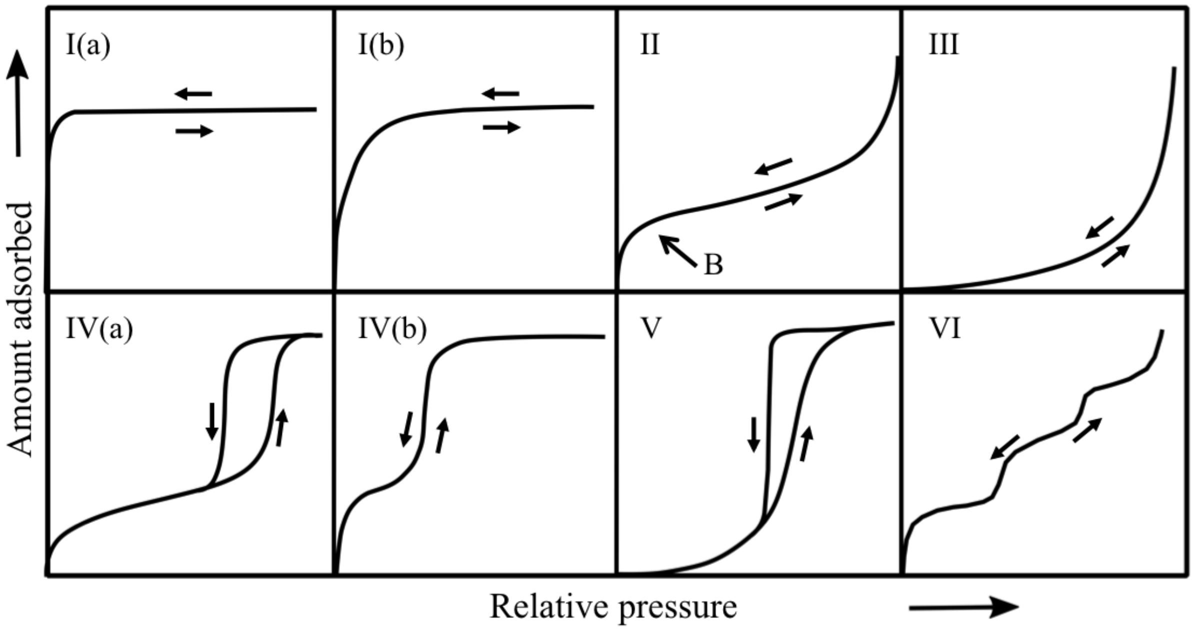

Figure 2.17: IUPAC classification of physisorption isotherms.

Type-I adsorption isotherm is concave to the P/P_0 axis and are typically observed for microporous materials. Volume filling of the micropores lead to the high uptake at low relative pressures and once the micropores are filled, adsorption saturates. The revised IUPAC classification [2], has subdivided type-I adsorption isotherm into type-I(a) and type-1(b). Adsorption by materials having mainly very narrow micropores of width $< 1\,\text{nm}$ give rise to type-I(a) while materials with slightly broader pore size distribution including micropores and narrow mesopores ($< 2.5\,\text{nm}$) leads to type-I(b) adsorption isotherms. Type-II isotherms are obtained for non-porous or macroporous materials and is the result of unrestricted monolayer-multilayer adsorption. The inflection point B, corresponds to the completion of monolayer and start of multilayer [205]. Type-III isotherms are convex to the relative pressure axis and are observed for systems with high adsorbate-adsorbate interaction. This type of isotherm is not common and one of the most cited example is the adsorption of water on graphite surface. Type-IV isotherm is typical for mesorporous materials and is similar to type-II isotherm except for the presence of adsorption hysteresis at high relative pressure. Capillary condensation in the mesopores leads to the observed steep increase in the adsorption as well as the adsorption hysteresis at high relative pressures. In the revised isotherm classification, type-IV isotherms are subdivided into type-IV(a) and type-IV(b). Type-IV(a) adsorption isotherms are exhibited by materials having pore width exceeding a certain width, which is dependent on the adsorption system and temperature. For N_2 at 77 K and adsorbents with cylindrical pores, the lower limit of this critical pore width is determined to be about 4 nm. Capillary condensation accompanied by hysteresis occurs in these pores. When the adsorbents have pores mainly in the lower mesopore regime ($< 4\,\text{nm}$), a completely reversible type-IV(b) isotherms are observed. This type of isotherm is also given by conical and cylindrical mesopores that are closed at the tapered end. Type-V isotherms are similar to type-III isotherms but are characterized by the presence of adsorption hysteresis. Similar to type-III isotherms, this type of isotherm arises due to weak adsorbent-adsorbate interactions. Type-VI isotherms represents a special case and is due to stepwise multilayer adsorption on non-porous uniform surfaces.

Determination of specific surface area is one of the preliminary steps in adsorption studies. The most common method for determining the specific surface area is the BET method named after Brunauer, Emmett and Teller [206]. The BET equation is given by:

$$\frac{1}{n[P_0/P - 1]} = \frac{1}{n_m C} + \frac{C - 1}{n_m C}\frac{P}{P_0} \tag{2.4}$$

where n is the specific amount adsorbed, n_m is the specific monolayer capacity. The BET constant C is an indication of the adsorbate/adsorbent interaction and is related to the energy of adsorption in the first adsorbed layer. A plot of $1/[n(P_0/P)-1]$ vs. P/P_0 for most solids, using N_2 as the adsorbate, yields a straight line in the P/P_0 range $0.05 \leq P/P_0 \leq 0.3$. Once the slope and intercept are known, monolayer capacity can be determined. The specific surface area can then be calculated by:

$$SSA = \frac{n_m N \sigma_m}{m} \tag{2.5}$$

where σ_m is the molecular cross-sectional area (0.162 nm^2 for N_2), N is Avogadro's number and m is the mass.

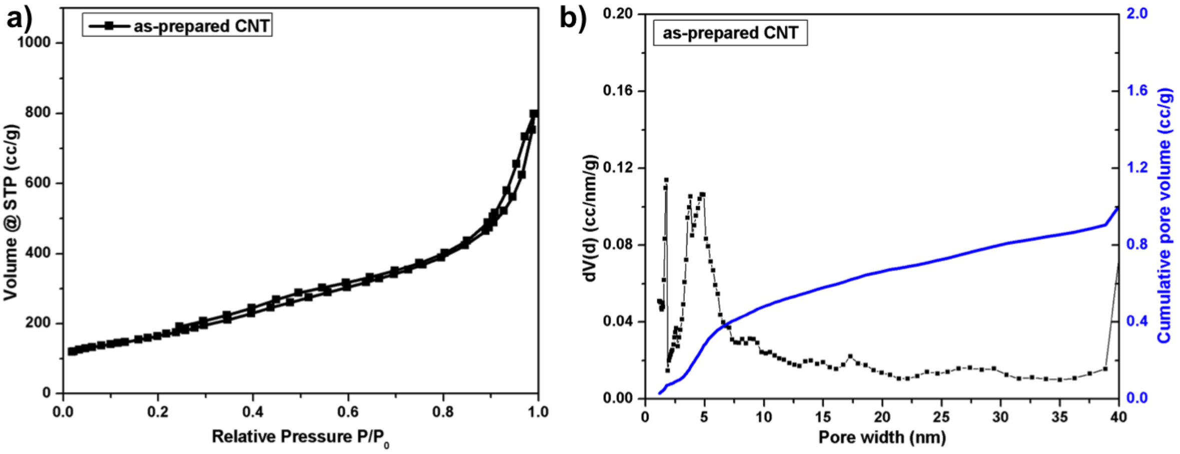

Figure 2.18: N_2 adsorption isotherm and pore size distribution of as-prepared VACNTs.

N_2 adsorption isotherm of as-prepared CNTs is shown in figure 2.18a. The shape of the curve resembles a type-IV(a) isotherm with hysteresis at high partial pressure corresponding to capillary condensation in the mesopores. The porosity is mainly in the mesopore region and arises from the interior of the CNT (average internal diameter = 8 nm) as well as the interstitial sites between parallel CNTs (average intertube distance ~15 nm). A small amount of adsorption is also observed at very low partial pressures indicating the presence of micropores. The micropores in the as-prepared VACNTs may be due to the defects in the outer walls of the CNTs or can also be due to the small slit shaped pores formed when two CNTs touch each other. Pore size distribution was calculated by non-local density functional theory (NLDFT) based method included with the commercial software NovaWin from Quantachrome instruments. Two peaks corresponding to the micropores and mesopores are present in the pore size distribution graph shown in figure 2.18b.

The broad peak at ~5 nm roughly corresponds to the more defined internal diameter of the CNT. The cumulative pore volume of the VACNTs is estimated to be about 1.02 $\mathrm{g\,cm^{-3}}$. The specific surface area of the as-prepared VACNTs structure is found to be ~500 $\mathrm{m^2\,g^{-1}}$.

2.6 Concluding remarks

To summarize, water assisted CVD as an attractive method for the synthesis of well-aligned catalyst free CNTs was presented. The two basic growth mechanisms and the role of various influencing parameters like water, hydrogen, substrate and catalyst were discussed in detail. Details of the WACVD setup used in the present work were presented and the typical synthesis procedure was explained. The as-synthesized VACNTs are found to be mostly double to multiwalled with an average internal diameter of 8 nm and have a specific surface area of 500 $\mathrm{m^2\,g^{-1}}$. They are free from catalyst particles and are devoid of any functional groups.

3 Adsorption

In this chapter the most important techniques for determining adsorption capacity of a material are discussed. The ambient pressure adsorption setup and the self-built high pressure volumetric setup used in the study are described in detail.

3.1 Techniques for determining adsorption capacity

Adsorption capacity of a material is most commonly measured by using volumetric or gravimetric techniques. Volumetric method measures the change in pressure caused by the adsorbent when a gas is expanded to a calibrated known volume. Since volumetric technique basically measures the changes in pressure, the term manometry is also sometimes used. Careful and accurate volume calibration is critical in volumetric technique. Adsorbed amount is calculated by a mass balance before and after expansion, using equation of state (see section 3.3). The main advantage of volumetric technique is the low cost and the simplicity of the setup. However to obtain a significant pressure drop, larger quantities of adsorbent material are required. Also the uncertainties associated with the adsorbed mass increases almost exponentially with each step [3]. Hence the maximum number of steps (and hence the measurement points), is usually limited to three and the sample should be reactivated and brought to its original state before further measurements are performed.

In gravimetric technique, amount of gas adsorbed is determined by directly measuring the weight gain of the adsorbent when an adsorptive gas is introduced. A microbalance is typically used for the measurement and a pressure dependent buoyancy correction is mandatory. Magnetic suspension balance with a resolution of ± 1 µg is commercially available and is used widely for high pressure measurement. Such high resolution enables measurement of adsorption on small quantities of the sample with high accuracy. However, such microbalances are built in a fairly complex way and are sensitive to electromagnetic disturbances. Exact control and measurement of temperature pose difficulties in the gravimetric measurement.

A volumetric setup connected to a gas chromatograph is one of the most common methods employed to study co-adsorption equilibria of multicomponent gases [3]. Although gravimetric and volumetric setups for studying single component gases are commercially available, setups for investigating multi-component gas adsorption hardly exist. However for all practical purposes, multicomponent gas adsorption data is pivotal. The most common strategy employed is to measure single component adsorption isotherms of the respective gases and use some models like Ideal Adsorbed Solution Theory (IAST), to predict co-adsorption equilibria. However several studies have reported serious shortcomings of this approach [207]. A reliable experimental measurement of co-adsorption equilibria is thus imperative.

In the present work, two different experimental setups were used for measuring adsorption capacity: an ambient pressure setup and a high pressure volumetric setup. Ambient pressure setup is in principle similar to a gravimetric setup and a modified thermogravimetric (TG) instrument is used for this purpose. Since the amount of sample required for the measurement is low (6–10 mg), ambient pressure setup is primarily used for screening different samples by obtaining an initial estimation of the adsorption capacity. Those samples which show promising adsorption characteristics are produced in larger quantities and a high pressure adsorption isotherm is obtained using the volumetric setup. The volumetric setup is designed to measure multi-component gas adsorption data as well. The two experimental setups are discussed in detail in the subsequent sections.

3.2 Ambient pressure setup

Ambient pressure setup is used for a first estimation of the adsorption capacity of an adsorbent at 35 °C and at a fixed pressure of 1 bar pressure. A TG209F1 Iris, (Netzsch GmbH) instrument was used for this purpose. A schematic of the setup is shown in figure 3.1 and a photograph of the experimental setup is given in figure 3.2a.

Details of a typical measurement are as follows. About 6–10 mg of adsorbent was taken in an alumina crucible for each measurement. Mass flow controllers (BronkHorst High-Tech B.V., Netherlands) were used for delivering predetermined quantities of gas. High purity CO_2 (99.9 %) and argon (99.998%) gases were used for all measurements. The temperature profile for a typical measurement is shown in figure 3.2b and the gas flow rates for the different stages are listed in table 3.1.

After loading the sample in the alumina crucible, the sample was evacuated three times at 32 °C and heated to 300 °C under argon at a heating rate of 10 °C min^{-1}. The sample was maintained at 300 °C for 2 hours to remove any adsorbed species e.g. water. After the activation, sample was

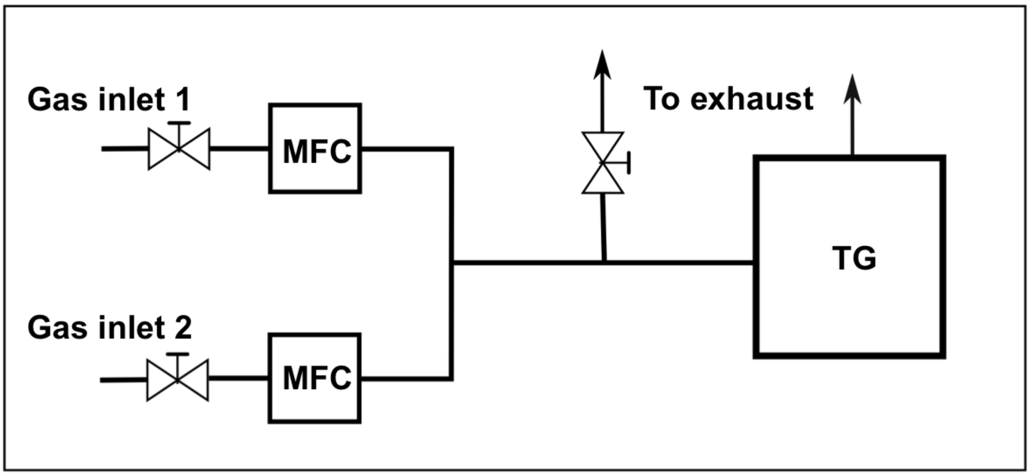

Figure 3.1: Schematic of the ambient pressure setup.

cooled down to 35 °C and maintained at the same temperature for another 30 min so as to ensure constant temperature. In the adsorption stage that followed, 50 sccm of CO_2 replaced the argon supply. In order to ensure equilibrium, adsorption step was maintained for one hour after which CO_2 supply was switched off. Before taking the sample out of the setup, the sample was heated to 300 °C. To account for the buoyancy effects, a correction measurement was carried out without the sample, before each actual measurement.

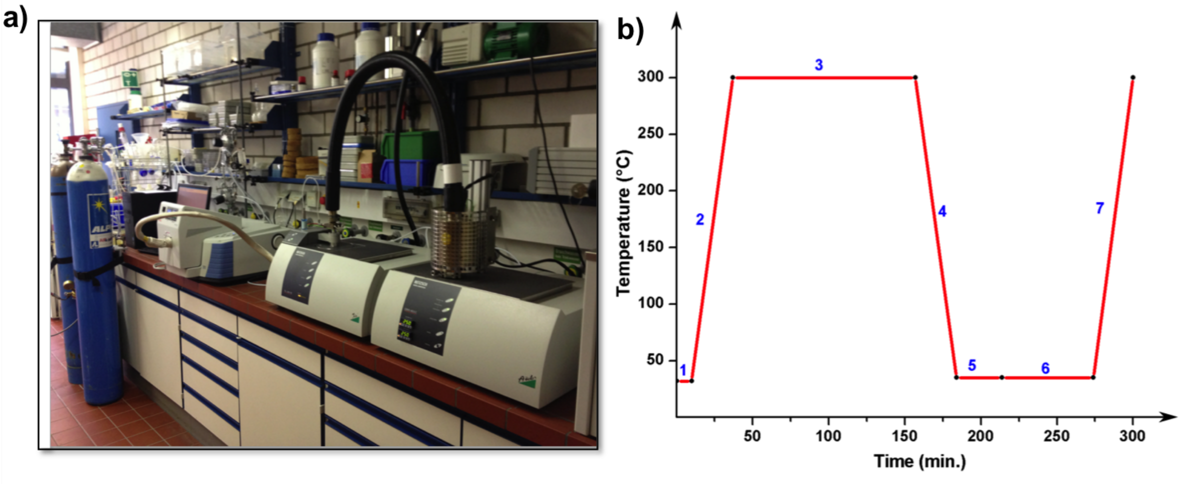

Figure 3.2: a) Photograph of the ambient pressure adsorption setup b)Temperature profile of a typical ambient pressure adsorption measurement.

The adsorption capacity is usually expressed in terms of milligrams of gas adsorbed per gram of the adsorbent.

$$\text{amount adsorbed} = \frac{\text{Weight gain due to adsorption in mg}}{\text{Weight of the adsorbent in g}} \tag{3.1}$$

Stage	**Temperature (°C)**	**Ar (sccm)**	**CO_2 (sccm)**	**Duration (min.)**
1	32	50	0	10
2	to 300	50	0	27
3	300	50	0	120
4	to 35	50	0	27
5	35	50	0	30
6	35	0	50	60
7	to 300	50	0	27

Table 3.1: Typical temperature and gas flow rate program used for ambient pressure adsorption measurements

Though the ambient pressure adsorption measurement outlined above is a rapid way to estimate the adsorption capacity, it falls short in some aspects. The most important being, the measurement gives the adsorption capacity only at a single point in the adsorption isotherm i.e. at 1 bar. Vertically aligned carbon nanotubes are mesoporous structures and are therefore expected to have better adsorption behavior at high pressures. The TG system is not designed for vacuum or high pressure measurement and therefore adsorption studies at pressures lower or higher than 1 bar are inaccessible. Also the lower limit of stable constant temperature achieved in the TG setup is limited to 35 °C. Since adsorption (physisorption) decreases with an increase in temperature, adsorbed amount will be lower at higher temperature and therefore to minimize the error in the measurement, adsorption was always carried out at 35 °C. An attempt was made to obtain more than one adsorption point by progressively increasing the concentration of the gas during the adsorption stage. This was done by increasing the CO_2 flow rate and subsequently decreasing the argon flow rate, so as to maintain a constant net flow rate. In this way, the adsorption capacity could be plotted as a function of gas concentration or partial pressure. However, the stepwise adsorption isotherm, that was expected from such a measurement, was not obtained. More detailed analysis in this direction is required to elucidate the factors responsible.

Another aspect in which the ambient pressure setup falls short is in the activation of the sample. Before measuring the adsorption capacity, the adsorbents should be degassed by heating in vacuum at temperatures around 150 °C for 12 hours . However in a TG setup this is not possible. The evacuation is carried out in cycles and is generally limited to few cycles spanning few minutes each. The activation process is therefore carried out only by heating to high temperature. Also unlike a magnetic suspension balance, the sample chamber is not magnetically suspended and is not isolated in a TG setup. The adsorption studies of corrosive or reactive gases are therefore problematic with a TG setup. Nevertheless, the ambient pressure setup is useful in providing a first estimate of the adsorption capacity and the values obtained are found to be consistent with the adsorption capacity obtained from a more standardized measurement technique. Therefore ambient pressure measurements provide a valuable first and fast quantitative test for analyzing the adsorption properties of a new material.

3.3 High pressure volumetric setup

In the volumetric method, a predetermined mass of gas is expanded into a known volume that hosts the adsorbent. Gas molecules adsorb on the adsorbent and lead to a decrease in the pressure. By a mass balance the amount adsorbed can be calculated if the pressure, temperature and volume are known accurately. Consider two volumes V_1 and V_2 placed in a thermostat separated by an expansion valve as shown in figure 3.3. A pressure transducer and thermocouple connected to the volumes accurately determine the pressure and temperature of the gas inside. After evacuating both the volumes, a certain amount of known gas is filled in volume V_1. By determining the temperature (T_1) and pressure (P_1) of the gas in V_1, density of the gas (ρ_1) and thereby the mass of gas (m_1) can be calculated as:

$$m_1 = \rho_1 V_1 \tag{3.2}$$

where $\rho_1 = f(P_1, T_1)$ is a function of temperature and pressure.

Once a stable temperature and pressure is obtained, the expansion valve is opened and gas from V_1 expands to V_2. The adsorption of gas molecules on the adsorbent surface, leads to a lowering of the pressure determined by the adsorption capacity of the adsorbent. After thermodynamic

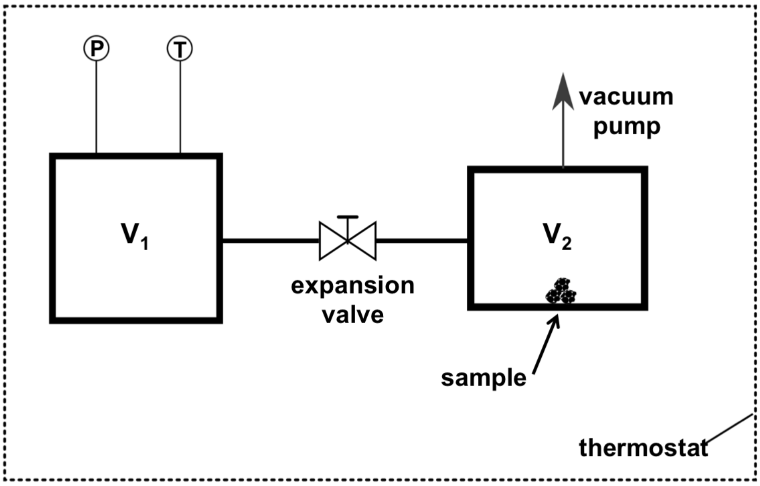

Figure 3.3: Schematic of a simple volumetric setup.

equilibrium is established, by a mass balance, the amount of gas adsorbed (m_a) can be calculated as:

$$m_1 = m_2 + m_a \tag{3.3}$$

$$\rho_1 V_1 = \rho_2(V_1 + V_2 - V_s) + m_a$$

$$m_a = \rho_1 V_1 - \rho_2(V_1 + V_2) + \rho_2 V_s \tag{3.4}$$

where m_2 is the mass of the remaining gas in the combined volume which is not adsorbed and V_s, also known as void-volume, is the volume of the adsorbent impervious to the gas. Void-volume is most commonly determined by using helium measurements which is based on the assumption that helium does not adsorb on the adsorbent surface.

3.3.1 Absolute, excess and reduced adsorption

Amount adsorbed can be expressed in terms of absolute adsorption, excess adsorption or reduced adsorption. These concepts are elucidated in this section.

Consider a closed system filled with a known gas at constant temperature and volume (V_{tot}). By knowing the pressure and temperature of the system, density of the gas can be calculated. Assuming negligible adsorption on the side walls, the density profile of the gas as a function of distance assumes a constant value (ρ_g) as shown in figure 3.4a.

When an adsorbent is placed in the system, adsorption occurs on the adsorbent surface. At equilibrium, two phases: adsorbed phase and gaseous phase co-exist in the system. The density

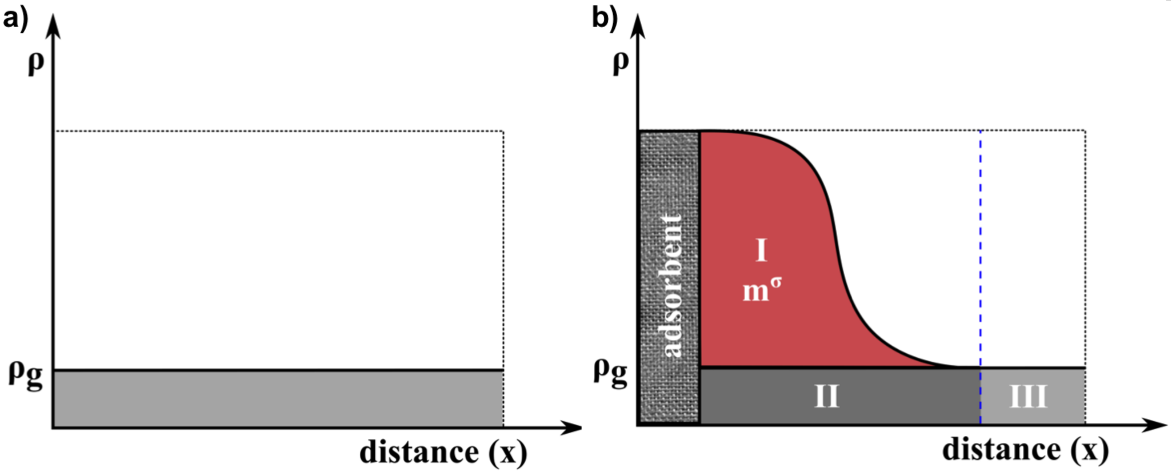

Figure 3.4: Schematic representation of absolute and excess adsorption a)density profile in the absence of an adsorbent b) Change in the density profile in the presence of an adsorbent.

of the gas is greater close to the adsorbent surface and decreases with an increase in distance from the surface as shown in figure 3.4b. The effect of the adsorbent is no longer felt after certain distance and the density assumes the gas phase density (ρ_g). By mass balance:

$$m_{tot} = m_a + m_g \tag{3.5}$$

where m$_{tot}$ is the total amount of gas in the system, m$_a$ is the adsorbed amount and m$_g$ is the amount in the gas phase. Here m$_a$ represents the absolute adsorption or total adsorption i.e. the sum of sections I and II in figure 3.4b and is given by the area under the curve. The absolute adsorption cannot be determined experimentally as the variation of density cannot be estimated accurately. To circumvent this, Gibbs proposed the concept of excess adsorption (m$^\sigma$) [208] given by the difference between the total amount of gas in the system and amount that is remaining in the gas phase.

$$m^\sigma = m_{tot} - m_g \tag{3.6}$$

$$i.e. \quad m^\sigma = (I + II + III) - (II + III)$$

$$m^\sigma = m_{tot} - \rho_g(V_{tot} - V_s) \tag{3.7}$$

Equation 3.7 is exactly similar to equation 3.4. Here m$_{tot}$, ρ_g, V$_{tot}$ are known quantities and V$_s$ (volume of the sorbent) or void volume, is calculated from helium measurements. The adsorption data is generally expressed in terms of m$^\sigma$ (Gibbs surface excess quantity).

However calculation of adsorbent volume V$_s$ is not often straightforward. Helium measurement does not always gives the true sorbent volume. Estimation from He measurement is based on the assumption that He does not adsorb on the sorbent. Several studies have questioned this assumption and He is shown to adsorb to a non-negligible extent on highly microporous materials especially at high pressures [3]. Moreover, pores that are accessible to helium may not be accessible to the adsorbate gas studied. Helium measurement thus may not reflect the true sorbent volume. An alternative is to present the adsorption devoid of any hypothesis in the form of reduced adsorption (Ω) [3, 209] given by,

$$\Omega = m^{\sigma} - \rho_g(V_s) \tag{3.8}$$

It should be noted that experimental techniques like volumetry or gravimetry measures only reduced adsorption. Excess adsorption or total adsorption is calculated from this measured data by using hypothesis like He measurement for sorbent volume determination mentioned above. Therefore for comparison of adsorption data, reduced adsorption is preferred over excess adsorption.

3.3.2 Design and construction details of the volumetric setup

The volumetric setup is designed to meet the following criteria:

- Sensitive enough to handle small quantities of sample ($\geq$ 75 mg)
- Pressure range of 0.1–100 bar
- Temperature of 10–50 °C
- Measure single as well as multicomponent co-adsorption equilibria
- Measure adsorption of corrosive gases.

Since volumetric method is primarily based on pressure measurement, it is imperative to measure even the small changes in pressure precisely and accurately. To achieve this, two factors have to be considered: the magnitude of pressure drop and sensitivity of pressure measurement. The magnitude of pressure drop is determined by the adsorption capacity of the material and volume of the setup. For a given amount of adsorption, smaller the volume of setup, larger is the pressure change. The first step involved was to find a suitable volume, small enough for causing large pressure changes but large enough to permit easy loading and unloading of the samples. This was done by calculating the volume V_1 and V_2 (fig. 3.3) for which pressure change, with and without the sample, is maximized. To carry out these calculations, a rough estimate of adsorption capacity of CNTs was required. As a lower limit of estimation, adsorption of N_2 on CNTs at 30 °C was considered. Its is known that at a given pressure and temperature, the amount of N_2 adsorbed on CNTs is much lower than the amount of CO_2 adsorbed. Any design of setup which is sensitive enough to measure N_2 adsorption would be definitely suitable for CO_2 adsorption. N_2 adsorption 30 °C and up to a pressure of 50 bar on VACNTs were determined externally and the values obtained were used to calculate the pressure drop. Reliable measurements can only be made if the difference in pressure so obtained is greater than the sensitivity of the pressure transducer. The sensitivity of a pressure transducer is generally given as a percentage of the maximum pressure rating e.g. 0.05 % sensitivity for a 0–3 bar transducer implies a sensitivity of 1.5 mbar. Calculations performed by taking these factors into consideration showed that the pressure drop could be maximized if the volume is $V_1 \leq V_2 \leq 30\,\mathrm{cm}^3$. For these volumes, to measure adsorption in the pressure range 0–100 bar three pressure transducers of range 0–3 bar, 0–30 bar and 0–100 bar were selected. A water bath connected to a cryostat was used for maintaining isothermal conditions.

A schematic of the volumetric setup is shown in fig. 3.5. The design is conceptually similar to the setup reported by Möllmer et al. [209]. The main parts of the adsorption setup are the pressure transducers, gas storage vessel, adsorption chamber, thermocouples and the circulation pump. Details of all the components used are given in table 3.2. In order to study adsorption of more than one gas, two storage vessels were used. A circulation pump (cp) connected between the two storage vessels ensures proper mixing of the gases. To measure the temperature before and after expansion, thermocouples T_1, T_2 and T_3 were inserted into the storage vessel 1 & 2 and adsorption chamber respectively. The setup was equipped with three pressure transducers P_1(0–100 bar), P_2(0–30 bar) and P_3(0–3 bar) for accurate measurement of pressure in the system. Valve V_7 acted as the expansion valve that separates the storage vessel and the adsorption chamber. Two filters were fixed near the two ends of the adsorption chamber to prevent the sample spillover to other sections of the setup during expansion or evacuation. All the tubings and connections were from Swagelok®. The all stainless steel construction facilitates the study of corrosive flue gases as well. Since the pressure transducers cannot be completely immersed in water, to maintain a constant temperature a water jacket was provided for the exposed parts of the transducer to minimize

Device	**Type**	**Company**	**Specification**
Pressure transducer	PAA33X-V-3 (0–3 bar) PAA33X-V-30 (0–30 bar) PAA33X-V-100 (0–100 bar)	Omega Newport electronics GmbH	0.05 % accuracy, 0.002 % resolution
Digital multimeter for pressure transducer	Model 3360	PeakTech	Resolution: 100 µV up to 4 V and 1 mV up to 40 V
Temperature sensor	type K (NiCr)	Omega Newport electronics GmbH	± 1.1 °C
Display for temperature sensor	HH11B	Omega Newport electronics GmbH	-50 to 1300 °C
Heating Jacket	Aluminum coated glass fiber	Horst GmbH	custom; 180 W, nominal temperature 300 °C
Regulator for heating jacket	HT20	Horst GmbH	0–500 °C
Circulation pump	GK-M-12/02	Gardner Denver Thomas GmbH	Max. system pressure 150 bar
Tubings, valve and connections	stainless steel	Swagelok	6 mm
Filter	Stainless steel in-line particulate filter	Swagelok	2 micron pore size
Cryostat	Haake N3 R Fisons	Haake	–

Table 3.2: Details of the components used in the high pressure volumetric setup.

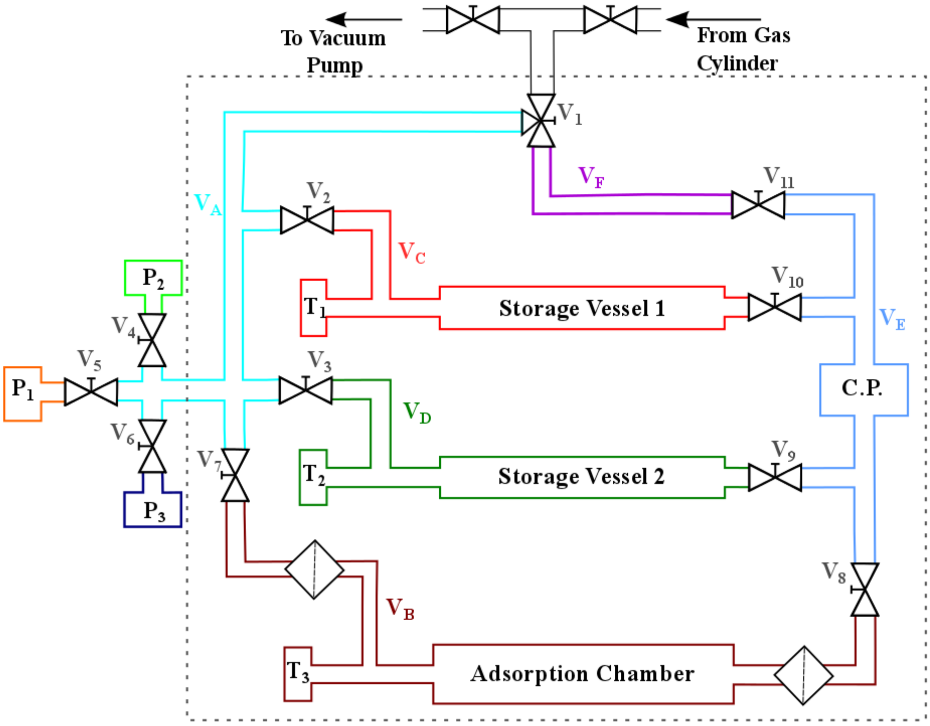

Figure 3.5: Schematic of the high pressure volumetric gas setup. [P_1, P_2, P_3: pressure transducers, V_{1-11}: ball valves, V_{A-F}: separate volume sections, T_1, T_2, T_3: thermocouples, C.P.: circulation pump].

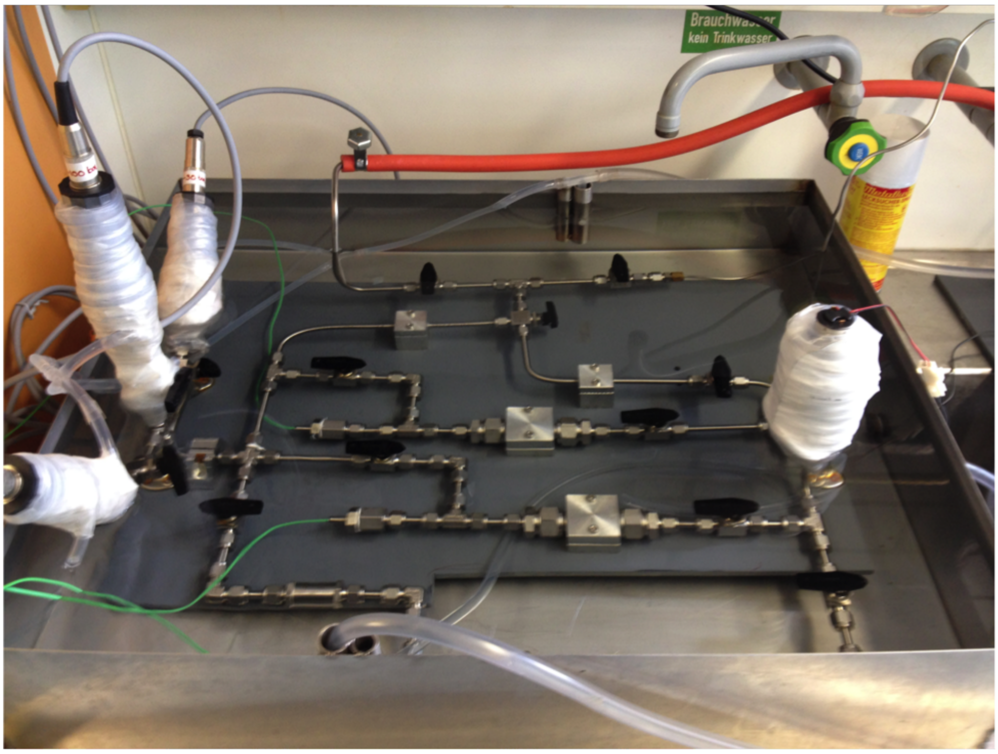

Figure 3.6: Photograph of the self-built high pressure volumetric gas setup.

the effect of temperature fluctuations. A photograph of the actual setup is shown in figure 3.6. Since volumetric measurements require a precise determination of the volume of the system, all the different colored sections had to calibrated and the calibration procedure is discussed in more detail in the next section.

3.3.3 Calibration

After checking the system for leakage with helium gas up to a pressure of 50 bar, calibration measurements were performed. All calibration measurements were carried out at 25 °C using high purity N_2 (99.999 %) gas. The calibration measurements were carried out according to the method outlined in Möllmer et al. [209]. Briefly, expansion experiments were carried out with and without a known volume for any two sections and by solving the two equations for the two unknown variables, volume of the two sections were obtained.

In the present case, expansion measurements were carried out from section V_A to V_B (see figure 3.5). Since three transducers were connected to section V_A, it was again subdivided into V_{a1} (including 0–100 bar transducer), V_{a2} (including 0–30 bar transducer) and V_{a3} (including 0–3 bar transducer). The three subsections had to be calibrated separately. At first, expansion measurements were carried from section V_{a3} to V_B and by mass balance:

$$\rho_1 V_{a3} = \rho_2 (V_{a3} + V_B) \tag{3.9}$$

$$V_{a3} = \frac{\rho_2 V_B}{\rho_1 - \rho_2} \tag{3.10}$$

Density of the gas at a given pressure and temperature was obtained from the NIST website [210]. For a similar pressure range, expansion experiments were repeated after placing a known volume in V_B. Steel balls of known density (ρ_{SB}=7.9 g cm^3) and mass were used as the known volume. By mass balance:

$$\rho_1^* V_{a3} = \rho_2^* (V_{a3} + V_B - V_{SB}) \tag{3.11}$$

$$V_{a3} = \frac{\rho_2^* (V_B - V_{SB})}{\rho_1^* - \rho_2^*} \tag{3.12}$$

Section	**Calibrated volume (cm^3)**
V_{a1}	12.614 ± 0.006
V_{a2}	12.658 ± 0.002
V_{a3}	12.699 ± 0.008
V_B	32.742 ± 0.03
V_C	15.857 ± 0.03
V_D	15.779 ± 0.02
V_E	9.184 ± 0.03
V_F	2.646 ± 0.003
V_{SC}	2.052 ± 0.003

Table 3.3: Calibrated volumes of different sections of the volumetric setup.

where V_{SB} is the known volume of steel balls and * symbolize expansion experiments carried out with the known volume. By solving equations 3.10 and 3.12, V_B and V_{a3} were found out. The procedure was repeated at least 3 times to obtain a reliable value. Similar steps were carried out for V_{a2} as well as V_{a3}. Once V_{a1}, V_{a2}, V_{a3} and V_B were calibrated, other sections like V_C or V_D were calibrated by expansion from one of the known calibrated volumes. For easy loading and unloading of the sample, a cylindrical sample cell made of stainless steel of diameter 14 mm and height 45 mm was used, the volume of which (V_{SC}) was also calibrated by expansion experiments. The calibrated values of the different sections are given in table 3.3

3.3.4 Isotherm determination

Details of a typical adsorption isotherm measurement are described in this section. Accurate determination of the sample mass was the first step involved in an adsorption isotherm measurement. The sample, taken in the stainless steel sample cell, was degassed by heating to 150 °C in vacuum for at least 12 hours. After measuring the actual mass of the sample, the sample cell along with the sample was carefully transferred to the adsorption chamber. Since the sample was exposed to the atmosphere during the transfer, it was further subjected to an in-situ evacuation at 150 °C for 12 hours.

Void volume of the sample (V_s) was determined by helium measurements performed at 25 °C. It should be noted that the void volume of the sample attempted to measure is a very small quantity. This can be understood by the following calculation. For an activated carbon of mass 100 mg and density of ~2 g cm^{-3}, void volume V_s is

$$V_s = \frac{mass}{density} = \frac{0.1\,\mathrm{g}}{2\,\mathrm{g\,cm^{-3}}} = 0.05\,\mathrm{cm^3}$$

This is an extremely small volume and uncertainties in measurements are larger than this value. One way of improving the measurement is to use larger mass, which is not always practical. This is a serious drawback for volumetric measurement and therefore the data is most often presented in terms of reduced adsorption i.e. without using the void volume hypothesis. In experiments for which larger amount of sample was available, helium measurements were carried out and the void volume V_s was calculated as follows. From equation 3.4

$$m_1 = m_2 + m_a$$

Assuming $m_a = 0$ for He, $$\rho_1 V_1 = \rho_2 (V_1 + V_2 - V_s)$$

Rearranging, $$V_s = \frac{\rho_2 (V_1 + V_2) - \rho_1 V_1}{\rho_2} \qquad (3.13)$$

Helium measurements were repeated at least three times and the average value was used for calculation.

Before measuring the actual adsorption isotherm, the sample was again regenerated by heating in vacuum at 150 °C for 12 hours. After regeneration of the sample, the expansion valve V_7 was closed. Section V_A was pressurized and based on the final pressure (pressure after expansion), sections V_C and/or V_D was used in conjunction with V_A. Once temperature and pressure stabilizes, valve V_7 was opened. Final pressure used for calculating the amount adsorbed was obtained after the system reached equilibrium. From equation 3.7 and 3.8,

$$\text{Excess adsorption,} \qquad m^{\sigma} = \frac{\rho_1 V_1 - \rho_2(V_1 + V_2) + \rho_2 V_s}{\text{mass of sample in gram}} \qquad \mathrm{mg\,g^{-1}} \tag{3.14}$$

$$\text{Reduced adsorption,} \qquad \Omega = \frac{\rho_1 V_1 - \rho_2(V_1 + V_2)}{\text{mass of sample in gram}} \qquad \mathrm{mg\,g^{-1}} \tag{3.15}$$

To obtain an adsorption isotherm multiple points need to be measured. After determining the amount adsorbed in the first expansion measurement, valve V_7 was closed and section V_A, V_C, V_D (which ever is applicable) was pressurized again. Expansion was carried out after the temperature and pressure stabilized. The amount adsorbed in the second expansion measurement step is given by

$$m^{\sigma *} = m_{a1} + \frac{\rho_1^* V_1 + \rho_2 V_2 - \rho_2^*(V_1 + V_2) + (\rho_2^* - \rho_2)V_s}{\text{mass of sample in gram}} \qquad \mathrm{mg\,g^{-1}} \tag{3.16}$$

$$\Omega^* = \Omega_{a1} + \frac{\rho_1^* V_1 + \rho_2 V_2 - \rho_2^*(V_1 + V_2)}{\text{mass of sample in gram}} \qquad \mathrm{mg\,g^{-1}} \tag{3.17}$$

where m_{a1} and Ω_{a1} represent the amount adsorbed in the first step and superscript * represents the parameters in the second step of measurement.

Since in a volumetric measurement, the uncertainty associated with adsorbed mass increases with each step, maximum number of steps were limited to 3. The sample was then subjected to a reactivation process by heating in vacuum at 150 °C for 12 hours. In a given cycle, the first measurement point is the most accurate, therefore the initial pressures are chosen such that the first measuring point lies in between the points measured in the previous cycle. This provides an internal consistency to the measurement. As all materials are not stable at high pressures, adsorption isotherm is usually measured starting from the low pressures.

3.3.5 Validation measurement

Validation of the calibration measurements were performed by measuring the adsorption isotherm of a standard adsorbent-adsorbate system. CO_2 adsorption on activated carbon Norit R1 extra (Norit N.V., Holland) at 25 °C was selected for this purpose as it is a widely investigated material system [209, 211–213]. The activated carbon is in the form of pellets of approximately 1 mm diameter and 2–4 mm length. The nitrogen adsorption isotherm of Norit R1 extra shown in figure 3.7a resembles a type-I isotherm. The steep slope in the low pressure region is a clear indication of the highly microporous nature of the adsorbent. The BET specific surface area is calculated to be 1375 $m^2\,g^{-1}$ close to the reported values [214]. SEM image of Norit R1 is shown in figure 3.7b.

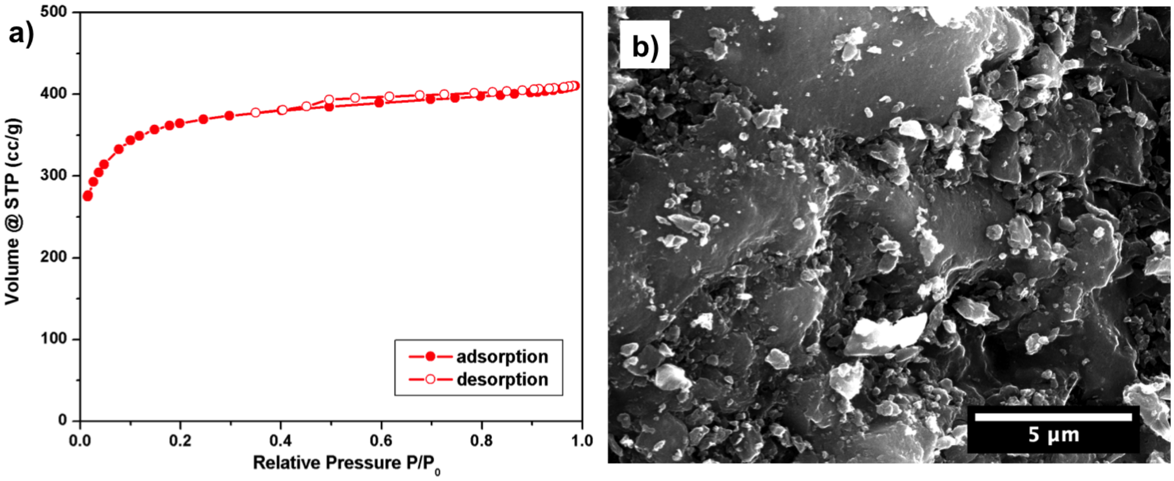

Figure 3.7: a) N_2 adsorption isotherm of Norit R1 extra at 77 K and b) SEM image of Norit R1 extra.

For validation measurements, about 450 mg of Norit R1 extra was used. As described in section 3.3.4, the sample was transferred to the high pressure adsorption setup after determining the actual mass. An attempt was made to measure the void volume of the adsorbent. To ensure maximum accuracy, expansion from V_{a3} (section with the most sensitive pressure transducer) to V_{B-SC} was performed [V_{B-SC} denotes the volume of the adsorption chamber with the sample cell volume subtracted]. The measurement was repeated at least 3 times. The void volume so obtained was found to be 0.204 cm^3 with a specific volume of 0.459 $cm^3\,g^{-1}$. This is in excellent agreement with other reported values of 0.459 $cm^3\,g^{-1}$ by Bazan [215], 0.462 $cm^3\,g^{-1}$ by Herbst [213] and Beutekamp [212] and 0.476 $cm^3\,g^{-1}$ by Möllmer [209].

Adsorption isotherm measurements were carried out at 25 °C using high purity CO_2 (99.999 %). Measurements were performed according to the procedure described in section 3.3.4. Adsorption capacity of Norit R1 extra was determined up to a pressure of ~45 bar. As seen from the graph 3.8 the results obtained are consistent with the reported values [209, 216, 217].

In figure 3.9a, the excess adsorption and reduced adsorption of CO_2 on Norit R1 extra at 25 °C is plotted. The difference is negligible at lower pressures but at high pressures, significant deviation

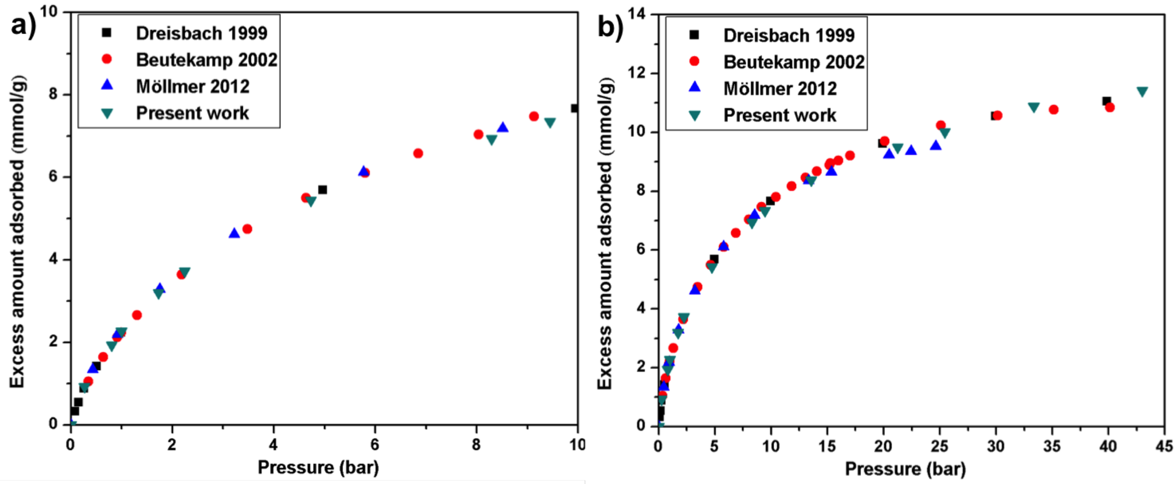

Figure 3.8: CO_2 adsorption on Norit R1 extra at 298 K a) in the pressure range of 0–10 bar b) in the pressure range of 0–45 bar.

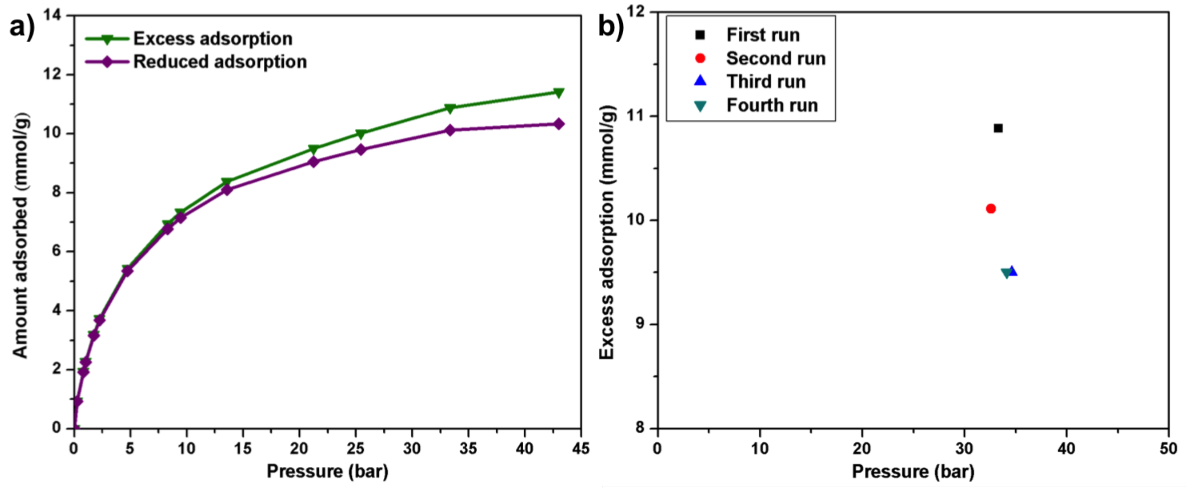

Figure 3.9: a) Excess and reduced adsorption of CO_2 on Norit R1 extra at 25 °C b) Decrease in adsorption capacity of Norit R1 extra with multiple measurements.

is observed. In the course of calibration, it was also observed that the adsorption capacity of Norit R1 extra decreased after several cycles (see figure 3.9b). This was especially evident at high pressures (> 30 bar). Even after regeneration at temperatures as high as 175 °C for 16 hours, the initial adsorption capacity was not restored.

3.3.6 Measurement with smaller sample quantity

One of the design criteria for the volumetric setup was that it should be sensitive enough to handle small quantities of sample. Lower amount of sample implies smaller changes in pressure due to

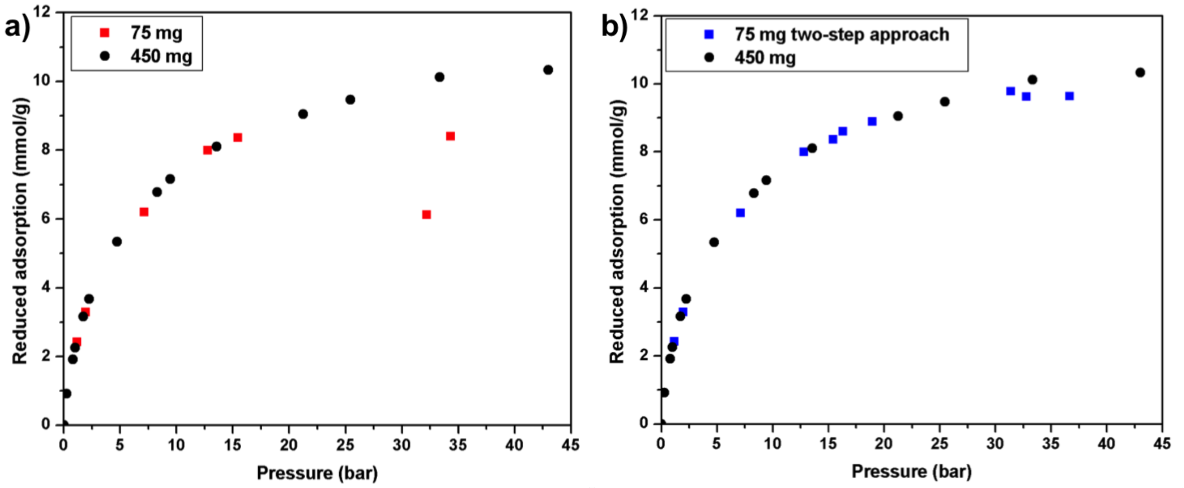

Figure 3.10: CO_2 adsorption on 75 mg of Norit R1 extra at 25 °C a) direct expansion to obtain pressures > 30 bar b) two-step approach.

adsorption. Experiments with smaller sample quantity have to be performed carefully because any slight variations in temperature or pressure results in large deviations.

To check the suitability of the volumetric setup to handle smaller quantities of sample, CO_2 adsorption was measured on a fresh batch of ~75 mg of Norit R1 extra at 25 °C. Similar procedure outlined in section 3.3.4 was followed. Measurements were carried up to a pressure of about 35 bar and the results obtained are plotted in figure 3.10a. Though in the low pressure region good agreement with the reported values were obtained, significant deviations were observed at pressures above 30 bar.

In order to obtain a final pressure of > 30 bar, the initial pressure, before opening the expansion valve, should be close to 50 bar. This leads to three major sources of error. First, the greater uncertainty in pressure (± 50 mbar) arising from the usage of 0–100 bar transducer. Compounding this problem is the non-linear variation of density of CO_2 at high pressures. The saturation pressure of CO_2 at 25 °C is about 72 bar. At pressures close to 50 bar, the small errors in pressure readings lead to large variations in density values. To give an example, for CO_2 at a pressure of about 1 bar, for a change in pressure (ΔP) of 0.1 bar, the change in density ($\Delta\rho$) is $0.1794\,\mathrm{kg\,m^{-3}}$. While for the same ΔP of 0.1 bar at pressures close to 50 bar, $\Delta\rho$ is $0.4488\,\mathrm{kg\,m^{-3}}$. In addition, the multimeter used in combination with the pressure transducer, displays one decimal place less for voltages above 4 V. These uncertainties are magnified when small quantities of sample are used.

To overcome this problem, higher pressures ($> 30\,\text{bar}$) were obtained by a two-step approach. In the first step, a well-defined adsorption point was obtained at about 20 bar using the more accurate 0–30 bar transducer. In the second step, expansion was carried out from pressures close to 40 bar to obtain a final pressure of $> 30\,\text{bar}$. Good agreement with the reported values were obtained by employing this two step approach as shown in figure 3.10b.

3.4 Concluding remarks

In summary, this chapter discussed two major techniques: gravimetry and volumetry, for assessing the adsorption capacity of a material. Detailed information on the ambient pressure setup and its use for fast screening of different types of samples were discussed. Design, calibration and validation of volumetric setup were outlined and its feasibility to handle relatively smaller sample quantities were also demonstrated.

4 Adsorption on Vertically Aligned Carbon Nanotubes

In this chapter, adsorption properties of vertically aligned CNTs are presented. A description of adsorption characteristics of pristine VACNTs in low pressure as well as in the high pressure regime is provided. In the subsequent sections the effect of various geometric modifications of VACNTs on its adsorption characteristics are described.

4.1 Adsorption characteristics of pristine VACNTs

The as-prepared VACNTs synthesized by the WACVD method are free from catalyst and are mostly double walled with an average diameter of about 8 nm and an intertube distance of ~> 15 nm. They have a specific surface area of about 500 $m^2 g^{-1}$ (see chapter 2).

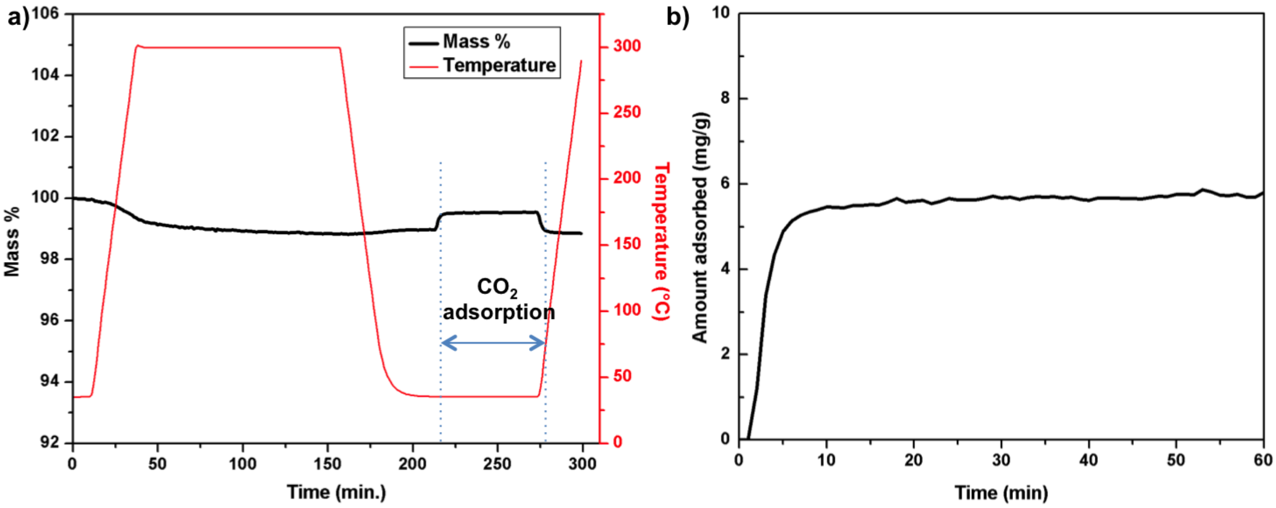

Figure 4.1: CO$_2$ adsorption on pristine VACNTs at 1 bar and 35 °C a) complete profile obtained from the ambient pressure measurement indicating the weight loss during the pre-heating stage, amount adsorbed and desorbed expressed in % b) amount adsorbed expressed in $mg\,g^{-1}$.

Ambient pressure CO$_2$ adsorption measurements were performed on these pristine VACNTs at 35 °C. Figure 4.1a shows the the complete mass change and temperature profile obtained from the ambient pressure measurement. Since measurements were carried out in a TG setup, continuous monitoring of sample mass was possible. Even after heating to 300 °C, the weight loss observed is only around 1 %. The observed weight loss can be attributed to the removal of adsorbed gases and traces of moisture. In Figure 4.1b, only the adsorption stage is depicted and the amount adsorbed is given in mg g^{-1}.

At 1 bar, the VACNTs adsorbed about 5.6 mg g^{-1} of CO_2. When compared with other adsorbents like activated carbon, zeolites or metal organic frameworks, the adsorption capacity of VACNTs at 1 bar is not impressive. It is almost one to two orders of magnitude lower than the standard adsorbents. This low value stems from the fact that VACNTs are mainly mesoporous materials with very small amount of micropores. The diameter and the intertube distance of pristine VACNTs falls in the mesoporous regime. For CO_2 gas, at 1 bar, adsorption predominantly occurs in the micropores, absence of which in VACNTs, leads to the poor adsorption capacity.

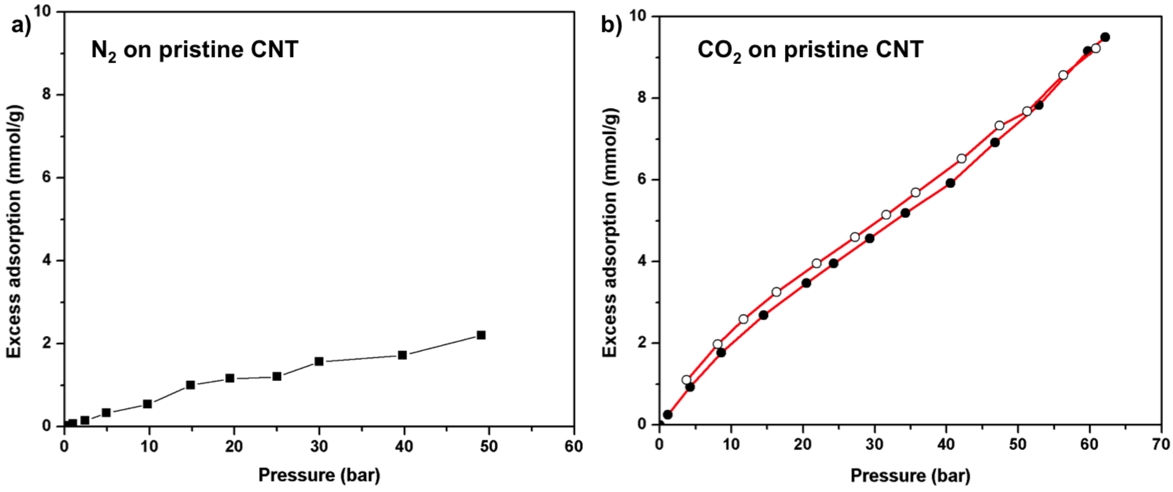

Figure 4.2: High pressure a) N_2 and b) CO_2 adsorption on pristine VACNTs at 30 °C. Closed symbols represent adsorption trace and open symbols represent desorption trace.

In figure 4.2a, high pressure N_2 adsorption characteristics of VACNTs at 30 °C is shown. VACNTs adsorbs only about 1.7 mmol g^{-1} of N_2 at a pressure of 30 bar. Compared to N_2, VACNTs display much higher affinity for CO_2 adsorption as shown in figure 4.2b. The amount of CO_2 adsorbed increases almost linearly with pressure and did not show any sign of saturation even up to a pressure of 60 bar. The presence of a slight deviations from the linearity (knee) at a pressure of 10 bar, suggests the completion of monolayer adsorption. During measurement it was observed that the adsorption kinetics were quite fast and the equilibrium was reached in less than half an hour at each pressure point measured. At a pressure of 30 bar, VACNTs adsorbed about 4.6 mmol g^{-1} of CO_2. This value is comparable to the adsorption capacity of other adsorbents exhibiting similar surface areas like aluminum hydroxide hollow spheres [218] or zeolites of type 13X [219].

Equally remarkable is the desorption characteristics of VACNTs shown in figure 4.2b. CO_2 desorbs easily and almost completely upon reducing the pressure in the setup. This implies a lower energy input for the regeneration process. Faster adsorption and desorption kinetics coupled with a low energy intensive regeneration process are one of the most desirable characteristics for an efficient adsorbent.

Once the basic adsorption properties of pristine vertically aligned CNTs were determined, influence of various parameters like CNT diameter or intertube distance on adsorption were explored.

4.2 Influence of CNT diameter

In WACVD synthesis of CNTs, the diameter of CNT is mainly determined by the thickness of the catalyst layer. It is known that by decreasing the Fe catalyst layer thickness, the diameter of the CNT can be tuned [183, 220]. Accordingly experiments were performed with smaller Fe thickness of about 0.6–0.8 nm range. CNT growth was not observed below 0.6 nm.

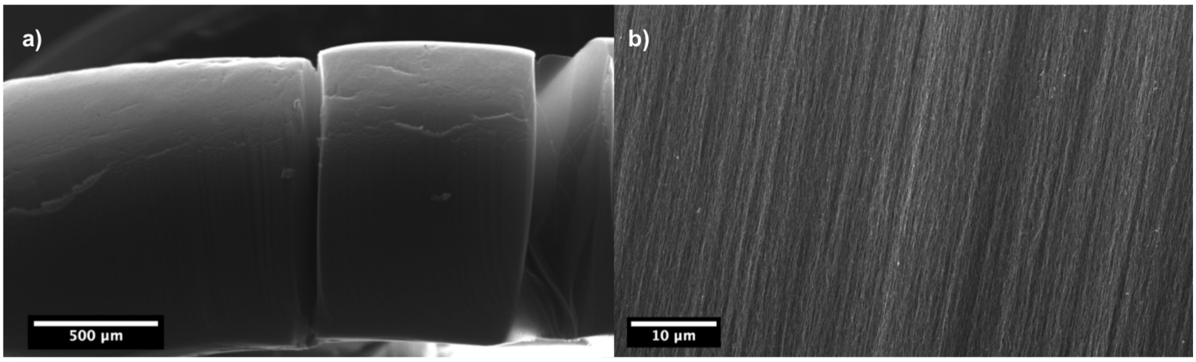

Figure 4.3: SEM image of VACNTs synthesized at a lower iron layer thickness a) low magnification image showing the height of the CNT array b) high magnification image demonstrating the vertical alignment of the CNTs.

Figure 4.3a shows a typical SEM image of the CNTs grown with reduced Fe layer thickness. For a synthesis time of 15 min, dense CNT arrays with an average height of about 800 µm was obtained. As seen from figure 4.3b, lowering the Fe catalyst layer thickness did not affect the vertical alignment. Decrease in diameter of the CNTs is evident from the TEM image shown in figure 4.4. The synthesized CNTs are found to be double walled and their average diameter is about 5 nm.

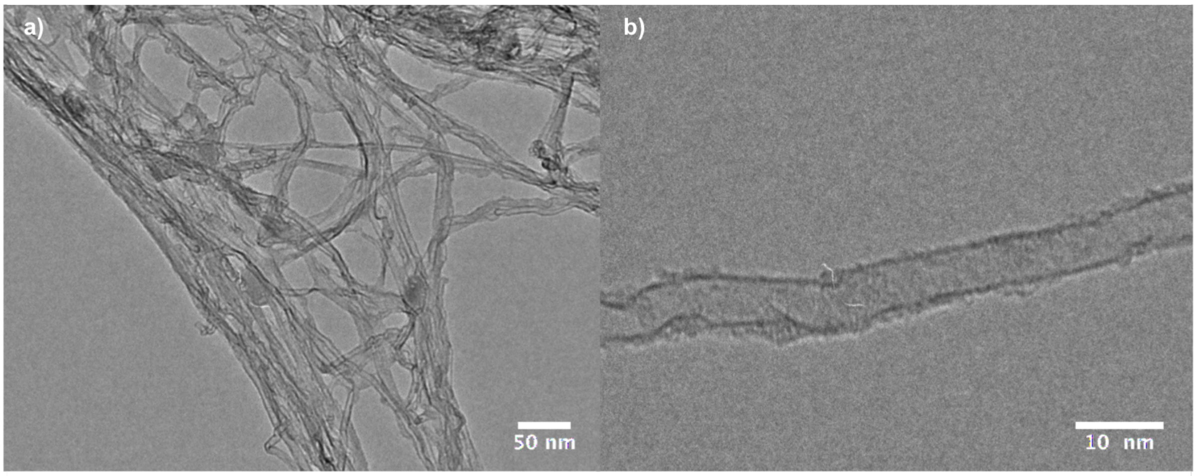

Figure 4.4: a) low magnification and b) high magnification TEM image of smaller diameter CNT.

N_2 adsorption isotherm of 5 nm VACNTs at 77 K is shown in figure 4.5a. The shape of the isotherm is similar to that of 8 nm CNTs exhibiting a type-IV(a) adsorption isotherm. The onset of the linear region of the adsorption isotherm is observed at a higher volume for the 5 nm CNTs. This is an indication of the presence of pores of smaller width in 5 nm VACNTs as compared to 8 nm diameter VACNTs. A more clear picture is obtained by the pore size distribution analysis by non-liner density functional theory (NLDFT) method. The observed peak at 4–5 nm (figure 4.5b) is consistent with the internal diameter obtained by TEM measurements. The BET surface area of the 5 nm VACNTs is determined to be 720 $m^2\,g^{-1}$.

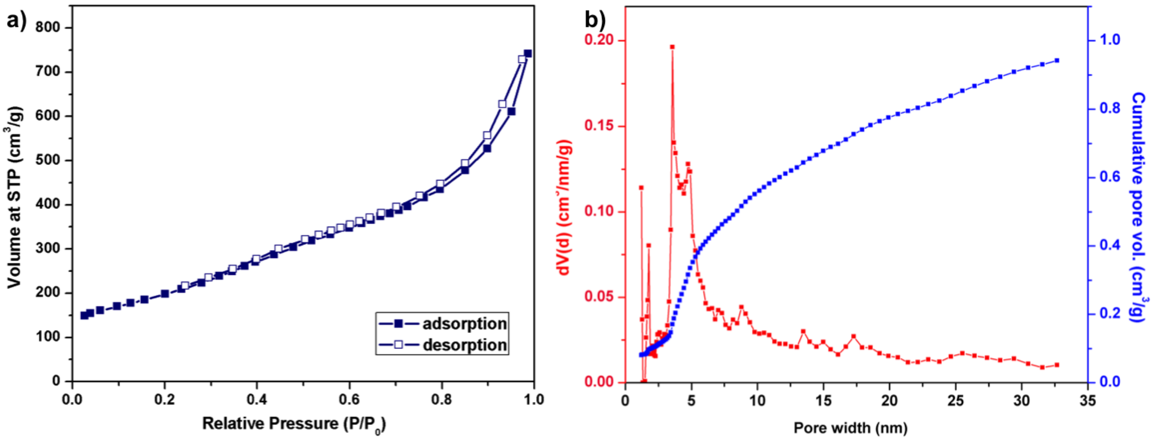

Figure 4.5: a) N_2 adsorption isotherm at 77 K and b) pore size distribution of 5 nm VACNTs.

In figure 4.6, Raman spectra of 5 nm and 8 nm VACNTs are compared. No discernible differences are observed in the spectra of CNTs with different diameters. The high D-band observed in both cases is due to a significant amount of defects in the structure. From TEM images (figure 4.4), it appears that a considerable amount of CNTs are curved. The bents and the curves observed contribute to the higher D-band intensity in the Raman spectrum. Decreasing the diameter did not alter their chemical environment as revealed by the XPS spectra (figure 4.6b). The small concentration of oxygen detected in the spectra is attributed to the atmospheric handling of the sample. High resolution C 1s spectra given in the inset of 4.6b, confirms that no oxygen functionalities are present on the CNT surface.

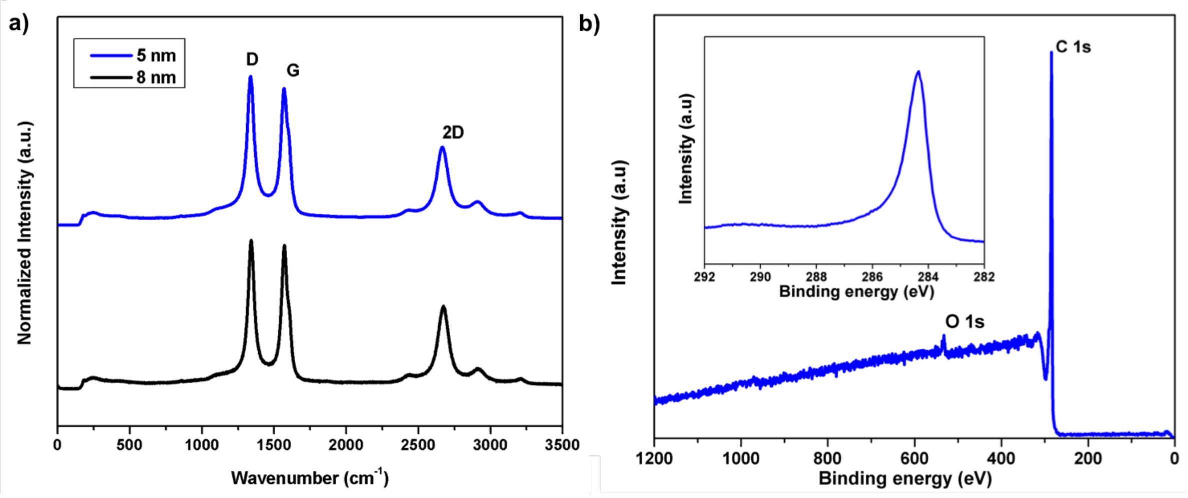

Figure 4.6: a) Raman spectra comparison of 5 nm and 8 nm VACNTs b) X-ray photoemission survey spectrum of 5 nm VACNTs (inset shows the high resolution C 1s spectrum).

Ambient pressure CO_2 adsorption measurement (figure 4.7a) carried out on 5 nm VACNTs at 35 °C revealed an increased adsorption capacity of $10.9\,\mathrm{mg\,g^{-1}}$. High pressure CO_2 adsorption measurement was carried out on 5 nm VACNTs up to a pressure of 60 bar and results obtained are compared with 8 nm CNTs in figure 4.7b. The shape of the adsorption isotherm is similar in both cases but 5 nm VACNTs exhibits an enhanced adsorption capacity over the complete pressure regime. No sign of saturation is observed until the highest measured pressure of 60 bar. At this pressure 5 nm VACNTs adsorb almost half its weight of CO_2.

The heat of adsorption is a measure of the strength of interaction between the adsorbate and the adsorbent. A high value naturally implies a stronger interaction and therefore more energy has to be spend to regenerate the adsorbent. An ideal adsorbent, therefore, should have a high adsorption capacity with low heat of adsorption. To determine the nature of interaction between VACNTs and CO_2, adsorption isotherms were measured at three different temperatures as shown in figure 4.8a. The observed decrease in adsorption with an increase in temperature is characteristic for a physisorption mechanism. By using the Clausius-Clapeyron relation, the heat of adsorption was

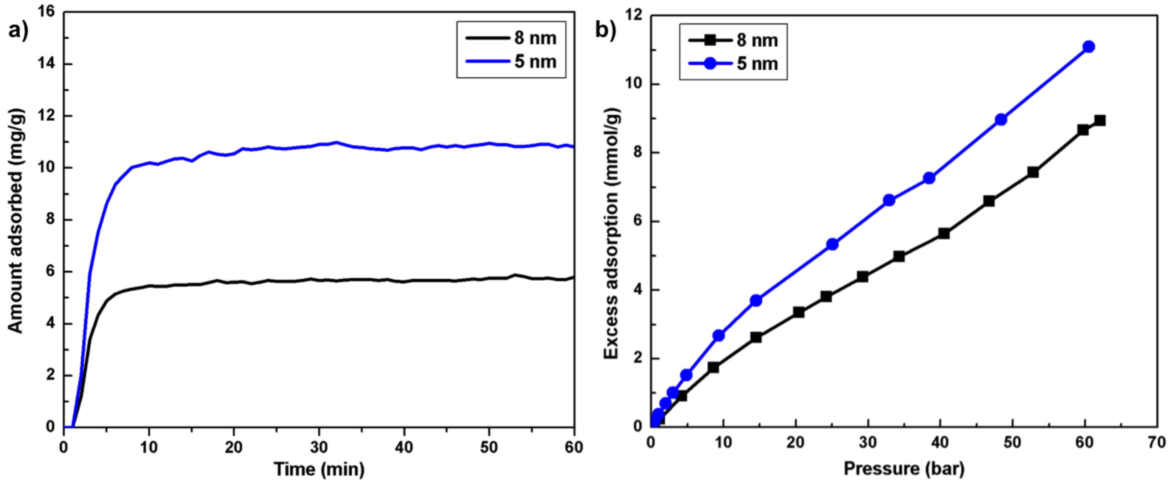

Figure 4.7: CO_2 adsorption on 5 nm VACNTs a) at 1 bar and 35 °C and b) at 30 °C and pressures up to 60 bar.

determined to be about 19 kJ mol^{-1} (figure 4.8). The heat of adsorption is in the ideal range as too low a value results in very low adsorption capacity and high heat of adsorption leads to more energy intensive approaches for the regeneration of the adsorbent. In the present case, almost complete desorption is obtained by reducing the pressure alone. This is certainly a remarkable feature of VACNTs.

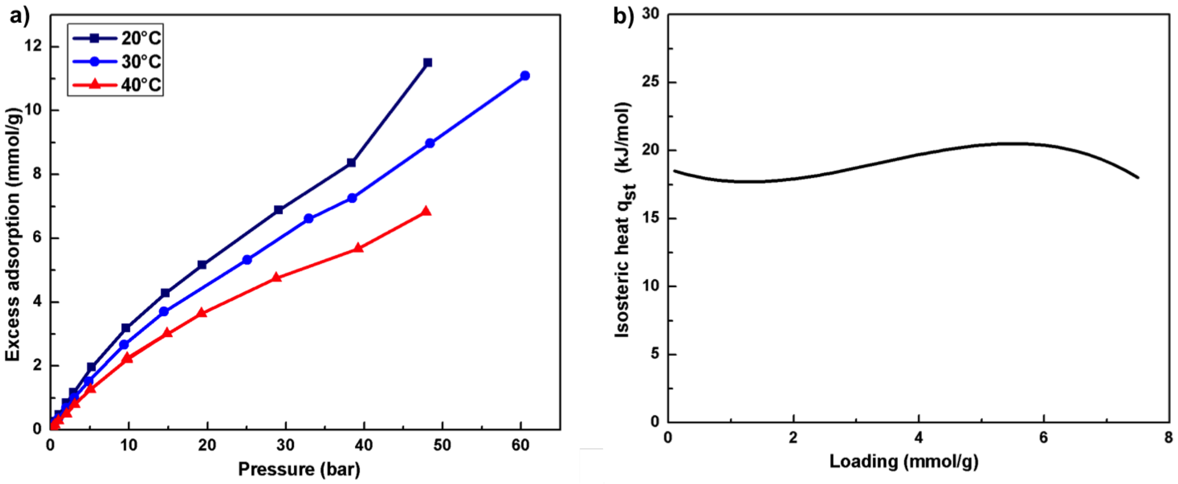

Figure 4.8: a) CO_2 adsorption isotherms on 5 nm VACNTs at 20 °C, 30 °C and 40 °C b) plot of heat adsorption vs. loading for 5 nm VACNTs.

Grand canonical Monte-Carlo (GCMC) simulations were carried out to understand the adsorption mechanism of CO_2 on these VACNT structures [221]. The simulations allowed a breakdown of experimentally observed adsorption isotherm into partial isotherms of contribution only from the certain adsorption sites. Three limiting cases of adsorption were considered (see figure 4.9) namely: a) unrestricted - adsorption may take place in all the different adsorption sites of VACNTs; b) inner only - adsorption can take place only on the interior of the CNTs (endohedral sites) and the interstitial and groove sites are assumed to be inaccessible; c) outer - the CNTs are assumed to be completely closed and adsorption can take place only on the interstitial and groove sites. The experimentally observed adsorption isotherm was fitted as a function of the inner and outer adsorption cases. Quantitative agreement with the experimental results were obtained when 48 % of the tubes were considered to be closed. In addition, simulation also predicted that the intertube distance has a strong influence on adsorption of CO_2. In the subsequent sections, the effect of intertube distance and opening of the CNTs are experimentally explored in detail.

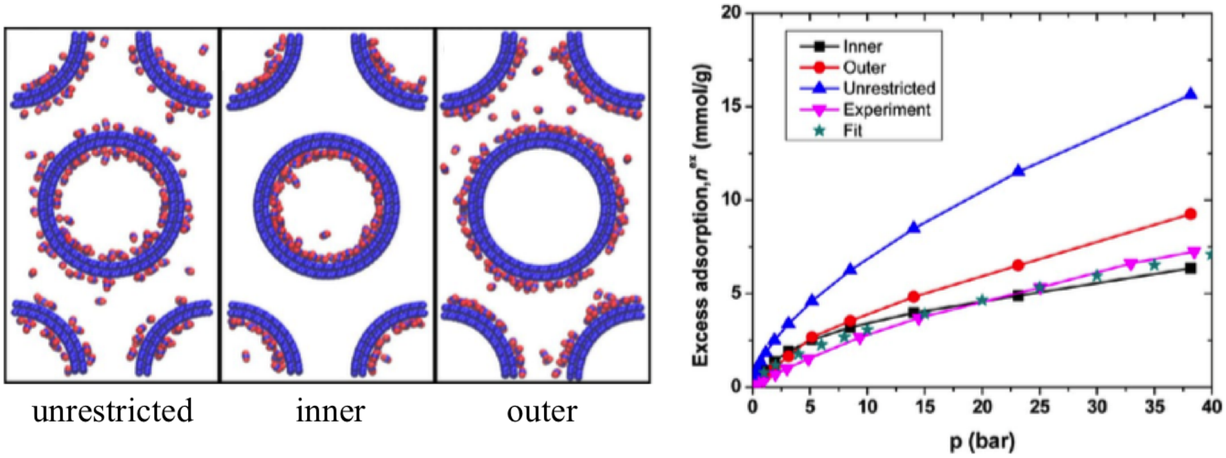

Figure 4.9: Grand Canonical Monte Carlo (GCMC) simulation of CO_2 adsorption on VACNTs. Three limiting cases for CO_2 adsorption were considered namely: unrestricted (adsorption on all regions), inner only (adsorption only on the interior of CNTs) and outer only (adsorption only on the interstitial and groove sites). The experimentally observed isotherm is fitted as function of inner and outer adsorption cases [221].

4.3 Influence of intertube distance

Simulation studies on VACNT structures have shown that interstitial sites are energetically favorable for adsorption and the adsorption capacity can be increased by decreasing the intertube distance [221, 222]. To experimentally verify these results, all other parameters like CNT diameter or specific surface have to be kept constant and only the intertube distance should be varied. Since in CVD synthesis of CNTs, the characteristics of CNTs are determined by the catalyst, intertube distance can be decreased by increasing the catalyst density [183, 220, 223]. However, this invariably leads to changes in CNT diameter as well as specific surface area.

To independently decrease the intertube distance without varying other characteristics, liquid induced densification of CNTs was used. When a liquid is introduced into the CNT array and allowed to evaporate, the surface tension of the liquid and the strong van der Waals interaction effectively zip the nanotubes together thereby densifying the structure [224]. This phenomenon is made use e.g. in applications like hierarchical self-assembly [224–227] super capacitors [228] or sliding electrical contacts [229] etc.

The liquid induced densification process had to be achieved without compromising the vertical alignment of the CNTs. To this end densification of patterned CNTs were explored first. By employing a mask during the catalyst deposition stage, VACNTs pillars of about 300 µm diameter were synthesized as shown in figure 4.10a-b. De volder et al. [224] have outlined 4 different densification approaches based on the method of exposure towards the liquid namely immersion, directed immersion, dipping and condensation. In immersion, the substrate with the material is directly immersed in a beaker filled with a wetting liquid while in directed immersion, the substrate is inserted into the beaker in a specific direction to the liquid surface so as to achieve a change in orientation. Dipping on the other hand leads to a more localized densification by exposing only the tips of the structure to the liquid surface. Condensation is used when more delicate control over the process is required. In this method, block of CNTs, placed upside down, are exposed to the vapors from the liquid as shown in figure 4.10c.

In the present study, condensation method was employed and patterned CNT arrays were exposed to ethanol vapor for 30 s and allowed to dry. SEM images of the densified structure obtained is shown in figure 4.10d. Though the individual pillars still retain their vertical structure, considerable twisting is observed (figure 4.10e). High magnification SEM image (figure 4.10f) reveals that the alignment of the tubes are compromised to a great extent and the individual CNTs are no longer parallel to each other. The twisting observed is a result of the large aspect ratio of CNTs as well as poor adhesion between the tubes[224, 230]. Kang et al. [230] have shown that a plasma treatment to activate surface functional groups promote adhesion and this in turn was found to substantially reduce the twisting of the pillar structures. Since plasma treatment can introduce large amount of surface functional groups which can influence the adsorption properties, this approach was not favored.

The twisting of the CNT arrays was not observed when CNT films peeled off from the substrate were densified. Densification was achieved by placing a few drops of ethanol on the freestanding

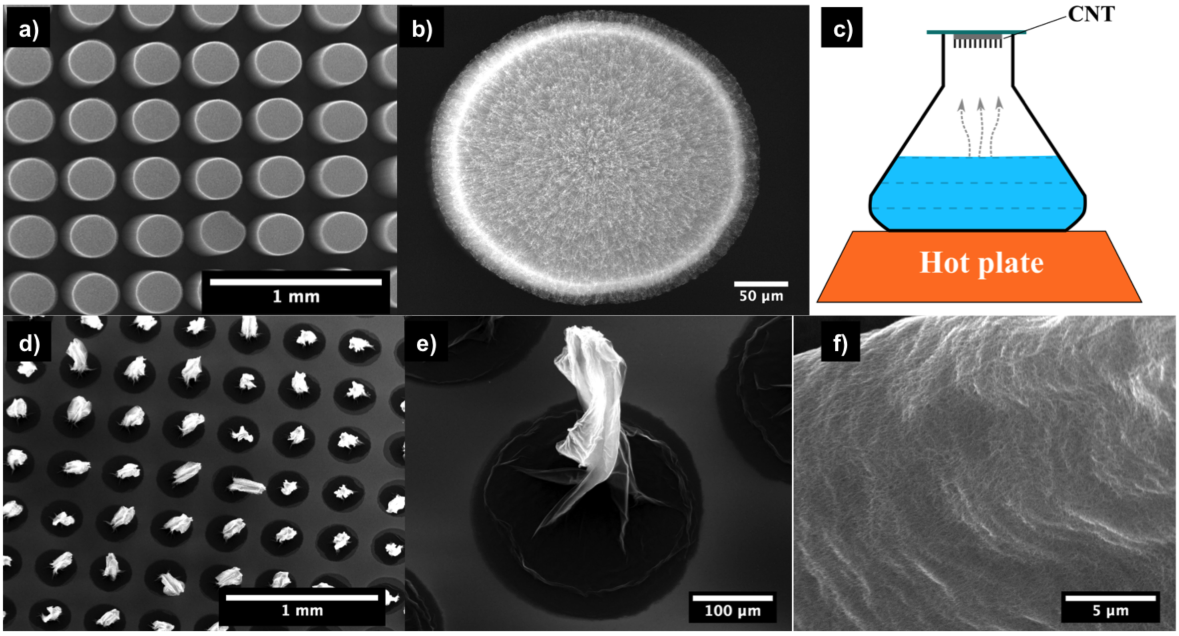

Figure 4.10: Liquid induced densification of the patterned CNT arrays. a-b) low and high magnification SEM image of 300 µm CNT pillars. c) Schematic of the setup used for densification d-e) SEM images of the resulting CNTs formed after densification. [SEM images d and e corresponds to SEM images a and b respectively] f) The high magnification image shows considerable loss of alignment of VACNTs.

films and allowed to evaporate at ambient conditions overnight. Figure 4.11a shows a photograph of VACNT film before and after densification. Though the macroscopic structure of the film is visibly distorted, the microscopic alignment is still intact to a certain degree. In figure 4.11b-c, SEM images of the CNT film before and after densification is shown. It can be seen that the alignment is still maintained after densification. This can be explained as follows: when one end of the CNTs is anchored to the substrate, volume shrinkage of the top structure leads to the observed twisting. But when CNTs are peeled off from the substrate, uniform shrinkage of top and bottom ends lead to retaining the alignment for the densified structure.

N_2 adsorption isotherms at 77 K were measured to determine the changes in specific surface before and after densification. As seen from figure 4.12a, in the low pressure regime ($P/P_0 < 0.5$), the two curves coincide and hence no significant change in specific surface areas is observed. Prior to densification the CNT arrays had a BET specific surface area of $423\,\mathrm{m}^2\,\mathrm{g}^{-1}$ and after densification, the surface area decreased only marginally to $400\,\mathrm{m}^2\,\mathrm{g}^{-1}$. This is consistent with the findings of Futaba et al. [228] with regard to the unaltered surface area after densification. At

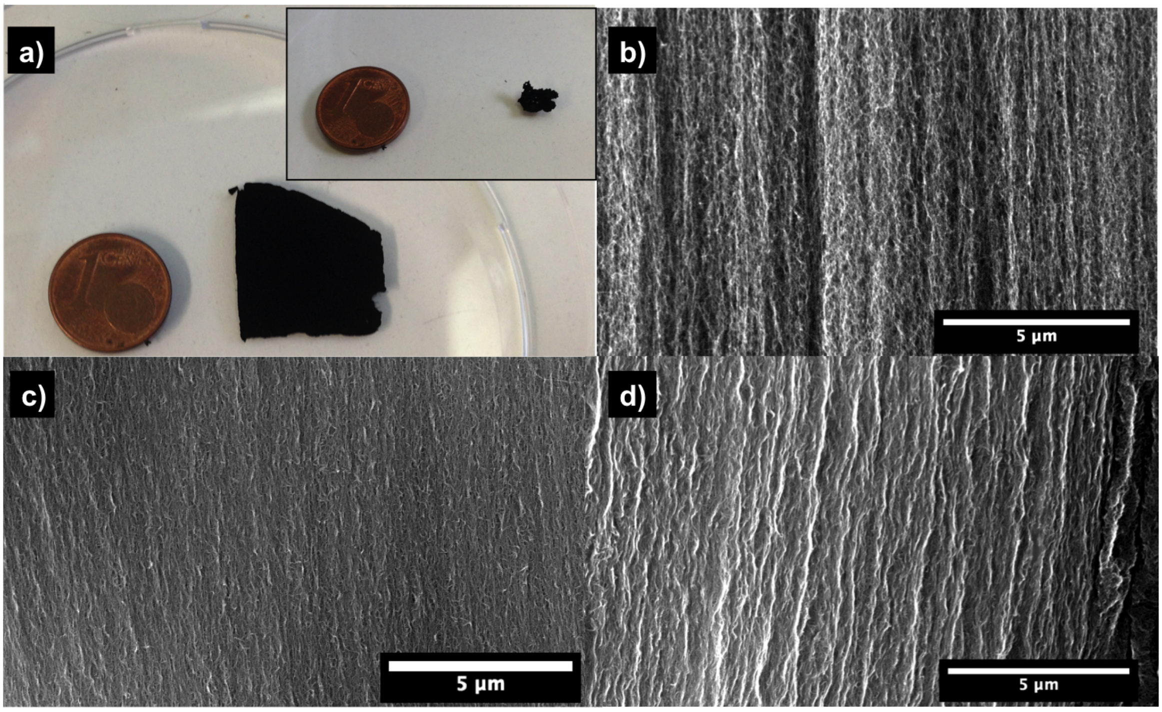

Figure 4.11: Liquid induced densification of free standing VACNTs a) Photograph of the as-prepared free standing VACNT film; inset shows the same structure after ethanol evaporation. SEM images of b) as-prepared VACNTs c) densified by ethanol evaporation d) densified by water evaporation.

high relative pressures ($P/P_0 > 0.6$), the observed deviation is due to the earlier onset of capillary condensation in the densified structure.

Ambient pressure CO_2 adsorption measurements were carried out on the densified structures and the results obtained are plotted in figure 4.12b. While the pristine structures had an adsorption capacity of $5.6\,\mathrm{mg\,g^{-1}}$, ethanol intercalated structures exhibited an enhanced adsorption capacity of $7.5\,\mathrm{mg\,g^{-1}}$. This corresponds to a relative increase of 34 % for the ethanol densified structure.

Densification was also carried out with water instead of ethanol. An SEM image of the densified structure is shown in figure 4.11d. No discernible differences could be observed between ethanol and water densified structures. However ambient pressure CO_2 adsorption measurements revealed significant differences. Water densified CNT structures exhibited an adsorption capacity of $8.8\,\mathrm{mg\,g^{-1}}$ at 35 °C corresponding to a relative increase of 57 % when compared with pristine CNT structure (figure 4.12b). De Volder and Hart [224] have shown that for a given material and geometry, the liquid induced compaction is proportional to the surface tension of the liquid. Water has a higher surface tension of $71.99\,\mathrm{mN\,m^{-1}}$ compared with $21.97\,\mathrm{mN\,m^{-1}}$ for ethanol at

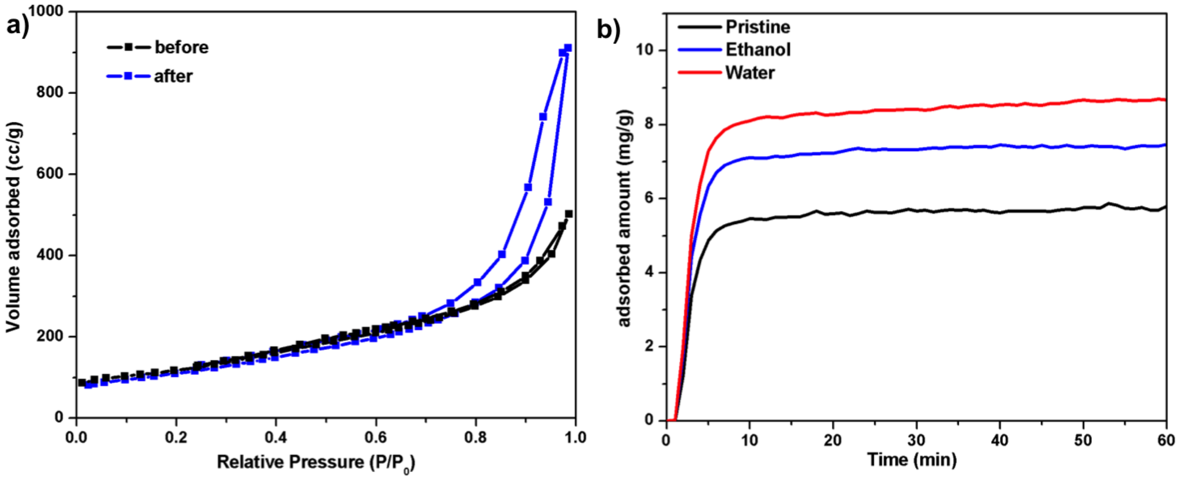

Figure 4.12: a) N_2 adsorption isotherm at 77 K of CNTs before and after ethanol induced densification b) Ambient pressure CO_2 adsorption at 35 °C of pristine and densified CNTs.

25 °C. The higher surface tension of water may account for the better compaction and higher adsorption observed for water intercalated structures.

Consistent with the theoretical predictions, it is experimentally found that intertube distance has a significant influence on gas adsorption. In the next section, experimental approaches to open CNT tips and its effect on gas adsorption are discussed.

4.4 Opening of VACNTs

Simulation studies on these VACNTs has predicted that almost 42 % of the as-prepared CNTs are closed [221]. This essentially means that inner area of these 42 % tubes are not accessible to the adsorbent molecule. An opening of the CNT structures should then lead to a further increase in the adsorption. Due to difference in curvature, the tips of the CNTs have a higher concentration of strain energy and are therefore more reactive [231]. This difference in reactivity can be made use to selectively etch away the CNT cap. The most commonly employed technique for CNT tip opening is the acid treatment of CNTs, also known as oxidative cutting [150]. However, this method leads to loss of alignment of VACNTs as well as addition of various functional groups, both of which can influence the adsorption characteristics. An alternative is to use gas phase techniques for opening the CNT tips so that the alignment stays intact. Shortly after the discovery of CNTs, Ajayan et al. [232] reported oxidation of CNTs in air above 700 °C to etch away the tube cap. Almost at the same time, Tsang et al. [233] presented their studies on opening of CNTs by CO_2. The effectiveness of these approaches was extensively investigated in the oxidative opening of carbon nanohorns [234–237]. From these studies it is seen that the mild oxidizing nature of CO_2 offers better control over the whole process especially in the pore development stage.

The reaction of CO_2 towards graphite is described by the Boudouard reaction which is used extensively in blast furnace for the production of iron [238].

$$C + CO_2 \rightleftharpoons 2CO \tag{4.1}$$

In the present study, opening of the CNT tips were carried out by treating the VACNTs at high temperature in CO_2 atmosphere. The first step involved in the CO_2 treatment of VACNTs was to find the optimum temperature range of the process. To this end, VACNTs were treated in a range of temperature from 600–800 °C and the resulting weight loss was noted. CNT samples with the substrate were placed inside the tube furnace and heated to the desired temperature under 500 sccm of Ar. Once the desired temperature was attained, argon supply was replaced by 100 sccm of CO_2 for 15 min. Thereafter the samples were cooled down in 500 sccm of argon. In figure 4.13 resulting weight loss is plotted as a function of temperature. A steep increase in weight loss is observed at a temperature of ~650 °C and VACNTs are completely consumed at about 800 °C. During the process, it was also observed that the extent of post synthesis hydrogen treatment, affected the onset of the weight loss. Post synthesis hydrogen treatment is typically carried out to weaken the adhesion between the CNTs and the catalyst layer [189]. The exposed catalyst layer is speculated to be the reason for the observed shift in temperature for the onset of rapid weight loss. For adsorption studies, a treatment temperature of ~680 °C was chosen so as to obtain a weight loss of 30–40 %.

Visual inspection of the treated CNTs, hinted an etching of the top layer. SEM images indeed reveal topological changes as shown in figure 4.14a. The alignment of the CNTs are however not affected (figure 4.14b) by the chosen high temperature CO_2 treatment. TEM measurements of the VACNTs treated with CO_2 at 680 °C (figure 4.15a) revealed the additional presence of carbonaceous debris formed due to the treatment and not present in the as-prepared VACNTs (see figure 2.8). The formation of this carbonaceous particulate residue is a known phenomenon [232, 233, 237] and is believed to be a by-product of the etching process. High magnification TEM image in figure 4.15b shows a partially etched CNT tip.

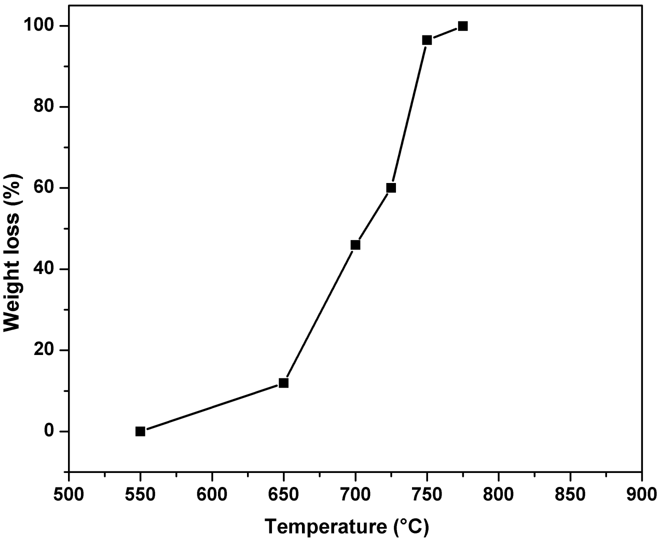

Figure 4.13: Weight loss of VACNTs as a function of temperature of CO_2 treatment.

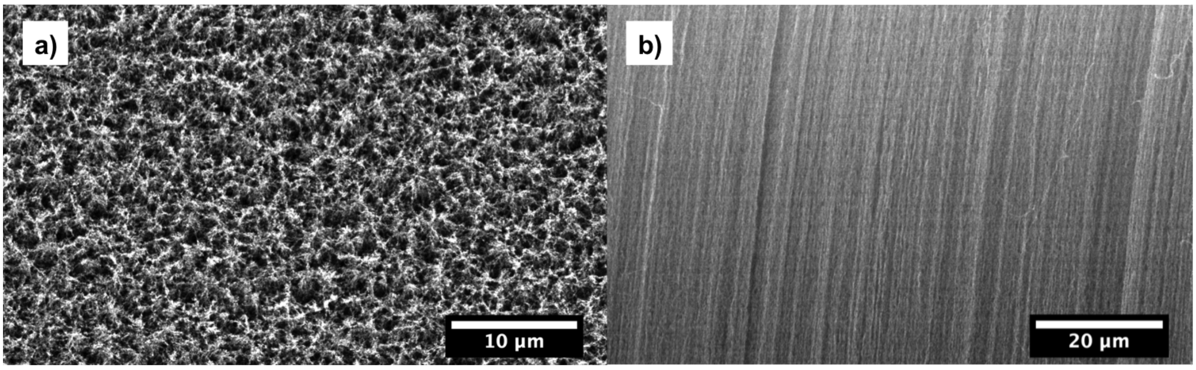

Figure 4.14: SEM image of VACNTs after high temperature CO_2 treatment for opening the tips a) top view b) side view showing the intact vertical alignment.

N_2 adsorption isotherms were measured at 77 K to determine the changes in porosity and specific surface area before and after high temperature CO_2 treatment (figure 4.16a). The as-prepared VACNTs had a specific surface surface area of 570 $m^2\,g^{-1}$. After the high temperature treatment, significant changes in the shape of the isotherm were observed. Though the CO_2 treated VACNTs still exhibit a type-IV(a) adsorption isotherm, an additional step was observed in the isotherm in the relative pressure of 0.4 - 0.7. This corresponds to capillary condensation of N_2 in the one-dimensional tubular pores of CNTs [78]. Though previous reports on open ended CNTs speculated the presence of this step, it was not observed in the measured N_2 adsorption isotherms [78]. The presence of such a step in the CO_2 treated VACNTs is a clear indication of the opening of the tubes. As a result of opening of the tubes and availability of the interior of the tubes for adsorption, the BET specific surface area increased significantly from 570 $m^2\,g^{-1}$ to 912 $m^2\,g^{-1}$.

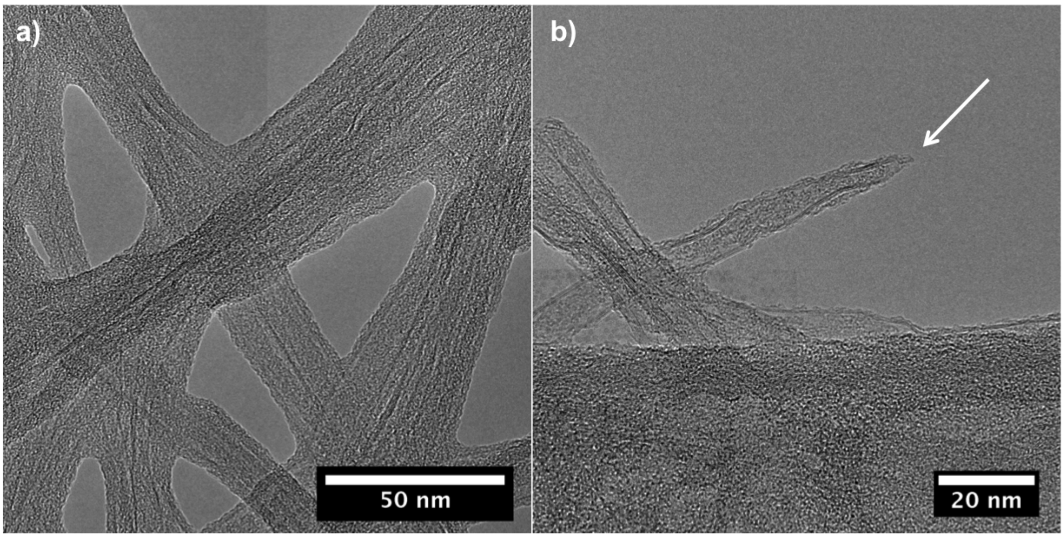

Figure 4.15: TEM image of VACNTs after high temperature CO_2 treatment for opening the tips a) low magnification image revealing the formation of carbonaceous by-products after the treatment b) high magnification image of an opened CNT.

In figure 4.16b, pore size distribution (PSD) analysis of VACNTs before and after CO_2 treatment are compared. Comparison of PSD data helps to track the development of porosity resulting from the CO_2 treatment. After the high temperature CO_2 treatment, the peak centered at ~5–6 nm corresponding roughly to the inner diameter of the CNT, became much more prominent indicating a larger fraction of open ended CNTs. Pore size distribution analysis also indicated an increased fraction of pores below 2 nm after CO_2 treatment. This might be due to the microporous defects produced by the etching of the outer walls of the VACNTs. Nevertheless PSD analysis unambiguously proves the opening of the CNTs and consequently the pore volume increased from 1.02 to $1.38\,\mathrm{cm^3\,g^{-1}}$.

The introduction of microporous defects in the VACNTs after the CO_2 treatment, as speculated from the PSD analysis, should also affect the crystallinity of the CNT structure. The presence of such defects should lead to a lower oxidation resistance for the CO_2 treated VACNTs. To verify this hypothesis, TG measurement was performed on CO_2 treated VACNTs and was compared against the TG of the as-prepared VACNTs. The measurements were carried out in air at a lower heating rate of $2.5\,\mathrm{K\,min^{-1}}$. As expected, the onset of oxidation of CNTs occurred at a lower temperature for CO_2 treated CNTs as shown in figure 4.17a. The differential of the TG curve shown in figure 4.17b, clearly indicates the difference in oxidation rate of the VACNTs before and after CO_2 treatment. For the CO_2 treated CNTs, the temperature of maximum rate of oxidation is at 588 °C, significantly lower than 626 °C observed for pristine VACNTs.

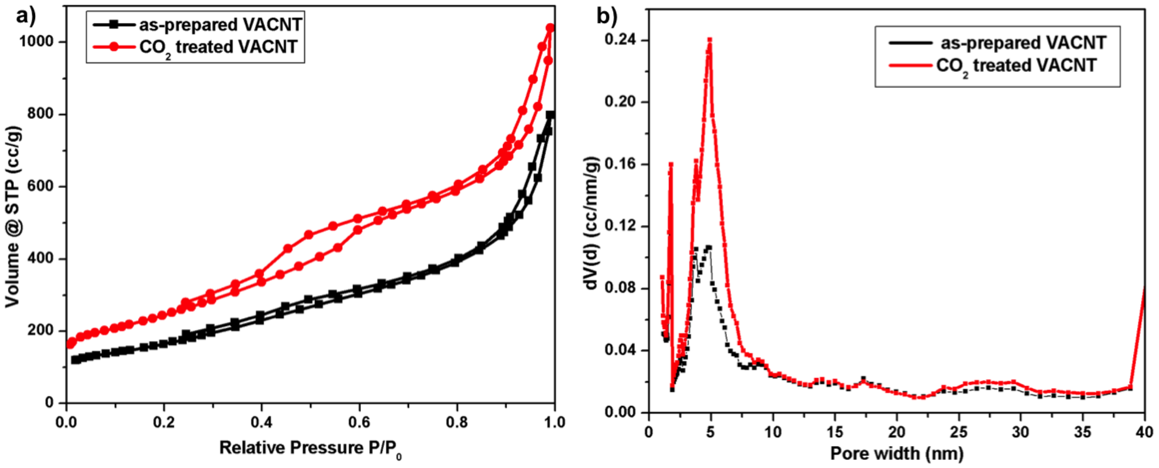

Figure 4.16: a) N_2 adsorption and b) pore size distribution of CO_2 treated VACNTs compared with as-prepared VACNTs.

The asymmetry of the differentiated TG (D-TG) profile indicates that more than one carbonaceous material might be present in the sample [239]. The D-TG profile of carbon nanotubes are usually deconvoluted into three peaks representing amorphous carbon, CNTs with defects and perfectly crystalline CNTs [239, 240]. In the present case, the same approach was followed and the fit obtained is shown in figure 4.17c,d. The peak position and the percentage area under each peak are tabulated in table 4.1. It is known that a large full width at half maximum (FWHM) ($>$ 70 °C) is an indication of a non-homogeneous phase and a small FWHM ($<$ 40 °C) is an indication of a homogeneous phase [240]. Peak 2 and Peak 3 representing CNTs with defects and perfectly crystalline CNTs respectively, represent in itself a homogeneous phase and as expected have a small FWHM. However amorphous carbon (peak 1) represents a wide spectrum of phases. It is reported that the oxidation temperature of amorphous carbon depends upon its aggregate size, composition, concentration of defects etc and are found to be stable up to temperatures as high as 600 °C. This explains the larger FWHM observed for amorphous carbon phase.

From the deconvolution of the D-TG profile it is seen that, the percentage of crystalline CNTs represented by peak 3 has decreased considerably from around 35 % for pristine VACNTs to less than 10 % for CO_2 treated VACNTs. The decrease in the percentage of perfectly crystalline CNTs is accompanied by an increase in the percentage of CNTs with defects (peak 2) and amorphous carbon (peak 1). This is consistent with increased micropore density seen in pore size distribution analysis and the presence of newly formed carbonaceous residue seen in TEM images (4.15) of CO_2 treated CNTs.

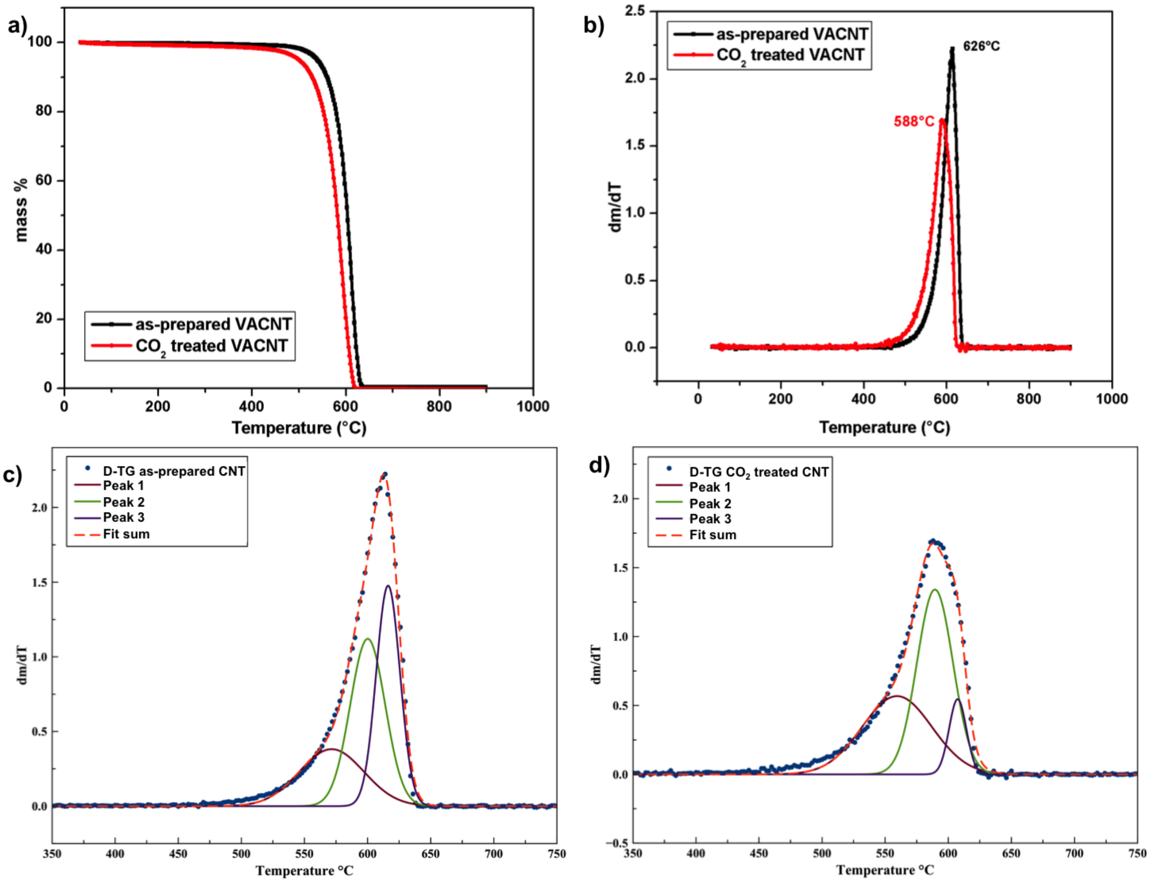

Figure 4.17: a) Thermogravimetric data of CO_2 treated VACNTs compared with as-prepared VACNTs b) differential of TG data c) deconvolution of the D-TG profile of as-prepared VACNTs d) deconvolution of the D-TG profile of the CO_2 treated VACNTs.

Interestingly Raman studies however indicated no changes after CO_2 treatment. The is intriguing as the D-band in the Raman spectrum arises typically from defect sites in the CNT structure and the ratio of I_D/I_G is an indication of the defect density. The average of I_D/I_G ratio from eight separate Raman measurements carried out on VACNTs before and after treatment however, did not reveal any significant changes.

To determine any chemical changes brought about by high temperature CO_2 treatment, XPS studies were carried out on the CO_2 treated VACNTs. The survey spectrum of the CO_2 treated CNTs shown in figure 4.18a is identical to that of pristine VACNTs. The presence of a small O 1s peak at 532 eV is attributed to the atmospheric handling of the sample. After a few seconds of sputtering, the O 1s signal disappeared almost completely as shown in the depth profile measurement in the inset, indicating that the oxygen present is indeed surface bound. The high resolution C 1s spectrum of as-prepared CNTs and CO_2 treated CNTs are shown in figure 4.18b. It should be noted that the high resolution C 1s spectra shown in figure 4.18b was recorded from

	as-prepared VACNTs		CO_2 treated VACNTs	
	Peak position (°C)	%	Peak position (°C)	%
Peak 1	571	24.38	559	39.36
Peak 2	600	38.93	589	47.9
Peak 3	616	34.87	607	9.36

Table 4.1: Results of D-TG deconvolution.

the native surface of the sample and not after sputter treatment. The C 1s spectrum before and after CO_2 treatment looks identical and no differences are observed. It is interesting to note that the percentage of sp^3 carbon phase, remains the same in both cases which implies that the observed carbonaceous residue formed after the CO_2 treatment does not contain sp^3 bound carbon. These are therefore assumed to be graphitic type sp^2 carbon formed as a by-product of the etching process.

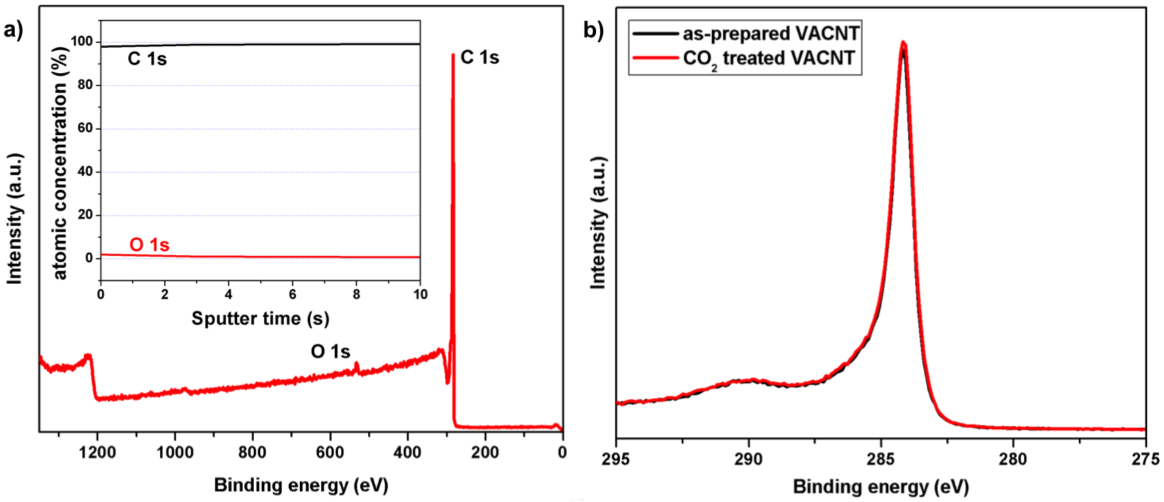

Figure 4.18: a) XPS survey spectrum of CO_2 treated VACNTs. The sputter depth profile measurement in the inset shows that the oxygen present is limited to the top few layers and arises from the atmospheric handling of sample b) C 1s spectra comparison of as-prepared and CO_2 treated VACNTs.

In order to study the effect of opening of the CNTs on gas adsorption, ambient pressure CO_2 adsorption measurements were carried out. In figure 4.19a, the adsorption capacity of CO_2 treated VACNTs is compared with that of pristine VACNTs. The tip opened CO_2 treated VACNTs are found to adsorb about 16 mg g^{-1} of CO_2 at 35 °C, which is about three times the adsorption capacity of pristine untreated VACNTs.

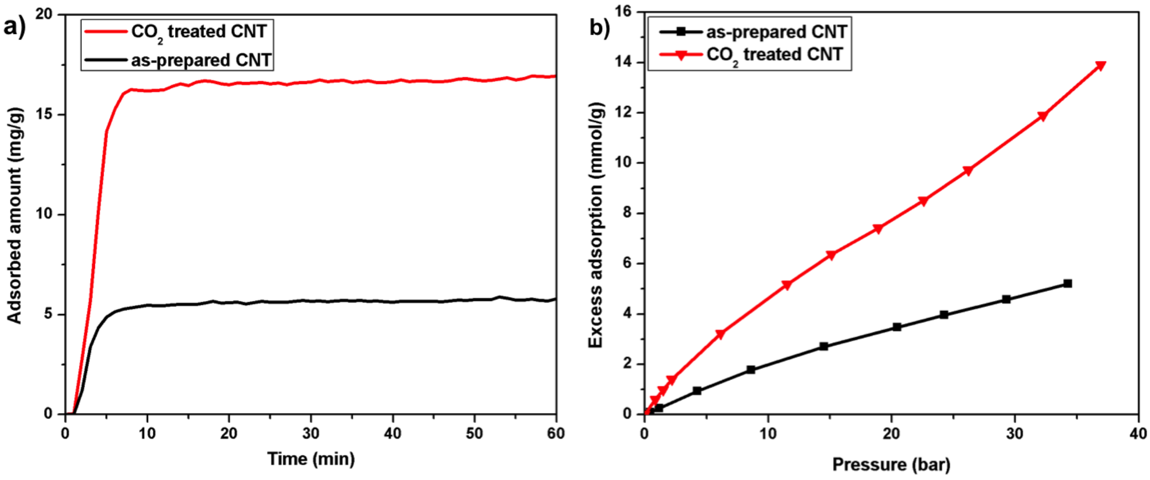

Figure 4.19: CO_2 adsorption on tip opened VACNTs at a) 1 bar and 35 °C b) high pressure up to 40 bar and 25 °C.

The significant improvement in CO_2 adsorption at ambient pressure for the tip opened VACNTs prompted the measurement of high pressure CO_2 adsorption isotherm. High pressure measurements were carried out at 25 °C up to a pressure of ~40 bar. The adsorption isotherm obtained is shown in figure 4.19b. The triple fold increase in adsorption capacity observed at 1 bar, extends over the complete pressure regime studied. At a pressure of 30 bar, VACNTs with tips open, adsorb almost half its weight of CO_2. The adsorption capacity at this mid pressure regime is found to be better than that of most of the standard adsorbents like activated carbon, zeolites, MCM-41 etc. and is found to be comparable to that of metal organic frameworks (MOF). It is interesting to note that unlike all other type of adsorbents, this remarkable adsorption capacity of VACNTs is the result of a chemically homogeneous system composed of only one atom type.

4.5 Concluding remarks

To conclude, in this chapter the adsorption characteristics of pristine VACNTs were outlined. The influence of various geometrical aspects of VACNTs like the tube diameter, intertube distance was discussed. Adsorption on VACNTs was found to increase with a decrease in tube diameter. Consistent with the theoretical findings, decreasing the intertube distance was found to increase the adsorption capacity of VACNTs. Opening of the CNTs by treating in high temperature CO_2 was found to significantly enhance the adsorption characteristics of VACNTs. All this points to the fact that tuning and modifying the structural characteristics of a hierarchical pore system composed of micro-meso and macro structured pores, has an enormous impact on their adsorption properties. In the next chapter the influence of various functional groups grafted to CNT surface on gas adsorption is discussed.

5 Plasma Functionalization of Vertically Aligned Carbon Nanotubes

In this chapter, plasma functionalization and its effect on gas adsorption properties of VACNTs are discussed. Different plasma systems like O_2, N_2, CF_4 and CO_2 are discussed and the chemical modifications brought about by each of these gases are described in detail. Gas adsorption characteristics of various plasma functionalized VACNTs are outlined.

5.1 Introduction

Chemical modification of the CNTs can be brought about by liquid phase methods or gaseous phase methods. As the interstitial sites in VACNTs are a direct result of the vertical alignment of the individual CNTs, it is important to maintain this alignment while subjecting it to chemical functionalization. Liquid phase methods like acid treatment [196, 241, 242] or treatment with oxidizing agents like KOH, $KMnO_4$ or H_2O_2 [138, 243] however, destroys the vertical alignment of the CNTs. Gas phase processes, on the other hand, functionalizes the CNTs without destroying their vertical alignment. Various gas phase functionalization strategies are reported in the literature. These include plasma functionalization [244–246], acid vapor treatment [247–249], ozone/UV treatment [250–252], ion irradiation [253–255] or annealing in various reactive atmospheres [256–258].

Among the various gas phase methods, plasma treatment is a simple and a versatile technique for grafting a wide range of functional groups without compromising the integrity or the vertical alignment of the CNTs. The functionalization itself is quite rapid and does not involve multiple washing/filtration cycles or toxic solvents. By varying the plasma conditions like power, chamber pressure or treatment time, the type and concentration of the functional groups can be controlled [259, 260]. Moreover the plasma process is scalable and non-polluting. These factors motivated the selection of plasma treatment as the preferred means of chemical functionalization for the present work.

5.2 Radio frequency plasma: fundamentals

Plasma in general, can be considered as a partially ionized gas consisting of equal numbers of positive and negative species as well as neutral molecules. On the basis of relative temperature between electrons, ions and neutral species, plasma can be classified as thermal equilibrium or hot plasmas and non-thermal equilibrium or cold plasmas [261]. In thermal equilibrium plasma, the temperature of all the active species are identical due to the frequent collisions between electrons and ions/neutrals inside the high temperature (T ~20 000 K) high density plasma. Such hot plasmas are typically found in stars or fusion reactors. In cold plasma, on the other hand, the temperature of the electrons are much high than that of ions/neutral species. This non-equilibrium is due to the inefficient momentum transfer between the light electrons which are easily accelerated in an applied electromagnetic field and the relatively heavy ions/neutrals. While the temperature of the electrons can be as high as > 5000 K, the gas temperature stays at about 300 K [262]. Cold plasmas are generally generated by glow discharge, arc discharge or corona discharge.

In a radio frequency (rf) plasma, the energy required to generate a plasma is supplied at a radio frequency. In the frequency between 1 MHz and 100 MHz, the free electrons are able to respond instantaneously to slight variations in the applied electric field and gain considerable energy [263]. The movement of heavier species like ions/neutrals are influenced very little by these electric fields. Majority of the sources use the industrially assigned 13.56 MHz or its harmonics [264]. The energized electrons collide with the feed gas inducing ionization, excitation and dissociation [265–267]. The three process can be represented as follows:

Ionization:

$$e + A \longrightarrow A^{+} + 2e \tag{5.1}$$

The high energy electron knocks out an orbital electron from the neutral atom or molecule creating an ion as well as an additional electron.

Excitation and relaxation:

$$e + A \longrightarrow A^{*} + e \tag{5.2}$$

$$A^{*} \longrightarrow A + h\nu \tag{5.3}$$

where A* is the excited state. The photons emitted during the relaxation process are sometimes in the ultraviolet/visible region of the electromagnetic spectrum and resulting glow is characteristic of the composition of the gas.

Dissociation:

$$e + AB \longrightarrow A^{\cdot} + B^{\cdot} + e \tag{5.4}$$

When the high energy electron collides with a molecule, the chemical bonds are broken leading to the generation of free radicals. The free radicals have at least one pair of free electrons and are chemically very reactive.

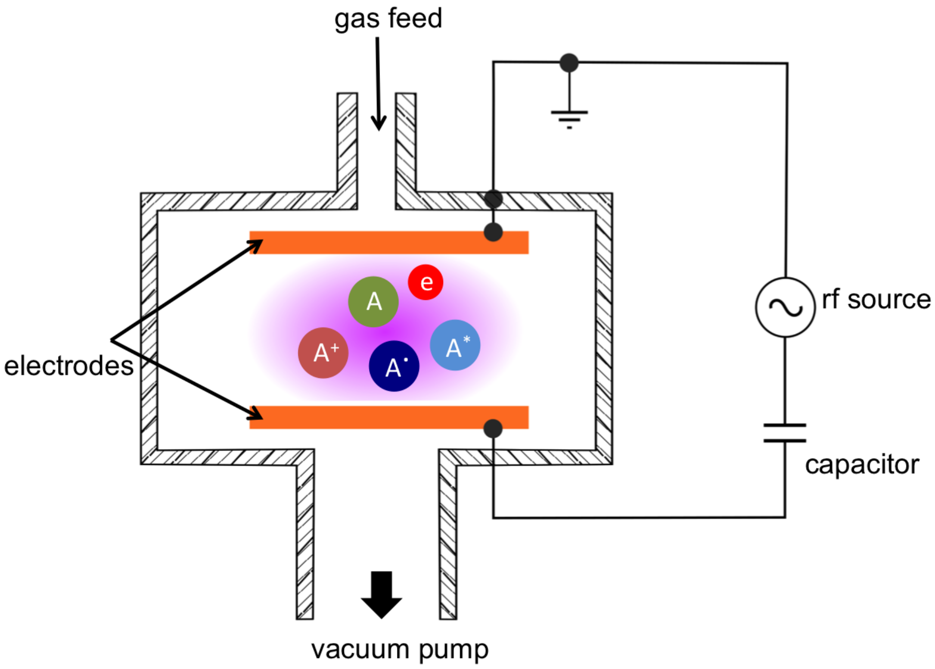

Figure 5.1: Schematic of a capacitively coupled parallel plate rf plasma

In the present work a capacitively coupled parallel plate radio frequency (13.56 MHz) was used for the CNT functionalization experiments. A schematic of the capacitively coupled parallel plate rf plasma system is shown in figure 5.1. The plasma is generated between the two metal electrodes separated by a small distance (typically 2–10 cm). The electrons generated in the plasma constantly collide with the plasma walls and the electrodes and are removed from the system leaving the plasma positively charged. A capacitor provided between the rf generator and the electrode helps to reduce this loss by repelling the electrons (the electrons that leave the electrode negatively charges the capacitor and repels the further incoming electrons). As the sample is placed near the electrode, directly immersed in the plasma generated, a major disadvantage of this type of plasma is the extensive ion bombardment. Nevertheless capacitively coupled rf plasmas are the most widely used plasma systems [266].

5.3 Oxygen rf plasma functionalization of VACNTs

Oxygen plasma functionalization is one of the most widely investigated plasma techniques for functionalizing CNTs. Early studies on O_2 plasma functionalization reported that even few minutes of plasma treatment is sufficient to graft large amount of functional groups, especially carboxyl and hydroxyl groups, on the CNT surface [259, 268]. Felten et al. [259] found that the concentration and type of functional groups tethered to the CNT surface can be tuned by optimizing the plasma parameters. Okpalugo et al. [269] investigated in detail the effect of plasma treatment on the physical and chemical behavior of CNTs and found that the functionalization obtained is comparable to those of acid treated CNTs. Later studies showed that plasma treatment could alter the wetting behavior of CNTs, turning the inherent hydrophobic surface to a hydrophilic surface [270, 271]. O_2 plasma functionalization was also found to alter the electronic properties of the CNTs [272, 273] and subsequently were used for various types of CNT based sensors. The studies on the effect of O_2 plasma functionalization on gas adsorption properties focused mainly on the sensor characteristics of the CNTs [272, 274].

The active species generated in an rf oxygen plasma include high energy electrons, positive and negative ions and radicals especially atomic oxygen [275–277]. Among these, atomic oxygen is found to be the most reactive [275, 278]. The main kinetic reactions of oxygen plasma [275, 277] are as follows

Ionization of oxygen molecule by the energetic electron:

$$O_2 + e \longrightarrow O_2^+ + 2e \tag{5.5}$$

Dissociation reaction involving the generation of a negative ion:

$$O_2 + e \longrightarrow O^- + O \tag{5.6}$$

Recombination reaction between positive and negative ions:

$$O_2^+ + O^- \longrightarrow O_2 + O \tag{5.7}$$

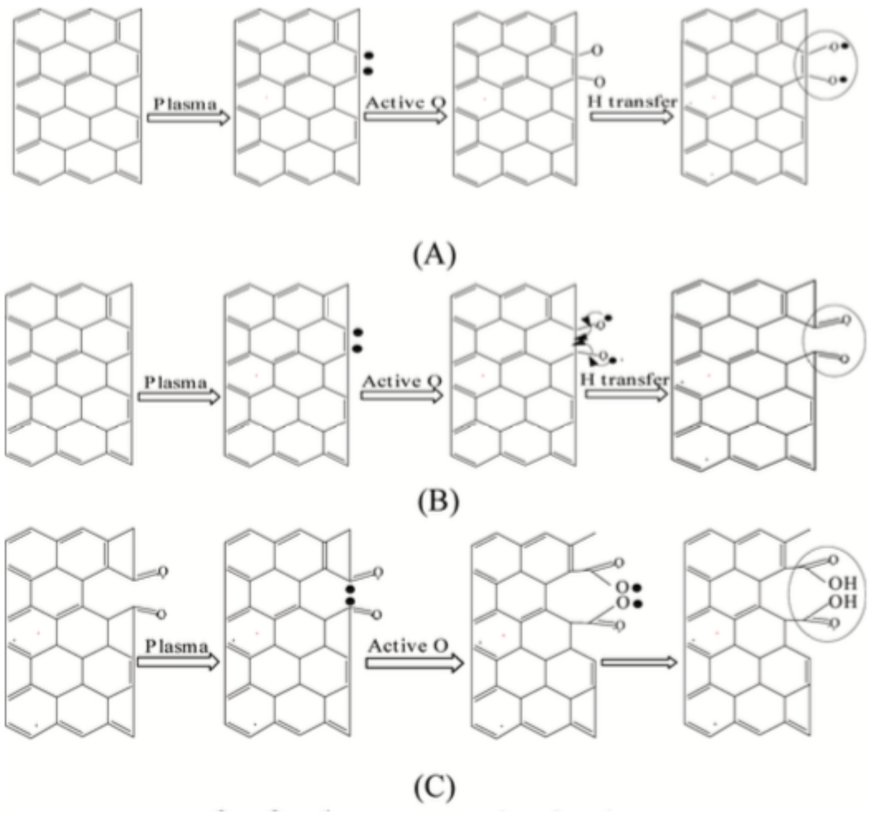

Figure 5.2: Possible mechanism of O_2 plasma functionalization of CNTs proposed by Chen et al. for the generation of (A) C-O bonds (B) C=O bonds and O-C=O bonds [270].

Recombination reaction between electron and positive ions:

$$O_2^+ + e \longrightarrow O + O \tag{5.8}$$

Recombination reaction between oxygen atoms and negative ions:

$$O^- + O \longrightarrow O_2 + e \tag{5.9}$$

Dissociative excitation reactions:

$$O_2 + e \longrightarrow O^* + O + e \tag{5.10}$$

The reaction in an O_2 plasma are not limited to the above reactions but these are the predominant reactions occurring. For example, the only negative ions considered in the above reactions are the O^- ions. Stoffels et al. [276] have shown that O^- ions are indeed the dominant ions and the O_2^- and O_3^- densities make up to only 10–20 % of the total negative ion density.

Chen et al. [270] proposed a possible reaction mechanism that occur during the plasma treatment of CNTs. The high energy species in the plasma breaks the π bonds of the C=C bond, creating carbon radicals which further reacts with the atomic oxygen to produce a C-O bond as shown in figure 5.2. By hydrogen atom transfer, C-O bond transforms to form the C-OH bond. The C=O bonds are assumed to be generated by the intramolecular reorganization of the oxygen radicals attached to the CNT surface. Carboxyl type groups are believed to be formed from by the reaction of atomic oxygen with the radicals generated on the C=O groups.

In the present study, the plasma parameters are optimized with a view of maximizing the extent of functionalization and the associated enhancement of gas adsorption characteristics. To this end, plasma parameters like power, chamber pressure and treatment time were varied systematically and its effect of VACNTs were analyzed by various characterization techniques.

5.3.1 Effect of plasma power

It is known that increasing the plasma power accelerates both physical and chemical effects associated with the plasma resulting in generation of more active species [279, 280]. In the plasma setup used in this study, the samples were kept between the parallel plates and therefore were in direct contact with the plasma. In addition, the reactive species generated in an oxygen plasma leads to significant etching of the CNTs. The combined effect of both these factors result in extensive CNT burn off at high plasma power. Oxygen rf plasma configuration in the present setup was so reactive that even at 50 % power, CNTs were completely consumed in a few minutes. At low power ($< 20\,\%$), the plasma ignition was found to be difficult and affected the reproducibility. Hence a plasma power of 20–30 % was selected for further O_2 plasma functionalization experiments. Raman spectra of VACNTs treated with O_2 plasma for 1 min at 20 % and 30 % power at a chamber pressure of 0.8 mbar is shown in figure 5.3a. Compared to as-prepared CNTs, a higher D band is observed after 1 minute of plasma functionalization. The high energy species generated in an rf plasma are known to induce structural defects in the carbon framework, explaining the observed increase in the D-band signal intensity [69, 280, 281] . Only slight variations were observed in the I_D/I_G ratio of VACNTs treated at 20 % and 30 % power.

An SEM image of the VACNTs treated at 30 % power is shown in figure 5.3b. Compared to the as-prepared VACNTs shown in the inset, some morphological changes are observed on the top surface after O_2 plasma treatment. However, the vertical alignment is unaffected by

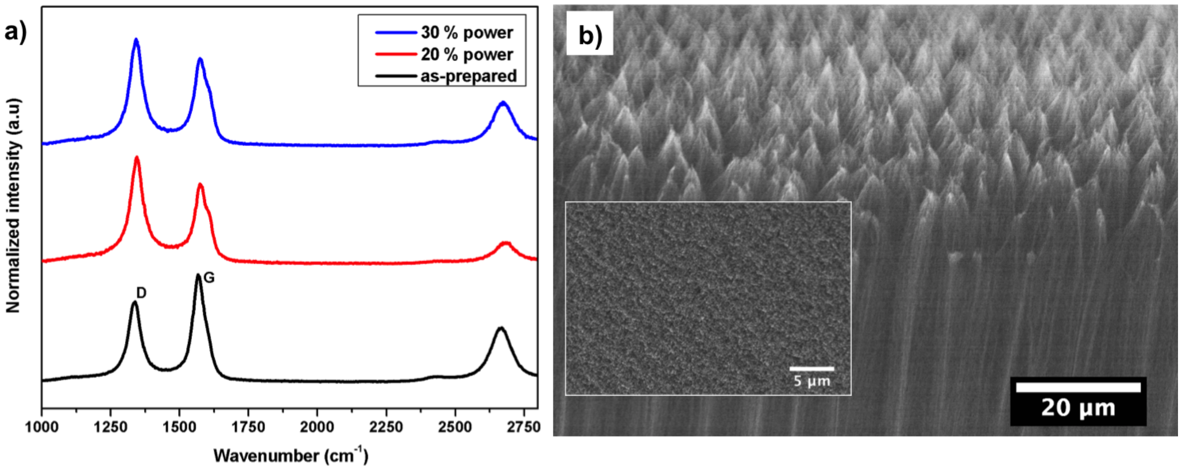

Figure 5.3: a) Raman spectra of VACNTs functionalized with O_2 plasma for 1 min at a chamber pressure of 0.8 mbar at different plasma powers b) SEM image of the top surface of the CNTs after O_2 plasma functionalization at 30 % power. Inset shows the SEM image of the top surface of the as-prepared VACNTs before plasma treatment.

plasma functionalization. Morphological changes in the form of agglomerate formation in irregular however periodic patterns is a known phenomena for the plasma functionalization of ultra long highly parallel CNTs [245, 280, 282, 283].

5.3.2 Effect of chamber pressure

Similar to an increase in the plasma power, increasing chamber pressure also leads to an increase in the plasma density [279, 284]. Chamber pressure can be raised by increasing the gas flow rate. To investigate the effect of chamber pressure on VACNTs functionalization, experiments were performed at 20 % power for 2 min with three different gas flow rates: 20 % or 4 sccm, 40 % or 8 sccm and 60 % or 12 sccm corresponding to 0.4, 0.6 and 0.8 mbar respectively. SEM images of the VACNTs treated at the three different gas flow rates are shown in figure 5.4a-c. No changes in morphology are observed for VACNTs treated at 20 % gas flow rate. However morphological changes (on the top surface) are seen for VACNTs treated at 40 % and 60 % gas flow and such morphologies, as noted in the previous section, are typical for plasma functionalization.

FTIR spectra of the VACNTs obtained from these three cases are shown in figure 5.4d. The peak at 1732 cm^{-1} corresponding to COOH group, increases with an increase in the gas flow rate. For VACNTs treated at 20 % gas flow rate, only a very small COOH signal is observed, indicating a lower extent of functionalization. This is consistent with the undisturbed morphology observed in SEM (figure 5.4a). Extensive sample burn off was observed at chamber pressure $>$ 0.8 mbar

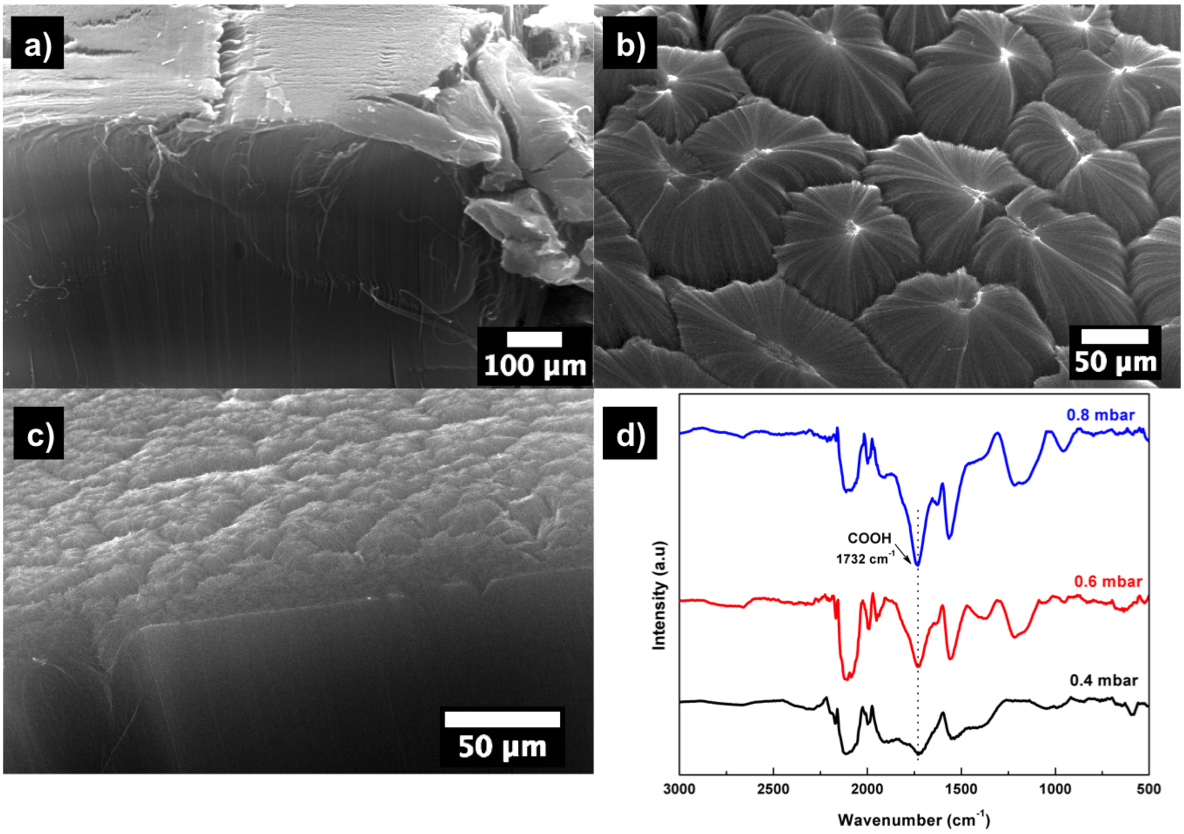

Figure 5.4: SEM images of VACNTs treated with O_2 plasma for 2 min at 20 % power at a chamber pressure of a) 0.4 mbar b) 0.6 mbar c) 0.8 mbar d) FTIR spectra of VACNTs indicating the increasing extent of functionalization with an increase in the chamber pressure.

(gas flow rates > 60 %). For further O_2 plasma experiments, a gas chamber pressure of 0.8 mbar was chosen.

5.3.3 Effect of plasma treatment time

To investigate the effect of plasma treatment time on the functionalization of VACNTs, experiments were carried out at 20 % power and 60 % gas flow rates with treatment times of 30 s, 1 min and 2 min. FTIR spectra of VACNTs treated for 1 min and 2 min are shown in figure 5.5a. The extent of functionalization increased with treatment time and for longer treatment time of > 5 min considerable amount of weight loss was observed.

It should be noted that, unlike other types of plasma atmospheres which will be discussed later, due to the highly reactive nature of the O_2 rf plasma, the room for optimization was quite limited. Raman spectroscopy measurements were not used as the primary characterization technique because it was found that the I_D/I_G ratio increased rapidly and reached a saturation

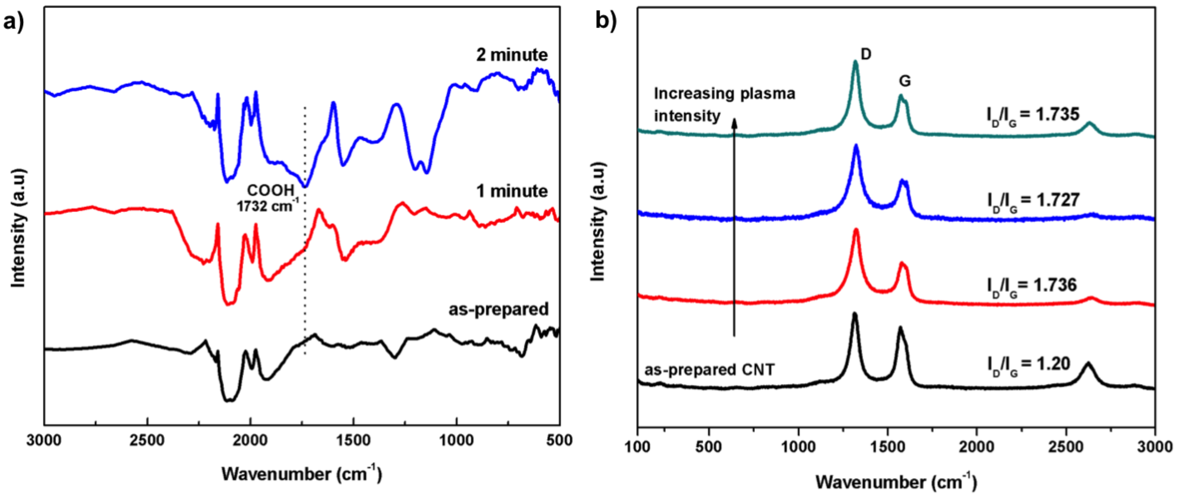

Figure 5.5: a) FTIR spectra of VACNTs treated with O_2 plasma for different treatment time b) Raman spectra of O_2 plasma functionalized CNTs at different plasma conditions. Increasing plasma intensity refers to an increase in plasma power and treatment time [Raman spectra was recorded with 633 nm laser].

even at 1 min of O_2 plasma functionalization. Thereafter no difference in the spectra was observed for prolonged treatment time or varied gas flow rates as shown in figure 5.5b.

5.3.4 Optimized conditions for O_2 rf plasma

Summarizing the different set of optimization experiments, the most suitable O_2 rf plasma conditions were found to be 20–30 % power at a gas flow rate of 60 % (0.8 mbar) and treatment time of 2–4 min. Subsequently O_2 plasma functionalization was carried out on VACNTs at 30 % power and a gas flow rate of 60 % for 4 min. SEM image of the functionalized VACNTs is shown in figure 5.6a. The morphological changes observed on the top surface are typical for plasma treatment and in the side view, the vertical alignment of the VACNTs are still seen to be intact after 4 min of plasma functionalization. N_2 adsorption isotherm at 77 K (figure 5.6b) were measured to determine the changes in porosity and specific surface area after the plasma functionalization. Compared with as-prepared VACNTs (fig. 2.18), no apparent changes in the shape of the isotherm are observed but the specific surface area increased from about 500 $m^2\,g^{-1}$ to 703 $m^2\,g^{-1}$ after 4 min of O_2 plasma functionalization.

To probe the nature and the concentration of the functional group grafted by O_2 rf plasma treatment, XPS spectra of functionalized sample (4 min) were recorded. Compared to the as-prepared VACNTs, a pronounced O 1s peak at binding energy $E_{bin} = 532.5$ eV is observed for the

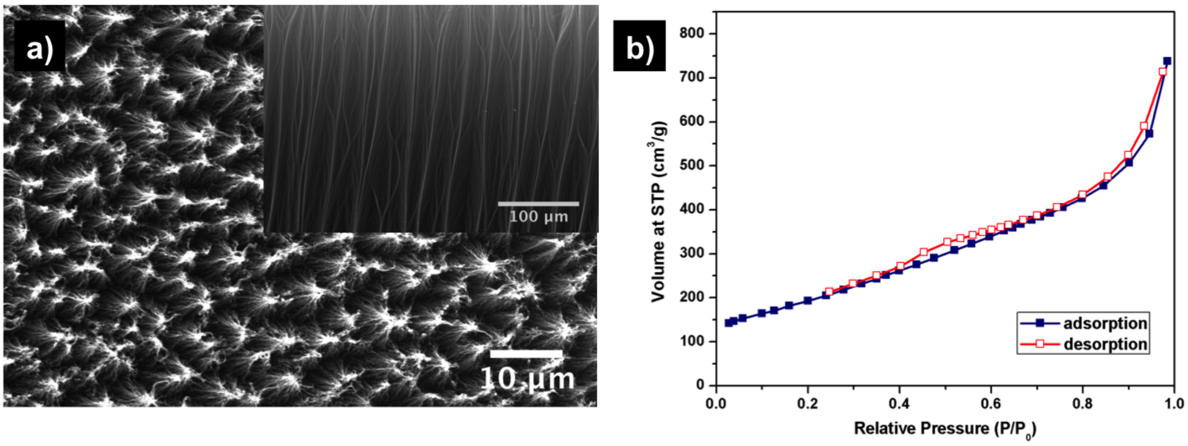

Figure 5.6: a)SEM image of the top surface of O_2 plasma functionalized VACNTs at 30 % power for 4 min at 60 % gas flow rate. Inset shows the vertical alignment is still maintained after 4 min of plasma treatment b) N_2 adsorption isotherm (77 K) of 4 min O_2 plasma treated VACNTs at 30 % power and 60 % gas flow rate.

plasma functionalized VACNTs (figure 5.7a). Unlike the as-prepared VACNTs, the high resolution O 1s spectrum of plasma functionalized VACNTs revealed a strong signal (figure 5.7b) confirming substantial amount of oxygen moieties grafted to the CNTs surface. A more detailed analysis of the nature of functionalization was carried out by deconvoluting the C 1s high resolution spectrum. The observed C 1s spectrum is fitted using four components as shown in figure 5.7c. The strong photoelectron emission at E_{bin}=284.1 eV is attributed to the graphitic structure of the CNTs [196]. The pronounced asymmetry of the C 1s photoelectron line to higher binding energies is an inherent feature for graphite [197] and is due to the neutralization of holes created during photoionization, by conduction band electrons [198]. The peak at E_{bin}=285.0 eV arises from structural defects of CNTs. The plasma functionalized VACNTs exhibit a predominant peak at E_{bin}=286.8 eV corresponding to C-O functional groups. The peak observed at still higher binding energy (E_{bin}=288.8 eV) is attributed to the presence of O-C=O functional groups [196, 242]. XPS quantitative analysis of the plasma functionalized VACNTs indicated an oxygen concentration of ~38 at.% on the surface of the VACNTs.

To determine the spatial uniformity of the plasma functionalization process, XPS depth profile measurements were conducted. XPS spectra were recorded after each sputter etching cycle and the process was carried out for about 140 s. The C 1s and O 1s sputter depth profile of plasma functionalized VACNTs is plotted in figure 5.7d. In the first few cycles of depth profile measurement, the O 1s signal intensity decreased rapidly accompanied by an almost similar magnitude

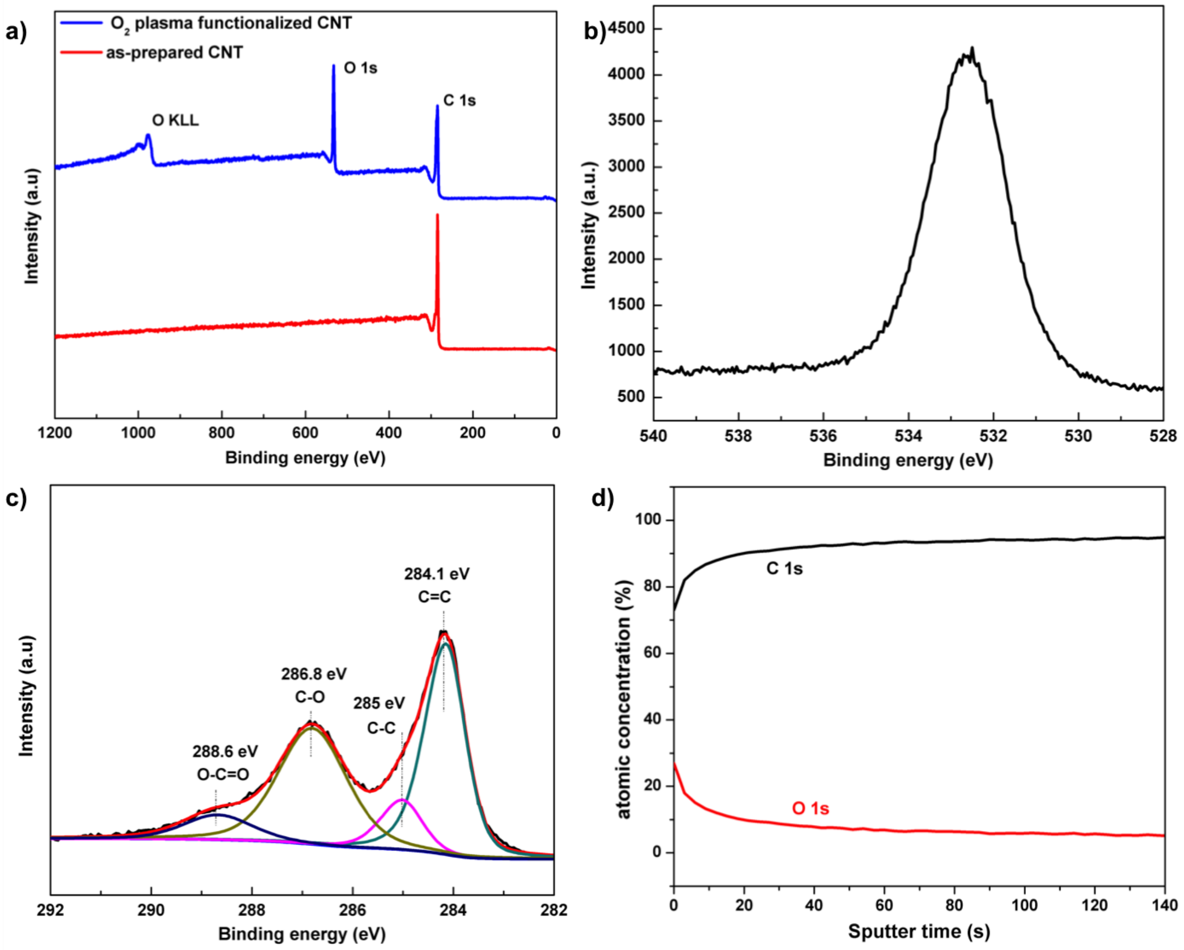

Figure 5.7: XPS studies on O_2 plasma functionalized VACNTs a) Survey spectra of as-prepared and O_2 plasma functionalized VACNTs b) high resolution O 1s spectrum of O_2 plasma functionalized CNTs c) high resolution C 1s spectrum of O_2 plasma functionalized VACNTs with peaks deconvoluted d) depth profile measurement studies of O_2 plasma functionalized VACNTs.

increase in the C 1s signal intensity. After about 20 s of etching, the rate of decrease of O 1s intensity became gradual and after 140 s of etching, oxygen atomic concentration was found to be ~6 %. The depth profile measurements indicate that the very high oxygen concentration (~38 at.%) is limited only to the top few nanometers of the VACNTs. Similar results were also observed by Bittencourt et al. in atomic oxygen functionalization of VACNTs [281].

5.3.5 CO_2 adsorption studies on O_2 plasma functionalized VACNTs

Ambient pressure CO_2 adsorption measurements were performed on VACNTs at the optimized conditions of 4 min of O_2 plasma at 20 % power and 60 % gas flow rate. Compared to the as-prepared VACNTs, CO_2 adsorption capacity of plasma functionalized VACNTs increased by more than two fold to 12.6 mg g^{-1} as shown in figure 5.8a. To confirm the optimized plasma parameters were in fact the right conditions for maximizing CO_2 adsorption, adsorption experiments were also performed on VACNTs subjected to 1 min of O_2 plasma treatment at a milder condition of 20 % power and 40 % gas flow rate. Adsorption capacity of the so treated VACNTs is found to be 9 mg g^{-1} as shown in figure 5.8a, indeed lower than the VACNTs treated under optimized conditions.

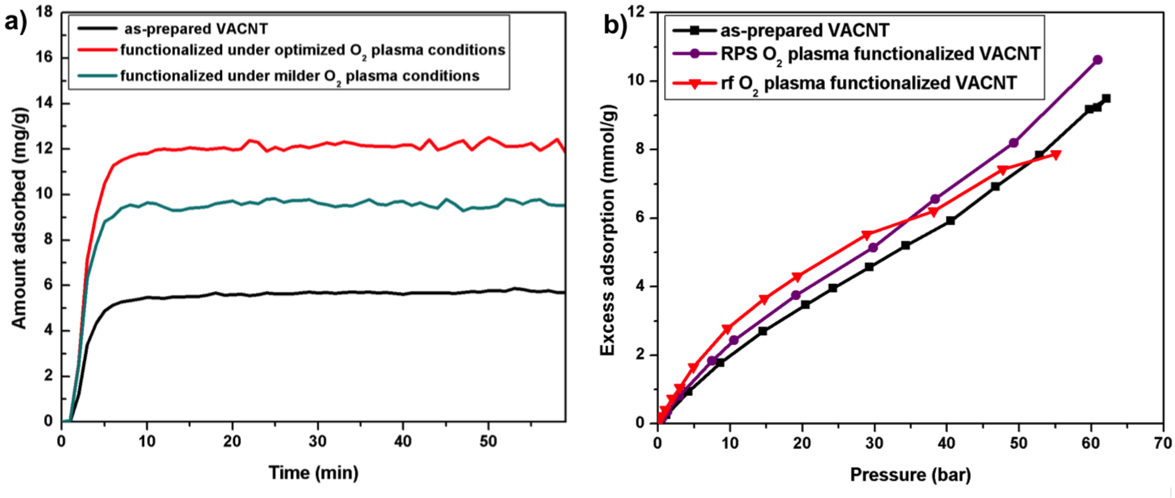

Figure 5.8: CO_2 adsorption on O_2 plasma functionalized VACNTs a) at 1 bar and 35 °C b) up to a pressure of about 60 bar at 30 °C. [rf: radio frequency, RPS: remote plasma source.]

High pressure adsorption CO_2 measurements at 30 °C were carried out on VACNTs functionalized with O_2 plasma under the optimized conditions. Compared to the as-prepared VACNTs, O_2 plasma functionalized VACNTs exhibited better adsorption capacity up to pressures ~50 bar as shown in figure 5.8b. The difference in adsorption capacity is maximum in the pressure range 10–30 bar. Since plasma functionalization is a complex process, a multitude of functional and structural changes like grafting of functional groups, creation of defects etc. take place simultaneously. It is assumed that the combined effect of these led to the observed increase in the adsorption characteristics.

5.4 O_2 plasma functionalization of VACNTs by a microwave remote plasma source

In a microwave plasma, the energy required for plasma generation is supplied at a microwave frequency. A microwave plasma typically uses electromagnetic radiation in the frequency range of 300 MHz to 10 GHz [267] and the most common frequency employed is 2.45 GHz. Compared to rf plasma, microwave plasmas offers few distinct advantages. Microwave plasmas are characterized by

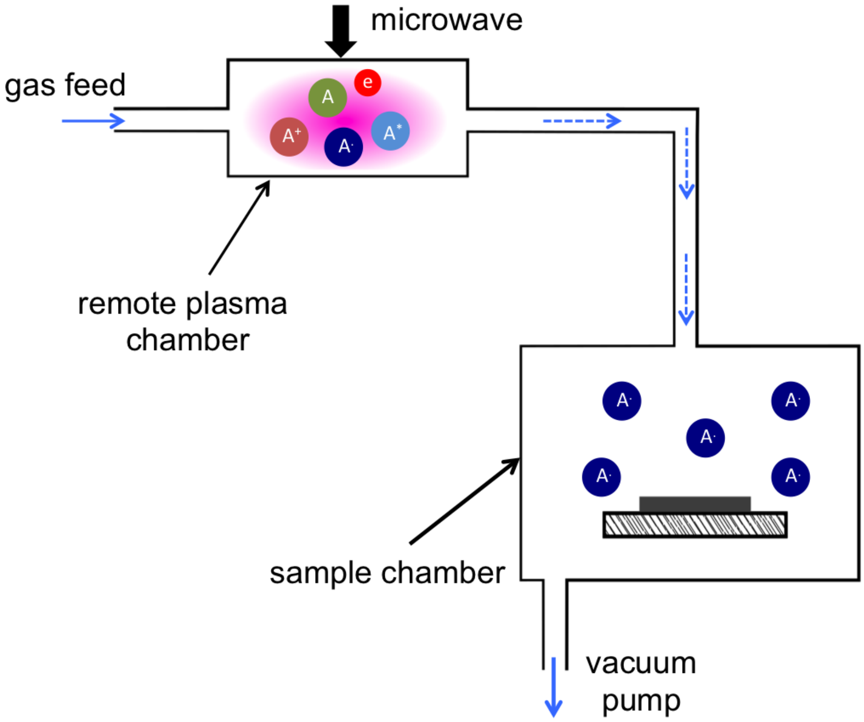

Figure 5.9: Schematic of a remote plasma source setup. Due to their short lifetime, the high energy species are confined to the remote plasma chamber. The sample is exposed to only the free radicals thereby minimizing the ion bombardment.

high ionization degree and high concentration of active species such as atoms, radicals and excited molecules [285]. It also offers the possibility of electrodeless acceleration thereby eliminating electrode contamination. However they typically require very high magnetic fields compared to rf plasma.

In a capacitively coupled parallel plate rf plasma setup, as described in the previous section, the samples are kept in the chamber directly between the parallel plates where the plasma is generated. This leads to extensive etching of CNTs due to the bombardment of the ions. In remote plasma source configuration (RPS), on the other hand, plasma is generated in a separate chamber and only the chemical radicals are brought in contact with the sample. A schematic of the RPS configuration is shown in figure 5.9. A microwave source is used for the plasma generation as it typically leads to a high density plasma. The microwave applied to the feed gas generates positive and negative ions, excited species and free radicals in addition to high energy electrons. However due to the short lifetime of the high energy electrons and ions, the concentration of these species becomes negligible when they are introduced into the main chamber. As a result, the sample damage due to ion bombardment is minimized and the chamber reactions are purely chemical [281, 286].

To study the effectiveness of functionalization by such a system, O_2 plasma functionalization was carried out on VACNTs by a microwave plasma (R3T muegge STP 2020, 2.45 GHz 3000 W) in RPS configuration. The plasma power and chamber pressure were fixed at 1000 W and 450 mtorr respectively and the functionalization time was varied from 1–8 min. Unlike in rf plasma, the weight loss was found to be negligible in microwave RPS plasma. Raman spectra of the RPS plasma functionalized VACNTs is shown in figure 5.10a. The mild nature of the RPS plasma is evident from the Raman spectra. In contrast to rf plasma, the defect concentration, measured by the ratio of intensities of D-band to G-band, did not saturate after a few seconds but increased progressively as a function of time. For a treatment time of 8 min, the I_D/I_G ratio increased from 0.63 before treatment to 1.27 after treatment.

To determine the nature and concentration of functional groups grafted by O_2 RPS functionalization, XPS spectra of functionalized VACNTs were recorded. Similar to the trend observed in Raman measurements, the progressive nature of the functionalization is evident from the survey spectra (figure 5.10b) and the high resolution O 1s spectra (figure 5.10c). However, the extent of functionalization obtained is much lower when compared to rf plasma functionalized VACNTs. Even after 8 min of plasma functionalization, only a small hump is observed at higher binding energies (> 286 eV) in the high resolution C 1s spectra of RPS functionalized VACNTs. In contrast, for rf plasma functionalized VACNTs, 4 min of functionalization led to a prominent peak at higher binding energies (figure 5.7c). This points to the need for prolonged plasma treatment time in RPS mode for obtaining the same extent of functionalization as in an rf plasma.

Ambient pressure adsorption measurements indicated only very little improvement in CO_2 adsorption capacity for RPS functionalized VACNTs. However high pressure measurements on 8 min functionalized VACNTs, revealed a different trend as shown in figure 5.8b. Consistent with ambient pressure measurements, no improvement in adsorption capacity is observed at pressures less than 5 bar. But at still higher pressures, adsorption capacity is found to improve relative to that of as-prepared VACNTs and unlike rf plasma functionalized VACNTs, no eventual leveling off of adsorption capacity is observed. It is hypothesized that the prolonged treatment time (as seen later, in detail, under N_2 plasma functionalization) might have resulted in a more uniform functionalization and is supposed to be the reason for the observed increase in adsorption capacity at

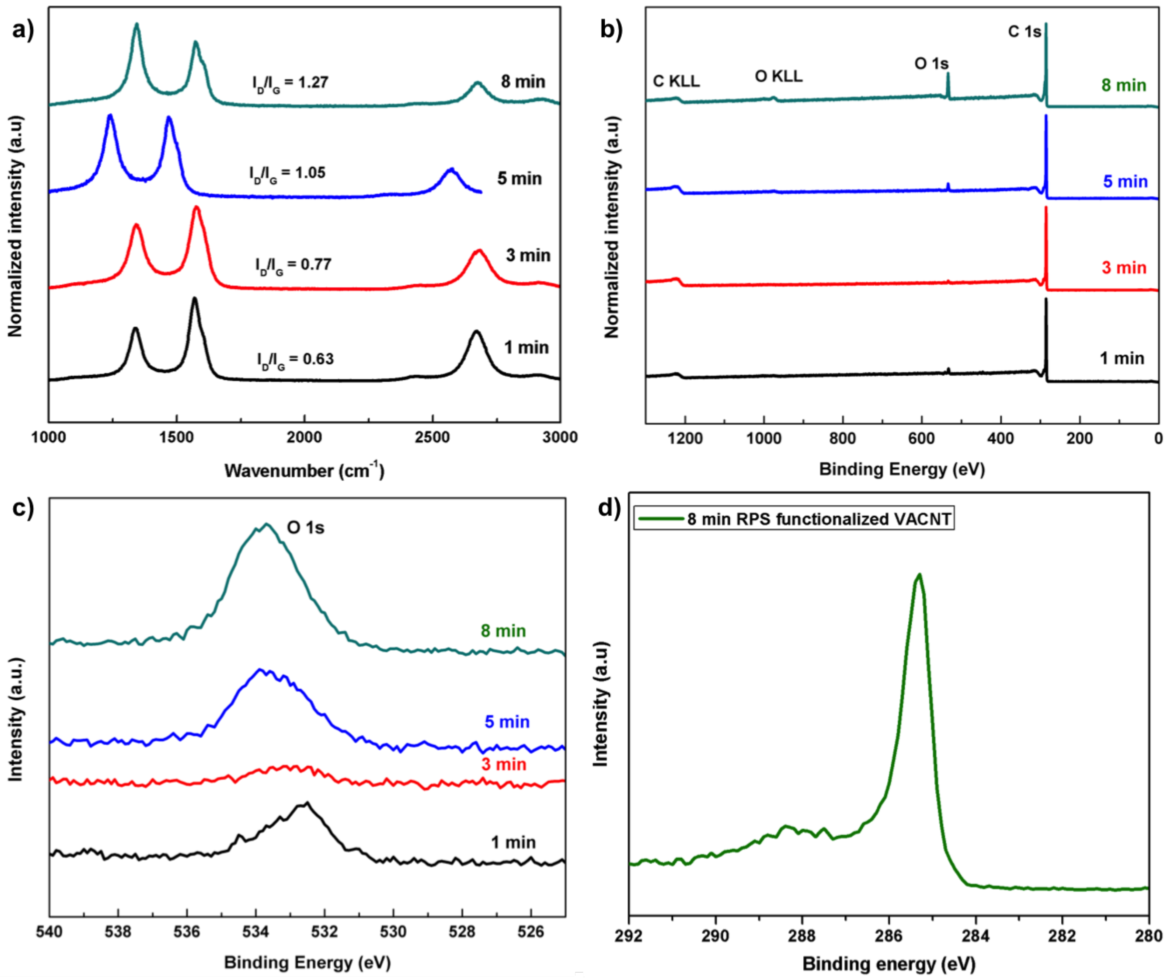

Figure 5.10: Characterization of O_2 RPS functionalized VACNTs treated for different plasma durations a) Raman spectra showing the increasing defect density with treatment time b) XPS survey spectra and c) high resolution O 1s spectra revealing the progressive nature of functionalization d) high resolution C 1s spectra of 8 min O_2 RPS functionalized VACNTs.

high pressures. Nevertheless from the O_2 plasma functionalization studies, it is clear that grafting of various functional groups can improve the CO_2 adsorption capacity of VACNTs.

To check the reproducibility of the adsorption behavior, high pressure CO_2 adsorption measurements were repeated on 8 min RPS functionalized VACNTs after a full adsorption-desorption cycle. VACNTs exhibited excellent reproducibility with no tangible signs of adsorption capacity deterioration even up to the highest measured pressure of 50 bar as shown in figure 5.11. Larger error bars at high pressures are due to the condensation effect of CO_2 at high relative pressures. Unlike for activated carbon (fig. 3.9b), no significant decrease in adsorption capacity is observed in the second cycle of measurement. This indicates the structural stability of VACNTs to high pressure and multiple adsorption-desorption cycles.

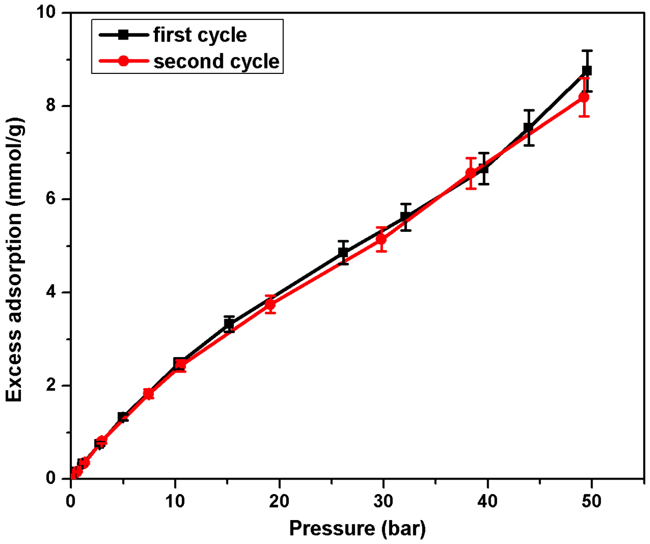

Figure 5.11: High pressure CO_2 adsorption at 30 °C on 8 min RPS functionalized VACNTs for 2 cycles of measurement. The reproducibility of the measurement indicates complete desorption and stability of the adsorbent.

5.5 Nitrogen plasma functionalization

Traditionally CO_2 is removed from the gas stream by amine scrubbing process [84, 287, 288] in which aqueous amines strip CO_2 from the gas stream by the reaction:

$$2RNH_2 + CO_2 \longleftrightarrow RNHCO_2^- + RNH_3^+ \tag{5.11}$$

Along this line, CO_2 adsorption enhancement by incorporation/impregnation of various amine functional groups on carbon nanotubes have been reported [105, 108, 124, 289, 290]. The irreversible reaction of CO_2 with these amine functional groups makes the regeneration of the spent adsorbent quite difficult and energy intensive.

However, nitrogen groups like pyridinic or pyrrolic/pyridonic groups are known to reversibly adsorb CO_2 [291–294]. These groups have a weak basic character and CO_2, a weak Lewis acid, experiences an enhanced interaction with surfaces of Lewis base type [289, 295]. Though majority of the works report a positive influence on CO_2 adsorption [289, 295–298], there are also reports of observed indifference to CO_2 adsorption after N-incorporation in the carbon framework [299, 300]. Most of these studies are however limited to pressures of up to only ambient pressure and hence do not provide the complete picture. In an attempt to address these issues, CO_2 adsorption on nitrogen functionalized VACNTs is carried out for a range of pressure and temperature. The heat of adsorption is also calculated to study the nature of CO_2/CNT interaction.

5.5.1 Nitrogen rf plasma functionalization of VACNTs

Due to the highly stable N_2 bond ($\sim$9.67 eV), the degree of N_2 dissociation and ionization in pure nitrogen plasma is low compared to other plasma systems like O_2 [301]. The active species generated in a nitrogen plasma include N_2^+, N^+, atomic N and their excited states [301, 302]. N_2 plasma treatment of CNTs is known to incorporate various nitrogen functionalities like pyridinic type, pyrrolic/pyridonic type or graphitic N type in the graphene framework of CNTs as shown schematically in figure 5.12

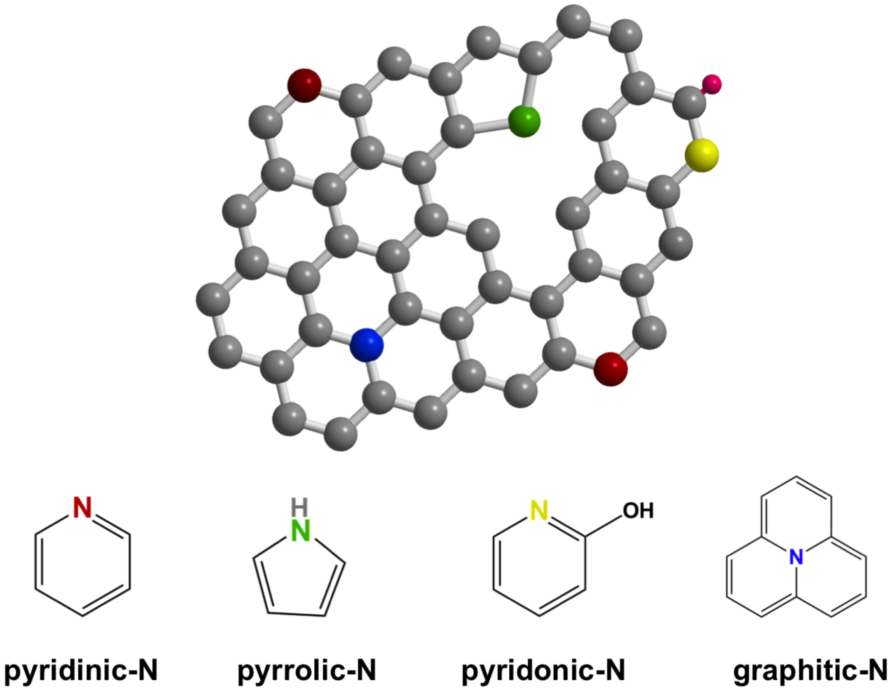

Figure 5.12: Schematic of different nitrogen incorporation in graphene

In the present study, as-prepared VACNTs were subjected to rf N_2 plasma functionalization at 20 % power and at a chamber pressure of 0.9 mbar (60 % gas flow rate). Since no significant etching occurs in N_2 plasma, prolonged treatment was possible and subsequently VACNTs were subjected to 60 min of plasma functionalization. An SEM image of the CNTs after 60 min of N_2 plasma treatment is shown in figure 5.13a. Considerable changes in morphology are observed after the plasma treatment. Though the top surface agglomeration is similar to what is observed with O_2 plasma treatment, the exposed outer surface of the side of CNT array have aggregated as well in N_2 plasma treated CNTs (figure 5.13a). TEM investigations (figure 5.13b) however indicated no apparent changes in the structure. Even after subjecting to 60 min of plasma treatment, no major damages to the tubular structure or CNT walls are observed.

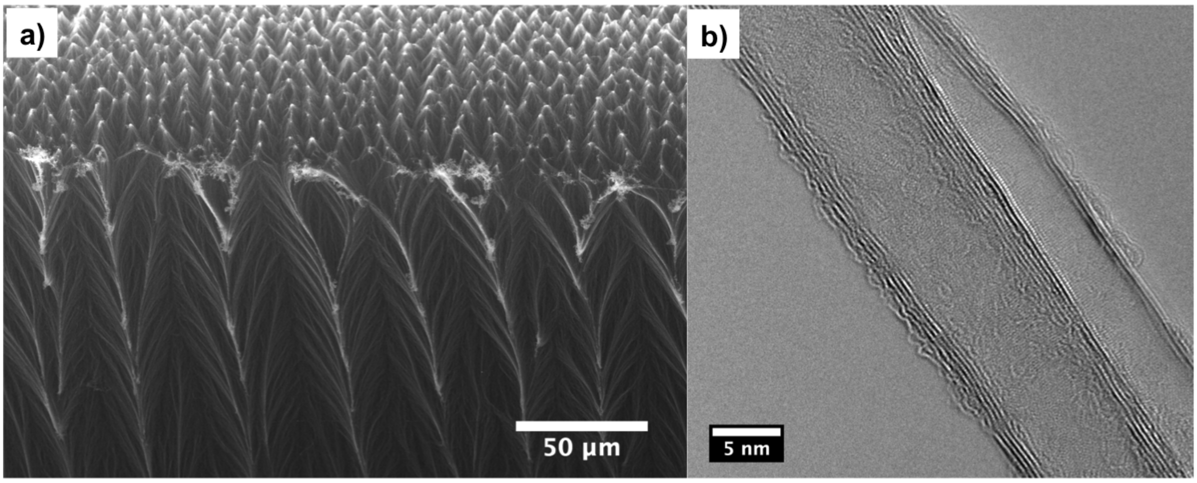

Figure 5.13: a) SEM and b) TEM images of VACNTs subjected to 60 min of N_2 plasma functionalization.

Raman measurements before and after N_2 plasma treatment revealed an increase in the D-band intensity as shown in figure 5.14a. The I_D/I_G ratio increased from 0.8 to 1.43 after 60 min of plasma functionalization. The increase of D-band is typical for plasma functionalization and is believed to be due to the creation of defects as well as grafting of functional groups on the CNT surface. N_2 adsorption measurements at 77 K indicated only minor changes in the adsorption isotherm after 60 min of plasma treatment (figure 5.14b). The shape of the isotherm essentially remains the same however, a slight decrease in the amount adsorbed is observed at low relative pressures. This is reflected in a lower BET specific surface area of 447 $m^2\,g^{-1}$ as compared to 500 $m^2\,g^{-1}$ for the as-prepared untreated VACNTs. Similar trends are observed in the pore size distribution analysis shown in the inset of figure 5.14b. Prolonged N_2 plasma treatment lead to a decrease in the pore density in the lower mesopore regime.

XPS measurement confirmed the grafting of nitrogen functionalities on the CNT surface. A prominent N 1s peak is observed in the survey spectrum (figure 5.15a). High resolution C 1s spectrum of the N_2 plasma functionalized CNTs is shown in figure 5.15b. Since the binding energy difference between carbon-oxygen and carbon-nitrogen groups is negligible, the peak assignment of the C 1s spectrum is complicated. Nevertheless a characteristic major hump in C 1s spectrum indicates significant functionalization by either nitrogen or oxygen groups. To obtain a more de-

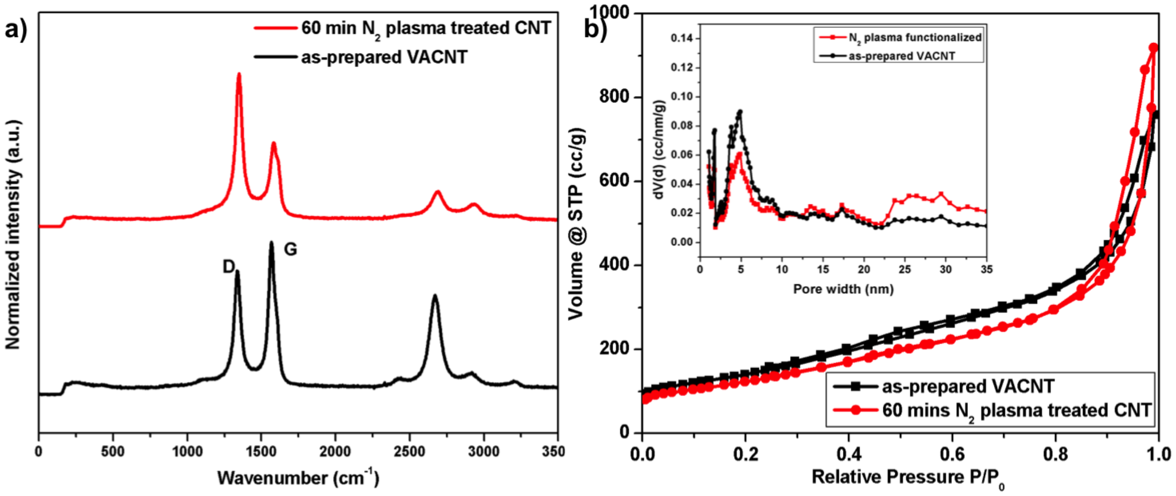

Figure 5.14: a) Raman spectra and b) N_2 adsorption isotherm (at 77 K) of VACNTs before and after 60 min of N_2 plasma functionalization.

tailed picture, the high resolution N 1s spectrum of the plasma functionalized CNTs was recorded. As shown in figure 5.15c, the N 1s spectrum is deconvoluted into 2 curves with a peak maximum at 399.2 eV and 400.5 eV and are assigned to pyridinic and pyrrolic/pyridonic type respectively [248, 303–305]. A quantitative analysis of the XPS data indicated a total nitrogen content of ~15.52 atomic percentage on the surface with pyridinic and pyrrolic/pyridonic group constituting 5.93 and 9.59 atomic percentage respectively. To ascertain the uniformity of the obtained functionalization, XPS sputter depth profile measurements were carried out. As shown in figure 5.15d, the functionalization indeed is found to be mainly at the surface and decreases with an increase in the sputter etch penetration deeper into the sub-surface of the sample. Compared to O_2 plasma functionalization, the decrease in the N-content with depth is rather gradual, indicating a more uniform functionalization. This might be attributed to the much longer treatment time for N_2 plasma functionalized CNTs. After 150 s of etching, N-concentration decreased from 15.52 at.% at the VACNT surface to about 5.5 at.%. This value is close to the commonly reported N-doping values (4 - 6 at.%) on carbon materials [291, 306, 307].

To investigate the improvement in adsorption properties, ambient pressure CO_2 adsorption measurements were carried on N_2 plasma functionalized CNTs. As shown in figure 5.16a, 60 min of N_2 plasma functionalization led to an enhanced CO_2 adsorption capacity of 12.4 mg g^{-1} at 35 °C. The adsorption capacity obtained for 60 min N_2 plasma functionalized sample is almost equal to the adsorption capacity obtained for O_2 plasma functionalized CNTs. To obtain the adsorption

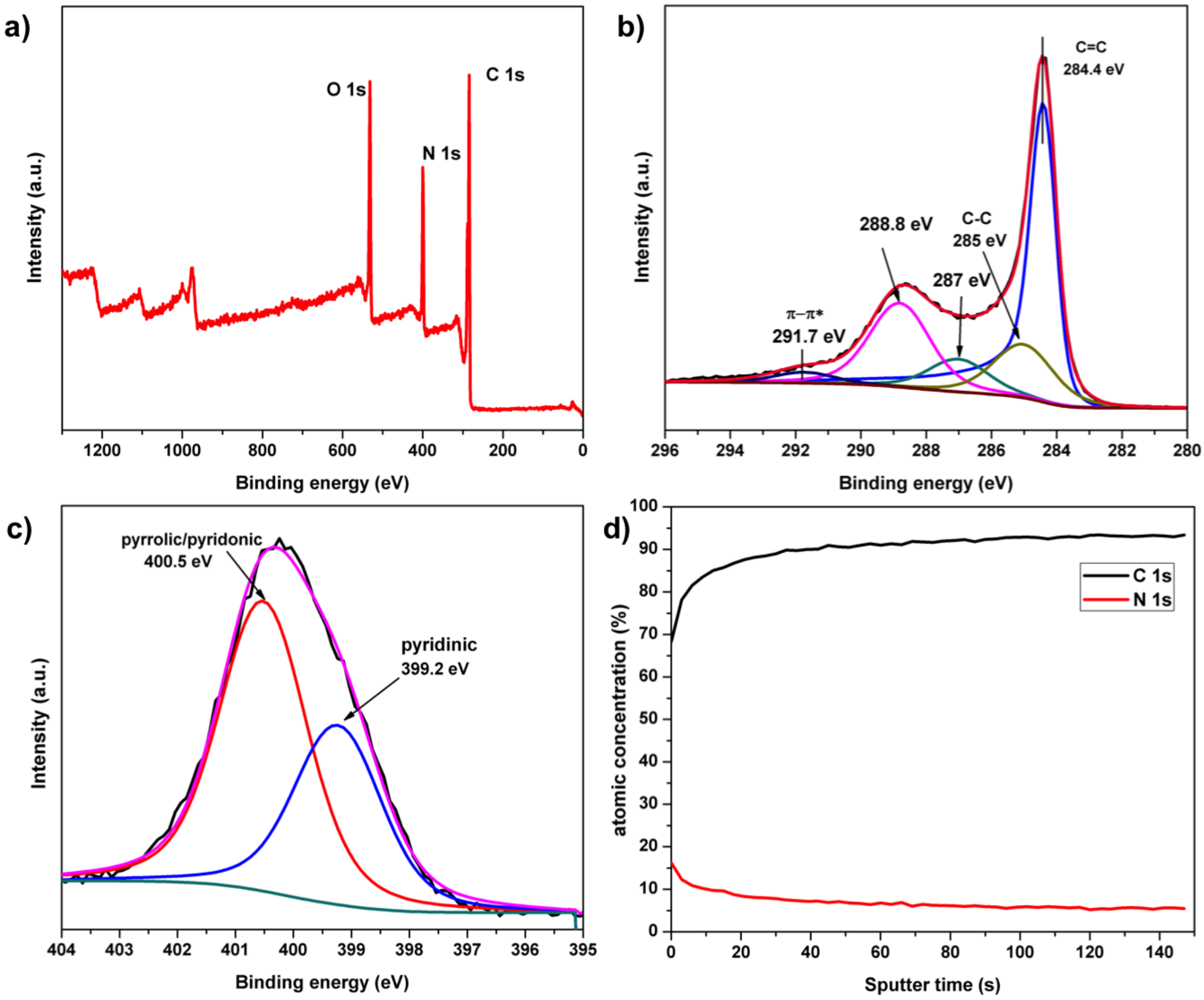

Figure 5.15: XPS spectra of 60 min N_2 plasma functionalized CNTs a) Survey spectrum b) high resolution C 1s spectrum c) high resolution N 1s spectrum d) XPS depth profile measurement.

characteristics over a wide pressure range, high pressure CO_2 adsorption measurements were carried out on N_2 plasma functionalized CNTs. In figure 5.16b the adsorption isotherm at 30 °C of N_2 plasma functionalized CNTs is compared with the adsorption isotherm of as-prepared VACNTs and O_2 plasma functionalized CNTs. Compared with pristine VACNTs, N_2 plasma functionalized CNTs exhibited an enhanced adsorption capacity over the complete pressure regime. A comparison with O_2 plasma functionalized CNTs is intriguing. At low pressures ($P < 10$ bar), O_2 plasma functionalized CNTs have a higher adsorption capacity while at higher pressures, N_2 plasma functionalized CNTs exhibits greater adsorption capability. The exact reason for this behavior is currently not yet clear but one of the contributing factors could be the concentration and distribution of functional groups on the CNT surface. O_2 plasma functionalization led to a much higher concentration of functional groups on the CNT surface than N_2 plasma functionalization (37 at.% compared to 16 at.% for N_2 plasma). This might have resulted in a better adsorption at low relative pressures. However, the prolonged N_2 plasma treatment resulted in a more uniform distribution of functional groups and this is supposed to be the reason for better adsorption at high pressures.

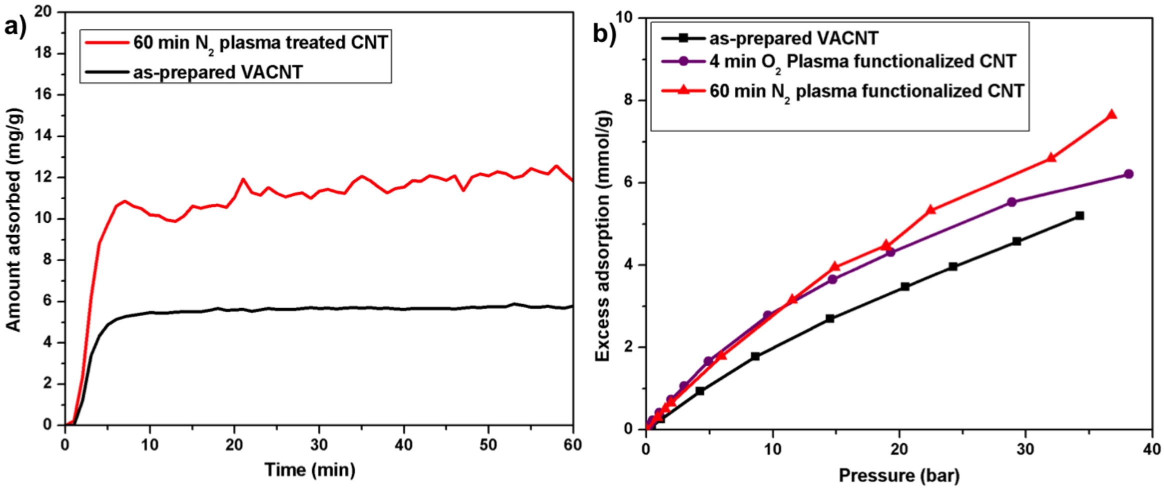

Figure 5.16: CO_2 adsorption results on 60 min N_2 plasma functionalized CNTs at a) ambient pressure and 35 °C b) Comparison of high pressure CO_2 adsorption characteristics at 30 °C of N_2 plasma functionalized CNTs, as-prepared VACNTs and O_2 plasma functionalized CNTs.

To determine the heat of adsorption, CO_2 adsorption isotherms were measured on N_2 plasma functionalized CNTs at three different temperatures of 20 °C, 25 °C and 30 °C as shown in figure 5.17a. The decrease of adsorption capacity with an increase in temperature is typical for a physisorption process. To obtain a more exact picture, these isotherms were used to calculate the isosteric heat of adsorption according to the method of Czepirski et al. [308] and Sun et al. [309]. The isotherms were first fitted using a virial type equation [308] given by:

$$\ln(P) = \frac{1}{T}\sum_{i=0}^{l1} a_i n^i + \sum_{i=0}^{l2} b_i n^i + \ln(n) \tag{5.12}$$

where n is the amount adsorbed at pressure P and temperature T. a_i and b_i are empirical parameters. The equation was fitted using least square fit method and the best fit was obtained for

$l1 = 3$ and $l2 = 3$. The best fit obtained is shown in figure 5.17b. From these parameters the isosteric heat of adsorption was calculated using the relation:

$$Q_{st} = -R \sum_{i=0}^{l1} a_i n^i \tag{5.13}$$

where R is the universal gas constant.

The heat of adsorption thus obtained is plotted as a function of loading in the inset of figure 5.17b. The calculated heat of adsorption value of 19.5 kJ $\mathrm{mol^{-1}}$ at 0.5 mmol $\mathrm{g^{-1}}$ of CO_2 loading, clearly indicates a physisorption process. The low heat of adsorption value is also a clear indication of the absence of other type of nitrogen functional groups like amine, which typically lead to CO_2 chemisorption accompanied by a high heat of adsorption.

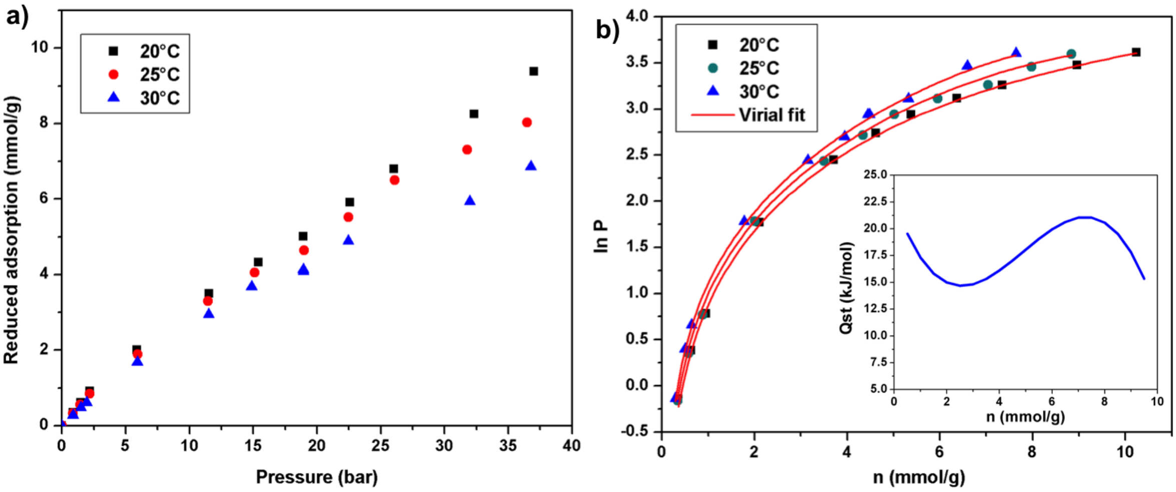

Figure 5.17: a) CO_2 adsorption isotherms of N_2 plasma functionalized CNTs at 20 °C, 25 °C and 30 °C. b) Virial fit of adsorption isotherms measured at the three different temperatures. Inset shows the calculated heat of adsorption as a function of loading.

From the calculated heat of adsorption value, it is clear that the addition of pyridinic and pyrrolic/pyridonic nitrogen groups leads to a reversible CO_2 interaction. In addition, the mild nature of the N_2 plasma is advantageous for obtaining a more uniform functionalization which enhances the adsorption characteristics at high pressures. In the next section, the effect of adding Ar gas to a N_2 plasma system is discussed in detail.

5.5.2 Comparison between N_2 plasma and N_2/Ar gas mixture plasma

Nitrogen dissociation efficiency in an rf plasma is low compared with microwave activated plasma [310]. It is known that addition of an easily dissociable gas like Ar can significantly increase the dissociation efficiency of the N_2 plasma [301, 311–313]. To study the effect of Ar addition on functionalizing CNTs and its influence on gas adsorption characteristics, adsorption studies were carried out on VACNTs subjected to 10 min of N_2/Ar gas mixture plasma functionalization. The results obtained are compared with the adsorption properties of 10 min N_2 plasma functionalized VACNTs.

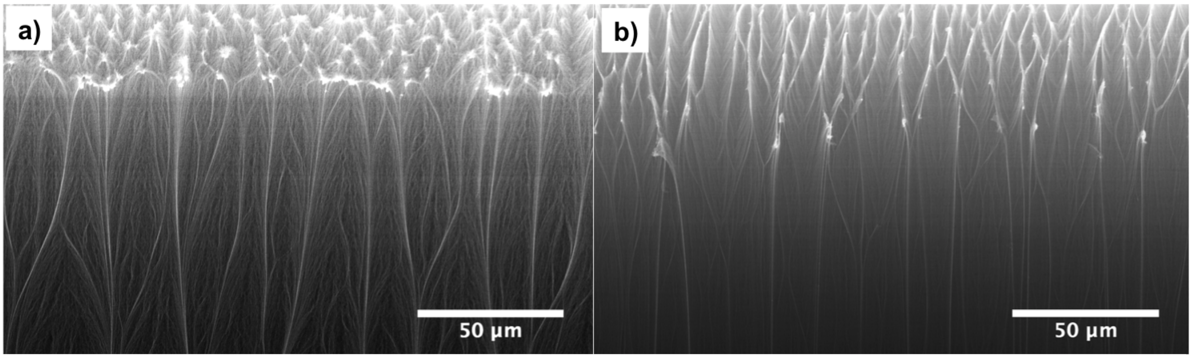

Figure 5.18: SEM images of a) N_2 plasma and b) N_2/Ar gas mixture plasma treated VACNTs for 10 min.

For both set of samples, plasma functionalization was carried out at 20 % power for 10 min at a chamber pressure of ~0.8 mbar. In the case of N_2/Ar plasma, the ratio of flow rate of N_2 to Ar was set to about 1:3. SEM images of the plasma functionalized CNTs are shown in figure 5.18. In both samples, almost similar morphological changes are observed after 10 min of plasma functionalization. Typical changes in the morphology after plasma functionalization like agglomeration of the tips, are observed but the vertical alignment is found to be intact in both cases. However weight measurements before and after functionalization indicated a greater weight loss for N_2/Ar plasma treated CNTs. This can be attributed to the pronounced increase in etching effect with the addition of Ar gas.

Raman measurements confirmed the strong effect of the N_2/Ar gas mixture plasma on CNT etching compared to the N_2 plasma. As shown in figure 5.19a, I_D/I_G ratio showed only a mild increase from 0.64 to 0.71 for N_2 plasma treated CNTs where as for N_2/Ar plasma treated CNTs, the ratio increased considerably to 0.91. Consistent with the weight loss measurements, addition

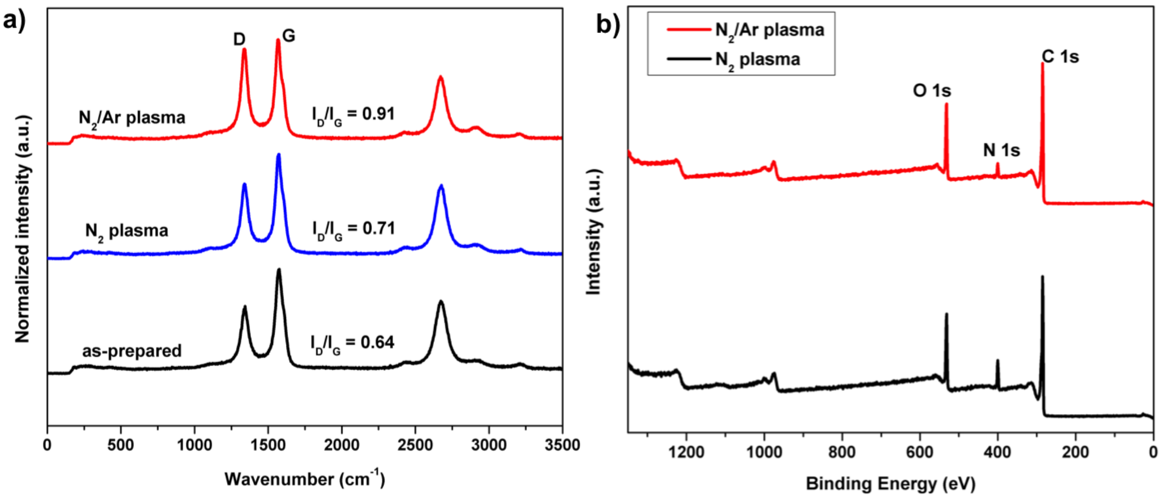

Figure 5.19: a) Raman spectra of as-prepared VACNTs, N_2 plasma treated CNTs and N_2/Ar gas mixture plasma treated CNTs b) Survey spectra of N_2 plasma and N_2/Ar gas mixture plasma treated CNTs.

of Ar gas leads to an increased etching of CNTs and is believed to be the reason for the higher amount of defects observed.

XPS studies were carried out on both N_2 plasma and N_2/Ar plasma functionalized CNTs and the survey spectra is plotted in figure 5.19b. A clear N 1s peak is observed in both cases confirming the successful incorporation of nitrogen by 10 min of plasma treatment. A quantitative analysis however revealed a higher nitrogen concentration for N_2 plasma treated CNTs (~7.87 %) compared with N_2/Ar plasma treatment (~4.25 %) indicating that increasing the dissociation efficiency by adding Ar did not lead to a higher amount of nitrogen incorporation. It should also be noted that the ratio of N_2 to Ar flow rates was 1:3 and the low concentration of N_2 in the gas mixture may also be the reason for the observed lower amount of incorporation.

To obtain a more detailed picture regarding the nature of functionalization, high resolution C 1s and N 1s spectra of both the samples were recorded. Deconvolution of the C 1s spectra (figure 5.20a,b) indicated a higher amount of sp^3 carbon type for N_2/Ar plasma treated CNTs (5.94 %) compared with N_2 plasma treated CNTs (2.2 %). This is in line with the higher defect concentration observed in the Raman spectrum of N_2/Ar plasma treated CNTs. Deconvolution of the N 1s spectrum indicated the presence of pyrrolic/pyridonic type nitrogen functionalities for N_2 plasma treated CNTs (figure 5.20c) while the addition of Ar led to the incorporation of a minor amount of graphitic nitrogen (0.58 %) in addition to the pyrrolic/pyridonic group as shown

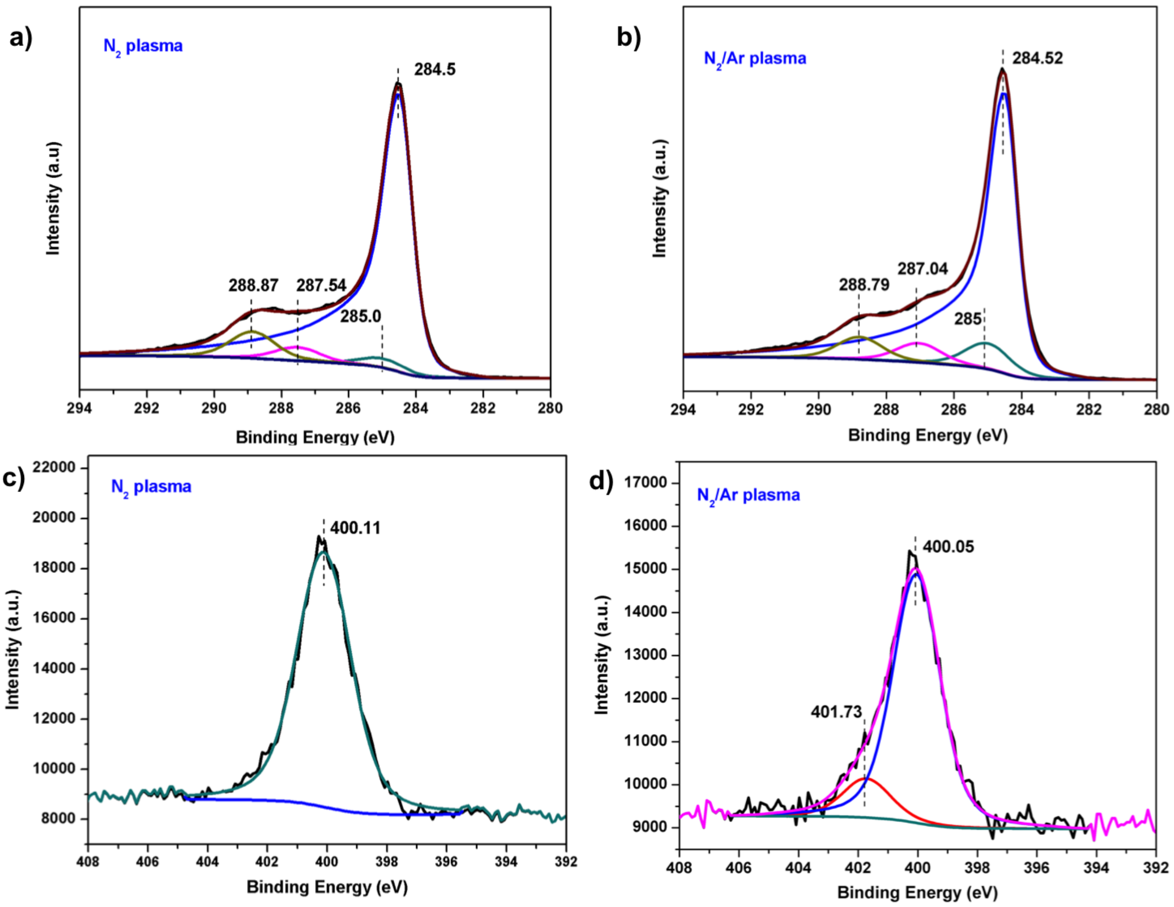

Figure 5.20: High resolution C 1s spectra of a) N_2 plasma treated CNTs b) N_2/Ar gas mixture plasma treated CNTs. High resolution N 1s spectra of c) N_2 plasma treated CNTs d) N_2/Ar gas mixture plasma treated CNTs.

in figure 5.20d. Graphitic nitrogen is supposed to be the result of incorporation of nitrogen in the newly created defects formed by the addition of Ar gas.

Ambient pressure gas adsorption studies were carried out on 10 min N_2 plasma treated CNTs as well as on N_2/Ar gas mixture plasma treated CNTs to ascertain the influence of Ar addition on the gas adsorption characteristics. As shown in figure 5.21, 10 min of N_2 plasma treatment, led to an increase in CO_2 adsorption capacity from 5.6 mg g^{-1} to 7.9 mg g^{-1}. With the addition on Ar in the N_2 plasma system, the functionalized CNTs exhibited an enhanced adsorption capacity of 8.8 mg g^{-1} at 35 °C. It is interesting to note that though the N_2 plasma treated CNTs have a higher nitrogen content, the adsorption capacity is found to be lower than that of N_2/Ar plasma functionalized CNTs. This indicates that the CO_2 adsorption capacity is not directly proportional to the nitrogen content. The combined effect of incorporated nitrogen groups as well as the

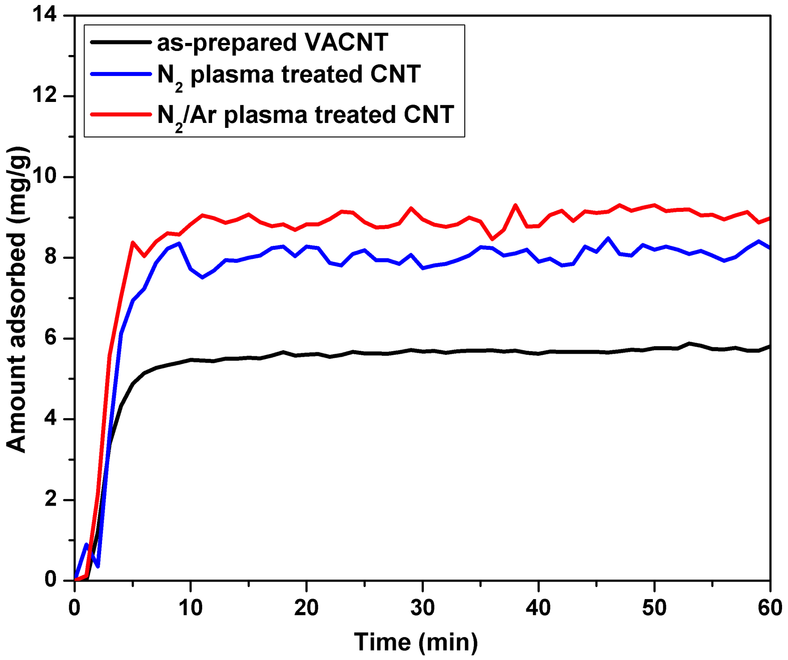

Figure 5.21: Ambient pressure CO_2 adsorption studies on N_2 plasma and N_2/Ar gas mixture plasma treated VACNTs.

presence of newly introduced defects in the CNT structure is assumed to be the reason for the higher CO_2 adsorption capacity observed for N_2/Ar gas mixture plasma functionalized CNTs.

5.6 CO_2 rf plasma functionalization of VACNTs

Oxygen plasma functionalization as a successful route for functionalizing VACNTs without destroying their vertical alignment was already described in detail in section 5.3. One major disadvantage with O_2 plasma is its highly reactive nature leading to almost complete consumption of CNTs within a few minutes. Raman studies have also shown O_2 plasma functionalization leads to large defect density within the first few seconds of plasma exposure. This leaves only a narrow operating window for an O_2 plasma functionalization of CNTs. Addition of an inert gas like Ar or He does not decrease the etching rate, on the contrary, the addition further aggravates the plasma process by creation of more reactive species [270, 314].

Compared with O_2, CO_2 offers a mild oxidizing atmosphere and may represent a valuable alternative. The mild nature of CO_2 gas indeed is helpful in the physical activation of adsorbents for the development of micropores [6, 236, 315]. However, the effect of CO_2 plasma on CNTs is so far largely unexplored. Consequently the feasibility of CO_2 plasma as an alternative for O_2 plasma functionalization was explored during the course of this work.

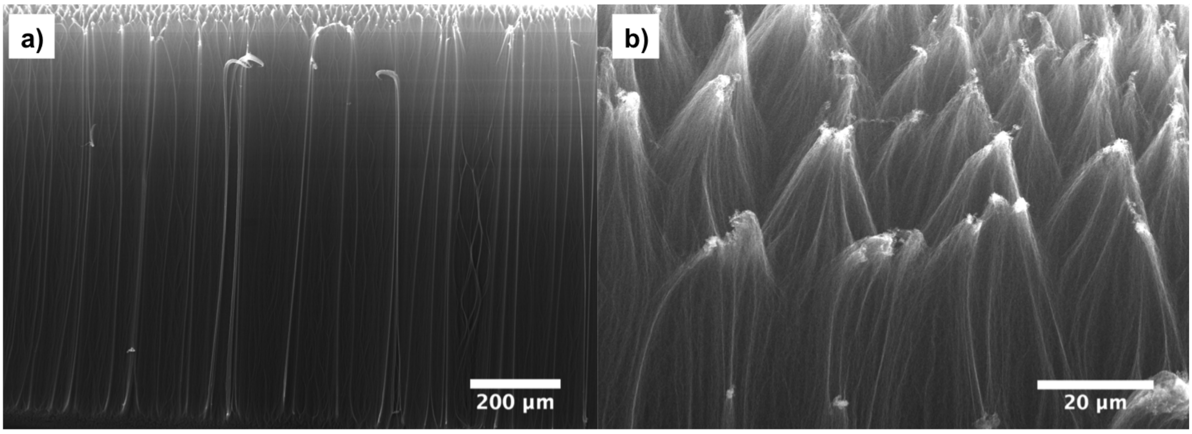

Figure 5.22: SEM image of 10 min CO_2 plasma functionalized VACNTs a) side view showing the intact vertical alignment after functionalization b) top view showing the typical agglomeration of the top surface.

VACNTs were subjected to CO_2 plasma functionalization at 20 % power and at a chamber pressure of 0.52 mbar for a plasma treatment time up to 10 min. Even after 10 min of plasma functionalization, negligible weight loss was observed. An SEM image VACNTs after subjecting to 10 min of CO_2 plasma functionalization is shown in figure 5.22. Though the top surface displayed the typical agglomeration observed in plasma functionalization, the vertical alignment is found to be intact even after 10 min of functionalization.

XPS survey spectra of VACNTs subjected to different duration of plasma exposure is shown in figure 5.23a. Quantitative XPS analysis of 4 min functionalized VACNTs indicated an oxygen atomic concentration of ~37.5 % on the surface. This is remarkably similar to the functionalization obtained by O_2 plasma (section 5.3.4). In addition, the VACNTs exposed to still longer treatment time of 8 min and 10 min also showed similar surface O_2 concentration. This indicates a saturation of surface oxygen groups by plasma treatment at a concentration of ~38 at %. Zhao et al. [280] also observed a similar maximum in oxygen concentration after subjecting the VACNTs to an rf O_2/Ar plasma treatment.

For a detailed analysis of the nature of functionalization, the high resolution C 1s spectrum of 10 min plasma functionalized VACNTs is deconvoluted as shown in figure 5.23b. The C 1s photoelectron spectrum is fitted by four components corresponding to C=C at 284.1 eV, C-C at 285 eV, C-O at 286.6 eV and O-C=O at 288.6 eV. The C 1s spectrum and the distribution of functional groups is strikingly similar to O_2 plasma functionalized CNTs indicating that CO_2 plasma, though much milder, is as effective as O_2 plasma in functionalizing VACNTs.

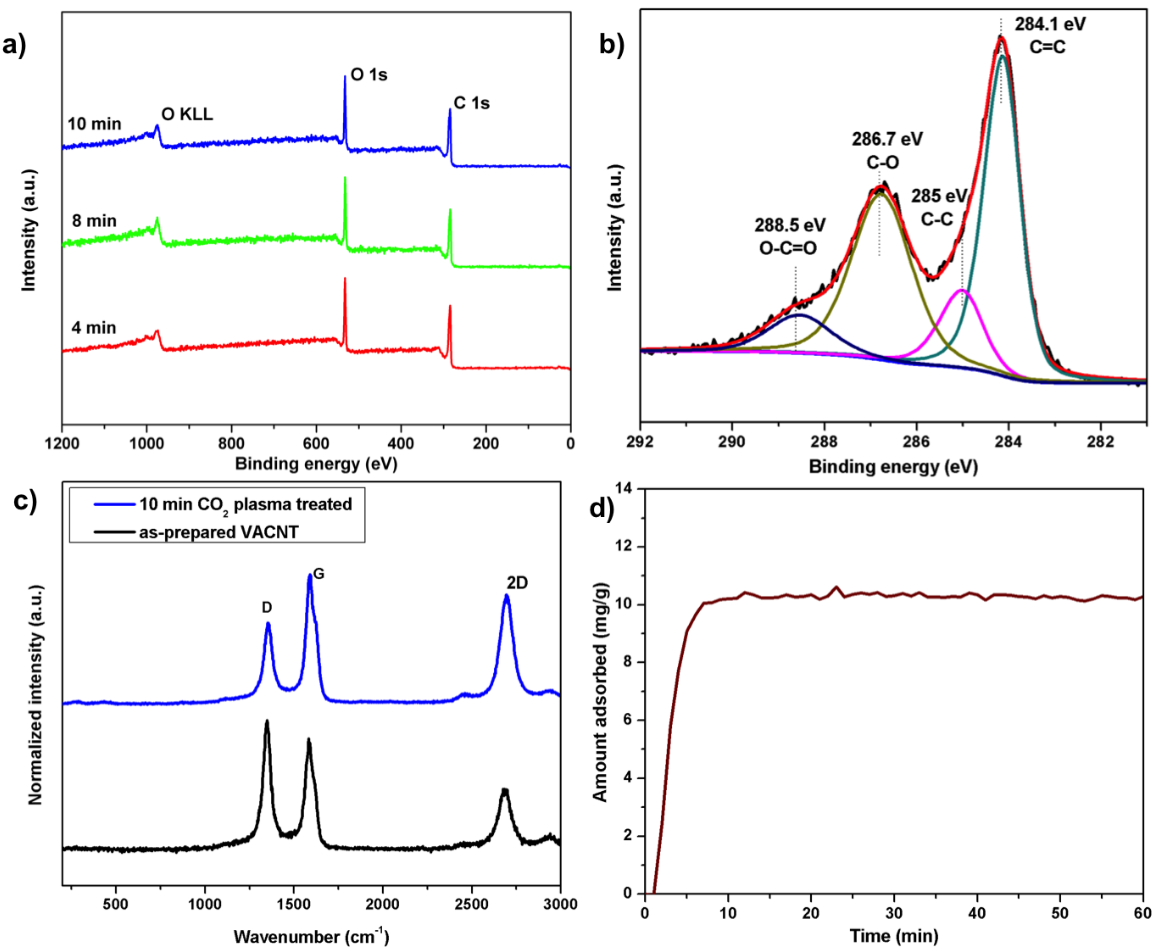

Figure 5.23: a) XPS survey spectra of VACNTs subjected to different duration of CO_2 plasma exposure b) High resolution C 1s spectra of 10 min CO_2 plasma treated CNTs c) Raman spectra of VACNTs before and after 10 min of CO_2 plasma treatment d) Ambient pressure CO_2 adsorption on 10 min CO_2 plasma functionalized VACNTs.

Raman measurements on CO_2 plasma functionalized CNTs however revealed a different behavior. As shown in figure 5.23c, the D-band intensity decreased significantly after 10 min of plasma functionalization. This is in stark contrast with an O_2 plasma treatment where the D-band intensity increases considerably even after a few seconds of plasma treatment. The decrease in D-band intensity after CO_2 plasma functionalization indicates the lower amount of defects induced by the plasma treatment and the overall improvement in the crystallinity of the CNTs.

To investigate the influence of CO_2 plasma functionalization on the gas adsorption characteristics of CNTs, ambient pressure CO_2 adsorption measurements were carried out on CNT samples which were treated for 10 min in a CO_2 plasma. As shown in figure 5.23d, the functionalized VACNTs exhibited an adsorption capacity of 10.29 mg g^{-1} slightly lower than that of O_2 plasma functionalized CNTs (12.6 mg g^{-1}) but higher than that of as-prepared VACNTs (5.6 mg g^{-1}). Defect sites in CNTs are known to be high energy sites for gas adsorption [51, 316]; therefore an increase in defect density, as observed in an O_2 plasma functionalized CNTs, should lead to a higher adsorption. Since the extent of functionalization obtained is similar for both CO_2 and O_2 plasma, the slightly lower adsorption capacity for CO_2 plasma functionalized CNTs can be attributed to the lower defect density produced in a CO_2 plasma.

5.6.1 Purifying nature of CO_2 plasma

To investigate in detail the effect of CO_2 plasma on VACNTs, Raman measurements were carried out on CO_2 plasma treated CNTs subjected to different duration of plasma exposure. As shown in figure 5.24a, the D-band intensity decreased with an increase in plasma exposure time while the 2D band intensity displayed an increase in intensity. To obtain a more detailed picture, the ratio of I_D/I_G and I_{2D}/I_G is plotted as a function of time in figure 5.24b. The defect density given by I_D/I_G ratio decreased with plasma treatment up to an exposure time of 4 min, thereafter it displayed a slight increase. The behavior of I_{2D}/I_G ratio was complimentary to that of I_D/I_G and showed an increase till 4 min of treatment time. Okpalugo et al. [269] have reported that the I_{2D}/I_G ratio may be regarded as a measure of crystallinity of CNTs. The observed decrease in the I_D/I_G ratio and simultaneous increase in I_{2D}/I_G ratio is assumed to be the result of removal of disordered amorphous carbon phase. Compared to crystalline CNTs, amorphous carbons are more reactive due to presence of high defect density [317]. The resulting difference in oxidation rate of amorphous carbon and CNTs, allows a selective removal of the amorphous carbon phase. The same can also happen in an O_2 plasma, however the highly reactive nature of O_2 plasma hampers the selective oxidation resulting in removal of crystalline CNT phase as well. It should be noted that the observed significant decrease in defect ratio is unique for CO_2 plasma and almost all of the commonly employed plasma treatment process like O_2 [270, 280, 318] N_2 [282, 311], Ar [282], air [319], CF_4 [320, 321], NH_3 [322], H_2 [323] or H_2O [324] lead to an increase in the defect ratio.

For a plasma treatment time greater than 4 min, an increase in the defect concentration is observed. This is assumed to be due to the slow etching of CNT walls after most of the amorphous carbons are etched away. This assumption is validated by the observed decrease in the I_{2D}/I_G ratio indicating a decrease in the crystallinity. Etching of the CNT walls leads to the formation of new amorphous like carbon phase, which are subsequently purified upon longer exposure times. This explains the observed increase followed by the decrease of the I_D/I_G ratio. VACNTs exposed to plasma for t > 10 min also displayed the same trend of increase and then decrease of defect concentration.

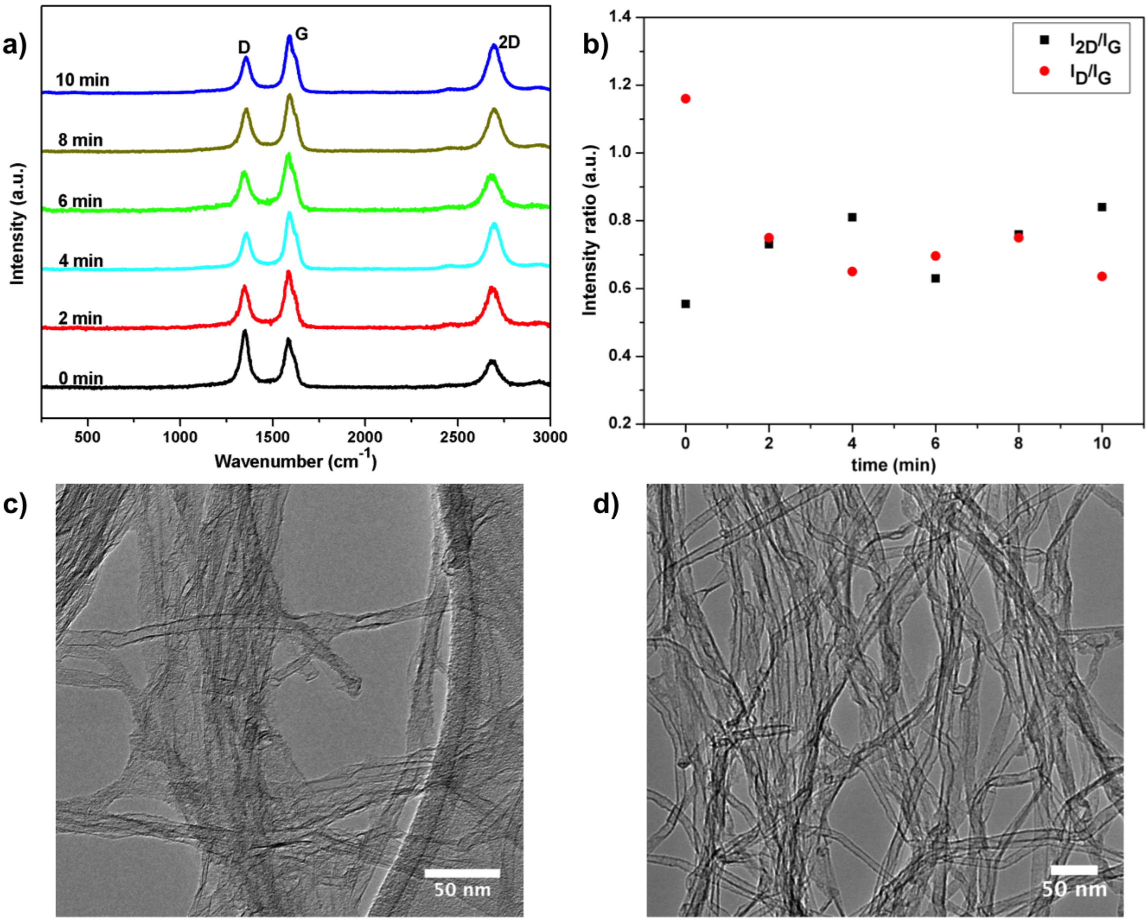

Figure 5.24: a) Raman spectra of VACNTs subjected to different duration of plasma treatment b) Plot of I_D/I_G and I_{2D}/I_G as a function of CO_2 plasma exposure time c) TEM image as-prepared VACNTs d) TEM image of CNTs after 10 min of CO_2 plasma treatment.

The mild purifying nature of CO_2 plasma is substantiated with TEM measurements before and after plasma treatment as shown in figure 5.24c,d. Compared to the as-synthesized CNTs, the amount of amorphous carbon is significantly reduced after 10 min of CO_2 plasma exposure.

The mechanism for the observed unique purification property of CO_2 plasma can be explained as follows. Each plasma process is quite complex and a variety of different reactive species like neutral molecules, ions, free radicals etc. are generated in a plasma. However it is known that the free radical chemistry process is the dominant mechanism in plasma functionalization [325]. In oxygen plasma, for example, oxygen radicals are the most prominent and reactive species [245, 259, 280]. The large density of these oxygen radicals produced in a typical O_2 rf plasma, attacks not only the amorphous carbon but also the CNT walls leading to the creation of defects. This structural deterioration of CNTs is reflected in the high intensity of D-band in the Raman spectrum of O_2 plasma functionalized CNTs. However, in CO_2 plasma, a large fraction of the oxygen radicals are quenched due to the reaction [326, 327] $CO_2 + O^{\cdot} \rightarrow CO + O_2$. This is a plasma activated process and thus the deteriorating effect of reactive oxygen species is neutralized to a large extend in a CO_2 plasma. The lower density of the reactive oxygen species in a CO_2 plasma leads to a preferential removal of highly defective, unordered amorphous carbon phase compared to the more stable graphitic structures present in CNTs. Similar decrease in plasma activity and enhanced preferential reactivity was also reported for CH_4 plasma [328].

The influence of other plasma parameters like chamber pressure and plasma power was also systematically studied. Consistent with the reports on other plasma systems [279, 280, 284], increasing the chamber pressure as well as power led to an increase in the defects induced due to the accelerated physical and chemical effects produced by the plasma, more details of which could be found in the published work [329].

5.7 CF_4 rf plasma functionalization of VACNTs

Apart from O_2, N_2 and CO_2 plasma functionalization, fluorination of VACNTs were also carried out by treating VACNTs with CF_4 plasma. To compare with O_2 plasma functionalized CNTs, similar plasma parameters were chosen for CF_4 plasma. VACNTs were subjected to 4 min of CF_4 plasma at 30 % power and at a chamber pressure of 0.8 mbar. Weight measurements before and after indicated minimal weight loss after CF_4 plasma functionalization. SEM images of VACNTs after 4 min of functionalization is shown in figure 5.25a. No extensive agglomeration or significant changes in surface morphology are observed in SEM. Raman measurements however revealed a steep increase in the defect concentration after functionalization with CF_4 plasma consistent with the previous reports on CF_4 plasma functionalization of CNTs [321, 330]. The I_D/I_G ratio increased from 0.81 to 1.57 after 4 min of functionalization as shown in figure 5.25b.

XPS survey spectrum of CF_4 functionalized CNTs (figure 5.26a) revealed a strong peak at ~687 eV corresponding to photoelectrons emitted from F 1s core level. The presence of oxygen is attributed to the residual oxygen in the plasma treatment chamber. The appearance of a distinct peak at higher binding energies in the high resolution C 1s spectrum shown in figure 5.26b indicates fluorine atoms bonded to carbon. The exact assignment is complicated by the presence of C 1s

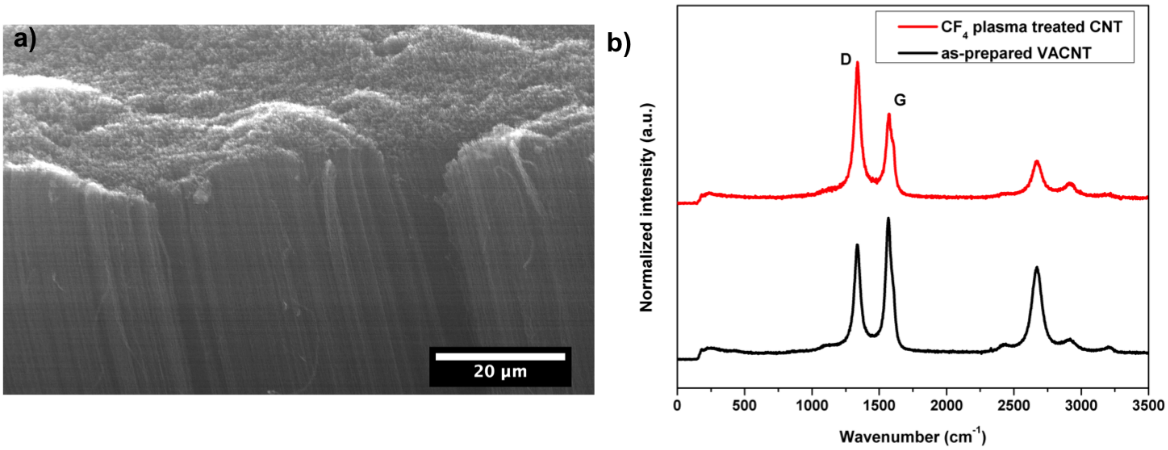

Figure 5.25: a) SEM image and b) Raman spectra of CF_4 plasma functionalized VACNTs.

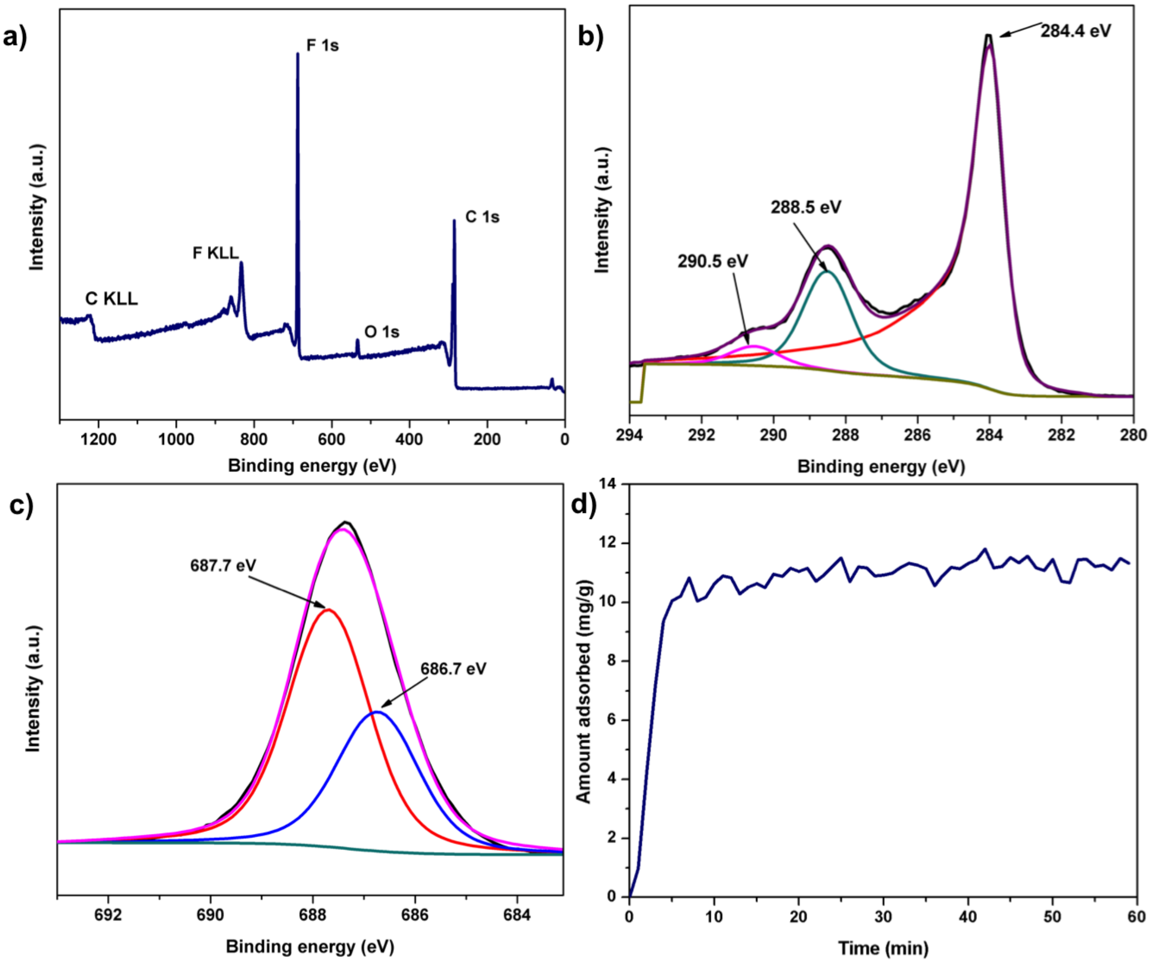

Figure 5.26: XPS measurement of 4 min CF_4 plasma functionalized VACNTs a) Survey spectrum b) high resolution C 1s spectrum c) high resolution F 1s spectrum d) Ambient pressure CO_2 adsorption on the CF_4 plasma functionalized CNTs.

satellite structure caused by the energy losses on excitation of plasmon oscillation of π electrons [331].High resolution F 1s spectrum revealed a broad peak centered at ~687.4 eV as shown in figure 5.26c. The broad F 1s peak was deconvoluted into 2 peaks at 687.7 eV and 686.7 eV. The peak at ~687.7 eV is generally assigned to the C-F bonding with a predominant covalent nature [320, 332] while the peak at lower binding energy is assigned to semi-ionic C-F bonding [331, 332]. Quantitative XPS analysis indicated a total fluorine concentration of 27.08 at % on the CNT surface with the covalent C-F bond accounting for almost 17 at %.

Ambient pressure CO_2 adsorption measurements on CF_4 plasma treated CNTs indicated an adsorption capacity of 11.05 mg g^{-1} as shown in figure 5.26d. The adsorption capacity of VACNTs subjected to CF_4 plasma functionalization is comparable with the O_2 plasma functionalized CNTs. It should be noted that under the optimized conditions, 4 min of plasma treatment lead to ~38 at % of oxygen functional groups on the CNT surface while under the same plasma treatment conditions, CF_4 plasma treatment grafted ~27 at % of fluorine groups. The plasma parameters for CF_4 functionalization were not optimized and still the adsorption capacity obtained was comparable to the O_2 plasma functionalized CNTs. High adsorption capacity and the negligible weight loss during plasma treatment, make CF_4 plasma treatment of VACNTs a promising functionalization strategy for future gas adsorption studies.

5.8 Comparison with acid vapor treatment

Besides plasma treatment, few other gas phase functionalization methods are reported for functionalizing CNTs without destroying its alignment. These include acid/base vapor treatment [247, 249, 333, 334], ozone/UV treatment [250–252, 335], annealing in a reactive atmosphere [256–258, 336], ion irradiation [337–341] etc. In the present work, an attempt was also made to functionalize CNTs by the acid vapor treatment in line with the work of Xia et al. [247].

A schematic of the setup used to carry out acid vapor functionalization of VACNTs is shown in figure 5.27a. About 100 ml of nitric acid (65 %) was taken in the 250 ml round bottomed flask and was slowly heated to its boiling point. VACNTs peeled off from the substrate were placed in the side bulb as shown in the figure 5.27a. To prevent the condensation of acid vapors on VACNTs, the side bulb was heated to 200 °C using a separate heating band. As the acid vapor passes through the condenser placed right above the round bottomed flask, it condenses and falls back into the flask.

Experiments were performed, at first, for $t > 10$ h with CNTs kept at ~200 °C. However, CNTs were completely consumed in the process. Subsequently functionalization was carried out

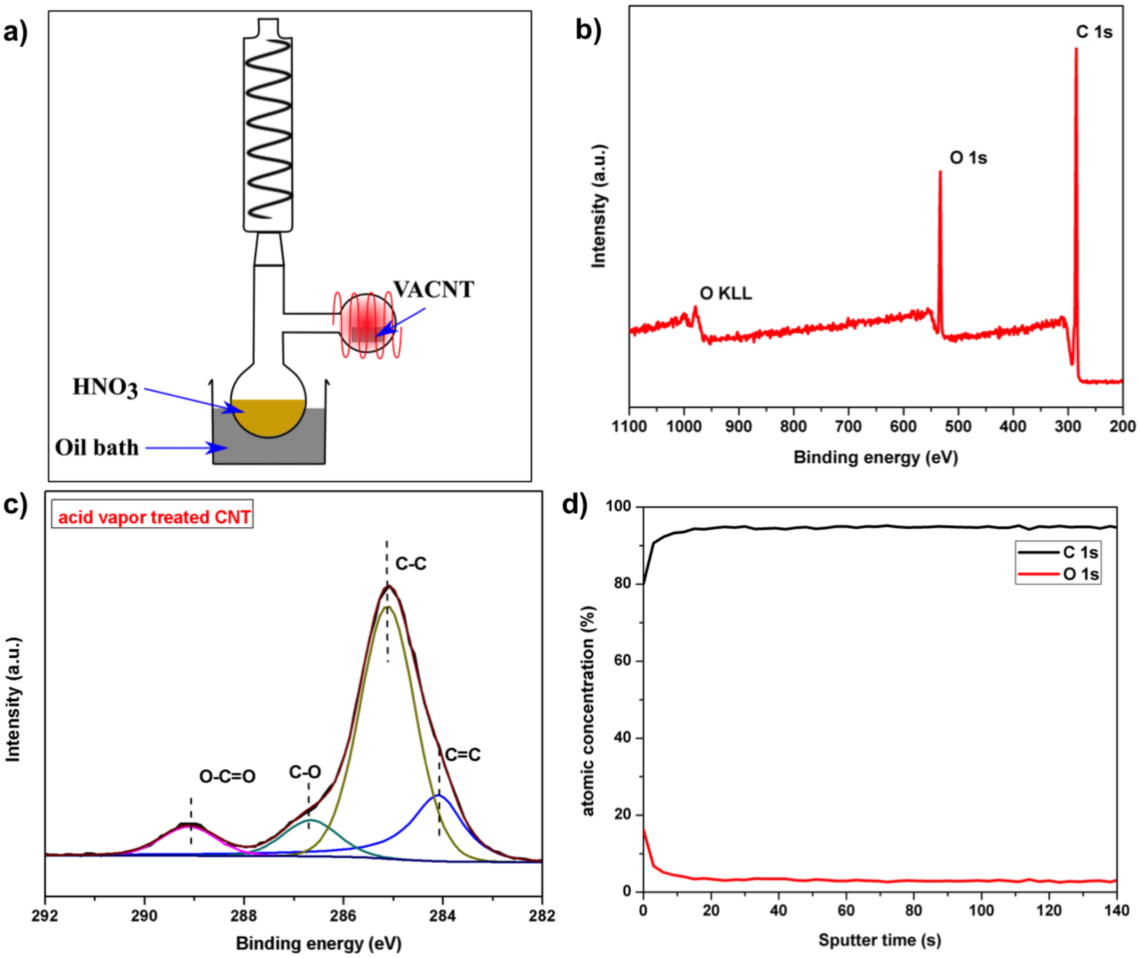

Figure 5.27: a) Schematic of the experimental setup for acid vapor treatment of VACNTs. XPS characterization of VACNTs subjected to 2 h of acid vapor treatment at 160 °C b) Survey spectrum c) deconvoluted high resolution C 1s spectrum d) XPS depth profile measurement.

at milder conditions for 2 h at 160 °C. Small amount of CNTs recovered after the treatment were subjected to XPS measurement to determine the type and extent of functionalization. The prominent O 1s peak in XPS survey spectrum shown in figure 5.27b indicates the grafting of oxygen functional groups onto CNT surface. To obtain a clear picture regarding the nature of functional groups, C 1s spectrum of acid vapor treated CNTs were recorded. Deconvolution of the C 1s spectrum (figure 5.27c) revealed a large increase in the concentration of C-C sp^3 type carbon and a significant decrease in the C=C sp^2 type carbon after acid vapor treatment indicating extensive damages to CNT structure. While oxygen plasma treatment lead to a majority of C-O groups, acid vapor functionalization generates almost equal amount of O-C=O and C-O groups. Quantitative analysis indicated an oxygen concentration of ~21 at % on the CNT surface. To determine whether these functionalities were uniformly distributed along the CNT array, XPS sputter depth profile measurements were performed on the acid vapor treated VACNTs. As shown in figure 5.27d, oxygen concentration decreased rapidly to less than 4 at % after few seconds of sputtering indicating the functionalization obtained is more concentrated on the surface.

Though the experimental conditions were not optimized, compared with plasma functionalization of VACNTs, acid vapor treatment did not offer any major advantages for functionalizing vertically aligned structures. On the contrary, acid vapor treatment revealed to inflict serious damages to CNT structure and more interestingly, even after 2 h of treatment, the functionalization was found to be limited to the surface.

5.9 Concluding remarks

In conclusion, plasma treatment was found to be a versatile technique for functionalizing VACNTs without compromising its alignment. Oxygen plasma, though reactive, is quite efficient in grafting a large amount of functional groups on CNT surface. The mild nature of nitrogen plasma is advantageous for obtaining a more uniform functionalization by prolonged plasma exposure. Addition of Ar to N_2 plasma, led to the creation of more defects. CO_2 plasma was found to be a versatile technique not only for functionalizing CNT arrays but also for removing amorphous type carbon from the vertically aligned 3D structures. CF_4 plasma functionalization was found to be an excellent alternative to O_2 plasma, to functionalize CNT structures without much weight loss. Finally, compared with plasma treatment, acid vapor treatment did not lead to any tangible benefits in terms of amount and uniformity of functional groups grafted to CNT surface.

6 Adsorption on Other Carbon Adsorbents

In this chapter, the adsorption characteristics of certain other carbon based adsorbents like carbon nanohorns and graphene oxide are studied. The adsorption properties of these adsorbents are compared with the adsorption characteristics of VACNTs, zeolites and metal organic frameworks.

6.1 Carbon nanohorns

Carbon nanohorns (CNHs) are sheaths of graphene with a closed cone tip at one end and they usually exist as aggregates of 50–100 nm in diameter [342, 343]. A schematic of a typical carbon nanohorn aggregate is shown in figure 6.1. The aggregate structure, with the cone tips protruding out, resembles a dahlia flower. Though the first report of such typical cone shaped hollow carbon tubes already appeared in 1994 [344], the first systematic investigation, production and isolation was carried out by Iijima et al. in 1999 [345]. Synthesis of CNHs does not require a metal catalyst and is typically produced by CO_2 laser ablation method [345–347] or sub-merged arc method [348, 349]. The fact that CNHs can be produced in high yield approaching kg/day at a purity of $> 90\,\%$ [350] makes them interesting nanomaterial for many technological applications including energy storage [351, 352] , field emission devices [353, 354], drug delivery [355, 356] etc.

Their carbon framework and tubular structure have already attracted a number of studies on the gas adsorption characteristics of CNHs. The as-prepared CNHs have a closed tip, hence gases cannot access the interior of the tubular structure. However heat treatment in an oxidizing atmosphere is known to open CNHs and significantly enhance the accessible surface area [235, 357]. The interstitial site between two CNHs, with a typical pore width of > 0.4 nm [358] are also attractive sites for gas adsorption. In addition, gases can also be adsorbed in the central region of the CNH aggregate which is found to consist of disordered single layered graphene sheets with an interlayer distance of 0.4–0.5 nm [359]. H_2 adsorption measurements carried out on CNHs, however revealed an adsorption capacity of less than 0.6 wt % at 30 °C [360]. Adsorption of other gases like CH_4 and CO_2 were also explored subsequently [361–363]. For CO_2 adsorption on CNHs, the current investigations are limited to the low temperature and low pressure region [362, 363].

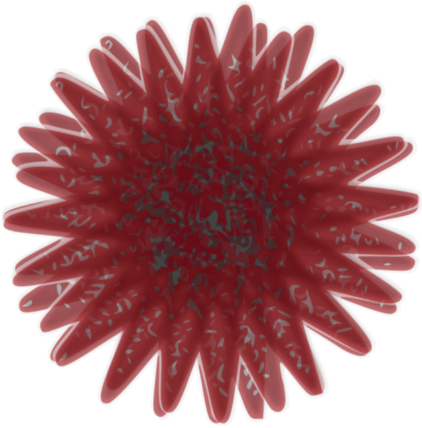

Figure 6.1: Schematic representation of a typical carbon nanohorn aggregate.

6.1.1 Characterization of as-obtained CNHs

Carbon nanohorns (CNHs) were prepared by the arc in water synthesis method under inert gas [364] and were obtained from TIE GmbH, Griesheim, Germany. Since water constitutes 90 % of as-obtained CNH paste (CNH type F), to obtain the CNH powder, the CNHs slurry was dried overnight at 200 °C in air. An SEM image of the as-obtained CNHs shown in figure 6.2a, revealed a largely aggregated structure. TEM image of the as-obtained CNHs (figure 6.2b) indicated a bud-type aggregate structure [342] with few tips protruding out. The high resolution TEM images shown in the figure 6.2c, confirms the presence of cone like tips typical for CNHs.

N_2 adsorption isotherm measurements were carried out at 77 K to determine the specific surface area and porosity of as-obtained CNH powder. As shown in figure 6.2d, the N_2 adsorption isotherm resembles a type-IV(a) isotherm with adsorption hysteresis at high relative pressures. At low relative pressure, due to the adsorption in the microporous interstitials and central aggregate sites, a steep increase in adsorption is observed. The specific surface area of the as-obtained CNH powder is determined to be $202\,m^2\,g^{-1}$. The pore size distribution analysis by NLDFT method (inset of figure 6.2d), reveals no peak in the range 2–5 nm corresponding to the internal diameter of the CNH, confirming that the as-obtained CNHs are indeed closed.

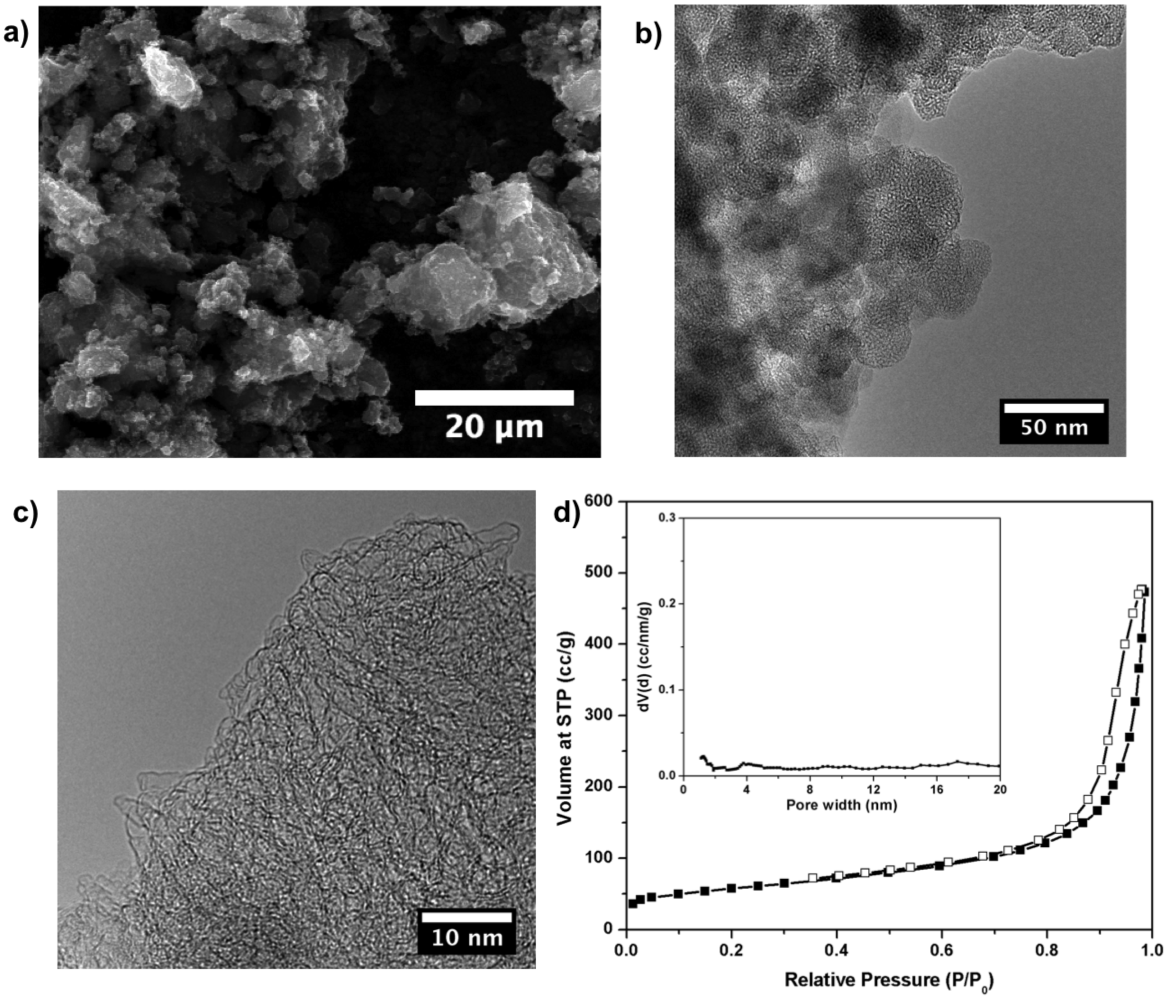

Figure 6.2: a) SEM image of as obtained CNHs b) low magnification TEM image revealing the bud-type aggregate structure of CNHs c) high magnification TEM image confirming the presence of conical tips of CNHs d) N_2 adsorption isotherm of as-obtained CNHs, closed symbols represent adsorption trace and open symbols represent desorption trace. Inset shows the pore size distribution of CNHs by NLDFT analysis.

6.1.2 Opening of CNHs

Heating in an oxidative atmosphere like O_2 [234, 235], air [237] or CO_2 [236] is the most common method employed to open the CNHs. Bekyarova et al. [236] have reported that heating in CO_2 offers better control over the entire pore development process. Accordingly, in the present study, similar to the method employed for opening VACNTs described in section 4.4, CNHs were treated in CO_2 atmosphere in a range of temperature from 500–800 °C and the weight loss observed was recorded. As shown in figure 6.3a, the S-shaped curve obtained, displayed a steep increase in weight loss at a temperature of ~550 °C. For further studies, a treatment temperature of 600 °C was selected so as to obtain a weight loss of 30–40 %.

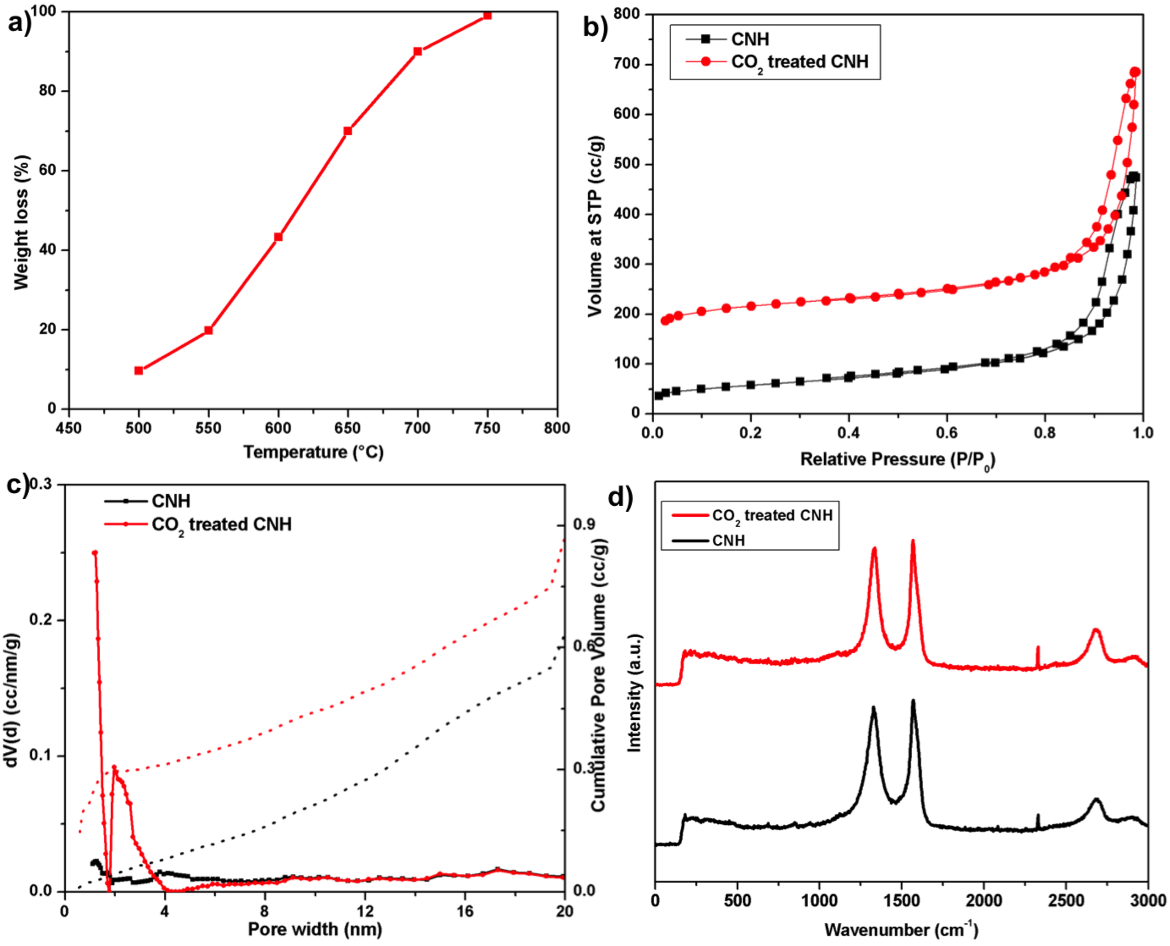

Figure 6.3: a) Weight loss of CNHs in CO_2 atmosphere as a function of temperature b) N_2 adsorption isotherm (at 77 K) comparison of CNHs before and after high temperature CO_2 treatment c) NLDFT pore size distribution of CO_2 treated CNHs confirming the opening of CNHs d) Raman spectrum of CNHs before and after high temperature CO_2 treatment.

N_2 adsorption isotherm at 77 K of CO_2 treated CNHs, displayed a significant increase in adsorption at low relative pressures as shown in figure 6.3b. NLDFT pore size distribution analysis (figure 6.3c) revealed an additional peak at 2–4 nm after the CO_2 treatment, confirming the opening of the CNHs. Consequently the BET surface area displayed an almost four fold increase from 202 $m^2\,g^{-1}$ to 808 $m^2\,g^{-1}$ after the high temperature CO_2 treatment.

Raman spectrum of CNHs before and after high temperature CO_2 treatment is shown in figure 6.3d. The Raman spectra consist of D- and G-band of almost equal intensity. The high intensity of the D-band is an inherent feature of CNHs and arises from the broken symmetry in the cone region due to the presence of the pentagon rings which are necessary to realize the closed structure [365]. Similar to what was observed with VACNTs, the high temperature heat treatment in CO_2 atmosphere did not lead to any noticeable changes in the Raman spectra.

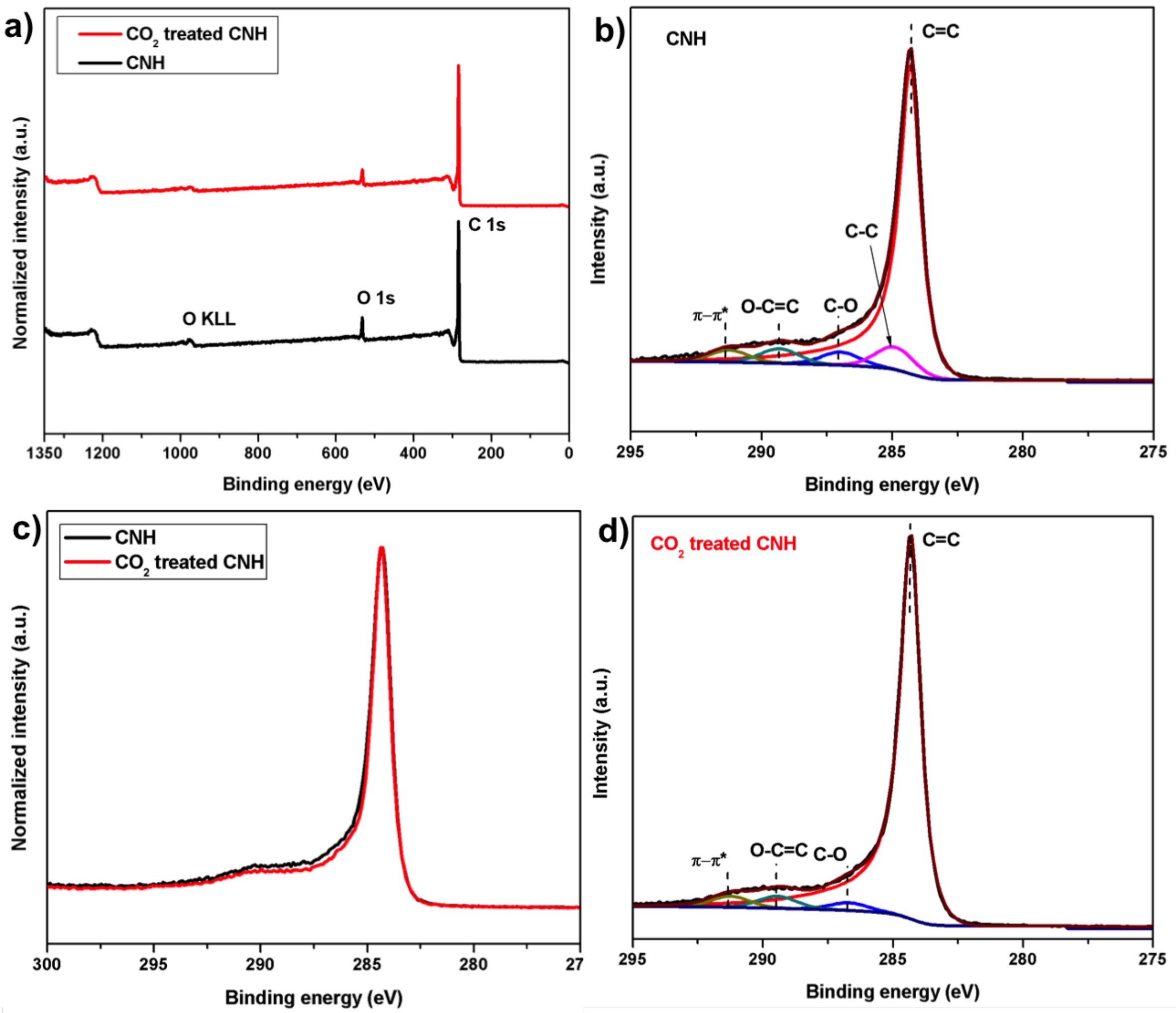

Figure 6.4: XPS measurement of CNHs and CO_2 treated CNHs a) survey spectra b) deconvoluted high resolution C 1s spectrum of CNHs c) superimposed C 1s spectrum of CNHs and CO_2 treated CNHs d) deconvoluted high resolution C 1s spectrum of CO_2 treated CNHs.

To identify the different functional groups on the CNH surface and to probe the changes in chemical nature brought about by the high temperature CO_2 treatment, XPS study was carried out on CNHs and CO_2 treated CNHs. XPS survey spectrum of CNHs, shown in figure 6.4a, consist of peaks arising only from carbon and oxygen, confirming the overall purity of the obtained CNHs. The as-prepared CNHs is known to have some oxygen functionalities tethered to the surface [366, 367] explaining the observation of 5.9 at % of oxygen in the XPS spectrum. The high resolution C 1s spectrum of CNHs shown in figure 6.4b confirms the presence of oxygen functionalities grafted to the CNH surface as C-O and O-C=O. As seen from the survey spectra in figure 6.4a, the high temperature CO_2 treatment did not lead to any significant changes in the chemical nature of CNHs. Quantitative XPS analysis indicated a slight decrease in the oxygen concentration from 5.9 at % to 4.9 at % after the CO_2 treatment. The high temperature of the CO_2 treatment process might have stripped some oxygen functionalities from the CNH surface leading to the observed decrease in the oxygen content. In figure 6.4c, the C 1s spectrum of CNHs before and after CO_2 treatment is superimposed to reveal the minor differences in the C 1s spectra. The deconvoluted C 1s spectrum of CO_2 treated CNHs revealed a decrease in the sp^3 type carbon content below the detectable limits, after the CO_2 treatment at 600 °C.

6.1.3 High pressure CO_2 adsorption measurements

High pressure CO_2 adsorption characteristics of CNHs and CO_2 treated CNHs were investigated at 25 °C up to a pressure of ~40 bar. CO_2 adsorption isotherm of CNHs (figure 6.5a) reveals a steep increase in adsorption at low pressures. This steep increase corresponds to adsorption in the microporous sites of CNHs. Since as-synthesized CNHs have closed tips, the only available adsorption sites are the microporous sites and once these microporous sites are filled, the adsorption eventually levels off at a pressure close to 2 bar. At higher pressures, adsorption further proceeds on the non-porous external surface of the CNHs by a layer by layer mechanism which is indicated by the positive slope in the linear region (3–36 bar) of the adsorption isotherm.

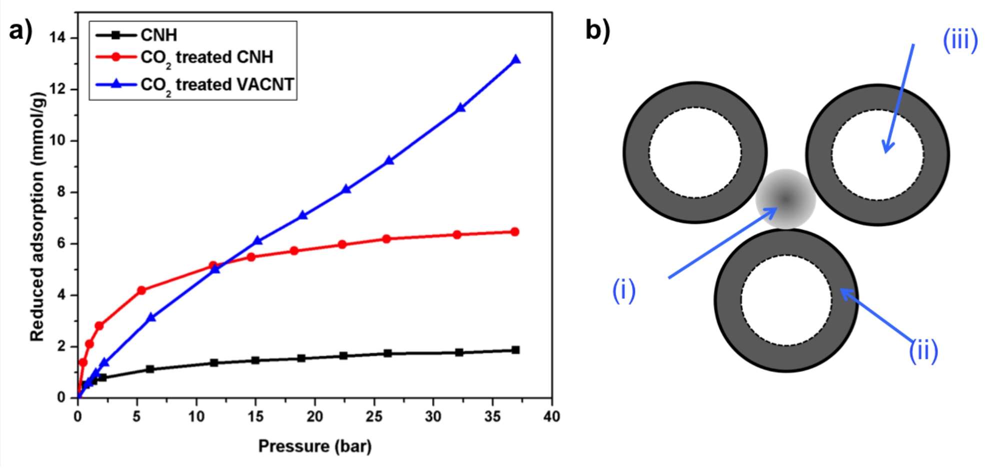

Figure 6.5: a) High pressure CO_2 adsorption characteristics of CNHs and CO_2 treated CNHs. For comparison, CO_2 adsorption on CO_2 treated VACNTs is also provided. b) Schematic of the different adsorption sites in an opened CNH aggregate (i) interstitial sites (ii) intraparticle monolayer surface sites and (iii) intraparticle core sites.

CO_2 adsorption performed on high temperature CO_2 treated CNHs revealed a considerably increased adsorption capacity as compared to untreated CNHs, over the complete pressure regime (figure 6.5a). By analyzing the interaction potentials of the opened CNHs, Murata et al. [357] have shown that opening of CNHs leads to two more possible adsorption sites namely the intraparticle monolayer site and the intraparticle core site (see figure 6.5b). Adsorption in the intraparticle monolayer proceeds in a manner similar to the micropores i.e. by a volume filling mechanism. This explains the much higher increase in the adsorption at lower pressure. The adsorption in the intraparticle core site on the other hand, proceeds by a layer by layer filling mechanism. The combined layer by layer adsorption on the intraparticle core site and the external non-porous site, explains the difference in slope observed in the linear region of the CO_2 treated CNHs and untreated CNHs. By employing the high temperature CO_2 treatment, almost a triple fold increase in CO_2 adsorption capacity is observed for the opened CNHs as compared to the untreated CNHs.

Compared with CNHs, VACNTs have only fewer pores in the micropore regime. Hence a lower amount of CO_2 is adsorbed in the low pressure region for VACNTs (figure 6.5a). However the presence of multiple adsorption sites in VACNTs in the lower mesopore regime (the interior of the tubes or interstitial sites) leads to an almost linear increase in the adsorption with pressure, exhibiting no sign of saturation in the studied pressure range.

6.2 Graphene oxide

Recently graphene oxide has attracted widespread research interest not only as a precursor for graphene synthesis but also due to its own interesting properties like high specific surface area, layered structure and distributed oxygen functional groups. Consequently graphene oxide finds interesting applications in fields of energy, gas storage, sensors, catalysis etc [368–370]. Graphene oxide can be prepared in large scale from the relatively inexpensive starting material: graphite. Graphite is first extensively oxidized to form graphite oxide which is later exfoliated to obtain graphene oxide. Though chemically almost similar, structurally graphite oxide is different from graphene oxide. Graphite oxide retain the stacked interlayer structure but with a large interlayer spacing of 6–12 Å. However in graphene oxide, the layers are exfoliated into monolayer or few layer stacks and does not retain the stacked structure (see figure 6.6).

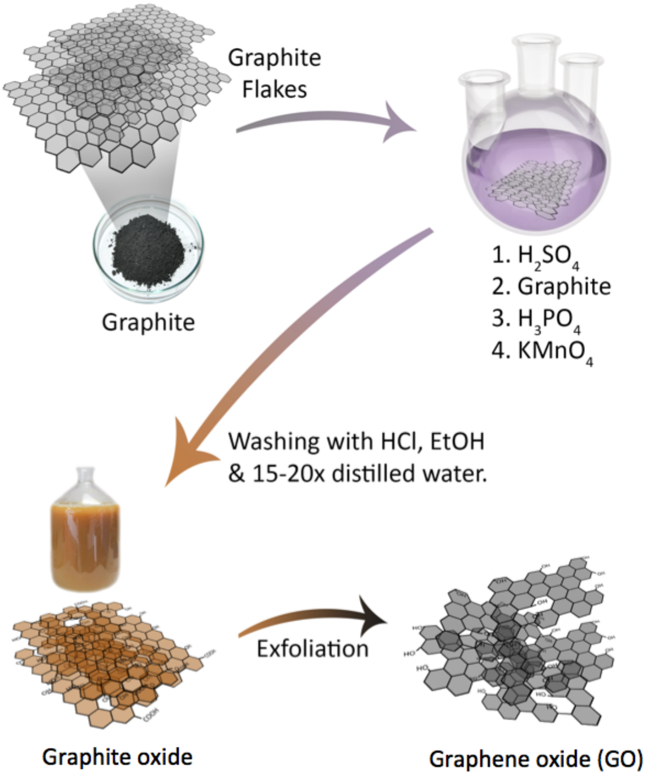

Figure 6.6: Schematic of the synthesis process of graphene oxide starting from commercial graphite.

6.2.1 CO_2 adsorption on graphene oxide

Graphene oxide (GO) was synthesized according to the method described in Wang et al. [371] and supplied by Sandeep Yadav belonging to our research group. A schematic of the different steps involved in the synthesis process is shown in figure 6.6. The oxidation of graphite was carried out according to the improved synthesis technique of Marcano et al. [372] and the graphite oxide obtained was subjected to a combination of repeated freeze-thaw cycles and ultra-sonication to produce graphene oxide. Nitrogen adsorption measurements before and after exfoliation revealed significant changes in specific surface area confirming successful exfoliation. Before exfoliation, as shown in figure 6.7a, very little amount of nitrogen is adsorbed over the complete pressure regime and consequently BET surface area was found to be only $6\,\mathrm{m^2\,g^{-1}}$. After exfoliation, considerable amount of N_2 is adsorbed as observed as shown in figure 6.7b. With the observed capillary condensation at high relative pressures, the N_2 adsorption isotherm of GO resembles a type-IV(a) isotherm and the BET surface area is found to be $268\,\mathrm{m^2\,g^{-1}}$. The mesoporous nature of GO is in accord with the previous literature reports [91]. The 2D layered morphology can be inferred from the SEM image shown in figure 6.7c and TEM image (figure 6.7d) reveals the characteristic wrinkled morphology of GO [373].

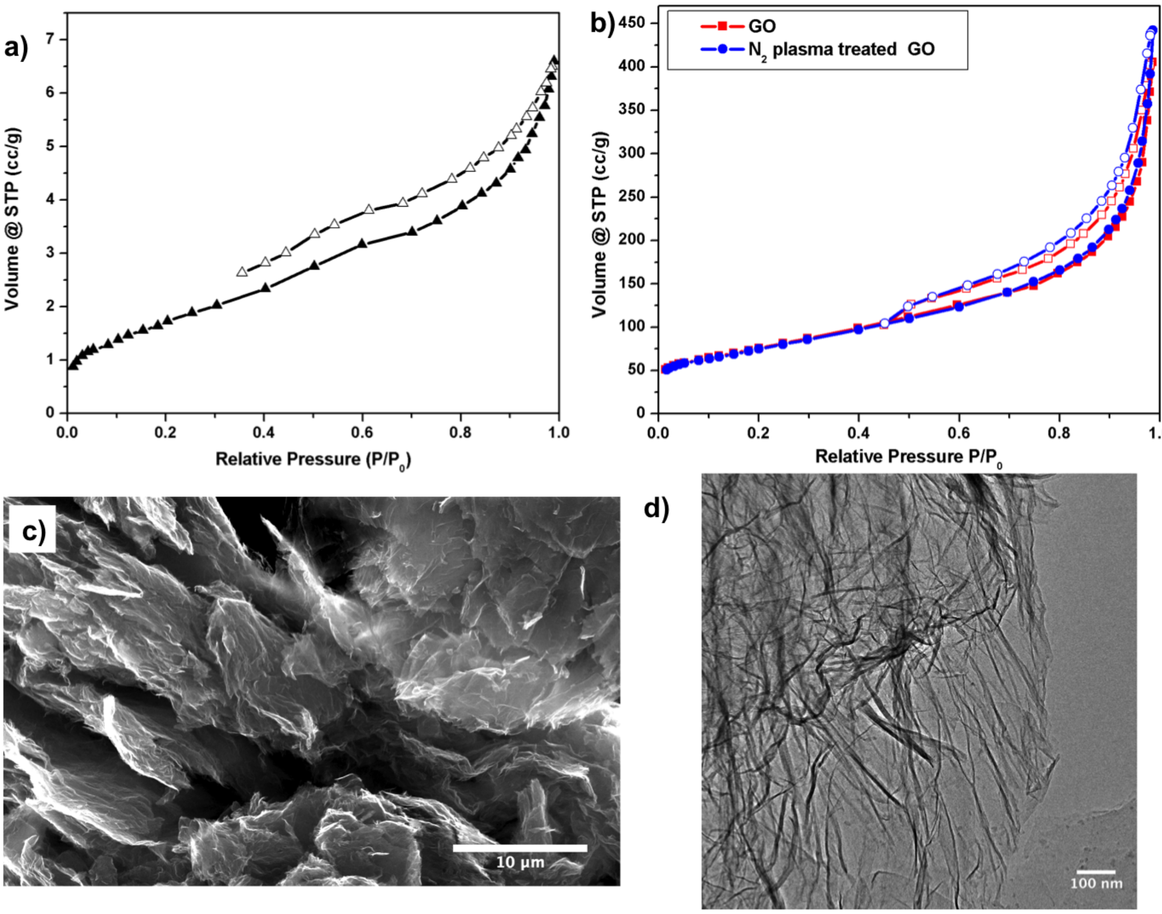

Figure 6.7: a) N_2 adsorption isotherm of as-prepared graphite oxide b) N_2 adsorption isotherm of GO and N_2 plasma treated GO c) SEM image of GO d) TEM image of GO.

Raman spectra before and after exfoliation is compared in figure 6.8a. The higher D-band in both samples is due to the structural distortion brought about by the attachment of a large number of functional groups on to the graphene layers [374]. After exfoliation, the I_D/I_G ratio decreased slightly to 0.91 from an initial ratio of 0.96. The decrease in D-band intensity is attributed to the removal of some functional groups during the exfoliation stage. XPS survey spectrum (figure 6.8b) revealed a prominent O 1s peak confirming the presence of a large amount of oxygen on the surface. As shown in figure 6.8c, the high resolution C 1s spectrum is fitted using 3 components corresponding to C=C (284.4 eV), C-O (286.1 eV) and O-C=O (288.3 eV). A quantitative XPS analysis (see table 6.1) indicated an oxygen concentration of 19.3 at % on the prepared GO.

Ambient pressure CO_2 adsorption measurements were carried out on GO at 35 °C. As with the normal procedure, the sample was heated to 300 °C before the adsorption step. However during

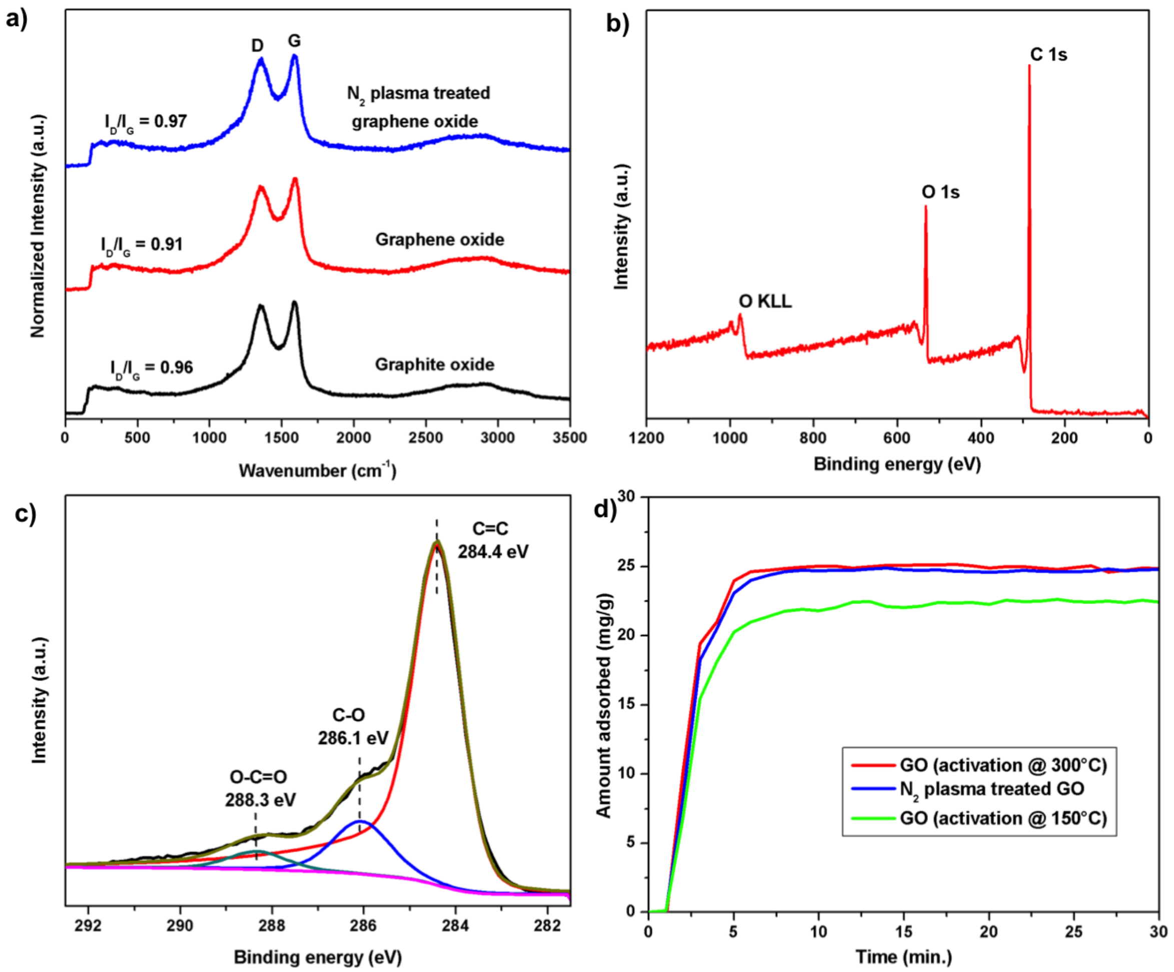

Figure 6.8: a) Raman spectra of Graphite oxide, GO and N_2 plasma treated GO b) XPS survey spectrum of GO b) deconvoluted high resolution C 1s spectrum of GO d) Ambient pressure CO_2 adsorption results on GO and N_2 plasma treated GO.

this preheating stage, a significant weight loss of about 7.05 % was observed and based on previous reports, the observed weight loss can be attributed to the removal of oxygen functional groups [370, 374]. Nevertheless GO exhibited significant CO_2 adsorption of ~24.9 $\mathrm{mg\,g^{-1}}$ as shown in figure 6.8d.

To investigate the effect of the weight loss during the preheating stage, an adsorption measurement was also carried out by heating GO to 150 °C instead of the usual 300 °C. Only 2.3 % weight loss was observed in this case, however the adsorption capacity slightly decreased from 24.9 $\mathrm{mg\,g^{-1}}$ to 22.4 $\mathrm{mg\,g^{-1}}$ as shown in figure 6.8d. Previous studies have shown that the removal of functional groups in GO is associated with an increase in the porosity of the material. The observed higher adsorption capacity for GO heated to higher temperature can be due to the increased porosity in the GO heated to 300 °C.

at. %	C	N	O
GO	80.7	0	19.3
N_2 plasma treated GO	77.5	3.5	19

Table 6.1: Quantitative XPS analysis result of GO and N_2 plasma treated GO.

To probe the influence of nitrogen functionalities on the GO surface when investigating its CO_2 adsorption characteristics, GO was subjected to 60 min of N_2 rf plasma treatment. No changes in morphology are observed in SEM images of the plasma treated GO. N_2 adsorption isotherm also did not reveal significant differences as shown in figure 6.7b. The surface area slightly decreased from $268\,m^2\,g^{-1}$ to $264\,m^2\,g^{-1}$ after N_2 plasma treatment. Raman measurements indicated an increase in the I_D/I_G ratio from 0.91 to 0.97 after plasma treatment (figure 6.8a). The high energy species generated in the plasma process are known to induce damage to the carbon framework of the GO. This explains the observed increase in the defect density of the lattice.

The successful incorporation of nitrogen functionalities on GO by an rf plasma treatment is confirmed by XPS (figure 6.9a). Deconvoluted high resolution C 1s XPS spectrum of N_2 plasma treated GO (figure 6.9b) shows an additional peak at 287.1 eV which is assigned to the C=N-C groups [375]. The shift of the C-O component to lower binding energies (figure 6.9c) indicates the formation of additional C-NH. Deconvolution of the high resolution N 1s spectra (figure 6.9d) revealed the presence of two nitrogen species corresponding to C=N-C at 398.7 eV and C-NH at 400 eV. A quantitative XPS analysis indicated a total nitrogen concentration of 3.5 at % (table 6.1).

Ambient pressure CO_2 measurements on N_2 plasma treated GO, however indicated no improvement in the adsorption capacity as shown in figure 6.8. It is interesting to note that, the oxygen atomic concentration for GO and N_2 plasma treated GO are almost similar ~19 at %. The additional incorporation of 3.5 at % of nitrogen functionalities did not result in any improvement in CO_2 adsorption characteristics at least at ambient conditions. This was also observed for N_2 plasma treated VACNTs. Compared to the O_2 plasma treated VACNTs, N_2 plasma treated VACNTs exhibited a better adsorption only at higher pressures and not at ambient pressures. Thus it is safe to assume that at near ambient conditions, adsorption characteristics of CNTs or GO

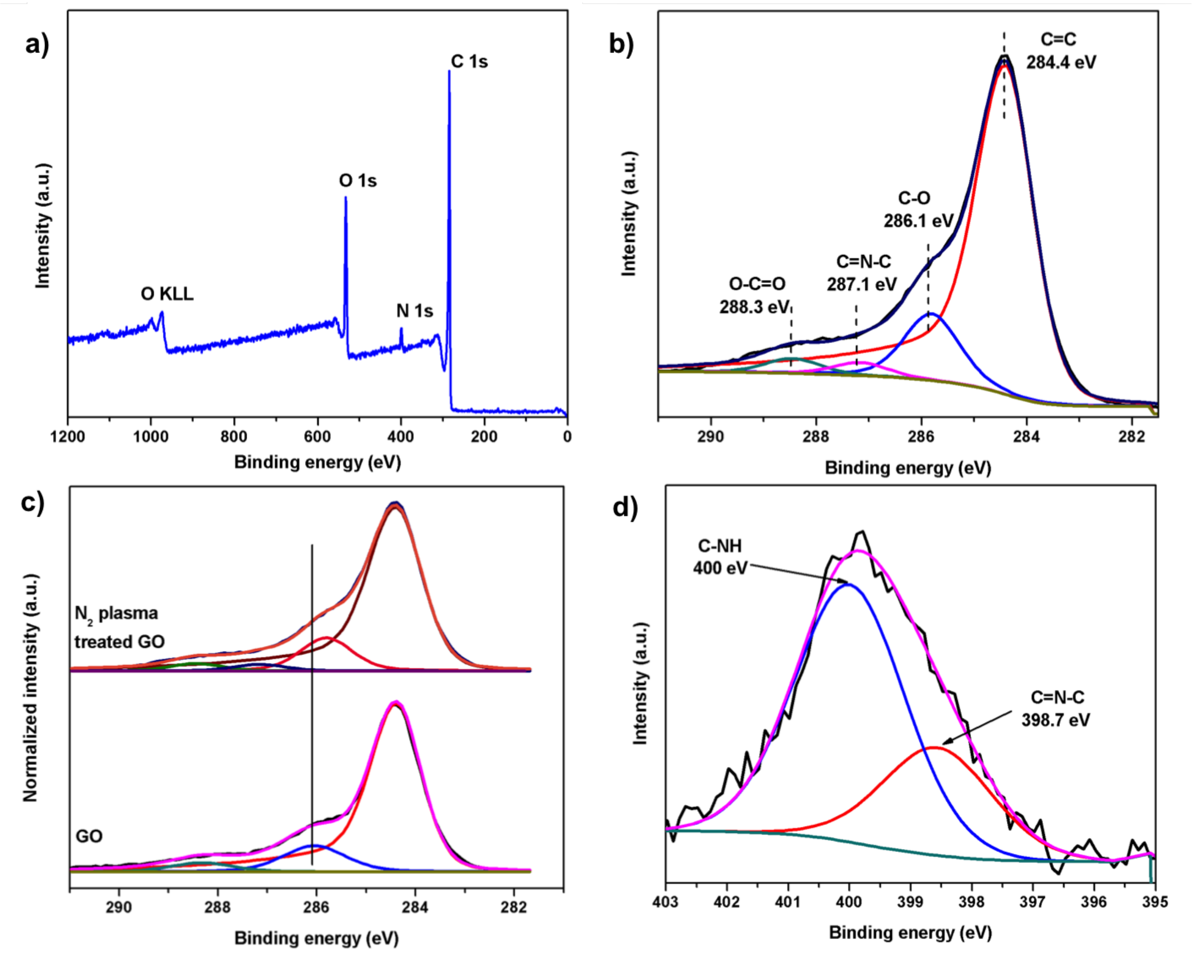

Figure 6.9: a) XPS survey spectrum of N_2 plasma treated GO b) deconvoluted high resolution C 1s spectrum of N_2 plasma treated GO c) Comparison of C 1s spectra of GO and N_2 plasma treated GO d) deconvoluted high resolution N 1s spectrum of N_2 plasma treated GO.

are more strongly influenced by the presence of oxygen functionalities than N-functionalities (of C=N-C and C-NH type).

6.3 Comparison with other standard adsorbents

A comparison of the adsorption behavior of different material class of adsorbents allows a deeper insight into the structural features that governs the gas adsorption characteristics with respect to the presence of different pore systems or pore hierarchy. In figure 6.10, CO_2 adsorption characteristics of all the selected adsorbents are plotted for T = 298 K and p = 0–40 bar. CO_2 adsorption studies on zeolite 13X by Cavenati et al. [219], on MCM-41 by Belmabkhout et al. [377] and on MOF-MIL-53(Al) by Bourrelly et al. [376] are chosen for comparison as the adsorption conditions are similar to the one used in the present study. Due to the absence of extensive micropores

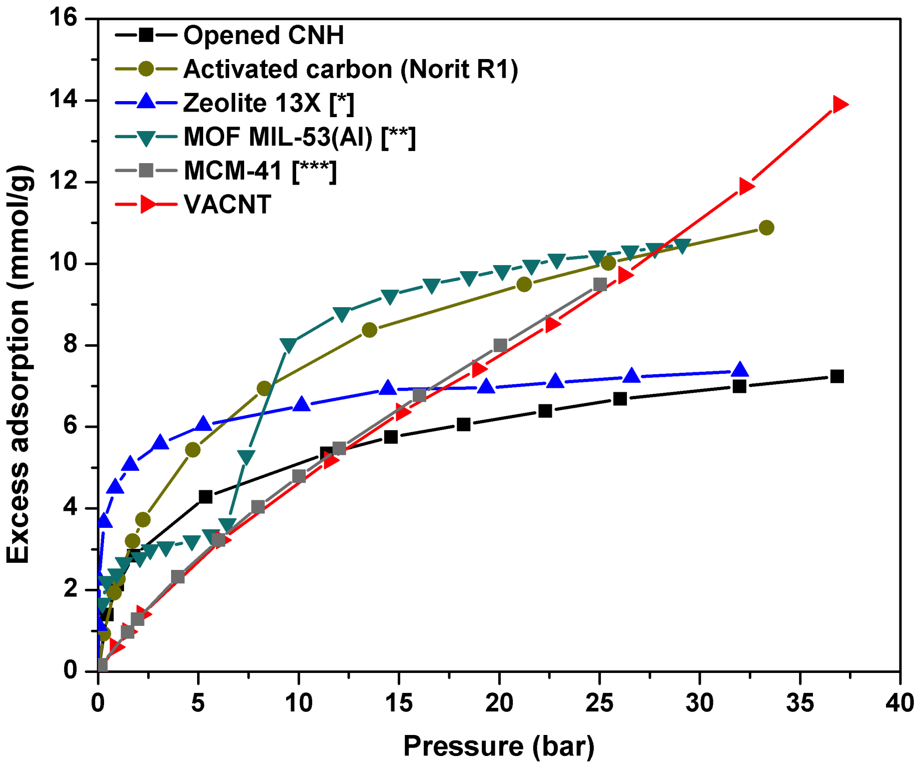

Figure 6.10: Comparison of CO_2 adsorption characteristics of various sorbents at T = 298 K. (* ref. [219], ** ref. [376], *** ref. [377]; for MOF MIL-53(Al), T = 304 K).

in VACNTs, at low pressures, the adsorption capacity of VACNTs is very low. Adsorbents like zeolites, activated carbons and MOFs have micropores to varying extent. Zeolite 13X is a highly microporous adsorbent with pore diameter less than 1 nm. Hence very high CO_2 intake is observed at low pressures (< 1 bar) and once these microporous sites are filled, adsorption saturates. Opened CNHs have a lower density of micropores than zeolites and therefore has a low adsorption capacity at low pressures. However due to the opening of CNHs, CO_2 gas molecules can access the interior of the CNHs which are in the lower mesopore range. Adsorption in these mesopores proceeds by a layer by layer filling mechanism. The presence of these mesopores accounts for a different slope from that of zeolites at high pressures.

Norit R1 activated carbon has a surface area in excess of 1350 $m^2\,g^{-1}$ and is highly microporous. It has an excellent CO_2 adsorption capacity surpassing that of zeolites, and opened CNHs. Adsorption isotherm of MOF is characterized by a distinct step in adsorption at pressures around 6 bar. This steep increase in adsorption at a distinct above ambient pressure is ascribed to what is known as a breathing behavior [376, 378]. With a further increase in the pressure above 6 bar, CO_2 can access the opened sites and eventually leads to complete pore filling.

VACNTs and MCM-41 are mesoporous materials and exhibit very similar CO_2 adsorption characteristics. Adsorption increases almost linearly with pressure and at pressures ~30 bar, the adsorption capacity of VACNTs exceeds that of activated carbon and MOF-MIL-53(Al). It is interesting to note that though the specific surface area of opened VACNTs ($912\,\mathrm{m}^2\,\mathrm{g}^{-1}$) is significantly lower than that of MCM-41 ($1490\,\mathrm{m}^2\,\mathrm{g}^{-1}$), the CO_2 uptake is nearly identical. This might be due to the presence of multiple adsorption sites in VACNTs like the endohedral sites, interstitial and groove sites. It should be noted that the reported adsorption capacity of VACNTs is that of opened VACNTs without any additional modification. This leaves room for further improvement in the adsorption capacity by the addition of functional groups or decreasing CNT diameter or intertube distance as shown earlier in this work.

7 Wettability Studies on Vertically Aligned Carbon Nanotubes

During the course of the work, some studies were also conducted in the area of wettability of VACNTs. In this chapter, the important results from these studies are presented. The chapter starts with an introduction to the phenomena of wettability, discussing the relevant terms and describing different types of superhydrophobic surfaces. Various reported methods to achieve superhydrophobic surfaces are briefly discussed and the details of the novel approach used in the present study are described. The interesting properties of the prepared superhydrophobic VACNTs are discussed in the final section.

7.1 Introduction

Wettability is defined as the tendency of a fluid to spread on or adhere to a solid surface. Determining the wetting characteristics of a surface is crucial for a number of applications like printing, immersion lithography, dip coating, synthesis of composites, developing self-cleaning surfaces etc. The wetting behavior of a surface can generally be described in terms of two parameters: i) static contact angle and ii) contact angle hysteresis (θ_h). Contact angle is defined as the "angle at which a liquid/vapor interface meets the solid surface" (see fig. 7.1). Young's equation relates contact angle to the interfacial tensions as

$$\cos\theta = (\gamma_{SV} - \gamma_{SL})/\gamma_{LV} \tag{7.1}$$

where γ_{SV}, γ_{SL} and γ_{LV} are the solid-vapor, solid-liquid, liquid-vapor surface tensions. Contact angle hysteresis is the difference between the advancing and receding contact angle, when a liquid is added or removed from the droplet deposited on the surface. A high contact angle hysteresis leads to pinning of the liquid droplet on the surface. A surface is said to be hydrophobic when the water contact angle is $> 90°$ and hydrophilic when it is below 90°. When the water contact angle for a surface is less than 10°, the surface is termed as superhydrophilic. Self-cleaning or superhydrophobic surfaces eg. a lotus leaf [379], have a contact angle $> 150°$ and contact angle hysteresis $< 10°$.

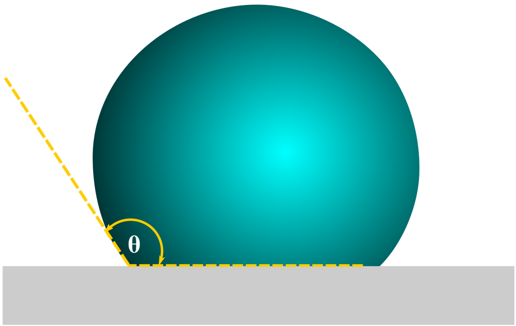

Figure 7.1: Schematic representation of contact angle.

Graphite is inherently hydrophobic with a water contact angle of 90–95° [380]. The nanoscale roughness produced by the vertical alignment of CNTs, makes the surface of VACNTs even more hydrophobic with a contact angle of 115°. It is known that plasma treatment of VACNTs, even for a few seconds, can turn the surface superhydrophilic [271, 318]. This is due to the change in surface morphology as well as due to the addition of large number of hydrophilic -OH groups on the surface of VACNTs by the plasma treatment.

More challenging is the synthesis of superhydrophobic VACNTs. In general two different approaches are reported for the synthesis of superhydrophobic CNTs: i) coating with low surface energy compounds [381, 382] or ii) micropatterning of the CNT surface structure [383]. Both these approaches have its own drawbacks. Coating with a foreign material leads to compromising the inherent CNT characteristics and the role of CNTs is reduced to a mere template structure due to the fact that surface properties viz. the superhydrophobic conditions are governed by the grafted functional groups. Micropatterning on the other hand, relies heavily on expensive and complex lithography techniques involving multiple process steps. A rather straightforward way of obtaining superhydrophobic VACNTs, without using micropatterning or coating with a polymeric compound is therefore highly desirable.

7.2 Synthesis of superhydrophobic VACNTs

To tackle this issue, the surface roughness of the VACNTs has to be increased and hydrophilic groups present on the surface of native VACNTs have to be removed [384, 385]. In the present study, various approaches were explored to address these issues.

The morphological characteristics of VACNTs like diameter, length, intertube distance etc. are determined to a large extent by the catalyst type and size. Increasing the iron layer thickness

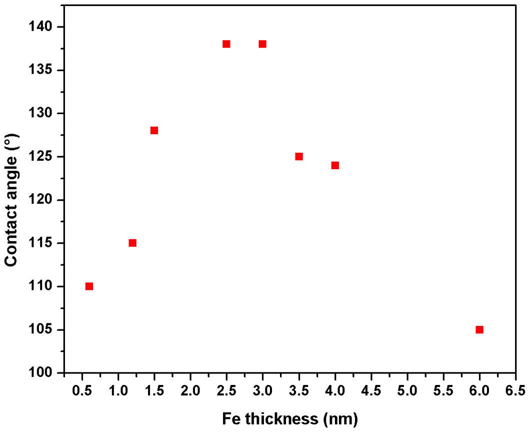

Figure 7.2: Dependence of the water contact angle of the resulting VACNTs on the thickness of iron catalyst layer.

is known to increase the CNT diameter as well as number of walls, both of which are known to increase the hydrophobicity [220]. Along this line, the iron catalyst layer thickness was increased from about 0.8–6 nm and the contact angle of the obtained VACNTs were measured subsequently. As shown in figure 7.2, the contact angle increased from 110° for 0.8 nm to 137° for a 3 nm iron layer thickness. With further increase in the iron layer thickness, the contact angle displayed a decreasing trend. More importantly, the contact angle hysteresis was found to be independent of iron catalyst layer thickness and was always higher than 90°. The observed high hysteresis and associated pinning behavior is typical for VACNTs [386, 387]. Several other approaches like heating in a reducing atmosphere or heating in vacuum for prolonged durations were also probed but in all these cases, the contact angle was always found to be less than 140° with very high hysteresis.

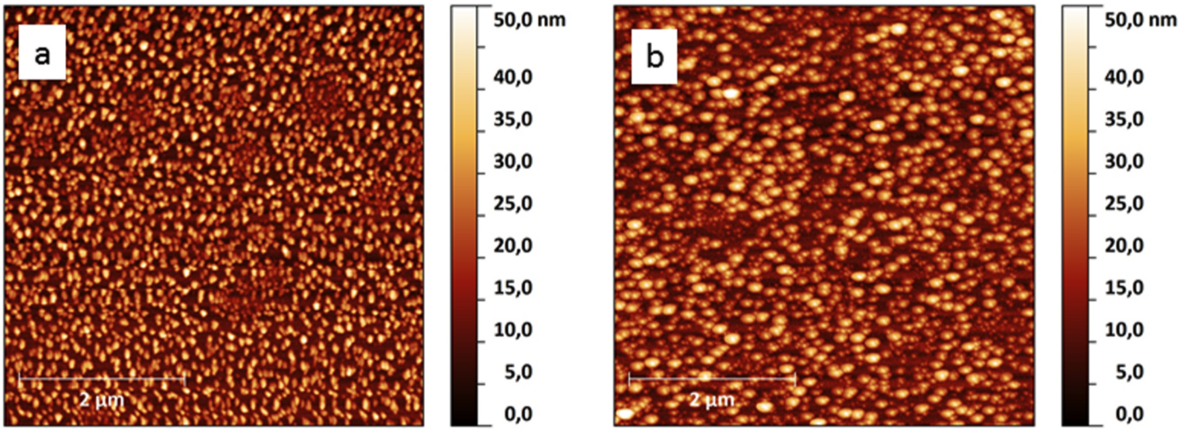

Figure 7.3: AFM image of catalyst particles on the Si/SiO$_2$ substrate subjected to a) standard cycle of VACNT growth b) second cycle of VACNT growth

However when the substrate along with the catalyst particles already deposited for standard VACNT growth was reused for a second cycle of VACNT synthesis (regrowth), an increase in contact angle > 140° and reduction in contact angle hysteresis were observed. This can be understood as follows. In a WACVD process using Fe/Al catalyst, the CNTs grow by a root growth mechanism (section 2.2). In such a growth process, the catalyst particles remain anchored to the substrate when the CNTs are peeled off after a synthesis. The left over catalyst particles are much bigger in size and are sparsely distributed due to Ostwald ripening process that has occurred during the initial (first cycle) CNT growth process [388]. In the present work, AFM images of the substrate with catalyst particles were recorded at the end of first cycle as well as after a second cycle of growth. As shown in figure 7.3b, the catalyst particles at the end of the second cycle are much bigger compared to the one after the first cycle (fig 7.3a). These bigger and sparsely distributed catalyst particles are in theory, ideal for synthesizing VACNTs with increased roughness.

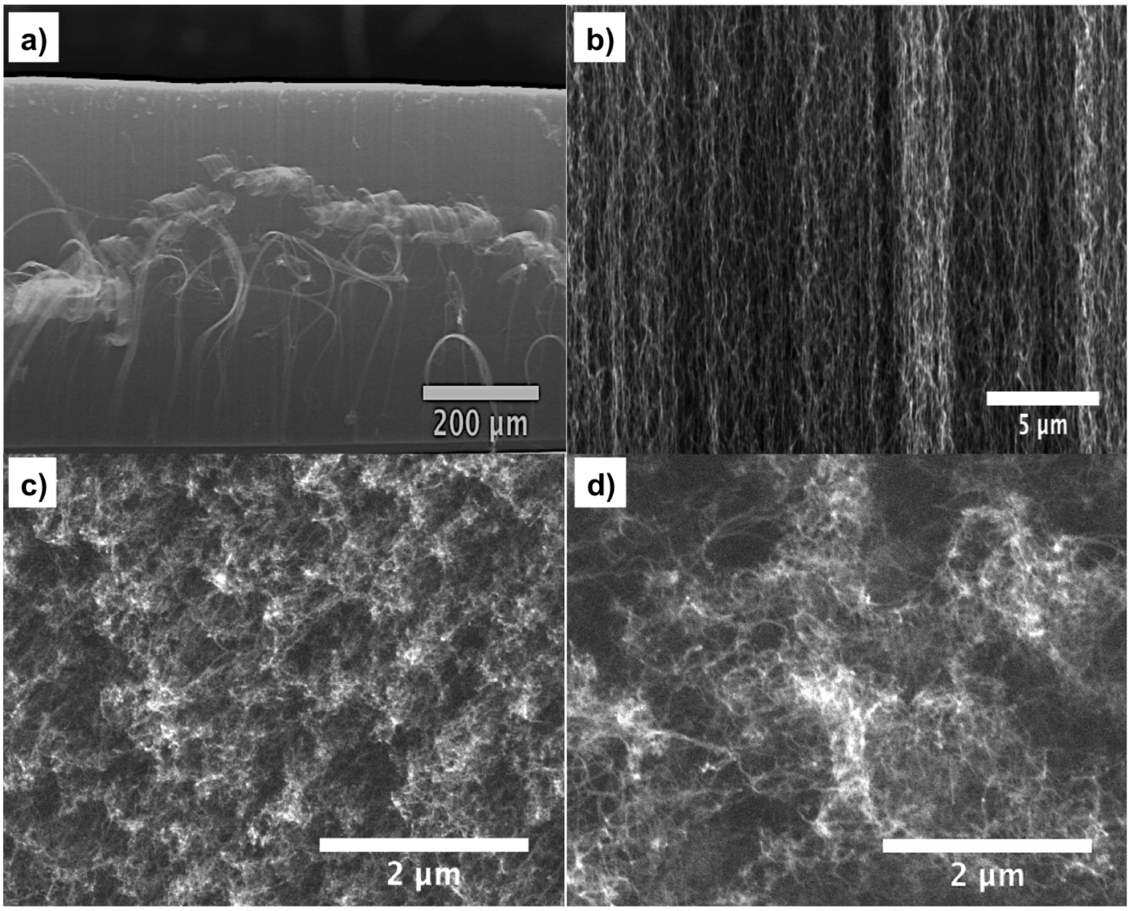

Figure 7.4: SEM image of regrown VACNTs a) low resolution image revealing a total height of ~500 µm b) high resolution image showing the vertical alignment within a VACNT array c) top view of the VACNTs obtained in the first cycle d) top view of the regrown VACNTs.

VACNTs were regrown on these used substrate and the regrown structures still displayed a high degree of vertical alignment with an average height of 500 µm as seen from the SEM image in 7.4a,b. The top view of the VACNTs grown in first cycle and second cycle are compared in figure 7.4c,d. The voids and sparse CNT distribution are evident in the regrown VACNTs. TEM investigations (7.5a) revealed that the regrown CNTs are multiwalled (no. of walls: 2-10) with a larger internal diameter of about 14 nm as compared to the initially formed CNTs. Increase in the surface roughness is confirmed by the AFM image of the top surface of the CNTs shown in figure 7.5b. The VACNTs synthesized in the first cycle had a relatively smooth surface with an average roughness of 200 nm and a crest to trough height of 2 µm. The regrown VACNTs exhibited a three fold increase in roughness to about 600 nm with an average crest to trough height of 6 µm.

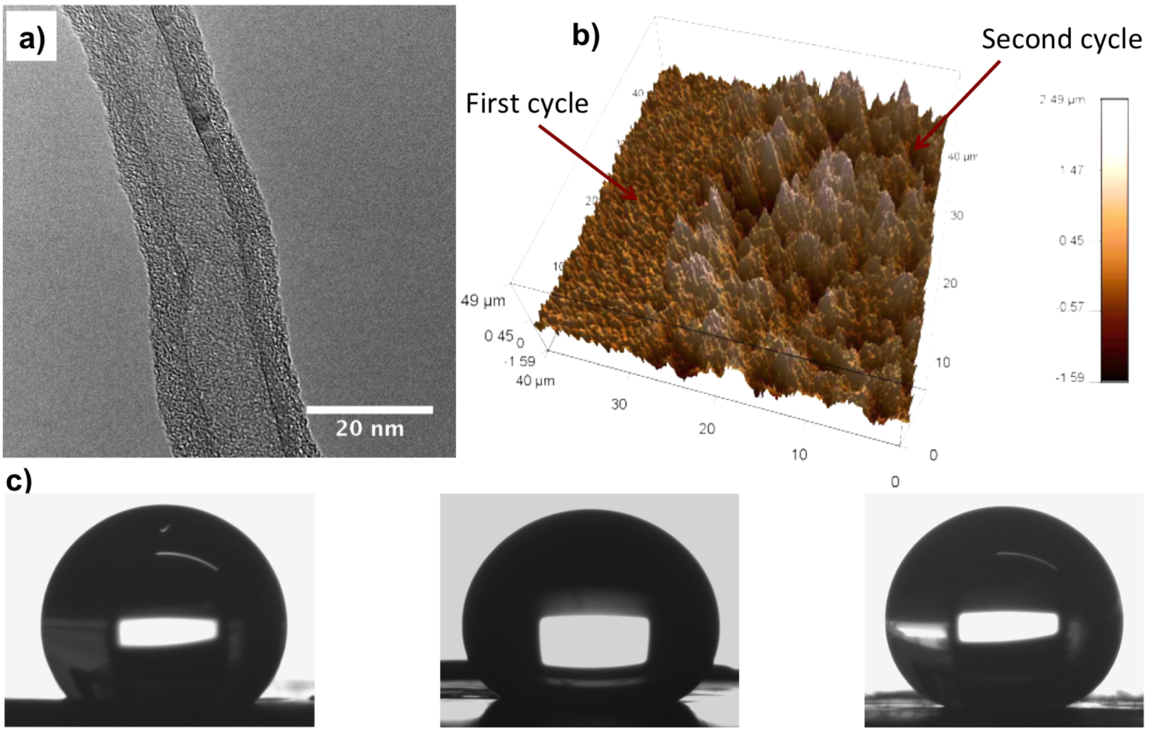

First cycle CNT
CA ~ 137°
Hysteresis > 90°

Regrown CNT
CA ~ 152°
Hysteresis ~ 60°

Superhydrophobic CNT
CA ~ 162°
Hysteresis < 2°

Figure 7.5: a)TEM image of regrown VACNTs b) AFM image of the CNT top surface in first and second cycle c) contact angle and contact angle hysteresis of first cycle, regrown and superhydrophobic VACNTs.

The triple fold increase in the surface roughness is indeed reflected in the static and dynamic water contact angle measurements. The regrown VACNTs displayed an increased contact angle of

152° (see figure 7.5c) with a reduced contact angle hysteresis of 60°. The presence of voids and the increased roughness of the regrown CNTs lead to a larger gas-liquid interfacial area responsible for the observed increase in hydrophobicity. Similar to a liquid wetting a surface which is in Cassie state [389], an increase in the surface roughness results in a reduced number of pinning states per unit area. This leads to the observed decrease in the contact angle hysteresis.

The contact angle hysteresis of 60° is still high to qualify the regrown VACNTs as superhydrophobic. To further reduce the hysteresis, the hydrophilic groups present on the surface have to be removed. A high temperature vacuum annealing ($<$ 5 mbar at 250 °C) was suggested by Aria et al. [385] to strip off the hydrophilic groups present on the surface of VACNTs. A significant decrease in hysteresis was indeed observed while applying this treatment, but the spatially large 3D CNT arrays used in the present study, required prolonged treatment of more than 24 h to observe these significant changes.

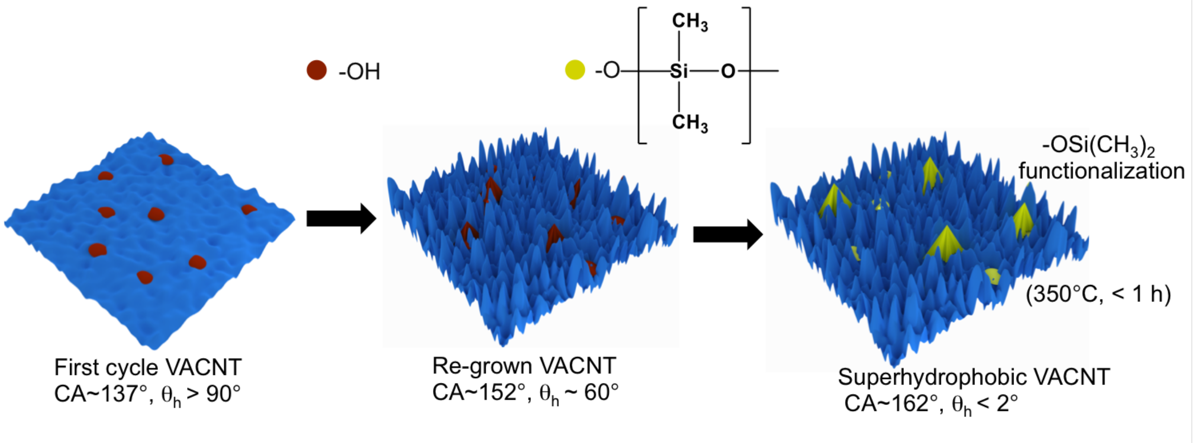

Figure 7.6: Schematic of the process involved in the synthesis of superhydrophobic VACNTs. Superhydrophobic VACNTs can be obtained by increasing the roughness as well as by removing the hydrophilic groups present on the CNT surface. The roughness is increased by a regrowth process and the CNT surface is passivated by -$OSi(CH_3)_2$ functionalization.

A more convenient approach is to exchange the hydrophilic hydroxyl groups on the surface of CNTs against organosilicon residues so as to passivate the CNT surface [390, 391]. However to preserve the alignment, the treatment has to be carried in gas phase and not in liquid phase. It is known that the main component of high vacuum silicon grease is polydimethysiloxane, decomposition of which leads to the formation of organosilicon fragments which can preferentially react with the hydroxyl groups on the CNT surface and passivate it due to the coordination of -$OSi(CH_3)_2$ moieties. The regrown VACNTs were subsequently heated in a tubular furnace at

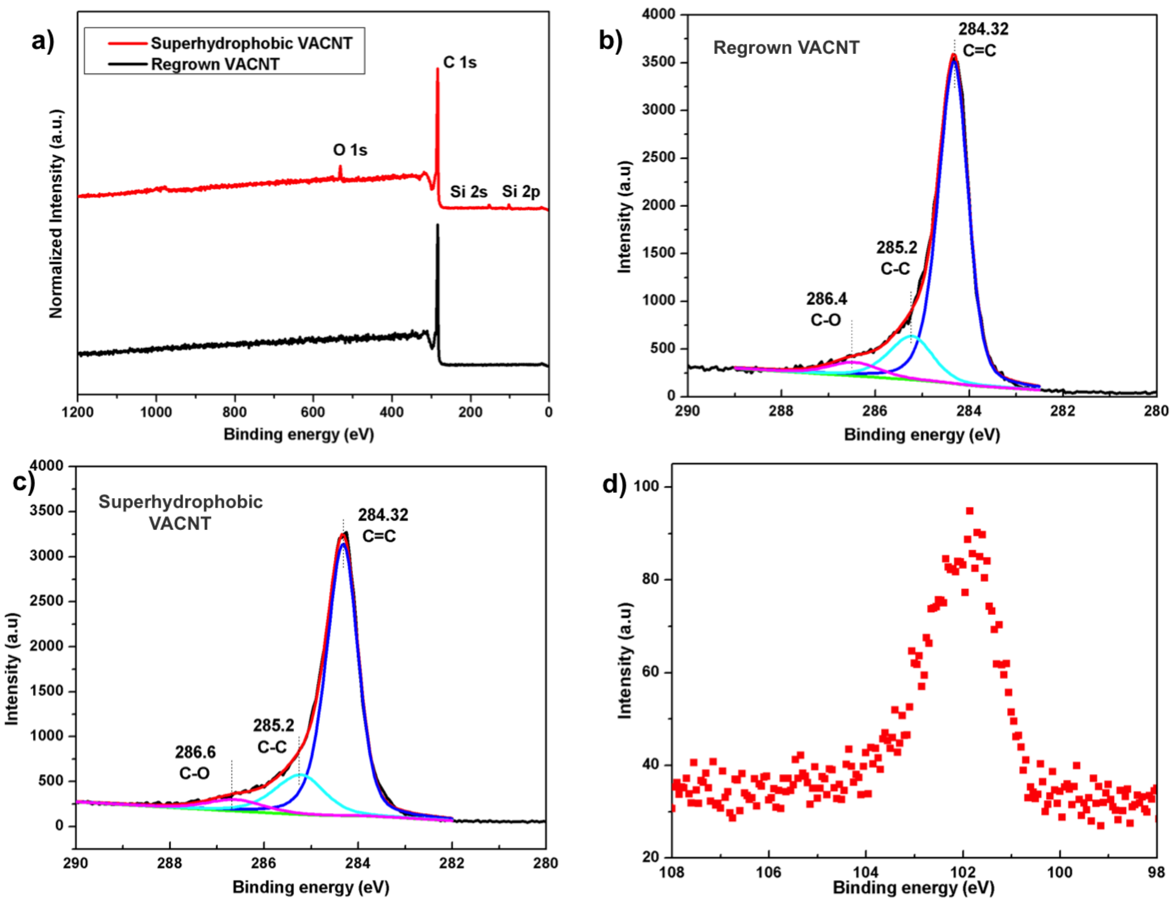

Figure 7.7: XPS studies of regrown and superhydrophobic VACNTs a) Survey spectra comparison of regrown and superhydrophobic VACNTs b) deconvoluted high resolution C 1s spectrum of regrown VACNTs c) deconvoluted high resolution C 1s spectrum of superhydrophobic VACNTs d) high resolution Si 2p spectrum of superhydrophobic VACNTs.

350 °C for 30 min in the presence of a small amount of high vacuum silicon grease. No structural deterioration of the sample was observed in the SEM images. The as-treated samples were found to be superhydrophobic with a contact angle of 162° (figure 7.5) and a contact angle hysteresis of ~2°. A schematic of the steps involved in the synthesis of the superhydrophobic VACNTs is summarized in figure 7.6.

XPS survey spectra of regrown VACNTs and superhydrophobic VACNTs are shown in figure 7.7a. Superhydrophobic VACNTs displays the additional presence of silicon and oxygen indicating a successful functionalization. Deconvoluted high resolution C 1s spectra of regrown VACNTs and superhydrophobic VACNTs, shown in figure 7.7b and c did not reveal any significant changes. The C 1s peak position of both the samples are unchanged indicating no direct Si-C bonding but a CNT-O-Si$(CH_3)_2$ surface coordination. The presence of methyl groups from the polydimethysiloxane functionalization causes a sight broadening of the C 1s spectrum for the superhydrophobic VACNTs (fig. 7.7c). The Si 2p at $E_b = 102.2\,eV$ (fig. 7.7d) and the O 1s photoelectron emission at $E_b = 532\,eV$ confirms the Si-O-Si linkage. XPS quantitative analysis indicated only 2.5 at % of Si on the CNT surface. Raman spectroscopy and IR measurements did not reveal any traces of silicon containing compounds on the surface. AFM phase contrast (fig. 7.8a) also did not indicate any secondary phase. All these measurements point to the absence of a continuous coating on the CNT surface. This in agreement with the findings of Gaspar et al. [392] who reported a surface functionalization of MWNTs. It should also be noted that VACNTs from first cycle of CNT growth, subjected to the same polydimethysiloxane functionalization did not exhibit superhydrophobicity even after 8 h of treatment confirming the importance of increased surface roughness obtained by the regrowth procedure.

7.3 Characteristics of superhydrophobic VACNTs

The prepared superhydrophobic VACNTs have many remarkable characteristics over superhydrophobic structures obtained by coating or micropatterning. One of the important features is the tunability of the contact angle hysteresis. As shown in figure 7.8b the contact angle hysteresis of the superhydrophobic VACNTs is found to be a function of treatment temperature and the desired degree of pinning can be obtained by tuning the temperature.

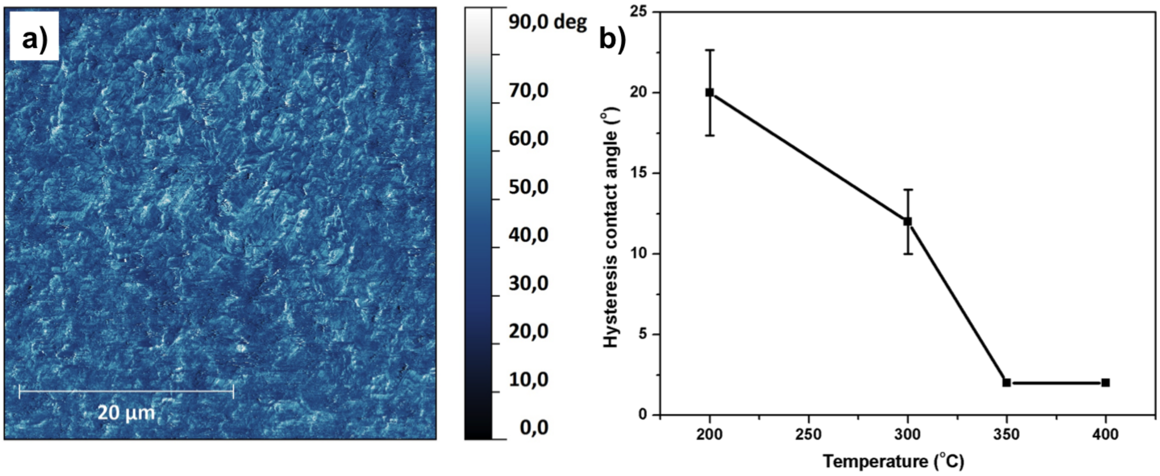

Figure 7.8: a) AFM phase contrast image of superhydrophobic VACNTs b) Variation of contact angle hysteresis with annealing temperature.

The superhydrophobic VACNTs retained their superhydrophobicity over a wide range of pH and temperature. Superhydrophobic character was unaffected even after heating to above 200 °C.

Typical superhydrophobic polymer coatings decompose at such high temperature. In addition, the superhydrophobic VACNTs have a very long shelf life. The samples were found to be superhydrophobic even after two years of its synthesis and no deterioration of the superhydrophobic properties were observed.

Another interesting aspect of superhydrophobic VACNTs is the tunability of its wetting characteristics in response to a number of different stimuli like ozone, UV treatment or plasma exposure under a certain atmosphere. Exposing superhydrophobic VACNTs to UV, ozone or O_2 plasma, leads to the grafting of hydrophilic groups on its surface. The controlled addition or removal of these hydrophilic groups can serve as a handle for tuning the wettability of VACNTs. In addition, the strong anisotropic nature of VACNTs can lead to localized changes in the wetting behavior and this facilitates the creation of distinct wettability patterns on the surface.

Along this line, localized changes in wettability were created by exposing the superhydrophobic VACNTs to a DC corona discharge. The resulting gradient in surface energy from the non-uniform charge distribution, led to the formation of a wettability gradient on the VACNT surface, which was employed to demonstrate fast droplet transport [393].

7.4 Concluding remarks

In this chapter the synthesis of superhydrophobic VACNTs by a two step method was presented. The regrowth process increased the surface roughness of VACNTs and the passivation of the surface was achieved by polydimethylsiloxane functionalization. The obtained superhydrophobic VACNTs had a water contact angle of 162° and a very low contact angle hysteresis of 2°. The superhydrophobic VACNTs were found to be stable over a wide pH and temperature range. By varying the annealing temperature, the hysteresis of the surface can be tuned. The anisotropic nature of the VACNTs enabled the creation of localized changes in the wetting characteristics.

8 Summary and Outlook

In this work, gas adsorption characteristics of vertically aligned carbon nanotubes (VACNTs) were investigated experimentally and the feasibility of VACNTs as a model structure for understanding fundamentals of gas adsorption in carbon materials was explored. Well-defined vertically aligned CNTs free from catalyst particles were synthesized by a water assisted CVD method (WACVD). The as-synthesized VACNTs were found to be mostly double to multiwalled (no. of walls ≤ 6) with an average internal diameter of 8 nm and a specific surface area of about $500\,\mathrm{m^2\,g^{-1}}$. The as-synthesized structures were found to be devoid of any functional groups and with the well-defined adsorption sites and surface chemistry, VACNTs serves as an ideal model structure for understanding gas adsorption in CNTs in particular and carbon materials in general.

To measure the adsorption capacity of VACNTs, two adsorption setups were constructed during the course of the work. A commercial TG setup was modified for measuring the adsorption capacity at atmospheric pressure. The sensitive microbalance enabled the measuring of gas adsorption on relatively small sample quantities and was primarily used to provide a rapid estimate of the adsorption capacity, facilitating faster screening of different samples. The single main disadvantage of the ambient pressure setup is that the measurements could only be made at a single pressure (ambient pressure) and VACNTs typically exhibited very low adsorption at ambient conditions. To measure an adsorption isotherm over a range of different pressures, a high pressure volumetric setup was designed and constructed. The different volumes were calibrated and the calibration was validated by measuring an adsorption isotherm of a standard adsorbent-adsorbate system.

CO_2 adsorption on VACNTs was found to increase almost linearly with pressure and at high pressures, the adsorption capacity was found to be comparable to zeolites. Almost complete desorption, with barely any hysteresis, was observed upon releasing the pressure indicating the need for very little energy input during adsorbent regeneration. Once the basic adsorption characteristics of as-prepared VACNTs were established, the influence of various other parameters were investigated.

Influence of curvature on gas adsorption characteristics was investigated by studying the adsorption properties of VACNTs with smaller internal diameters. Lower diameter VACNTs were synthesized by adjusting the catalyst layer thickness in the WACVD synthesis. The so obtained

VACNTs were mostly double walled with an internal diameter of 5 nm and had a specific surface area of 720 $m^2 g^{-1}$. Decreasing the CNT diameter led to an increase in the CO_2 adsorption capacity over the complete pressure regime investigated. In addition, the adsorption capacity decreased with an increase in temperature indicating a physisorption process and the heat of adsorption was calculated to be about 19 $kJ mol^{-1}$.

Grand Canonical Monte Carlo (GCMC) simulation studies on these VACNTs by the theoretical group predicted an increase in adsorption capacity with a decrease in the intertube distance. Subsequently experiments were performed to validate these findings. The intertube distance of as-synthesized VACNTs were reduced by liquid induced densification method and consistent with the theoretical findings, the adsorption capacity was found to increase with a decrease in the intertube distance.

By comparing the adsorption characteristics of as-prepared VACNTs with the simulation results, a large fraction (~42 %) of VACNTs were found to be closed at both ends. A high temperature CO_2 treatment method was successfully employed to open the CNT tips and consequently the surface area increased to about 912 $m^2 g^{-1}$. The opened VACNTs exhibited a triple fold increase in the CO_2 adsorption capacity and adsorbed half its weight of CO_2 at pressures close to 30 bar.

Plasma functionalization was found to be an effective method for grafting a range of functional groups on the VACNT surface without destroying their vertical alignment. O_2 radio frequency (rf) plasma functionalization, even for a few minutes, was found to significantly alter the surface characteristics of VACNTs by grafting a large amount of oxygen functional groups. Adsorption measurements on O_2 plasma functionalized VACNTs revealed an increase in the adsorption capacity at near ambient pressures. XPS sputter depth profile measurements indicated a non-uniform distribution of functional groups along the VACNT arrays and the extent of functionalization was found to decrease dramatically with depth from the surface. Microwave plasma in remote plasma source (RPS) configuration was found to be less reactive than rf plasma but prolonged treatment time was required for bringing about the same extent of functionalization. The longer treatment ensured better uniformity and resulted in higher adsorption at high pressures.

Unlike O_2 rf plasma, VACNTs had to be treated for much longer durations in rf N_2 plasma to bring about substantial increase in CO_2 adsorption capacity. This longer treatment time made possible by the non-aggressive nature of N_2 plasma, ensured better uniformity in functionalization and subsequently N_2 plasma functionalized VACNTs exhibited better CO_2 adsorption capacity than O_2 rf plasma functionalized VACNTs at high pressures. The employment of a mixture of N_2/Ar gas in the plasma led to an increase in the defect density in VACNTs and the presence of defects positively influenced the gas adsorption characteristics of VACNTs.

CO_2 plasma was found to be as effective as O_2 plasma in functionalizing VACNTs albeit with introducing only minimal structural damages. In addition, the mild nature of CO_2 plasma was found to selectively etch the amorphous carbon and purify VACNT structures without destroying its alignment. With negligible weight loss during plasma treatment, CF_4 plasma was found to be an excellent alternative to O_2 plasma for enhancing the VACNTs gas adsorption characteristics.

Adsorption characteristics of other carbon nanostructures like carbon nanohorns (CNHs) and graphene oxide (GO) were also investigated. Similar to other microporous materials like activated carbon, zeolite or metal organic frameworks (MOFs), opened CNHs were found to have high adsorption capacity at low pressures. However, in the mid-high pressure range, the adsorption capacity of VACNTs were found to be better than other standard adsorbents like zeolites or activated carbons.

In summary, the well-defined pore structure and surface chemistry of VACNTs makes these materials ideal model structures for a systematic investigation of gas adsorption characteristics in carbon materials. The robust sp^2 carbon framework of CNTs, high adsorption capacity especially at high pressures, stability over multiple adsorption-desorption cycle and excellent desorption characteristics are attractive from a practical perspective as well.

8.1 Future works

The high pressure volumetric setup is basically designed to investigate adsorption of gas mixtures. Although the results are of great significance, there are only very few experimental works in this regard. With simulation studies already predicting a high adsorption selectivity of VACNTs, it would be interesting to carry out experimental selectivity studies on VACNTs. It is also interesting to see how different functional groups grafted by plasma treatment influence gas selectivity.

Simulation studies have predicted that charging the CNTs could influence the adsorption characteristics of VACNTs with positive charge increasing the adsorption and negative charge decreasing the CO_2 adsorption [394]. A possibility of electric swing adsorption by switching the charges was put forth. Experimentally it would be interesting to investigate this idea and as a first step, adsorption under electric field and changes in adsorption by switching the polarity could be explored.

Opened VACNTs have excellent adsorption capacity at high pressure and opened CNHs have remarkable gas adsorption characteristics at low pressure. It would be interesting to investigate the adsorption characteristics of a composite of the two in different proportions. The all carbon composite is expected to have reasonably good adsorption capacity in both low and high pressure.

Another area of interest is the effect of humidity on gas adsorption and selectivity. There are already few reports which suggest changes in the adsorption characteristics in the presence of water. It would be interesting to see how humidity affects CO_2 adsorption characteristics of as-prepared hydrophobic VACNTs and hydrophilic plasma functionalized VACNTs.

9 Experimental

9.1 Aluminum deposition

Aluminum deposition was carried out by thermal evaporation method. In the present study, a commercially available thermal evaporator unit - Auto 306 (HHV ltd., U.K.) was employed. Aluminum thickness of 10–13 nm was typically used for the experiments. SQM-160 (Inficon) thickness monitor was used for monitoring the thickness of the deposited Al layer.

9.2 Iron deposition

Iron deposition was carried out by sputter deposition method. Deposition of iron was carried out in a commercially available magnetron sputter coater - Cressington 208 HR (Cressington Scientific Instruments Ltd. U.K.). A circular iron target with a diameter of 57 mm and a purity 99.95% (Evochem GmbH, Germany) was used as the target. Deposition rate was controlled by adjusting the current and monitored by a thickness monitored built into the setup. For a typical synthesis, 1.2–1.4 nm iron was deposited at 60 mA current, at a pressure of 0.2 mbar.

9.3 Details of characterization techniques

9.3.1 XPS

XPS measurements were carried out on a PHI 5000 spectrometer (Physical electronics) as well as on a K-Alpha spectrometer (Thermo Fisher Scientific, UK). For measurements, CNTs were loaded into the XPS chamber along with the substrates. Since charging can lead to peak shifts, charge compensation was carried out using electrons of 8 eV energy and low-energy argon ions. Monochromatic Al kα radiation was used for all the measurements.

9.3.2 Raman

Raman measurements were carried out on a LabRAM HR 800 high resolution microscope (Horiba Jobin Yvon, Japan) with an Ar laser ($\lambda = 514.5\,\text{nm}$). For measurement, CNT arrays peeled off from the substrate were pressed in between glass slides and spectra were recorded for wavenumbers 0–3500 cm^{-1}.

9.3.3 N_2 isotherm measurements

N_2 adsorption (77 K) measurements were carried out on a Quantachrome NOVA3000e system. The samples were heated in vacuum overnight at 150 °C. Surface area was calculated by using multipoint BET method. Pore size distributions were determined by using non-local density functional theory (NLDFT) kernel assuming a slit/cylindrical pore, available in the software NOVAWin10.

9.4 Details of the plasma setup

A commercially available radio frequency (rf) (13.56 MHz) plasma apparatus (Diener, model Femto) was used in the present study. The rf generator has an original power rating of 300 W, however the maximum rf power is limited to 200 W. The parallel plate capacitively coupled setup is fitted with 2 mass flow controllers (MKS instruments) having a maximum flow rate of 20 sccm, for precise delivery of the desired gas. The distance between the plate is fixed at 55 mm and the plasma chamber has a dimension of $280 \times 100 \times 100\,\mathrm{mm}^3$. The power transfer from the generator to the discharge is optimized by an automatic impedance matching network. The setup is connected to a rotary pump for evacuation and the samples are generally degassed to pressures less than 0.2 mbar before introducing the desired gas. The rf generator is switched on only after achieving a stable chamber pressure at the set flow rate.

Bibliography

[1] K. S. Sing, "Reporting physisorption data for gas/solid systems with special reference to the determination of surface area and porosity (recommendations 1984)," *Pure and applied chemistry*, vol. 57, no. 4, pp. 603–619, 1985.

[2] M. Thommes, K. Kaneko, A. V. Neimark, J. P. Olivier, F. Rodriguez-Reinoso, J. Rouquerol, and K. S. Sing, "Physisorption of gases, with special reference to the evaluation of surface area and pore size distribution (IUPAC technical report)," *Pure and Applied Chemistry*, vol. 87, no. 9–10, pp. 1051–1069, 2015.

[3] J. Keller and R. Staudt, *Gas adsorption equilibria: experimental methods and adsorptive isotherms.* Springer, 2005.

[4] F. Rouquerol, J. Rouquerol, and K. Sing, *Adsorption by powders and porous solids: principles, methodology and applications.* Academic Press, 1999.

[5] G. I. A. Inc., "The global activated carbon market trends, drivers and projections.," February 2015.

[6] H. Marsh and F. Reinoso, *Activated carbon.* Elsevier Science, 2006.

[7] J. Patrick, *Porosity in carbons: characterization and applications.* Wiley, 1995.

[8] L. Nilsson, P. Persson, L. Ryden, S. Darozhka, and A. Zaliauskiene, *Cleaner production: technologies and tools for resource efficient production.* Baltic University Press, 2007.

[9] D. M. Ruthven, *Principles of adsorption and adsorption processes.* Wiley, 1984.

[10] D. Stirling, *The sulfur problem: cleaning up industrial feedstocks.* Royal Society of Chemistry, 2000.

[11] C. Brasquet, B. Rousseau, H. Estrade-Szwarckopf, and P. Le Cloirec, "Observation of activated carbon fibres with SEM and AFM correlation with adsorption data in aqueous solution," *Carbon*, vol. 38, no. 3, pp. 407–422, 2000.

[12] M. Suzuki, *Adsorption engineering.* Kodansha, 1990.

[13] F. Hoffmann, M. Cornelius, J. Morell, and M. Fröba, “Silica-based mesoporous organic-inorganic hybrid materials,” *Angewandte Chemie International Edition*, vol. 45, pp. 3216–3251, May 2006.

[14] J. S. Beck, D. C. Calabro, S. B. McCullen, B. P. Pelrine, K. D. Schmitt, and J. C. Vartuli, “Method for functionalizing synthetic mesoporous crystalline material,” 1992.

[15] J. S. Beck, J. C. Vartuli, W. J. Roth, M. E. Leonowicz, C. T. Kresge, K. D. Schmitt, C. T. W. Chu, D. H. Olson, E. W. Sheppard, S. B. McCullen, J. B. Higgins, and J. L. Schlenker, “A new family of mesoporous molecular sieves prepared with liquid crystal templates,” *J. Am. Chem. Soc.*, vol. 114, pp. 10834–10843, Dec. 1992.

[16] Z. Alothman, “A review: Fundamental aspects of silicate mesoporous materials,” *Materials*, vol. 5, no. 12, p. 2874, 2012.

[17] F. Tang, L. Li, and D. Chen, “Mesoporous silica nanoparticles: synthesis, biocompatibility and drug delivery,” *Adv. Mater.*, vol. 24, no. 12, pp. 1504–1534, 2012.

[18] D. Zhao, J. Feng, Q. Huo, N. Melosh, G. H. Fredrickson, B. F. Chmelka, and G. D. Stucky, “Triblock copolymer syntheses of mesoporous silica with periodic 50 to 300 angstrom pores,” *Science*, vol. 279, pp. 548–552, Jan. 1998.

[19] D. Zhao, Q. Huo, J. Feng, B. F. Chmelka, and G. D. Stucky, “Nonionic triblock and star diblock copolymer and oligomeric surfactant syntheses of highly ordered, hydrothermally stable, mesoporous silica structures,” *Journal of the American Chemical Society*, vol. 120, no. 24, pp. 6024–6036, 1998.

[20] Y. Zhao, X. Liu, K. X. Yao, L. Zhao, and Y. Han, “Superior capture of CO_2 achieved by introducing extra-framework cations into N-doped microporous carbon,” *Chemistry of Materials*, vol. 24, no. 24, pp. 4725–4734, 2012.

[21] R. T. Yang, *Adsorbents: fundamentals and applications.* Wiley, 2003.

[22] S. Kulprathipanja, *Zeolites in industrial separation and catalysis.* Wiley, 2010.

[23] O. M. Yaghi, M. O’Keeffe, N. W. Ockwig, H. K. Chae, M. Eddaoudi, and J. Kim, “Reticular synthesis and the design of new materials,” *Nature*, vol. 423, pp. 705–714, June 2003.

[24] H. Furukawa, K. E. Cordova, M. O'Keeffe, and O. M. Yaghi, "The chemistry and applications of metal-organic frameworks," *Science*, vol. 341, p. 1230444, Aug. 2013.

[25] D. Farrusseng, *Metal-organic frameworks: applications from catalysis to gas storage.* Wiley, 2011.

[26] M. Eddaoudi, J. Kim, N. Rosi, D. Vodak, J. Wachter, M. O'Keeffe, and O. M. Yaghi, "Systematic design of pore size and functionality in isoreticular mofs and their application in methane storage," *Science*, vol. 295, pp. 469–472, Jan. 2002.

[27] M. Schröder, *Functional metal-organic frameworks: gas storage, separation and catalysis.* Springer, 2010.

[28] M. P. Suh, H. J. Park, T. K. Prasad, and D.-W. Lim, "Hydrogen storage in metal-organic frameworks," *Chem. Rev.*, vol. 112, pp. 782–835, Feb. 2012.

[29] J.-R. Li, R. J. Kuppler, and H.-C. Zhou, "Selective gas adsorption and separation in metal-organic frameworks," *Chem. Soc. Rev.*, vol. 38, no. 5, pp. 1477–1504, 2009.

[30] K. Sumida, D. L. Rogow, J. A. Mason, T. M. McDonald, E. D. Bloch, Z. R. Herm, T.-H. Bae, and J. R. Long, "Carbon dioxide capture in metal-organic frameworks," *Chem. Rev.*, vol. 112, pp. 724–781, Feb. 2012.

[31] R. J. Kuppler, D. J. Timmons, Q.-R. Fang, J.-R. Li, T. A. Makal, M. D. Young, D. Yuan, D. Zhao, W. Zhuang, and H.-C. Zhou, "Potential applications of metal-organic frameworks," *Coordination Chemistry Reviews*, vol. 253, pp. 3042–3066, Dec. 2009.

[32] B. Chen and G. Qian, *Metal-organic frameworks for photonics applications.* Springer Berlin Heidelberg, 2014.

[33] R. Heimann, S. Evsvukov, and Y. Koga, "Carbon allotropes: a suggested classification scheme based on valence orbital hybridization," *Carbon*, vol. 35, no. 10, pp. 1654–1658, 1997.

[34] L. Shi, P. Rohringer, K. Suenaga, Y. Niimi, J. Kotakoski, J. C. Meyer, H. Peterlik, M. Wanko, S. Cahangirov, A. Rubio, Z. J. Lapin, L. Novotny, P. Ayala, and T. Pichler, "Confined linear carbon chains as a route to bulk carbyne," *Nat Mater*, vol. 15, pp. 634–639, June 2016.

[35] E. Bottani and J. Tascón, *Adsorption by carbons.* Elsevier Science, 2011.

[36] P. A. Thrower and L. R. Radovic, *Chemistry & physics of carbon.* Taylor & Francis, 1999.

[37] P. Harris, A. Burian, and S. Duber, “High-resolution electron microscopy of a microporous carbon,” *Philosophical Magazine Letters*, vol. 80, pp. 381–386, June 2000.

[38] S. Iijima, “Helical microtubules of graphitic carbon,” *Nature*, vol. 354, pp. 56–58, 1991.

[39] S. Iijima and T. Ichihashi, “Single-shell carbon nanotubes of 1-nm diameter,” *Nature*, vol. 363, pp. 603–605, June 1993.

[40] M. Meyyappan, *Carbon nanotubes: science and applications.* CRC Press, 2004.

[41] M. M. Calbi, M. W. Cole, S. M. Gatica, M. J. Bojan, and J. K. Johnson, “Chapter Nine - Adsorbed gases in bundles of carbon nanotubes: theory and simulation A2 - Bottani, Eduardo J.,” in *Adsorption by Carbons* (J. M. TascÃşn, ed.), pp. 187–210, Amsterdam: Elsevier, 2008.

[42] A. C. Dillon, K. M. Jones, T. A. Bekkedahl, C. H. Kiang, D. S. Bethune, and M. J. Heben, “Storage of hydrogen in single-walled carbon nanotubes,” *Nature*, vol. 386, pp. 377–379, Mar. 1997. ESR.

[43] P. Chen, X. Wu, J. Lin, and K. L. Tan, “High H_2 uptake by alkali-doped carbon nanotubes under ambient pressure and moderate temperatures,” *Science*, vol. 285, no. 5424, pp. 91–93, 1999.

[44] Y. Ye, C. C. Ahn, C. Witham, B. Fultz, J. Liu, A. G. Rinzler, D. Colbert, K. A. Smith, and R. E. Smalley, “Hydrogen adsorption and cohesive energy of single-walled carbon nanotubes,” *Applied Physics Letters*, vol. 74, no. 16, pp. 2307–2309, 1999.

[45] C. Liu, Y. Y. Fan, M. Liu, H. T. Cong, H. M. Cheng, and M. S. Dresselhaus, “Hydrogen storage in single-walled carbon nanotubes at room temperature,” *Science*, vol. 286, pp. 1127–1129, Nov. 1999.

[46] A. Dillon and M. Heben, “Hydrogen storage using carbon adsorbents: past, present and future,” *Applied Physics A*, vol. 72, no. 2, pp. 133–142, 2001.

[47] R. T. Yang, “Hydrogen storage by alkali-doped carbon nanotubes-revisited,” *Carbon*, vol. 38, no. 4, pp. 623–626, 2000.

[48] M. Hirscher, M. Becher, M. Haluska, U. Dettlaff-Weglikowska, A. Quintel, G. Duesberg, Y.-M. Choi, P. Downes, M. Hulman, S. Roth, I. Stepanek, and P. Bernier, “Hydrogen storage in sonicated carbon materials,” *Applied Physics A*, vol. 72, no. 2, pp. 129–132, 2001.

[49] A. Züttel, C. Nützenadel, P. Sudan, P. Mauron, C. Emmenegger, S. Rentsch, L. Schlapbach, A. Weidenkaff, and T. Kiyobayashi, “Hydrogen sorption by carbon nanotubes and other carbon nanostructures,” *Journal of Alloys and Compounds*, vol. 330, pp. 676–682, Jan. 2002.

[50] A. D. Migone, “Chapter Sixteen - adsorption on carbon nanotubes: experimental results A2 - Bottani, Eduardo J.,” in *Adsorption by Carbons* (J. M. Tascón, ed.), pp. 403–430, Amsterdam: Elsevier, 2008.

[51] M. L. Terranova, S. Orlanducci, and M. Rossi, *Carbon nanomaterials for gas adsorption*. Pan Stanford, 2012.

[52] M. Hirscher, M. Becher, M. Haluska, A. Quintel, V. Skakalova, Y.-M. Choi, U. Dettlaff-Weglikowska, S. Roth, I. Stepanek, P. Bernier, A. Leonhardt, and J. Fink, “Hydrogen storage in carbon nanostructures,” *Journal of Alloys and Compounds*, vol. 330, pp. 654–658, Jan. 2002.

[53] M. Ritschel, M. Uhlemann, O. Gutfleisch, A. Leonhardt, A. Graff, C. Täschner, and J. Fink, “Hydrogen storage in different carbon nanostructures,” *Applied Physics Letters*, vol. 80, no. 16, pp. 2985–2987, 2002.

[54] G. G. Tibbetts, G. P. Meisner, and C. H. Olk, “Hydrogen storage capacity of carbon nanotubes, filaments, and vapor-grown fibers,” *Carbon*, vol. 39, pp. 2291–2301, Dec. 2001.

[55] F. Liu, X. Zhang, J. Cheng, J. Tu, F. Kong, W. Huang, and C. Chen, “Preparation of short carbon nanotubes by mechanical ball milling and their hydrogen adsorption behavior,” *Carbon*, vol. 41, no. 13, pp. 2527–2532, 2003.

[56] L. Zhou, Y. Zhou, and Y. Sun, "A comparative study of hydrogen adsorption on superactivated carbon versus carbon nanotubes," *International Journal of Hydrogen Energy*, vol. 29, pp. 475–479, Apr. 2004.

[57] B. Panella, M. Hirscher, and S. Roth, "Hydrogen adsorption in different carbon nanostructures," *Carbon*, vol. 43, pp. 2209–2214, Aug. 2005.

[58] A. Züttel, P. Sudan, P. Mauron, T. Kiyobayashi, C. Emmenegger, and L. Schlapbach, "Hydrogen storage in carbon nanostructures," *International Journal of Hydrogen Energy*, vol. 27, pp. 203–212, Feb. 2002.

[59] Q. Zheng, A. Gu, X. Lu, and W. Lin, "Temperature-dependent state of hydrogen molecules within the nanopore of multi-walled carbon nanotubes," *International Journal of Hydrogen Energy*, vol. 29, pp. 481–489, Apr. 2004.

[60] X. Li, H. Zhu, L. Ci, C. Xu, Z. Mao, B. Wei, J. Liang, and D. Wu, "Hydrogen uptake by graphitized multi-walled carbon nanotubes under moderate pressure and at room temperature," *Carbon*, vol. 39, pp. 2077–2079, Nov. 2001.

[61] H. Lee, Y.-S. Kang, S.-H. Kim, and J.-Y. Lee, "Hydrogen desorption properties of multiwall carbon nanotubes with closed and open structures," *Applied Physics Letters*, vol. 80, no. 4, pp. 577–579, 2002.

[62] P.-X. Hou, S.-T. Xu, Z. Ying, Q.-H. Yang, C. Liu, and H.-M. Cheng, "Hydrogen adsorption/desorption behavior of multi-walled carbon nanotubes with different diameters," *Carbon*, vol. 41, no. 13, pp. 2471–2476, 2003.

[63] H. Kajiura, S. Tsutsui, K. Kadono, M. Kakuta, M. Ata, and Y. Murakami, "Hydrogen storage capacity of commercially available carbon materials at room temperature," *Applied Physics Letters*, vol. 82, no. 7, pp. 1105–1107, 2003.

[64] H. Zhu, A. Cao, X. Li, C. Xu, Z. Mao, D. Ruan, J. Liang, and D. Wu, "Hydrogen adsorption in bundles of well-aligned carbon nanotubes at room temperature," *Applied Surface Science*, vol. 178, pp. 50–55, July 2001.

[65] A. Cao, H. Zhu, X. Zhang, X. Li, D. Ruan, C. Xu, B. Wei, J. Liang, and D. Wu, “Hydrogen storage of dense-aligned carbon nanotubes,” *Chemical Physics Letters*, vol. 342, pp. 510–514, July 2001.

[66] G. Gundiah, A. Govindaraj, N. Rajalakshmi, K. S. Dhathathreyan, and C. N. R. Rao, “Hydrogen storage in carbon nanotubes and related materials,” *J. Mater. Chem.*, vol. 13, no. 2, pp. 209–213, 2003.

[67] B. B. Pradhan, A. A. Harutyunyan, D. Stojkovic, J. J. Grossman, P. Zhang, M. M. Cole, V. Crespi, H. Goto, J. Fujiwara, and P. P. Eklund, “Large cryogenic storage of hydrogen in carbon nanotubes at low pressures,” *Journal of Materials Research*, vol. 17, no. 09, pp. 2209–2216, 2002.

[68] T. Pietraß, *Modern magnetic resonance*, ch. Gas Adsorption on Carbon Nanotubes, pp. 1479–1485. Dordrecht: Springer, 2006.

[69] T. Xu, J. Yang, J. Liu, and Q. Fu, “Surface modification of multi-walled carbon nanotubes by O_2 plasma,” *Applied Surface Science*, vol. 253, pp. 8945–8951, Sept. 2007.

[70] L. Wang and R. T. Yang, “New sorbents for hydrogen storage by hydrogen spillover - a review,” *Energy Environ. Sci.*, vol. 1, no. 2, pp. 268–279, 2008.

[71] G. E. Froudakis, “Hydrogen storage in nanotubes & nanostructures,” *Materials Today*, vol. 14, pp. 324–328, July 2011.

[72] Y. Xia, Z. Yang, and Y. Zhu, “Porous carbon-based materials for hydrogen storage: advancement and challenges,” *J. Mater. Chem. A*, vol. 1, no. 33, pp. 9365–9381, 2013.

[73] M. Bienfait, B. Asmussen, M. Johnson, and P. Zeppenfeld, “Methane mobility in carbon nanotubes,” *Surface Science*, vol. 460, pp. 243–248, July 2000.

[74] S. Talapatra and A. D. Migone, “Adsorption of methane on bundles of closed-ended single-wall carbon nanotubes,” *Phys. Rev. B*, vol. 65, pp. 045416–, Jan. 2002.

[75] M. Muris, N. Dufau, M. Bienfait, N. Dupont-Pavlovsky, Y. Grillet, and J. P. Palmari, “Methane and krypton adsorption on single-walled carbon nanotubes,” *Langmuir*, vol. 16, pp. 7019–7022, Aug. 2000.

[76] C.-M. Yang, K. Kaneko, M. Yudasaka, and S. Iijima, “Effect of purification on pore structure of HiPco single-walled carbon nanotube aggregates,” *Nano Lett.*, vol. 2, pp. 385–388, Apr. 2002.

[77] W.-F. Du, L. Wilson, J. Ripmeester, R. Dutrisac, B. Simard, and S. Dénommée, “Investigation of the pore structure of as-prepared and purified HiPco single-walled carbon nanotubes by N_2/Ar adsorption-implication for H_2 storage,” *Nano Lett.*, vol. 2, pp. 343–346, Apr. 2002.

[78] Z. Li, Z. Pan, and S. Dai, “Nitrogen adsorption characterization of aligned multiwalled carbon nanotubes and their acid modification,” *Journal of Colloid and Interface Science*, vol. 277, pp. 35–42, Sept. 2004.

[79] S. Talapatra and A. D. Migone, “Existence of novel quasi-one-dimensional phases of atoms adsorbed on the exterior surface of close-ended single wall nanotube bundles,” *Phys. Rev. Lett.*, vol. 87, p. 206106, Oct 2001.

[80] M. Bienfait, P. Zeppenfeld, N. Dupont-Pavlovsky, J.-P. Palmari, M. R. Johnson, T. Wilson, M. DePies, and O. E. Vilches, “Adsorption of argon on carbon nanotube bundles and its influence on the bundle lattice parameter,” *Phys. Rev. Lett.*, vol. 91, p. 035503, Jul 2003.

[81] R. Q. Long and R. T. Yang, “Carbon nanotubes as a superior sorbent for nitrogen oxides,” *Industrial & Engineering Chemistry Research*, vol. 40, no. 20, pp. 4288–4291, 2001.

[82] S. Santucci, S. Picozzi, F. Di Gregorio, L. Lozzi, C. Cantalini, L. Valentini, J. Kenny, and B. Delley, “NO_2 and CO gas adsorption on carbon nanotubes: experiment and theory,” *Journal of Chemical Physics*, vol. 119, pp. 10904–10910, Nov 2003.

[83] F. Sun, J. Gao, Y. Zhu, G. Chen, S. Wu, and Y. Qin, “Adsorption of SO_2 by typical carbonaceous material: a comparative study of carbon nanotubes and activated carbons,” *Adsorption*, vol. 19, no. 5, pp. 959–966, 2013.

[84] H. Yang, Z. Xu, M. Fan, R. Gupta, R. B. Slimane, A. E. Bland, and I. Wright, “Progress in carbon dioxide separation and capture: a review,” *Journal of Environmental Sciences*, vol. 20, no. 1, pp. 14–27, 2008.

[85] C.-H. Yu, C.-H. Huang, and C.-S. Tan, “A review of CO_2 capture by absorption and adsorption,” *Aerosol And Air Quality Research*, vol. 12, pp. 745–769, Oct. 2012.

[86] T. C. Drage, C. E. Snape, L. A. Stevens, J. Wood, J. Wang, A. I. Cooper, R. Dawson, X. Guo, C. Satterley, and R. Irons, "Materials challenges for the development of solid sorbents for post-combustion carbon capture," *J. Mater. Chem.*, vol. 22, no. 7, pp. 2815–2823, 2012.

[87] D. D'Alessandro, B. Smit, and J. Long, "Carbon dioxide capture: prospects for new materials," *Angewandte Chemie International Edition*, vol. 49, pp. 6058–6082, Aug. 2010.

[88] M. Sevilla and A. B. Fuertes, "CO_2 adsorption by activated templated carbons," *Journal of Colloid and Interface Science*, vol. 366, pp. 147–154, Jan. 2012.

[89] M. D. Hornbostel, J. Bao, G. Krishnan, A. Nagar, I. Jayaweera, T. Kobayashi, A. Sanjurjo, J. Sweeney, D. Carruthers, M. A. Petruska, and L. Dubois, "Characteristics of an advanced carbon sorbent for CO_2 capture," *Carbon*, vol. 56, pp. 77–85, May 2013.

[90] H. Seema, K. Christian Kemp, N. H. Le, S.-W. Park, V. Chandra, J. W. Lee, and K. S. Kim, "Highly selective co_2 capture by s-doped microporous carbon materials," *Carbon*, no. 0, pp. –, 2014.

[91] G. Srinivas, J. Burress, and T. Yildirim, "Graphene oxide derived carbons (GODCs): synthesis and gas adsorption properties," *Energy Environ. Sci.*, vol. 5, no. 4, pp. 6453–6459, 2012.

[92] Y. Wang, S. Yadav, T. Heinlein, V. Konjik, H. Breitzke, G. Buntkowsky, J. J. Schneider, and K. Zhang, "Ultra-light nanocomposite aerogels of bacterial cellulose and reduced graphene oxide for specific absorption and separation of organic liquids," *RSC Adv.*, vol. 4, no. 41, pp. 21553–21558, 2014.

[93] J. P. Marco-Lozar, M. Kunowsky, F. Suárez-García, and A. Linares-Solano, "Sorbent design for CO_2 capture under different flue gas conditions," *Carbon*, vol. 72, pp. 125–134, June 2014.

[94] M. Cinke, J. Li, C. W. Bauschlicher Jr., A. Ricca, and M. Meyyappan, "CO_2 adsorption in single-walled carbon nanotubes," *Chemical Physics Letters*, vol. 376, pp. 761–766, July 2003.

[95] J. Zhao, A. Buldum, J. Han, and J. P. Lu, "Gas molecule adsorption in carbon nanotubes and nanotube bundles," *Nanotechnology*, vol. 13, no. 2, pp. 195–200, 2002.

[96] A. Kleinhammes, S.-H. Mao, X.-J. Yang, X.-P. Tang, H. Shimoda, J. P. Lu, O. Zhou, and Y. Wu, “Gas adsorption in single-walled carbon nanotubes studied by NMR,” *Phys. Rev. B*, vol. 68, pp. 075418–, Aug. 2003.

[97] C. Matranga, L. Chen, M. Smith, E. Bittner, J. K. Johnson, and B. Bockrath, “Trapped CO_2 in carbon nanotube bundles,” *J. Phys. Chem. B*, vol. 107, pp. 12930–12941, Oct. 2003.

[98] W.-L. Yim, O. Byl, J. T. Yates, and J. K. Johnson, “Vibrational behavior of adsorbed CO_2 on single-walled carbon nanotubes,” *The Journal of Chemical Physics*, vol. 120, no. 11, pp. 5377–5386, 2004.

[99] C. Matranga, L. Chen, B. Bockrath, and J. K. Johnson, “Displacement of CO_2 by Xe in single-walled carbon nanotube bundles,” *Phys. Rev. B*, vol. 70, pp. 165416–, Oct. 2004.

[100] M. Bienfait, P. Zeppenfeld, N. Dupont-Pavlovsky, M. Muris, M. R. Johnson, T. Wilson, M. DePies, and O. E. Vilches, “Thermodynamics and structure of hydrogen, methane, argon, oxygen, and carbon dioxide adsorbed on single-wall carbon nanotube bundles,” *Phys. Rev. B*, vol. 70, pp. 035410–, July 2004.

[101] Y. H. Hu and E. Ruckenstein, “Applicability of Dubinin-Astakhov equation to CO_2 adsorption on single-walled carbon nanotubes,” *Chemical Physics Letters*, vol. 425, pp. 306–310, July 2006.

[102] C. Lu, H. Bai, B. Wu, F. Su, and J. F. Hwang, “Comparative study of CO_2 capture by carbon nanotubes, activated carbons, and zeolites,” *Energy & Fuels*, vol. 22, no. 5, pp. 3050–3056, 2008.

[103] F. S. Su, C. S. Lu, W. F. Cnen, H. L. Bai, and J. F. Hwang, “Capture of CO_2 from flue gas via multiwalled carbon nanotubes,” *Science Of The Total Environment*, vol. 407, pp. 3017–3023, Apr. 2009.

[104] S.-C. Hsu, C. Lu, F. Su, W. Zeng, and W. Chen, “Thermodynamics and regeneration studies of CO_2 adsorption on multiwalled carbon nanotubes,” *Chemical Engineering Science*, vol. 65, pp. 1354–1361, Feb. 2010.

[105] F. Su, C. Lu, and H.-S. Chen, “Adsorption, desorption, and thermodynamic studies of CO_2 with high-amine-loaded multiwalled carbon nanotubes,” *Langmuir*, vol. 27, pp. 8090–8098, June 2011.

[106] M. M. Gui, Y. X. Yap, S.-P. Chai, and A. R. Mohamed, “Multi-walled carbon nanotubes modified with (3-aminopropyl)triethoxysilane for effective carbon dioxide adsorption,” *International Journal of Greenhouse Gas Control*, vol. 14, pp. 65–73, May 2013.

[107] E. P. Dillon, C. A. Crouse, and A. R. Barron, “Synthesis, characterization, and carbon dioxide adsorption of covalently attached polyethyleneimine-functionalized single-wall carbon nanotubes,” *ACS Nano*, vol. 2, no. 1, pp. 156–164, 2008.

[108] M.-S. Lee, S.-Y. Lee, and S.-J. Park, “Preparation and characterization of multi-walled carbon nanotubes impregnated with polyethyleneimine for carbon dioxide capture,” *International Journal of Hydrogen Energy*, vol. 40, pp. 3415–3421, Mar. 2015.

[109] Q. Ye, J. Jiang, C. Wang, Y. Liu, H. Pan, and Y. Shi, “Adsorption of low-concentration carbon dioxide on amine-modified carbon nanotubes at ambient temperature,” *Energy Fuels*, vol. 26, pp. 2497–2504, Apr. 2012.

[110] Q. Liu, B. Xiong, J. Shi, M. Tao, Y. He, and Y. Shi, “Enhanced tolerance to flue gas contaminants on carbon dioxide capture using amine-functionalized multiwalled carbon nanotubes,” *Energy Fuels*, vol. 28, pp. 6494–6501, Oct. 2014.

[111] Z. Xiang, Z. Hu, D. Cao, W. Yang, J. Lu, B. Han, and W. Wang, “Metal-organic frameworks with incorporated carbon nanotubes: improving carbon dioxide and methane storage capacities by lithium doping,” *Angew. Chem. Int. Ed.*, vol. 50, pp. 491–494, Jan. 2011.

[112] M. Anbia and V. Hoseini, “Development of MWCNT@MIL-101 hybrid composite with enhanced adsorption capacity for carbon dioxide,” *Chemical Engineering Journal*, vol. 191, pp. 326–330, May 2012.

[113] Y. Yang, L. Ge, V. Rudolph, and Z. Zhu, “In situ synthesis of zeolitic imidazolate frameworks/carbon nanotube composites with enhanced CO_2 adsorption,” *Dalton Trans.*, vol. 43, no. 19, pp. 7028–7036, 2014.

[114] Y. Kong, L. Jin, and J. Qiu, "Synthesis, characterization, and CO_2 capture study of micro-nano carbonaceous composites," *Science of The Total Environment*, vol. 463-464, pp. 192–198, Oct. 2013.

[115] Y. Jin, S. C. Hawkins, C. P. Huynh, and S. Su, "Preparation optimization of carbon nanotube/carbon fiber incorporated carbon composite monoliths for high CO_2 adsorption capacity," *Asia-Pac. J. Chem. Eng.*, vol. 10, no. 6, pp. 842–850, 2015.

[116] G. P. Lithoxoos, A. Labropoulos, L. D. Peristeras, N. Kanellopoulos, J. Samios, and I. G. Economou, "Adsorption of N_2, CH_4, CO and CO_2 gases in single walled carbon nanotubes: a combined experimental and monte carlo molecular simulation study," *The Journal of Supercritical Fluids*, vol. 55, pp. 510–523, Dec. 2010.

[117] A. K. Mishra and S. Ramaprabhu, "Nano magnetite decorated multiwalled carbon nanotubes: a robust nanomaterial for enhanced carbon dioxide adsorption," *Energy Environ. Sci.*, vol. 4, no. 3, pp. 889–895, 2011.

[118] S. Fatemi, M. Vesali-Naseh, M. Cyrus, and J. Hashemi, "Improving CO_2/CH_4 adsorptive selectivity of carbon nanotubes by functionalization with nitrogen-containing groups," *Chemical Engineering Research and Design*, vol. 89, pp. 1669–1675, Sept. 2011.

[119] A. Kumar Mishra and S. Ramaprabhu, "Polyaniline/multiwalled carbon nanotubes nanocomposite-an excellent reversible CO_2 capture candidate," *RSC Adv.*, vol. 2, no. 5, pp. 1746–1750, 2012.

[120] S. Khalili, A. A. Ghoreyshi, M. Jahanshahi, and M. Davoodi, "A comparative study of carbon dioxide adsorption on multi-walled carbon nanotubes versus activated charcoal," *AIP Conf. Proc.*, vol. 1476, pp. 95–99, Sept. 2012.

[121] A. Garcia-Gallastegui, D. Iruretagoyena, M. Mokhtar, A. M. Asiri, S. N. Basahel, S. A. Al-Thabaiti, A. O. Alyoubi, D. Chadwick, and M. S. P. Shaffer, "Layered double hydroxides supported on multi-walled carbon nanotubes: preparation and CO_2 adsorption characteristics," *J. Mater. Chem.*, vol. 22, no. 28, pp. 13932–13940, 2012.

[122] Y. Jin, S. C. Hawkins, C. P. Huynh, and S. Su, "Carbon nanotube modified carbon composite monoliths as superior adsorbents for carbon dioxide capture," *Energy Environ. Sci.*, vol. 6, no. 9, pp. 2591–2596, 2013.

[123] A. Surapathi, H.-y. Chen, E. Marand, J. Karl Johnson, and Z. Sedlakova, "Gas sorption properties of zwitterion-functionalized carbon nanotubes," *Journal of Membrane Science*, vol. 429, pp. 88–94, Feb. 2013.

[124] S. Khalili, A. A. Ghoreyshi, M. Jahanshahi, and K. Pirzadeh, "Enhancement of carbon dioxide capture by amine-functionalized multi-walled carbon nanotube," *Clean Soil Air Water*, vol. 41, no. 10, pp. 939–948, 2013.

[125] B. Yang, H. Hu, Q. Yu, X. Zhang, Z. Li, and L. Lei, "Pretreated multiwalled carbon nanotube adsorbents with amine-grafting for removal of carbon dioxide in confined spaces," *RSC Adv.*, vol. 4, no. 99, pp. 56224–56234, 2014.

[126] J. Yoo, S. Lee, C. K. Lee, C. Kim, T. Fujigaya, H. J. Park, N. Nakashima, and J. K. Shim, "Homogeneous decoration of zeolitic imidazolate framework-8 (ZIF-8) with core-shell structures on carbon nanotubes," *RSC Adv.*, vol. 4, no. 91, pp. 49614–49619, 2014.

[127] P. Li, R. Yang, Y. Zheng, P. Qu, and L. Chen, "Effect of polyether amine canopy structure on carbon dioxide uptake of solvent-free nanofluids based on multiwalled carbon nanotubes," *Carbon*, vol. 95, pp. 408–418, Dec. 2015.

[128] X. Ren, C. Chen, M. Nagatsu, and X. Wang, "Carbon nanotubes as adsorbents in environmental pollution management: a review," *Chemical Engineering Journal*, vol. 170, pp. 395–410, June 2011.

[129] S. Agnihotri, J. P. B. Mota, M. Rostam-Abadi, and M. J. Rood, "Theoretical and experimental investigation of morphology and temperature effects on adsorption of organic vapors in single-walled carbon nanotubes," *J. Phys. Chem. B*, vol. 110, pp. 7640–7647, Apr. 2006.

[130] K. Williams and P. Eklund, "Monte carlo simulations of H_2 physisorption in finite-diameter carbon nanotube ropes," *Chemical Physics Letters*, vol. 320, pp. 352–358, Apr. 2000.

[131] D. Zilli, P. R. Bonelli, and A. L. Cukierman, “Effect of alignment on adsorption characteristics of self-oriented multi-walled carbon nanotube arrays,” *Nanotechnology*, vol. 17, no. 20, pp. 5136–5141, 2006.

[132] L. Dai, A. Patil, X. Gong, Z. Guo, L. Liu, Y. Liu, and D. Zhu, “Aligned nanotubes,” *ChemPhysChem*, vol. 4, pp. 1150–1169, Nov. 2003.

[133] Y. Yan, M. B. Chan-Park, and Q. Zhang, “Advances in carbon-nanotube assembly,” *Small*, vol. 3, pp. 24–42, Jan. 2007.

[134] L. Huang, Z. Jia, and S. O’Brien, “Orientated assembly of single-walled carbon nanotubes and applications,” *J. Mater. Chem.*, vol. 17, no. 37, pp. 3863–3874, 2007.

[135] I. Konstantin, “Techniques of aligning carbon nanotubes,” *Open Physics*, vol. 7, no. 4, pp. 645–653, 2009.

[136] Z. Ren, Y. Lan, and Y. Wang, *Aligned carbon nanotubes: physics, concepts, fabrication and devices*. Springer, 2012.

[137] L. Jin, C. Bower, and O. Zhou, “Alignment of carbon nanotubes in a polymer matrix by mechanical stretching,” *Applied Physics Letters*, vol. 73, no. 9, pp. 1197–1199, 1998.

[138] Y.-H. Li, S. Wang, Z. Luan, J. Ding, C. Xu, and D. Wu, “Adsorption of cadmium(II) from aqueous solution by surface oxidized carbon nanotube,” *Carbon*, vol. 41, no. 5, pp. 1057–1062, 2003.

[139] P. M. Ajayan, O. Stephan, C. Colliex, and D. Trauth, “Aligned carbon nanotube arrays formed by cutting a polymer resin–nanotube composite,” *Science*, vol. 265, pp. 1212–1214, Aug. 1994.

[140] K. Yamamoto, S. Akita, and Y. Nakayama, “Orientation of carbon nanotubes using electrophoresis,” *Japanese Journal of Applied Physics*, vol. 35, no. 7B, pp. L917–, 1996.

[141] K. Yamamoto, S. Akita, and Y. Nakayama, “Orientation and purification of carbon nanotubes using ac electrophoresis,” *Journal of Physics D: Applied Physics*, vol. 31, no. 8, pp. L34–, 1998.

[142] X. Q. Chen, T. Saito, H. Yamada, and K. Matsushige, “Aligning single-wall carbon nanotubes with an alternating-current electric field,” *Applied Physics Letters*, vol. 78, no. 23, pp. 3714–3716, 2001.

[143] J. P. Lu, “Novel magnetic properties of carbon nanotubes,” *Phys. Rev. Lett.*, vol. 74, pp. 1123–1126, Feb. 1995.

[144] D. Walters, M. Casavant, X. Qin, C. Huffman, P. Boul, L. Ericson, E. Haroz, M. O’Connell, K. Smith, D. Colbert, and R. Smalley, “In-plane-aligned membranes of carbon nanotubes,” *Chemical Physics Letters*, vol. 338, pp. 14–20, Apr. 2001.

[145] M. J. Casavant, D. A. Walters, J. J. Schmidt, and R. E. Smalley, “Neat macroscopic membranes of aligned carbon nanotubes,” *Journal of Applied Physics*, vol. 93, no. 4, pp. 2153–2156, 2003.

[146] K. M. Seemann, J. Ebbecke, and A. Wixforth, “Alignment of carbon nanotubes on pre-structured silicon by surface acoustic waves,” *Nanotechnology*, vol. 17, no. 17, pp. 4529–, 2006.

[147] B. Vigolo, A. Pénicaud, C. Coulon, C. Sauder, R. Pailler, C. Journet, P. Bernier, and P. Poulin, “Macroscopic fibers and ribbons of oriented carbon nanotubes,” *Science*, vol. 290, no. 5495, pp. 1331–1334, 2000.

[148] Y. Guo, N. Minami, S. Kazaoui, J. Peng, M. Yoshida, and T. Miyashita, “Multi-layer LB films of single-wall carbon nanotubes,” *Physica B: Condensed Matter*, vol. 323, pp. 235–236, Oct. 2002.

[149] M. Kumar and Y. Ando, “Chemical vapor deposition of carbon nanotubes: a review on growth mechanism and mass production,” *Journal of Nanoscience and Nanotechnology*, vol. 10, no. 6, pp. 3739–3758, 2010.

[150] A. Krueger, *Carbon materials and nanotechnology*. Wiley-VCH, 2010.

[151] M. Meyyappan, L. Delzeit, A. Cassell, and D. Hash, “Carbon nanotube growth by PECVD: a review,” *Plasma Sources Science and Technology*, vol. 12, no. 2, p. 205, 2003.

[152] K. Koziol, B. Boskovic, and N. Yahya, “Synthesis of carbon nanostructures by CVD Method,” in *Advanced Structured Materials*, vol. 5, pp. 23–49, Springer, 2011.

[153] G. Che, B. B. Lakshmi, C. R. Martin, E. R. Fisher, and R. S. Ruoff, "Chemical vapor deposition based synthesis of carbon nanotubes and nanofibers using a template method," *Chem. Mater.*, vol. 10, pp. 260–267, Jan. 1998.

[154] J. J. Schneider, N. I. Maksimova, J. Engstler, R. Joshi, R. Schierholz, and R. Feile, "Catalyst free growth of a carbon nanotube-alumina composite structure," *Inorganica Chimica Acta*, vol. 361, no. 6, pp. 1770 – 1778, 2008.

[155] G. Hornyak, A. Dillon, P. Parilla, J. Schneider, N. Czap, K. Jones, F. Fasoon, A. Mason, and M. Heben, "Template synthesis of carbon nanotubes," *Nanostructured Materials*, vol. 12, pp. 83–88, 1999.

[156] J. J. Schneider, J. Engstler, S. Franzka, K. Hofmann, B. Albert, J. Ensling, P. Gütlich, P. Hildebrandt, S. Döpner, W. Pfleging, B. Günther, and G. Müller, "Carbon nanotube bags: catalytic formation, physical properties, two-dimensional alignment and geometric structuring of densely filled carbon tubes," *Chem. Eur. J.*, vol. 7, pp. 2888–2895, July 2001.

[157] W. Z. Li, S. S. Xie, L. X. Qian, B. H. Chang, B. S. Zou, W. Y. Zhou, R. A. Zhao, and G. Wang, "Large-scale synthesis of aligned carbon nanotubes," *Science*, vol. 274, pp. 1701–1703, Dec. 1996.

[158] C. V. Thompson, "Solid-state dewetting of thin films," *Annual Review of Materials Research*, vol. 42, pp. 399–434, 2012.

[159] S. Fan, M. G. Chapline, N. R. Franklin, T. W. Tombler, A. M. Cassell, and H. Dai, "Self-oriented regular arrays of carbon nanotubes and their field emission properties," *Science*, vol. 283, no. 5401, pp. 512–514, 1999.

[160] A. V. Melechko, V. I. Merkulov, T. E. McKnight, M. A. Guillorn, K. L. Klein, D. H. Lowndes, and M. L. Simpson, "Vertically aligned carbon nanofibers and related structures: Controlled synthesis and directed assembly," *Journal of Applied Physics*, vol. 97, no. 4, p. 041301, 2005.

[161] Y. Chai, J. Gong, K. Zhang, P. C. H. Chan, and M. M. F. Yuen, "Flexible transfer of aligned carbon nanotube films for integration at lower temperature," *Nanotechnology*, vol. 18, no. 35, p. 355709, 2007.

[162] P. M. Parthangal, R. E. Cavicchi, and M. R. Zachariah, “A generic process of growing aligned carbon nanotube arrays on metals and metal alloys,” *Nanotechnology*, vol. 18, no. 18, p. 185605, 2007.

[163] M. Xu, D. N. Futaba, M. Yumura, and K. Hata, “Alignment control of carbon nanotube forest from random to nearly perfectly aligned by utilizing the crowding effect,” *ACS Nano*, vol. 6, pp. 5837–5844, July 2012.

[164] R. S. Wagner and W. C. Ellis, “Vapor-liquid-solid Mechanism of single crystal growth,” *Applied Physics Letters*, vol. 4, no. 5, pp. 89–90, 1964.

[165] R. Baker, M. Barber, P. Harris, F. Feates, and R. Waite, “Nucleation and growth of carbon deposits from the nickel catalyzed decomposition of acetylene,” *Journal of Catalysis*, vol. 26, pp. 51–62, July 1972.

[166] R. Baker and R. Waite, “Formation of carbonaceous deposits from the platinum-iron catalyzed decomposition of acetylene,” *Journal of Catalysis*, vol. 37, pp. 101–105, Apr. 1975.

[167] J.-P. Tessonnier and D. S. Su, “Recent progress on the growth mechanism of carbon nanotubes: a review,” *ChemSusChem*, vol. 4, pp. 824–847, July 2011.

[168] S. Helveg, C. López-Cartes, J. Sehested, P. L. Hansen, B. S. Clausen, J. R. Rostrup-Nielsen, F. Abild-Pedersen, and J. K. Nørskov, “Atomic-scale imaging of carbon nanofibre growth,” *Nature*, vol. 427, pp. 426–429, Jan. 2004.

[169] S. Hofmann, R. Sharma, C. Ducati, G. Du, C. Mattevi, C. Cepek, M. Cantoro, S. Pisana, A. Parvez, F. Cervantes-Sodi, A. C. Ferrari, R. Dunin-Borkowski, S. Lizzit, L. Petaccia, A. Goldoni, and J. Robertson, “In situ observations of catalyst dynamics during surface-bound carbon nanotube nucleation,” *Nano Lett.*, vol. 7, pp. 602–608, Mar. 2007.

[170] S. Hofmann, R. Blume, C. T. Wirth, M. Cantoro, R. Sharma, C. Ducati, M. Hävecker, S. Zafeiratos, P. Schnoerch, A. Oestereich, D. Teschner, M. Albrecht, A. Knop-Gericke, R. Schlögl, and J. Robertson, “State of transition metal catalysts during carbon nanotube growth,” *J. Phys. Chem. C*, vol. 113, pp. 1648–1656, Feb. 2009.

[171] S. Hofmann, G. Csányi, A. C. Ferrari, M. C. Payne, and J. Robertson, “Surface diffusion: the low activation energy path for nanotube growth,” *Phys. Rev. Lett.*, vol. 95, pp. 036101–, July 2005.

[172] A. Rinaldi, J.-P. Tessonnier, M. E. Schuster, R. Blume, F. Girgsdies, Q. Zhang, T. Jacob, S. B. Abd Hamid, D. S. Su, and R. Schlögl, “Dissolved carbon controls the initial stages of nanocarbon growth,” *Angew. Chem. Int. Ed.*, vol. 50, pp. 3313–3317, Mar. 2011.

[173] K. Hata, D. N. Futaba, K. Mizuno, T. Namai, M. Yumura, and S. Iijima, “Water-assisted highly efficient synthesis of impurity-free single-walled carbon nanotubes,” *Science*, vol. 306, pp. 1362–1364, Nov. 2004.

[174] Y. Yao, L. K. L. Falk, R. E. Morjan, O. A. Nerushev, and E. E. B. Campbell, “Cross-sectional TEM investigation of nickel-catalysed carbon nanotube films grown by plasma-enhanced CVD,” *Journal of Microscopy*, vol. 219, pp. 69–75, Aug. 2005.

[175] M. OConnell, *Carbon nanotubes: properties and applications.* CRC Press, 2006.

[176] S. Huang, M. Woodson, R. Smalley, and J. Liu, “Growth mechanism of oriented long single walled carbon nanotubes using fast-heating chemical vapor deposition process,” *Nano Lett.*, vol. 4, pp. 1025–1028, June 2004.

[177] A. Gohier, C. Ewels, T. Minea, and M. Djouadi, “Carbon nanotube growth mechanism switches from tip- to base-growth with decreasing catalyst particle size,” *Carbon*, vol. 46, pp. 1331–1338, Aug. 2008.

[178] J. Dijon, P. Szkutnik, A. Fournier, T. Goislard de Monsabert, H. Okuno, E. Quesnel, V. Muffato, E. De Vito, N. Bendiab, A. Bogner, and N. Bernier, “How to switch from a tip to base growth mechanism in carbon nanotube growth by catalytic chemical vapour deposition,” *Carbon*, vol. 48, pp. 3953–3963, Nov. 2010.

[179] S. Seraphin and D. Zhou, “Singlewalled carbon nanotubes produced at high yield by mixed catalysts,” *Applied Physics Letters*, vol. 64, no. 16, pp. 2087–2089, 1994.

[180] C. Altavilla and E. Ciliberto, *Inorganic nanoparticles: synthesis, applications, and perspectives.* CRC Press, 2010.

[181] C. Mattevi, C. T. Wirth, S. Hofmann, R. Blume, M. Cantoro, C. Ducati, C. Cepek, A. Knop-Gericke, S. Milne, C. Castellarin-Cudia, S. Dolafi, A. Goldoni, R. Schloegl, and J. Robertson, “In-situ x-ray photoelectron spectroscopy study of catalystsupport interactions and growth of carbon nanotube forests,” *J. Phys. Chem. C*, vol. 112, pp. 12207–12213, Aug. 2008.

[182] D. N. Futaba, K. Hata, T. Yamada, K. Mizuno, M. Yumura, and S. Iijima, “Kinetics of water-assisted single-walled carbon nanotube synthesis revealed by a time-evolution analysis,” *Phys. Rev. Lett.*, vol. 95, p. 056104, July 2005.

[183] T. Yamada, T. Namai, K. Hata, D. N. Futaba, K. Mizuno, J. Fan, M. Yudasaka, M. Yumura, and S. Iijima, “Size-selective growth of double-walled carbon nanotube forests from engineered iron catalysts,” *Nature Nanotechnology*, vol. 1, pp. 131–136, Nov. 2006.

[184] T. Yamada, A. Maigne, M. Yudasaka, K. Mizuno, D. N. Futaba, M. Yumura, S. Iijima, and K. Hata, “Revealing the secret of water-assisted carbon nanotube synthesis by microscopic observation of the interaction of water on the catalysts,” *Nano Lett.*, vol. 8, pp. 4288–4292, Dec. 2008.

[185] D. N. Futaba, J. Goto, S. Yasuda, T. Yamada, M. Yumura, and K. Hata, “General rules governing the highly efficient growth of carbon nanotubes,” *Adv. Mater.*, vol. 21, no. 47, pp. 4811–4815, 2009.

[186] A. Magrez, J. W. Seo, V. L. Kuznetsov, and L. Forró, “Evidence of an equimolar C_2H_2-CO_2 reaction in the synthesis of carbon nanotubes,” *Angewandte Chemie*, vol. 119, pp. 445–448, Jan. 2007.

[187] R. Joshi, J. Engstler, L. Houben, M. Bar-Sadan, A. Weidenkaff, P. Mandaliev, A. Issanin, and J. J. Schneider, “Catalyst composition, morphology and reaction pathway in the growth of super-long carbon nanotubes,” *ChemCatChem*, vol. 2, no. 9, pp. 1069–1073, 2010.

[188] P. B. Amama, C. L. Pint, L. McJilton, S. M. Kim, E. A. Stach, P. T. Murray, R. H. Hauge, and B. Maruyama, “Role of water in super growth of single-walled carbon nanotube carpets,” *Nano Lett.*, vol. 9, pp. 44–49, Dec. 2008.

[189] R. K. Joshi, *Synthesis, alignment, growth mechanism and functional properties of carbon nanotubes and their hybrid materials with inorganic and biomaterials.* PhD thesis, T. U. Darmstadt, 2010.

[190] S. R. C. Vivekchand, A. Govindaraj, M. M. Seikh, and C. N. R. Rao, “New method of purification of carbon nanotubes based on hydrogen treatment,” *The Journal of Physical Chemistry B*, vol. 108, no. 22, pp. 6935–6937, 2004.

[191] G. Zhang, D. Mann, L. Zhang, A. Javey, Y. Li, E. Yenilmez, Q. Wang, J. P. McVittie, Y. Nishi, J. Gibbons, and H. Dai, “Ultra-high-yield growth of vertical single-walled carbon nanotubes: hidden roles of hydrogen and oxygen,” *Proceedings of the National Academy of Sciences of the United States of America*, vol. 102, pp. 16141–16145, Nov. 2005.

[192] Z. F. Ren, Z. P. Huang, J. W. Xu, J. H. Wang, P. Bush, M. P. Siegal, and P. N. Provencio, “Synthesis of large arrays of well-aligned carbon nanotubes on glass,” *Science*, vol. 282, no. 5391, pp. 1105–1107, 1998.

[193] Y. J. Jung, “Controlled synthesis of carbon nanotubes using chemical vapor deposition methods,” in *Nanomanufacturing Handbook* (A. Busnaina, ed.), CRC Press, 2006.

[194] T. Heinlein, *Untersuchungen zum wachstumsprozess und anwendungspotenzial flächig angeordneter kohlenstoffnanoröhren.* PhD thesis, T. U. Darmstadt, 2015.

[195] J. Watts and J. Wolstenholme, *An introduction to surface analysis by XPS and AES.* Wiley, 2003.

[196] V. Datsyuk, M. Kalyva, K. Papagelis, J. Parthenios, D. Tasis, A. Siokou, I. Kallitsis, and C. Galiotis, “Chemical oxidation of multiwalled carbon nanotubes,” *Carbon*, vol. 46, pp. 833–840, May 2008.

[197] H. Estrade-Szwarckopf, “XPS photoemission in carbonaceous materials: a "defect" peak beside the graphitic asymmetric peak,” *Carbon*, vol. 42, no. 8-9, pp. 1713–1721, 2004.

[198] G. K. Wertheim and P. H. Citrin, *Fermi surface excitations in X-ray photoemission line shapes from metals.* Springer-Verlag, 1978.

[199] A. Jorio, M. S. Dresselhaus, R. Saito, and G. Dresselhaus, *Raman spectroscopy in graphene related systems.* Wiley, 2011.

[200] A. M. Rao, E. Richter, S. Bandow, B. Chase, P. C. Eklund, K. A. Williams, S. Fang, K. R. Subbaswamy, M. Menon, A. Thess, R. E. Smalley, G. Dresselhaus, and M. S. Dresselhaus, “Diameter-selective Raman scattering from vibrational modes in carbon nanotubes,” *Science*, vol. 275, pp. 187–191, Jan. 1997.

[201] A. C. Ferrari and D. M. Basko, “Raman spectroscopy as a versatile tool for studying the properties of graphene,” *Nat Nano*, vol. 8, pp. 235–246, Apr. 2013.

[202] S. N. Shirodkar and U. V. Waghmare, “Electronic and vibrational signatures of stone-wales defects in graphene: first-principles analysis,” *Phys. Rev. B*, vol. 86, pp. 165401–, Oct. 2012.

[203] J. Rouquerol, D. Avnir, C. Fairbridge, D. Everett, J. Haynes, N. Pernicone, J. Ramsay, K. Sing, and K. Unger, “Recommendations for the characterization of porous solids (technical report),” *Pure and Applied Chemistry*, vol. 66, no. 8, pp. 1739–1758, 1994.

[204] S. Lowell, J. Shields, M. Thomas, and M. Thommes, *Characterization of porous solids and powders: surface area, pore size and density.* Springer Netherlands, 2012.

[205] S. J. Gregg and K. Sing, *Adsorption, surface area, and porosity.* Academic Press, 1991.

[206] S. Brunauer, P. H. Emmett, and E. Teller, “Adsorption of gases in multimolecular layers,” *Journal of the American Chemical Society*, vol. 60, pp. 309–319, Feb. 1938.

[207] J. Toth, *Adsorption.* Taylor & Francis, 2002.

[208] J. W. Gibbs, *The collected works of J. Willard Gibbs.* Longmans, Green and Co., 1877.

[209] J. Möllmer, *Adsorption der reinen gase CO_2, CH_4 und N_2 sowie deren gemische an mikroporösen koordinationspolymeren.* PhD thesis, University of Leipzig, 2012.

[210] NIST, “Thermophysical properties of fluid systems.” Website: http://webbook.nist.gov/chemistry/fluid/.

[211] F. Dreisbach, “Untersuchung von adsorptionsgleichgewichten methanhaltiger gasgemische an aktivkohle als grundlage zur auslegung technischer adsorptionsanlagen,” *Forschungsberichte VDI, Reihe 3*, no. 547, pp. 167–167, 1998.

[212] S. Beutekamp, *Adsorptionsgleichgewichte der reinen Gase Methan, Kohlendioxid, Stickstoff und deren binärer Gemische an verschiedenartigen porösen Stoffen.* PhD thesis, University of Leipzig, 2001.

[213] A. Herbst, *Exzessadsorption reiner gase im druckbereich bis 50 MPa.* PhD thesis, University of Leipzig, 2002.

[214] J. Möllmer, M. Lange, A. Moller, C. Patzschke, K. Stein, D. Lassig, J. Lincke, R. Glaser, H. Krautscheid, and R. Staudt, “Pure and mixed gas adsorption of CH_4 and N_2 on the metal-organic framework Basolite A100 and a novel copper-based 1,2,4-triazolyl isophthalate MOF,” *J. Mater. Chem.*, vol. 22, no. 20, pp. 10274–10286, 2012.

[215] R. E. Bazan, *Adsorptionsuntersuchungen von methanhaltigen Gasgemischen an Aktivkohle Norit R1.* PhD thesis, University of Leipzig, 2010.

[216] F. Dreisbach, R. Staudt, and J. Keller, “High pressure adsorption data of methane, nitrogen, carbon dioxide and their binary and ternary mixtures on activated carbon,” vol. 5, no. 3, pp. 215–227–, 1999.

[217] S. Beutekamp and P. Harting, “Experimental determination and analysis of high pressure adsorption data of pure gases and gas mixtures,” *Adsorption*, vol. 8, no. 4, pp. 255–269–, 2002.

[218] S. Simonato, H. Groger, J. Mollmer, R. Staudt, A. Puls, F. Dreisbach, and C. Feldmann, “Sorption and separation of CO_2 via nanoscale AlO(OH) hollow spheres,” *Chem. Commun.*, vol. 48, no. 6, pp. 844–846, 2012.

[219] S. Cavenati, C. A. Grande, and A. E. Rodrigues, “Adsorption equilibrium of methane, carbon dioxide, and nitrogen on zeolite 13x at high pressures,” *Journal of Chemical & Engineering Data*, vol. 49, no. 4, pp. 1095–1101, 2004.

[220] B. Zhao, D. N. Futaba, S. Yasuda, M. Akoshima, T. Yamada, and K. Hata, “Exploring advantages of diverse carbon nanotube forests with tailored structures synthesized by supergrowth from engineered catalysts,” *ACS Nano*, vol. 3, no. 1, pp. 108–114, 2009.

[221] M. Rahimi, J. K. Singh, D. J. Babu, J. J. Schneider, and F. Müller-Plathe, "Understanding carbon dioxide adsorption in carbon nanotube arrays: molecular simulation and adsorption measurements," *J. Phys. Chem. C*, vol. 117, pp. 13492–13501, June 2013.

[222] M. Rahimi, D. J. Babu, J. K. Singh, Y.-B. Yang, J. J. Schneider, and F. Müller-Plathe, "Double-walled carbon nanotube array for CO_2 and SO_2 adsorption," *The Journal of Chemical Physics*, vol. 143, no. 12, p. 124701, 2015.

[223] S. Esconjauregui, M. Fouquet, B. C. Bayer, C. Ducati, R. Smajda, S. Hofmann, and J. Robertson, "Growth of ultrahigh density vertically aligned carbon nanotube forests for interconnects," *ACS Nano*, vol. 4, pp. 7431–7436, Dec. 2010.

[224] M. De Volder and A. J. Hart, "Engineering hierarchical nanostructures by elastocapillary self-assembly," *Angew. Chem. Int. Ed.*, vol. 52, pp. 2412–2425, Feb. 2013.

[225] M. De Volder, S. H. Tawfick, S. J. Park, D. Copic, Z. Zhao, W. Lu, and A. J. Hart, "Diverse 3D microarchitectures made by capillary forming of carbon nanotubes," *Adv. Mater.*, vol. 22, no. 39, pp. 4384–4389, 2010.

[226] M. F. L. D. Volder, S. J. Park, S. H. Tawfick, D. O. Vidaud, and A. J. Hart, "Fabrication and electrical integration of robust carbon nanotube micropillars by self-directed elastocapillary densification," *Journal of Micromechanics and Microengineering*, vol. 21, no. 4, p. 045033, 2011.

[227] S. Tawfick, Z. Zhao, M. Maschmann, A. Brieland-Shoultz, M. De Volder, J. W. Baur, W. Lu, and A. J. Hart, "Mechanics of capillary forming of aligned carbon nanotube assemblies," *Langmuir*, vol. 29, pp. 5190–5198, Mar. 2013.

[228] D. N. Futaba, K. Hata, T. Yamada, T. Hiraoka, Y. Hayamizu, Y. Kakudate, O. Tanaike, H. Hatori, M. Yumura, and S. Iijima, "Shape-engineerable and highly densely packed single-walled carbon nanotubes and their application as super-capacitor electrodes," *Nature Materials*, vol. 5, pp. 987–994, Dec. 2006.

[229] D. N. Futaba, K. Miyake, K. Murata, Y. Hayamizu, T. Yamada, S. Sasaki, M. Yumura, and K. Hata, "Dual porosity single-walled carbon nanotube material," *Nano Lett.*, vol. 9, pp. 3302–3307, Aug. 2009.

[230] S. H. Kang, B. Pokroy, L. Mahadevan, and J. Aizenberg, "Control of shape and size of nanopillar assembly by adhesion-mediated elastocapillary interaction," *ACS Nano*, vol. 4, pp. 6323–6331, Nov. 2010.

[231] D. M. Guldi and N. Martín, *Carbon nanotubes and related structures: synthesis, characterization, functionalization, and applications.* Wiley, 2010.

[232] T. W. Ajayan, P. M.and Ebbesen, T. Ichihashi, S. Iijima, K. Tanigaki, and H. Hiura, "Opening carbon nanotubes with oxygen and implications for filling," *Nature*, vol. 362, pp. 522–525, Apr 1993.

[233] S. Tsang, P. Harris, and M. L. H. Green, "Thinning and opening of carbon nanotubes by oxidation using carbon-dioxide," *Nature*, vol. 362, pp. 520–522, Apr. 1993.

[234] K. Murata, K. Kaneko, W. A. Steele, F. Kokai, K. Takahashi, D. Kasuya, M. Yudasaka, and S. Iijima, "Porosity evaluation of intrinsic intraparticle nanopores of single wall carbon nanohorn," *Nano Lett.*, vol. 1, pp. 197–199, Apr. 2001.

[235] E. Bekyarova, K. Kaneko, D. Kasuya, K. Murata, M. Yudasaka, and S. Iijima, "Oxidation and porosity evaluation of budlike single-wall carbon nanohorn aggregates," *Langmuir*, vol. 18, pp. 4138–4141, May 2002.

[236] E. Bekyarova, K. Kaneko, M. Yudasaka, D. Kasuya, S. Iijima, A. Huidobro, and F. Rodriguez-Reinoso, "Controlled opening of single-wall carbon nanohorns by heat treatment in carbon dioxide," *J. Phys. Chem. B*, vol. 107, pp. 4479–4484, May 2003.

[237] J. Fan, M. Yudasaka, J. Miyawaki, K. Ajima, K. Murata, and S. Iijima, "Control of hole opening in single-wall carbon nanotubes and single-wall carbon nanohorns using oxygen," *J. Phys. Chem. B*, vol. 110, pp. 1587–1591, Feb. 2006.

[238] C. Bodsworth, *The extraction and refining of metals.* Taylor & Francis, 1994.

[239] D. K. Singh, P. K. Iyer, and P. K. Giri, "Diameter dependence of oxidative stability in multiwalled carbon nanotubes: role of defects and effect of vacuum annealing," *Journal of Applied Physics*, vol. 108, no. 8, p. 084313, 2010.

[240] J. P. C. Trigueiro, G. G. Silva, R. L. Lavall, C. A. Furtado, S. Oliveira, A. S. Ferlauto, R. G. Lacerda, L. O. Ladeira, J.-W. Liu, R. L. Frost, and G. A. George, "Purity evaluation of carbon nanotube materials by thermogravimetric, TEM, and SEM methods," *Journal of Nanoscience and Nanotechnology*, vol. 7, no. 10, pp. 3477–3486, 2007.

[241] M. Liu, Y. Yang, T. Zhu, and Z. Liu, "Chemical modification of single-walled carbon nanotubes with peroxytrifluoroacetic acid," *Carbon*, vol. 43, pp. 1470–1478, June 2005.

[242] T. Okpalugo, P. Papakonstantinou, H. Murphy, J. McLaughlin, and N. Brown, "High resolution XPS characterization of chemical functionalised MWCNTs and SWCNTs," *Carbon*, vol. 43, no. 1, pp. 153–161, 2005.

[243] J. Wang and S. Kaskel, "KOH activation of carbon-based materials for energy storage," *J. Mater. Chem.*, vol. 22, no. 45, pp. 23710–23725, 2012.

[244] B. N. Khare, M. Meyyappan, A. M. Cassell, C. V. Nguyen, and J. Han, "Functionalization of carbon nanotubes using atomic hydrogen from a glow discharge," *Nano Lett.*, vol. 2, pp. 73–77, Dec. 2002.

[245] Z. Hou, B. Cai, H. Liu, and D. Xu, "Ar, O_2, CHF_3, and SF_6 plasma treatments of screen-printed carbon nanotube films for electrode applications," *Carbon*, vol. 46, pp. 405–413, Mar. 2008.

[246] J. E. Johns and M. C. Hersam, "Atomic covalent functionalization of graphene," *Acc. Chem. Res.*, vol. 46, pp. 77–86, Oct. 2013.

[247] W. Xia, C. Jin, S. Kundu, and M. Muhler, "A highly efficient gas-phase route for the oxygen functionalization of carbon nanotubes based on nitric acid vapor," *Carbon*, vol. 47, pp. 919–922, Mar. 2009.

[248] S. Kundu, W. Xia, W. Busser, M. Becker, D. A. Schmidt, M. Havenith, and M. Muhler, "The formation of nitrogen-containing functional groups on carbon nanotube surfaces: a quantitative XPS and TPD study," *Phys. Chem. Chem. Phys.*, vol. 12, no. 17, pp. 4351–4359, 2010.

[249] C. Li, A. Zhao, W. Xia, C. Liang, and M. Muhler, “Quantitative studies on the oxygen and nitrogen functionalization of carbon nanotubes performed in the gas phase,” *J. Phys. Chem. C*, vol. 116, pp. 20930–20936, Sept. 2012.

[250] L. Cai, J. L. Bahr, Y. Yao, and J. M. Tour, “Ozonation of single-walled carbon nanotubes and their assemblies on rigid self-assembled monolayers,” *Chem. Mater.*, vol. 14, pp. 4235–4241, Sept. 2002.

[251] O. Byl, J. Liu, and J. T. Yates, “Etching of carbon nanotubes by ozone-A surface area study,” *Langmuir*, vol. 21, pp. 4200–4204, Mar. 2005.

[252] J. M. Simmons, B. M. Nichols, S. E. Baker, M. S. Marcus, O. M. Castellini, C.-S. Lee, R. J. Hamers, and M. A. Eriksson, “Effect of ozone oxidation on single-walled carbon nanotubes,” *The Journal of Physical Chemistry B*, vol. 110, no. 14, pp. 7113–7118, 2006.

[253] V. A. Basiuk, K. Kobayashi, T. Kaneko, Y. Negishi, E. V. Basiuk, and J.-M. Saniger-Blesa, “Irradiation of single-walled carbon nanotubes with high-energy protons,” *Nano Lett.*, vol. 2, pp. 789–791, May 2002.

[254] B. Khare, M. Meyyappan, M. H. Moore, P. Wilhite, H. Imanaka, and B. Chen, “Proton irradiation of carbon nanotubes,” *Nano Lett.*, vol. 3, pp. 643–646, Mar. 2003.

[255] D.-Q. Yang, J.-F. Rochette, and E. Sacher, “Controlled chemical functionalization of multiwalled carbon nanotubes by kiloelectronvolt argon ion treatment and air exposure,” *Langmuir*, vol. 21, pp. 8539–8545, Aug. 2005.

[256] K. H. An, J. G. Heo, K. G. Jeon, D. J. Bae, C. Jo, C. W. Yang, C.-Y. Park, Y. H. Lee, Y. S. Lee, and Y. S. Chung, “X-ray photoemission spectroscopy study of fluorinated single-walled carbon nanotubes,” *Applied Physics Letters*, vol. 80, no. 22, pp. 4235–4237, 2002.

[257] R. Menzel, M. Q. Tran, A. Menner, C. W. M. Kay, A. Bismarck, and M. S. P. Shaffer, “A versatile, solvent-free methodology for the functionalisation of carbon nanotubes,” *Chem. Sci.*, vol. 1, no. 5, pp. 603–608, 2010.

[258] I. Peech, R. Peech, U. Narkiewicz, D. Moszyski, A. Jdrzejewska, and B. Witkowski, “Chlorination of carbon nanotubes obtained on the different metal catalysts,” *Journal of Nanomaterials*, vol. 2013, p. 9, 2013.

[259] A. Felten, C. Bittencourt, J. J. Pireaux, G. Van Lier, and J. C. Charlier, "Radio-frequency plasma functionalization of carbon nanotubes surface O_2, NH_3, and CF_4 treatments," *Journal Of Applied Physics*, vol. 98, p. 074308, Oct. 2005.

[260] E. V. Hooijdonk, C. Bittencourt, R. Snyders, and J.-F. Colomer, "Functionalization of vertically aligned carbon nanotubes," *Beilstein Journal of Nanotechnology*, vol. 4, pp. 129–152, 2013.

[261] P. Chu and X. Lu, *Low temperature plasma technology: methods and applications.* Low Temperature Plasma Technology: Methods and Applications, CRC Press, Taylor & Francis Group, 2013.

[262] Y. Kawai, H. Ikegami, N. Sato, A. Matsuda, K. Uchino, and M. Kuzuya, eds., *Industrial Plasma Technology: Applications from Environmental to Energy Technologies.* Wiley-VCH, 2010.

[263] P. Chabert and N. Braithwaite, *Physics of radio-frequency plasmas.* Cambridge University Press, 2011.

[264] F. Chen and J. Chang, *Lecture Notes on Principles of Plasma Processing.* Springer US, 2012.

[265] D. Smith, *Thin-film deposition: principles and practice.* McGraw-Hill Education, 1995.

[266] M. Lieberman and A. Lichtenberg, *Principles of Plasma Discharges and Materials Processing.* Wiley, 2005.

[267] B. Ruelle, *Functionalization of carbon nanotubes via plasma post-discharge surface treatment: Implication as nanofiller in polymeric matrices.* PhD thesis, Université de Mons, 2010.

[268] H. Bubert, S. Haiber, W. Brandl, G. Marginean, M. Heintze, and V. Brüser, "Characterization of the uppermost layer of plasma-treated carbon nanotubes," *Diamond and Related Materials*, vol. 12, pp. 811–815, Mar. 2003.

[269] T. Okpalugo, P. Papakonstantinou, H. Murphy, J. Mclaughlin, and N. Brown, "Oxidative functionalization of carbon nanotubes in atmospheric pressure filamentary dielectric barrier discharge (APDBD)," *Carbon*, vol. 43, pp. 2951–2959, Nov. 2005.

[270] C. Chen, B. Liang, A. Ogino, X. Wang, and M. Nagatsu, “Oxygen functionalization of multiwall carbon nanotubes by microwave-excited surface-wave plasma treatment,” *J. Phys. Chem. C*, vol. 113, pp. 7659–7665, Apr. 2009.

[271] A. O. Lobo, S. C. Ramos, E. F. Antunes, F. R. Marciano, V. J. Trava-Airoldi, and E. J. Corat, “Fast functionalization of vertically aligned multiwalled carbon nanotubes using oxygen plasma,” *Materials Letters*, vol. 70, pp. 89–93, Mar. 2012.

[272] R. Ionescu, E. Espinosa, E. Sotter, E. Llobet, X. Vilanova, X. Correig, A. Felten, C. Bittencourt, G. V. Lier, J.-C. Charlier, and J. Pireaux, “Oxygen functionalisation of MWNT and their use as gas sensitive thick-film layers,” *Sensors and Actuators B: Chemical*, vol. 113, pp. 36–46, Jan. 2006.

[273] A. Felten, J. Ghijsen, J.-J. Pireaux, R. L. Johnson, C. M. Whelan, D. Liang, G. V. Tendeloo, and C. Bittencourt, “Effect of oxygen rf-plasma on electronic properties of CNTs,” *Journal of Physics D: Applied Physics*, vol. 40, no. 23, pp. 7379–7382, 2007.

[274] X. Zhang, B. Yang, X. Wang, and C. Luo, “Effect of plasma treatment on multi-walled carbon nanotubes for the detection of H_2S and SO_2,” *Sensors*, vol. 12, no. 7, pp. 9375–9385, 2012.

[275] S. Saloum, M. Naddaf, and B. Alkhaled, “Active species characterization in RF remote oxygen plasma using actinometry OES and electrical probes,” *Vacuum*, vol. 85, pp. 439–442, Sept. 2010.

[276] E. Stoffels, W. W. Stoffels, D. Vender, M. Kando, G. M. W. Kroesen, and F. J. de Hoog, “Negative ions in a radio-frequency oxygen plasma,” *Phys. Rev. E*, vol. 51, pp. 2425–2435, Mar 1995.

[277] S. G. Belostotsky, D. J. Economou, D. V. Lopaev, and T. V. Rakhimova, “Negative ion destruction by $O(^3P)$ atoms and O_2 ($a^1\Delta_g$) molecules in an oxygen plasma,” *Plasma Sources Science and Technology*, vol. 14, no. 3, p. 532, 2005.

[278] A. K. Srivastava and P. Sakthivel, “Quartz-crystal microbalance study for characterizing atomic oxygen in plasma ash tools,” *Journal of Vacuum Science & Technology A*, vol. 19, no. 1, pp. 97–100, 2001.

[279] C.-K. Kim, "Analysis of Langmuir probe data in high density plasmas," *Korean Journal of Chemical Engineering*, vol. 21, no. 3, pp. 746–751, 2004.

[280] B. Zhao, L. Zhang, X. Wang, and J. Yang, "Surface functionalization of vertically-aligned carbon nanotube forests by radio-frequency Ar/O_2 plasma," *Carbon*, vol. 50, pp. 2710–2716, July 2012.

[281] C. Bittencourt, C. Navio, A. Nicolay, B. Ruelle, T. Godfroid, R. Snyders, J.-F. Colomer, M. J. Lagos, X. Ke, G. Van Tendeloo, I. Suarez-Martinez, and C. P. Ewels, "Atomic oxygen functionalization of vertically aligned carbon nanotubes," *J. Phys. Chem. C*, vol. 115, pp. 20412–20418, Sept. 2011.

[282] A. Gohel, K. Chin, Y. Zhu, C. Sow, and A. Wee, "Field emission properties of N_2 and Ar plasma-treated multi-wall carbon nanotubes," *Carbon*, vol. 43, pp. 2530–2535, Oct. 2005.

[283] A. I. Aria, B. J. Lyon, and M. Gharib, "Morphology engineering of hollow carbon nanotube pillars by oxygen plasma treatment," *Carbon*, vol. 81, pp. 376–387, Jan. 2015.

[284] T. Hori, M. D. Bowden, K. Uchino, K. Muraoka, and M. Maeda, "Measurements of electron temperature, electron density, and neutral density in a radio-frequency inductively coupled plasma," *Journal of Vacuum Science & Technology A*, vol. 14, no. 1, pp. 144–151, 1996.

[285] A. Paoletti, A. Tucciarone, and S. italiana di fisica, *Fisica Del Diamante*. International School of Physics Enrico Fermi Series, IOS Press, 1997.

[286] S. Raoux, T. Tanaka, M. Bhan, H. Ponnekanti, M. Seamons, T. Deacon, L.-Q. Xia, F. Pham, D. Silvetti, D. Cheung, K. Fairbairn, A. Jonhson, R. Pearce, and J. Langan, "Remote microwave plasma source for cleaning chemical vapor deposition chambers: Technology for reducing global warming gas emissions," *Journal of Vacuum Science & Technology B*, vol. 17, no. 2, pp. 477–485, 1999.

[287] G. T. Rochelle, "Amine scrubbing for CO_2 capture," *Science*, vol. 325, pp. 1652–1654, Sept. 2009.

[288] M. Wang, A. Lawal, P. Stephenson, J. Sidders, and C. Ramshaw, "Post-combustion CO_2 capture with chemical absorption: a state-of-the-art review," *Chemical Engineering Research and Design*, vol. 89, pp. 1609–1624, Sept. 2011.

[289] M. S. Shafeeyan, W. M. A. W. Daud, A. Houshmand, and A. Shamiri, "A review on surface modification of activated carbon for carbon dioxide adsorption," *Journal of Analytical and Applied Pyrolysis*, vol. 89, pp. 143–151, Nov. 2010.

[290] A. Sayari, Y. Belmabkhout, and E. Da'na, "CO_2 deactivation of supported amines: does the nature of amine matter?," *Langmuir*, vol. 28, pp. 4241–4247, Feb. 2012.

[291] C. Pevida, M. Plaza, B. Arias, J. Fermoso, F. Rubiera, and J. Pis, "Surface modification of activated carbons for CO_2 capture," *Applied Surface Science'*, vol. 254, pp. 7165–7172, Sept. 2008.

[292] M. Sevilla, P. Valle-Vigón, and A. B. Fuertes, "N-doped polypyrrole-based porous carbons for CO_2 capture," *Advanced Functional Materials*, vol. 21, no. 14, pp. 2781–2787, 2011.

[293] J. Wang, I. Senkovska, M. Oschatz, M. R. Lohe, L. Borchardt, A. Heerwig, Q. Liu, and S. Kaskel, "Highly porous nitrogen-doped polyimine-based carbons with adjustable microstructures for CO_2 capture," *J. Mater. Chem. A*, vol. 1, pp. 10951–10961, 2013.

[294] Y. Xia, R. Mokaya, G. S. Walker, and Y. Zhu, "Superior CO_2 adsorption capacity on N-doped, high-surface-area, microporous carbons templated from zeolite," *Advanced Energy Materials*, vol. 1, no. 4, pp. 678–683, 2011.

[295] J.-M. Gu, W.-S. Kim, Y.-K. Hwang, and S. Huh, "Template-free synthesis of N-doped porous carbons and their gas sorption properties," *Carbon*, vol. 56, pp. 208–217, May 2013.

[296] I. D. Mackie and G. A. DiLabio, "CO_2 adsorption by nitrogen-doped carbon nanotubes predicted by density-functional theory with dispersion-correcting potentials," *Phys. Chem. Chem. Phys.*, vol. 13, no. 7, pp. 2780–2787, 2011.

[297] K. S. Lakhi, W. S. Cha, S. Joseph, B. J. Wood, S. S. Aldeyab, G. Lawrence, J.-H. Choy, and A. Vinu, "Cage type mesoporous carbon nitride with large mesopores for CO_2 capture," *Catalysis Today*, vol. 243, pp. 209–217, Apr. 2015.

[298] Y. Shen and J. Bai, "A new kind CO_2/CH_4 separation material: open ended nitrogen doped carbon nanotubes formed by direct pyrolysis of metal organic frameworks," *Chem. Commun.*, vol. 46, no. 8, pp. 1308–1310, 2010.

[299] B. Adeniran and R. Mokaya, “Is N-doping in porous carbons beneficial for CO_2 storage ? Experimental demonstration of the relative effects of pore size and N-doping,” *Chem. Mater.*, vol. 28, pp. 994–1001, Feb. 2016.

[300] H. Chen, F. Sun, J. Wang, W. Li, W. Qiao, L. Ling, and D. Long, “Nitrogen doping effects on the physical and chemical properties of mesoporous carbons,” *J. Phys. Chem. C*, vol. 117, pp. 8318–8328, Apr. 2013.

[301] S. Saloum, M. Naddaf, and B. Alkhaled, “Diagnostics of N_2-Ar plasma mixture excited in a 13.56MHz hollow cathode discharge system: application to remote plasma treatment of polyamide surface,” *Journal of Physics D: Applied Physics*, vol. 41, no. 4, p. 045205, 2008.

[302] A. Ricard, S.-G. Oh, J. Jang, and Y. K. Kim, “Quantitative evaluation of the densities of active species of N_2 in the afterglow of Ar-embedded N_2 RF plasma,” *Current Applied Physics*, vol. 15, no. 11, pp. 1453 – 1462, 2015.

[303] R. Chetty, S. Kundu, W. Xia, M. Bron, W. Schuhmann, V. Chirila, W. Brandl, T. Reinecke, and M. Muhler, “PtRu nanoparticles supported on nitrogen-doped multiwalled carbon nanotubes as catalyst for methanol electrooxidation,” *Electrochimica Acta*, vol. 54, pp. 4208–4215, July 2009.

[304] R. Arrigo, M. Havecker, R. Schlogl, and D. S. Su, “Dynamic surface rearrangement and thermal stability of nitrogen functional groups on carbon nanotubes,” *Chem. Commun.*, no. 40, pp. 4891–4893, 2008.

[305] P. Ayala, R. Arenal, M. Rümmeli, A. Rubio, and T. Pichler, “The doping of carbon nanotubes with nitrogen and their potential applications,” *Carbon*, vol. 48, pp. 575–586, Mar. 2010.

[306] B. Zhu, K. Li, J. Liu, H. Liu, C. Sun, C. E. Snape, and Z. Guo, “Nitrogen-enriched and hierarchically porous carbon macro-spheres - ideal for large-scale CO_2 capture,” *J. Mater. Chem. A*, vol. 2, pp. 5481–5489, 2014.

[307] K. V. Kumar, K. Preuss, L. Lu, Z. X. Guo, and M. M. Titirici, “Effect of nitrogen doping on the CO_2 adsorption behavior in nanoporous carbon structures: a molecular simulation study,” *The Journal of Physical Chemistry C*, vol. 119, no. 39, pp. 22310–22321, 2015.

[308] L. Czepirski and J. Jagieo, “Virial-type thermal equation of gas-solid adsorption,” *Chemical Engineering Science*, vol. 44, no. 4, pp. 797–801, 1989.

[309] M. S. Sun, D. B. Shah, H. H. Xu, and O. Talu, “Adsorption equilibria of C1 to C4 Alkanes, CO_2, and SF_6 on silicalite,” *J. Phys. Chem. B*, vol. 102, pp. 1466–1473, Feb. 1998.

[310] L. Bardos, J. Musil, and P. Taras, “Differences between microwave and RF activation of nitrogen for the PECVD process,” *Journal of Physics D: Applied Physics*, vol. 15, no. 7, pp. L79–L82, 1982.

[311] G. Kalita, S. Adhikari, H. R. Aryal, R. Afre, T. Soga, M. Sharon, and M. Umeno, “Functionalization of multi-walled carbon nanotubes (MWCNTs) with nitrogen plasma for photovoltaic device application,” *Current Applied Physics*, vol. 9, pp. 346–351, Mar. 2009.

[312] B. Ruelle, S. Peeterbroeck, R. Gouttebaron, T. Godfroid, F. Monteverde, J.-P. Dauchot, M. Alexandre, M. Hecq, and P. Dubois, “Functionalization of carbon nanotubes by atomic nitrogen formed in a microwave plasma Ar + N_2 and subsequent poly(-caprolactone) grafting,” *J. Mater. Chem.*, vol. 17, no. 2, pp. 157–159, 2007.

[313] M. Abrar, G. Farwa, S. Naseer, A. Saeed, A. Khan, Z. Iqbal, S. Hussain, and M. Zakaullah, “Enhancement of the electrical properties of carbon nanotubes with Ar-N_2 plasma treatment,” *Current Applied Physics*, vol. 13, pp. 567–575, May 2013.

[314] S. L. Brock, M. Marquez, S. L. Suib, Y. Hayashi, and H. Matsumoto, “Plasma decomposition of CO_2 in the presence of metal catalysts,” *Journal of Catalysis*, vol. 180, pp. 225–233, Dec. 1998.

[315] M. Pérez-Mendoza, M. Domingo-García, and F. López-Garzón, “Modifications produced by O_2 and CO_2 plasma treatments on a glassy carbon: comparison with molecular gases,” *Carbon*, vol. 37, no. 9, pp. 1463–1474, 1999.

[316] J. A. Robinson, E. S. Snow, S. C. Bdescu, T. L. Reinecke, and F. K. Perkins, “Role of defects in single-walled carbon nanotube chemical sensors,” *Nano Lett.*, vol. 6, pp. 1747–1751, July 2006.

[317] P.-X. Hou, C. Liu, and H.-M. Cheng, “Purification of carbon nanotubes,” *Carbon*, vol. 46, pp. 2003–2025, Dec. 2008.

[318] D. J. Babu, M. Lange, G. Cherkashinin, A. Issanin, R. Staudt, and J. J. Schneider, "Gas adsorption studies of CO_2 and N_2 in spatially aligned double-walled carbon nanotube arrays," *Carbon*, vol. 61, pp. 616–623, Sept. 2013.

[319] N. Chakrapani, S. Curran, B. Wei, P. M. Ajayan, A. Carrillo, and R. S. Kane, "Spectral fingerprinting of structural defects in plasma-treated carbon nanotubes," *Journal of Materials Research*, vol. 18, no. 10, pp. 2515–2521, 2003.

[320] B. N. Khare, P. Wilhite, and M. Meyyappan, "The fluorination of single wall carbon nanotubes using microwave plasma," *Nanotechnology*, vol. 15, no. 11, pp. 1650–1654, 2004.

[321] Y. Zhu, F. Cheong, T. Yu, X. Xu, C. Lim, J. Thong, Z. Shen, C. Ong, Y. Liu, A. Wee, and C. Sow, "Effects of CF_4 plasma on the field emission properties of aligned multi-wall carbon nanotube films," *Carbon*, vol. 43, no. 2, pp. 395–400, 2005.

[322] C. Chen, B. Liang, D. Lu, A. Ogino, X. Wang, and M. Nagatsu, "Amino group introduction onto multiwall carbon nanotubes by NH_3/Ar plasma treatment," *Carbon*, vol. 48, pp. 939–948, Apr. 2010.

[323] A. Hassanien, M. Tokumoto, P. Umek, D. Vrbani, M. Mozeti, D. Mihailovi, P. Venturini, and S. Pejovnik, "Selective etching of metallic single-wall carbon nanotubes with hydrogen plasma," *Nanotechnology*, vol. 16, no. 2, pp. 278–281, 2005.

[324] S. Hussain, R. Amade, E. Jover, and E. Bertran, "Functionalization of carbon nanotubes by water plasma," *Nanotechnology*, vol. 23, no. 38, p. 385604, 2012.

[325] E. M. Liston, "Plasma treatment for improved bonding: a review," *The journal of Adhesion*, vol. 30, no. 1-4, pp. 199–218, 1989.

[326] I. Maezono and J.-S. Chang, "Reduction of CO_2 from combustion gases by DC corona torches," *Industry Applications, IEEE Transactions on*, vol. 26, no. 4, pp. 651–655, 1990.

[327] L. Spencer and A. Gallimore, "Efficiency of CO_2 dissociation in a radio-frequency discharge," *Plasma Chemistry and Plasma Processing*, vol. 31, no. 1, pp. 79–89, 2011.

[328] G. Zhang, P. Qi, X. Wang, Y. Lu, X. Li, R. Tu, S. Bangsaruntip, D. Mann, L. Zhang, and H. Dai, "Selective etching of metallic carbon nanotubes by gas-phase reaction," *Science*, vol. 314, no. 5801, pp. 974–977, 2006.

[329] D. J. Babu, S. Yadav, T. Heinlein, G. Cherkashinin, and J. J. Schneider, “Carbon dioxide plasma as a versatile medium for purification and functionalization of vertically aligned carbon nanotubes,” *J. Phys. Chem. C*, vol. 118, pp. 12028–12034, May 2014.

[330] K. Shoda and S. Takeda, “Systematic characterization of carbon nanotubes functionalized in CF_4 plasma,” *Japanese Journal of Applied Physics*, vol. 46, no. 12R, pp. 7977–, 2007.

[331] A. Felten, J. Ghijsen, J.-J. Pireaux, R. Johnson, C. Whelan, D. Liang, G. Van Tendeloo, and C. Bittencourt, “Photoemission study of CF_4 rf-Plasma treated multi-wall carbon nanotubes,” *Carbon*, vol. 46, pp. 1271–1275, Aug. 2008.

[332] N. O. V. Plank, L. Jiang, and R. Cheung, “Fluorination of carbon nanotubes in CF_4 plasma,” *Applied Physics Letters*, vol. 83, no. 12, pp. 2426–2428, 2003.

[333] P. Chen, L. M. Chew, A. Kostka, K. Xie, M. Muhler, and W. Xia, “Purified oxygen- and nitrogen-modified multi-walled carbon nanotubes as metal-free catalysts for selective olefin hydrogenation,” *Journal of Energy Chemistry*, vol. 22, pp. 312–320, Mar. 2013.

[334] K.-Y. Lin, J.-K. Chang, C.-Y. Chen, and W.-T. Tsai, “Effects of heat treatment on materials characteristics and hydrogen storage capability of multi-wall carbon nanotubes,” *Diamond and Related Materials*, vol. 18, pp. 553–556, Feb. 2009.

[335] D. B. Mawhinney, V. Naumenko, A. Kuznetsova, J. T. Yates, J. Liu, and R. E. Smalley, “Infrared spectral evidence for the etching of carbon nanotubes: ozone oxidation at 298 K,” *J. Am. Chem. Soc.*, vol. 122, pp. 2383–2384, Feb. 2000.

[336] H. F. Bettinger, “Experimental and computational investigations of the properties of fluorinated single-walled carbon nanotubes,” *ChemPhysChem*, vol. 4, pp. 1283–1289, Dec. 2003.

[337] B. Ni, R. Andrews, D. Jacques, D. Qian, M. B. J. Wijesundara, Y. Choi, L. Hanley, and S. B. Sinnott, “A combined computational and experimental study of ion-beam modification of carbon nanotube bundles,” *J. Phys. Chem. B*, vol. 105, pp. 12719–12725, Nov. 2001.

[338] M. Terrones, H. Terrones, F. Banhart, J.-C. Charlier, and P. M. Ajayan, “Coalescence of single-walled carbon nanotubes,” *Science*, vol. 288, no. 5469, pp. 1226–1229, 2000.

[339] A. Krasheninnikov, K. Nordlund, and J. Keinonen, “Production of defects in supported carbon nanotubes under ion irradiation,” *Phys. Rev. B*, vol. 65, pp. 165423–, Apr. 2002.

[340] M. S. Raghuveer, P. G. Ganesan, J. D'Arcy-Gall, G. Ramanath, M. Marshall, and I. Petrov, "Nanomachining carbon nanotubes with ion beams," *Applied Physics Letters*, vol. 84, no. 22, pp. 4484–4486, 2004.

[341] F. Xu, M. Minniti, P. Barone, A. Sindona, A. Bonanno, and A. Oliva, "Nitrogen doping of single walled carbon nanotubes by low energy ion implantation," *Carbon*, vol. 46, pp. 1489–1496, Sept. 2008.

[342] M. Yudasaka, S. Iijima, and V. Crespi, "Single-wall carbon nanohorns and nanocones," in *Topics in Applied Physics* (A. Jorio, G. Dresselhaus, and M. Dresselhaus, eds.), vol. 111, pp. 605–629, Springer, 2008.

[343] S. Zhu and G. Xu, "Single-walled carbon nanohorns and their applications," *Nanoscale*, vol. 2, pp. 2538–2549, 2010.

[344] P. J. F. Harris, S. C. Tsang, J. B. Claridge, and M. L. H. Green, "High-resolution electron microscopy studies of a microporous carbon produced by arc-evaporation," *J. Chem. Soc., Faraday Trans.*, vol. 90, no. 18, pp. 2799–2802, 1994.

[345] S. Iijima, M. Yudasaka, R. Yamada, S. Bandow, K. Suenaga, F. Kokai, and K. Takahashi, "Nano-aggregates of single-walled graphitic carbon nano-horns," *Chemical Physics Letters*, vol. 309, pp. 165–170, Aug. 1999.

[346] D. Kasuya, M. Yudasaka, K. Takahashi, F. Kokai, and S. Iijima, "Selective production of single-wall carbon nanohorn aggregates and their formation mechanism," *J. Phys. Chem. B*, vol. 106, pp. 4947–4951, May 2002.

[347] C.-M. Yang, D. Kasuya, M. Yudasaka, S. Iijima, and K. Kaneko, "Microporosity development of single-wall carbon nanohorn with chemically induced coalescence of the assembly structure," *J. Phys. Chem. B*, vol. 108, pp. 17775–17782, Nov. 2004.

[348] H. Wang, M. Chhowalla, N. Sano, S. Jia, and G. A. J. Amaratunga, "Large-scale synthesis of single-walled carbon nanohorns by submerged arc," *Nanotechnology*, vol. 15, no. 5, pp. 546–, 2004.

[349] K. Vasu, K. Pramoda, K. Moses, A. Govindaraj, and C. N. Rao, “Single-walled nanohorns and other nanocarbons generated by submerged arc discharge between carbon electrodes in liquid argon and other media,” *Materials Research Express*, vol. 1, no. 1, pp. 015001–, 2014.

[350] T. Azami, D. Kasuya, R. Yuge, M. Yudasaka, S. Iijima, T. Yoshitake, and Y. Kubo, “Large-scale production of single-wall carbon nanohorns with high purity,” *J. Phys. Chem. C*, vol. 112, pp. 1330–1334, Feb. 2008.

[351] Y. Zhao, J. Li, Y. Ding, and L. Guan, “Single-walled carbon nanohorns coated with Fe_2O_3 as a superior anode material for lithium ion batteries,” *Chem. Commun.*, vol. 47, no. 26, pp. 7416–7418, 2011.

[352] W. Xu, Z. Wang, Z. Guo, Y. Liu, N. Zhou, B. Niu, Z. Shi, and H. Zhang, “Nanoporous anatase TiO_2 single-wall carbon nanohorns composite as superior anode for lithium ion batteries,” *Journal of Power Sources*, vol. 232, pp. 193–198, June 2013.

[353] S. Berber, Y.-K. Kwon, and D. TomÃąnek, “Electronic and structural properties of carbon nanohorns,” *Phys. Rev. B*, vol. 62, pp. R2291–R2294, July 2000.

[354] J.-M. Bonard, R. Gaál, S. Garaj, L. Thien-Nga, L. Forró, K. Takahashi, F. Kokai, M. Yudasaka, and S. Iijima, “Field emission properties of carbon nanohorn films,” *Journal of Applied Physics*, vol. 91, no. 12, pp. 10107–10109, 2002.

[355] T. Murakami, K. Ajima, J. Miyawaki, M. Yudasaka, S. Iijima, and K. Shiba, “Drug-loaded carbon nanohorns: adsorption and release of dexamethasone in vitro,” *Mol. Pharmaceutics*, vol. 1, pp. 399–405, Nov. 2004.

[356] K. Ajima, T. Murakami, Y. Mizoguchi, K. Tsuchida, T. Ichihashi, S. Iijima, and M. Yudasaka, “Enhancement of in vivo anticancer effects of cisplatin by incorporation inside single-wall carbon nanohorns,” *ACS Nano*, vol. 2, pp. 2057–2064, Oct. 2008.

[357] K. Murata, K. Kaneko, W. A. Steele, F. Kokai, K. Takahashi, D. Kasuya, K. Hirahara, M. Yudasaka, and S. Iijima, “Molecular potential structures of heat-treated single-wall carbon nanohorn assemblies,” *J. Phys. Chem. B*, vol. 105, pp. 10210–10216, Oct. 2001.

[358] S. Bandow, F. Kokai, K. Takahashi, M. Yudasaka, L. Qin, and S. Iijima, "Interlayer spacing anomaly of single-wall carbon nanohorn aggregate," *Chemical Physics Letters*, vol. 321, pp. 514–519, May 2000.

[359] J. Xu, H. Tomimoto, and T. Nakayama, "What is inside carbon nanohorn aggregates?," *Carbon*, vol. 49, pp. 2074–2078, May 2011.

[360] K. Murata, K. Kaneko, H. Kanoh, D. Kasuya, K. Takahashi, F. Kokai, M. Yudasaka, and S. Iijima, "Adsorption mechanism of supercritical hydrogen in internal and interstitial nanospaces of single-wall carbon nanohorn assembly," *J. Phys. Chem. B*, vol. 106, pp. 11132–11138, Oct. 2002.

[361] E. Bekyarova, K. Murata, M. Yudasaka, D. Kasuya, S. Iijima, H. Tanaka, H. Kahoh, and K. Kaneko, "Single-wall nanostructured carbon for methane storage," *J. Phys. Chem. B*, vol. 107, pp. 4681–4684, May 2003.

[362] V. Krungleviciute, A. D. Migone, M. Yudasaka, and S. Iijima, "CO_2 adsorption on dahlia-like carbon nanohorns: isosteric heat and surface area measurements," *J. Phys. Chem. C*, vol. 116, pp. 306–310, Jan. 2012.

[363] V. Krungleviciute, C. A. Ziegler, S. R. Banjara, M. Yudasaka, S. Iijima, and A. D. Migone, "Neon and CO_2 adsorption on open carbon nanohorns," *Langmuir*, vol. 29, pp. 9388–9397, July 2013.

[364] N. Sano, "Low-cost synthesis of single-walled carbon nanohorns using the arc in water method with gas injection," *Journal of Physics D: Applied Physics*, vol. 37, no. 8, p. L17, 2004.

[365] S. Bandow, A. Rao, G. Sumanasekera, P. Eklund, F. Kokai, K. Takahashi, M. Yudasaka, and S. Iijima, "Evidence for anomalously small charge transfer in doped single-wall carbon nanohorn aggregates with Li, K and Br," *Applied Physics A*, vol. 71, no. 5, pp. 561–564, 2000.

[366] H. J. Jung, Y.-J. Kim, J. H. Han, M. Yudasaka, S. Iijima, H. Kanoh, Y. A. Kim, K. Kaneko, and C.-M. Yang, "Thermal-treatment-induced enhancement in effective surface area of

single-walled carbon nanohorns for supercapacitor application," *J. Phys. Chem. C*, vol. 117, pp. 25877–25883, Dec. 2013.

[367] M. Vizuete, M. J. Gómez-Escalonilla, M. Barrejón, J. L. G. Fierro, M. Zhang, M. Yudasaka, S. Iijima, P. Atienzar, H. García, and F. Langa, "Synthesis, characterization and photoinduced charge separation of carbon nanohorn-oligothienylenevinylene hybrids," *Phys. Chem. Chem. Phys.*, vol. 18, no. 3, pp. 1828–1837, 2016.

[368] D. R. Dreyer, S. Park, C. W. Bielawski, and R. S. Ruoff, "The chemistry of graphene oxide," *Chem. Soc. Rev.*, vol. 39, no. 1, pp. 228–240, 2010.

[369] D. Chen, H. Feng, and J. Li, "Graphene oxide: preparation, functionalization, and electrochemical applications," *Chem. Rev.*, vol. 112, pp. 6027–6053, Nov. 2012.

[370] G. Srinivas, J. W. Burress, J. Ford, and T. Yildirim, "Porous graphene oxide frameworks: synthesis and gas sorption properties," *J. Mater. Chem.*, vol. 21, no. 30, pp. 11323–11329, 2011.

[371] J. Wang, L. Huang, R. Yang, Z. Zhang, J. Wu, Y. Gao, Q. Wang, D. O'Hare, and Z. Zhong, "Recent advances in solid sorbents for CO_2 capture and new development trends," *Energy Environ. Sci.*, vol. 7, no. 11, pp. 3478–3518, 2014.

[372] D. C. Marcano, D. V. Kosynkin, J. M. Berlin, A. Sinitskii, Z. Sun, A. Slesarev, L. B. Alemany, W. Lu, and J. M. Tour, "Improved synthesis of graphene oxide," *ACS Nano*, vol. 4, no. 8, pp. 4806–4814, 2010.

[373] Y. Shao, J. Wang, M. Engelhard, C. Wang, and Y. Lin, "Facile and controllable electrochemical reduction of graphene oxide and its applications," *J. Mater. Chem.*, vol. 20, no. 4, pp. 743–748, 2010.

[374] D. Yang, A. Velamakanni, G. Bozoklu, S. Park, M. Stoller, R. D. Piner, S. Stankovich, I. Jung, D. A. Field, C. A. Ventrice Jr., and R. S. Ruoff, "Chemical analysis of graphene oxide films after heat and chemical treatments by X-ray photoelectron and Micro-Raman spectroscopy," *Carbon*, vol. 47, pp. 145–152, Jan. 2009.

[375] E. H. Lock, D. Y. Petrovykh, P. Mack, T. Carney, R. G. White, S. G. Walton, and R. F. Fernsler, "Surface composition, chemistry, and structure of polystyrene modified by electron-beam-generated plasma," *Langmuir*, vol. 26, pp. 8857–8868, June 2010.

[376] S. Bourrelly, P. L. Llewellyn, C. Serre, F. Millange, T. Loiseau, and G. Férey, "Different adsorption behaviors of methane and carbon dioxide in the isotypic nanoporous metal terephthalates MIL-53 and MIL-47," *J. Am. Chem. Soc.*, vol. 127, pp. 13519–13521, Oct. 2005.

[377] Y. Belmabkhout, R. Serna-Guerrero, and A. Sayari, "Adsorption of CO_2 from dry gases on MCM-41 silica at ambient temperature and high pressure. 1: Pure adsorption," *Chemical Engineering Science*, vol. 64, pp. 3721–3728, Sept. 2009.

[378] T. Loiseau, C. Serre, C. Huguenard, G. Fink, F. Taulelle, M. Henry, T. Bataille, and G. Férey, "A rationale for the large breathing of the porous aluminum terephthalate (MIL-53) upon hydration," *Chemistry:A European Journal*, vol. 10, no. 6, pp. 1373–1382, 2004.

[379] W. Barthlott and C. Neinhuis, "Purity of the sacred lotus, or escape from contamination in biological surfaces," *Planta*, vol. 202, no. 1, pp. 1–8, 1997.

[380] F. Taherian, V. Marcon, N. F. A. van der Vegt, and F. Leroy, "What is the contact angle of water on graphene?," *Langmuir*, vol. 29, pp. 1457–1465, Feb. 2013.

[381] K. K. S. Lau, J. Bico, K. B. K. Teo, M. Chhowalla, G. A. J. Amaratunga, W. I. Milne, G. H. McKinley, and K. K. Gleason, "Superhydrophobic carbon nanotube forests," *Nano Lett.*, vol. 3, pp. 1701–1705, Oct. 2003.

[382] H. Liu, J. Zhai, and L. Jiang, "Wetting and anti-wetting on aligned carbon nanotube films," *Soft Matter*, vol. 2, no. 10, pp. 811–821, 2006.

[383] Y. C. Jung and B. Bhushan, "Dynamic effects of bouncing water droplets on superhydrophobic surfaces," *Langmuir*, vol. 24, pp. 6262–6269, May 2008.

[384] J. Yang, Z. Zhang, X. Men, X. Xu, and X. Zhu, "Reversible superhydrophobicity to superhydrophilicity switching of a carbon nanotube film via alternation of uv irradiation and dark storage," *Langmuir*, vol. 26, pp. 10198–10202, Apr. 2010.

[385] A. I. Aria and M. Gharib, "Reversible tuning of the wettability of carbon nanotube arrays: the effect of ultraviolet/ozone and vacuum pyrolysis treatments," *Langmuir*, vol. 27, pp. 9005–9011, June 2011.

[386] L. J. Ci and P. M. Ajayan, "Modifying surface structure to tune surface properties of vertically aligned carbon nanotube films," *Journal of Nanoscience and Nanotechnology*, vol. 10, pp. 3854–3859, June 2010.

[387] J. Yang, Z. Zhang, X. Men, X. Xu, and X. Zhu, "Reversible conversion of water-droplet mobility from rollable to pinned on a superhydrophobic functionalized carbon nanotube film," *Journal of Colloid and Interface Science*, vol. 346, pp. 241–247, June 2010.

[388] S. M. Kim, C. L. Pint, P. B. Amama, D. N. Zakharov, R. H. Hauge, B. Maruyama, and E. A. Stach, "Evolution in catalyst morphology leads to carbon nanotube growth termination," *The Journal of Physical Chemistry Letters*, vol. 1, no. 6, pp. 918–922, 2010.

[389] A. B. D. Cassie and S. Baxter, "Wettability of porous surfaces," *Trans. Faraday Soc.*, vol. 40, pp. 546–551, 1944.

[390] P. C. Ma, J.-K. Kim, and B. Z. Tang, "Functionalization of carbon nanotubes using a silane coupling agent," *Carbon*, vol. 44, pp. 3232–3238, Dec. 2006.

[391] J. T. Han, S. Y. Kim, J. S. Woo, and G.-W. Lee, "Transparent, conductive, and superhydrophobic films from stabilized carbon nanotube/silane sol mixture solution," *Adv. Mater.*, vol. 20, pp. 3724–3727, Oct. 2008.

[392] H. Gaspar, C. Pereira, S. Rebelo, M. Pereira, J. Figueiredo, and C. Freire, "Understanding the silylation reaction of multi-walled carbon nanotubes," *Carbon*, vol. 49, pp. 3441–3453, Sept. 2011.

[393] D. J. Babu, S. N. Varanakkottu, A. Eifert, D. de Koning, G. Cherkashinin, S. Hardt, and J. J. Schneider, "Inscribing wettability gradients onto superhydrophobic carbon nanotube surfaces," *Adv. Mater. Interfaces*, vol. 1, p. 1300049, Apr. 2014.

[394] M. Rahimi, J. K. Singh, and F. Müller-Plathe, "CO_2 adsorption on charged carbon nanotube arrays: a possible functional material for electric swing adsorption," *J. Phys. Chem. C*, vol. 119, pp. 15232–15239, July 2015.

Curriculum Vitae

Personal Information

Name	:	Deepu J. Babu
Date of birth	:	02/04/1986
Place of birth	:	Kerala, India
Address	:	Muttathupadom (H) Palampra P.O., Kanjirappally, Kottayam Kerala, India. PIN: 686518

Education

12/2011 - present	:	Dr. rer. nat. Dept. of Chemistry Technische Universität Darmstadt.
6/2008 - 7/2011	:	Master of Science (by research) Dept. of Metallurgy and Materials Engineering Indian Institute of Technology, Madras, India.
9/2004 - 5/2008	:	Bachelor of Technology Dept. of Mechanical Engineering T.K.M. College of Engg., Kerala University.
4/2002 - 5/2004	:	Higher Secondary Education St. Antony's public school, Kanjirappally Central Board of Secondary Education

List of thesis related publications

1. **Babu**[†], **D. J.**; Herdt[†], T. ; Okeil, S.; Bruns, M.; Staudt, R.; Schneider, J. J. "Bud type carbon nanohorns: Materials for high pressure CO_2 capture and Li-ion storage". *J. Mat. Chem. A (accepted).* doi:10.1039/c6ta03933b.

2. **Babu**[†], **D. J.**; Kühl[†], F. G. ; Yadav, S.; Markert, D.; Bruns, M.; Hampe, M. J.; Schneider, J. J. "Adsorption of pure SO_2 on nanoscaled graphene oxide"*RSC Adv.* 2016, 6 (43), 36834-36839.

3. Rahimi[†], M.; **Babu**[†], **D. J.**; Singh, J. K.; Yang, Y.-B.; Schneider, J. J.; Müller-Plathe, F. "Double-walled carbon nanotube array for CO_2 and SO_2 Adsorption" *J. Chem. Phys.* 2015, 143 (12), 124701.

4. **Babu, D. J.**; Yadav, S.; Heinlein, T.; Cherkashinin, G.; Schneider, J. J. "Carbon dioxide plasma as a versatile medium for purification and functionalization of vertically aligned carbon nanotube" *J. Phys. Chem. C* 2014, 118 (22), 12028-12034.

5. **Babu**[†], **D. J.**; Varanakkottu[†], S. N.; Eifert[†], A.; de Koning, D.; Cherkashinin, G.; Hardt, S.; Schneider, J. J. "Inscribing wettability gradients onto superhydrophobic carbon nanotube surfaces" *Adv. Mater. Interfaces* 2014, 1 (2).

6. Rahimi, M.; Singh, J.; **Babu, D. J.**; Schneider, J. J.; Müller-Plathe, F. "Understanding carbon dioxide adsorption in carbon nanotube arrays: Molecular simulation and adsorption measurements" *J. Phys. Chem. C* 2013, 117, 13492-13501.

7. **Babu, D. J.**; Lange, M.; Cherkashinin, G.; Issanin, A.; Staudt, R.; Schneider, J. J. "Gas adsorption studies of CO_2 and N_2 in spatially aligned double-walled carbon nanotube arrays" *Carbon* 2013, 61, 616-623.

8. Dixon, D.; **Babu, D.J.**; Langner J.; Bruns, M.; Pfaffmann, L.; Bhaskar, A.; Schneider, J. J.; Scheiba, F.; Ehrenberg, H.; "Effect of oxygen plasma treatment on the electrochemical performance of the rayon and polyacrylonitrile based carbon felt for the vanadium redox flow battery application" (submitted).

9. **Babu, D. J.**; Bruns, M.; Schneider, R.; Schneider, J. J. "Influence of nitrogen doping on the CO_2 adsorption characteristics of carbon materials" (under preparation)

10. Patzsch, J; **Babu, D. J.**; Staudt, R.; Schneider, J. J. “Mesoscopic nanocrystalline silicon carbide tubes and nanoporous carbon tubes for high pressure carbon dioxide adsorption” (under preparation).
11. **Babu, D. J.**; Mail, M.; Barthlott, W.; Schneider, J. J. Salvinia effect in superhydrophobic vertically aligned carbon nanotubes (under preparation).

List of conferences/seminars

1. **Babu, D. J.**; and Schneider J. J. “Bridging the gap: Vertically aligned carbon nanotubes as unique mid-pressure gas adsorbents” *Deutsche Zeolith Tagung*, March 02 - 04, 2016, Gießen (Poster).
2. **Babu, D. J.**; and Schneider J. J. “Understanding gas adsorption in 3D CNT architectures” *MRS Fall Meeting*, November 29 - December 4, 2015, Boston, USA (Talk).
3. **Babu, D. J.**; and Schneider J. J. “High pressure adsorption studies on carbon tubes, vertically aligned carbon nanotubes and carbon nanohorns” *6. Doktorandenseminar Adsorption* (Organized by Max-Planck-Institut für Dynamik Komplexer Technischer Systeme, Magdeburg), August 25 - 26, 2015, Magdeburg (Talk).
4. **Babu, D. J.**; and Schneider J. J. ”Gas adsorption and selectivity studies on vertically aligned carbon nanotube arrays” *5. Doktorandenseminar Adsorption* (Organized by Hochschule Offenburg and ProcessNet), September 23 - 24, 2014, Offenburg (Talk).
5. **Babu, D. J.**; Rahimi, M.; Müller-Plathe, F.; Staudt, R.; Schneider, J. J. “Aligned carbon nanotubes as porous materials for gas adsorption” *Jahrestreffen der Fachgruppe Adsorption* March 5 - 6, 2014, Fulda (Poster).

Darmstadt 14.09.16